University of Nottingham
UK | CHINA | MALAYSIA

Investigation of PBF-LB stainless steels and lattice structures for crashworthiness applications

Diego Della Crociata

Thesis

Submitted to University of Nottingham

for the degree of

Doctor of Philosophy

Faculty of Engineering

October 2024

Acknowledgments

It seems yesterday that I started my PhD, enthusiastic about the project that I was about to undertake. And now here I am, sitting and writing the acknowledgements of my PhD thesis. I am still realising that it is time to wrap up my experience at CfAM. It has been intense 3 and a half years, made of challenges, learning and hard work, but also new great connections, perspectives, and lots of laughs and reciprocal support.

What I am taking away is a wide knowledge in my specialisation topics. Along with that, this experience has been fundamental for my personal growth. And I could reach that with the people that I met in this fantastic journey.

First of all, I would like to thank my supervisors Prof Ian Maskery, Prof Marco Simonelli and Prof Richard Hague, for giving me the opportunity to do research on this exciting project. It has been an honour for me to work with them and contribute to novelties in the project. I enjoyed the technical discussions on every topic, from metallurgy to printing process, testing, design. I learnt how to approach and develop a research project. Moreover, thank you for the relentless effort in supporting me any time I needed guidance and feedback on presentations or writing of papers. Moreover, I appreciated your effort into teaching me how to approach life in the most effective way. Being questioned, never taking anything for granted, thinking out of the box. It has been a challenging experience, but I was inspired by your work and the goals that you reached. That has been a decisive factor for me to put all the energies I had on this project.

I cannot forget to mention Prof Luke Parry, Prof Negar Gilani and Dr Zhiyi Zou. Thank you for the talks on technical topics, but also on sharing your experiences which were important lessons for me to work on my PhD as a whole.

Huge thanks go Mirela and Yuan, who were there to solve any problem I faced, as well as all technicians that made possible for me to perform any experiment planned for my project, at CfAM lab, nmRC and Wolfson. They are a fundamental part of University, having to deal with a lot of workload but still providing high value results. Special thanks go to the CfAM technicians. Mark East, for his precious help and information on anything that concerned the lab. Mark Hardy, for teaching me the secrets of PBF-LB and the SLM125. Adam Whitbread, for supporting me in solving many problems I encountered in the lab. But most of all, thank you guys for being one of the reasons why I liked to go to the lab every day even when experiments were failing. Nigel Neate, thank you for finding time to support me in my work at the nmRC, I learnt a lot every time I asked you a question. Finally, thank you Richard Omer, Kieran Orange and Daniel Flower for the support at the Wolfson facilities, your effort has been much appreciated.

How can I not mention the great friends I made during my time in AMB. If I am now submitting my PhD thesis, this is also thanks to you that supported me throughout my journey. Therefore, thank you very much Ally, Anna, Charlie, Dan, Dani, Francisco, Giuseppe, Hendrick, Huseyin, Ian, Inês, James, Jonty, Mohamed, Mostafa, Oliver, Sam, Seb, Siddhi, Sim, Xiangyun. I have not forgot about you Francesco; it was a pleasure to meet you even if just for a few months, although we will definitely meet again.

Being in Nottingham gave me the chance to sit again on a drum stool behind a drum kit, enjoying what I like the most in my life with some great people as Andrea, Andrea, Giorgio, Iriome, Matteo, Sofia. We smashed it together during our gigs, and it was great to hang out with you as friends.
It has been a pleasure to share, for almost my entire staying in Nottingham, the flat with Kamil. He has been a nice and serious friend, and I will remember all the nice conversations done during our meals or the moments shared while hanging out or watching movies. Even if for short time, it was nice to talk with Yukta.
Thank you, Katie, you are a great person. I am grateful to have met you, and I wish you all the best in your life.
It is hard to be far from great friends as you are: Alberto, Alessio, Giulia, Ilenia, Luca, Marco, Salvatore, Savino, Stefano. I am happy though to meet you any time there is the chance, to spend precious time with you.
I am extremely grateful to have such great friends that I have been knowing for so many years since school. Ale, Eli, Fra, Marco, Matteo, Santo: thank you for being such an important part of my life and supporting me from distance, when not being together in person.
Finally, the biggest thanks go to my family. They have always supported me in my choices and gave me precious advice when necessary. It is hard to live far from you, but you always made me feel close to you, any part of Europe I was living in. I am grateful to have such a supportive family, and I am looking forward to being as supportive of the new little members.

Abstract

Metal additive manufacturing, and in particular powder bed fusion – laser beam (PBF-LB), has proved to be an effective technology in the industrial field to produce complex designs with performant mechanical properties. However, the benefits of PBF-LB on microstructural tailoring and design of innovative structures are yet not fully investigated in industrial applications for energy absorption. The aim of this thesis is to exploit PBF-LB for controlling the microstructural features of two strain hardening stainless steels and resulting mechanical properties, as well as printing lattice structures made of a newly designed unit cell with the investigated materials, for structural investigations of better crashworthy applications in the industry.

The strain hardening mechanism of 316L, characterised by good strength values and exceptional ductility, was analysed by means of a tapered specimen at different strain values. The study suggested that the predominant deformation mechanism, up to the initial plastic regime, was deformation slip. Twin bands formed as soon as the material locally entered the plastic regime, suggesting that twinning-induced plasticity acted locally in [111] oriented grains. At a 26% plastic strain threshold, twinning became the main deformation mechanism, gradually affecting all grains up to 60% plastic strain. Twin bands formed in low amount in small grains, revealing the importance of grain size in the activation of twinning-induced plasticity, and up to a 28% concentration at the necking of the tapered specimen. This contributed to a hardness 65.2% higher than the as-printed condition. Experimental results were assisted by computational studies. This study provides a comprehensive approach for the characterisation of 316L strain hardening, for the understanding of the interaction between deformation glide and twinning and its evolution at different laser processing conditions.

The martensitic strain hardening steel 17-4 PH was investigated due to its transformation-induced plasticity and noteworthy strength values. The investigation was performed on two PBF-LB linear energy densities at the extremes of the process window, 0.67 and 0.29 J/mm, to determine the microstructural and phase content sensitivity to energy density. It was found that higher and lower energy densities provided dissimilar microstructures (complex bimodal versus homogeneous), gran size distribution (up to 33 μm versus up to 15 μm) and phases content (3.8% versus 11.1% retained austenite). The mechanical testing and in-situ x-ray diffraction showed contrasting mechanical properties, lower energy density produced lower yield strength but similar tensile strength due to more predominant transformation-induced plasticity. Transformation-induced plasticity caused a similar final austenite content, 2.1% and 2.3% for higher and lower energy density. These findings show that, investigating the material process window, different mechanical properties during plastic deformation can be achieved. This means understanding of the transformation-induced plasticity activity behaviour shown by 316L in a condition without post-printing heat treatments.

The investigation on 17-4 PH and its strain hardening mechanism was adopted for a study on the compressive behaviour of lattice structures, by means of experimental and computational approach. A newly designed unit

cell derived from TPMS structures, honeycomb gyroid, was utilised in the PBF-LB process for crashworthy applications in divergent configurations at different strain rates. The configurations were uniform or graded, on the volume fraction (from 0.2 to 0.7) and material model (higher and lower energy densities). The strain rates ranged from 10^{-3} s^{-1} to 2000 s^{-1}. The computational study confirmed the contrasting mechanical response at quasi-static conditions. Higher uniform 0.45 volume fraction and low energy density provided 13.9 J/g absorption for 4x4 unit cell repetition, while the high energy density 0.2/0.7 grading volume fraction increased up to 20.2 J/g thanks to a 28.3% more extended densification plateau. Computational dynamic tests proved the absorption capabilities of the honeycomb gyroid structures, with values up to a range of 18 J/g to 15.9 J/g at increasing strain rates for 2x2 unit cell repetition. Improvements in the computational model were considered and corrective actions proposed. This study enables a first approach for predicting the deformation behaviour of TPMS based lattice structures printed with strain hardening steels for crashworthy applications.

This thesis has dealt with the analysis and understanding of the onset and development of strain hardening mechanisms shown by twinning-induced plasticity and transformation-induced plasticity stainless steels. This comprehension has been applied to innovative lattice structures for crashworthy applications. The acquired knowledge on the materials can be used to explore in detail the application materials, for a deeper understanding of the most performant configurations in energy absorption, as well as different strain hardening steels or materials that show complex phenomena in the plastic regime. The study on the lattice structures enables to investigate several configurations of any other unit cell, existing or newly developed, to push further the absorption performance of industrial applications, and support physical experiments with a computational modelling.

Publications

D. Della Crociata, I. Maskery, R. Hague, M. Simonelli, “On the development of twinning-induced plasticity in additively manufactured 316L stainless steel”, Additive Manufacturing Letters, Volume 7, 2023, 100176, ISSN 2772-3690, https://doi.org/10.1016/j.addlet.2023.100176.

D. Della Crociata, I. Maskery, H. Eskandari Sabzi, P.E.J Rivera-Díaz-del-Castillo, R. Hague, M. Simonelli, “Microstructure and crystallographic phases sensitivity to process parameters in a bespoke PBF-LB 17-4 PH alloy”, to submit for review.

H. Eskandari Sabzi, S.H. Lim, D. Della Crociata, R. Castellote-Alvarez, D. San-Martín, X. Hao, P.P. Choi, M. Simonelli, P.E.J Rivera-Díaz-del-Castillo, “Genetic design of precipitation-hardening stainless steels for additive manufacturing”, Acta Materialia, Volume 274, 2024, 120018, ISSN 1359-6454, https://doi.org/10.1016/j.actamat.2024.120018.

Conferences

ILAS2023, speaker, 22 – 23 March 2023. “Twinning in 316L fine microstructures generated by L-PBF: opportunities for energy absorption applications”. D. Della Crociata, I. Maskery, R. Hague, M. Simonelli.

AAMS2023, speaker, 27 – 29 September 2023. “Phases evolution in additive manufactured TRIP custom 17-4PH alloy: opportunities for energy absorption applications”. D. Della Crociata, I. Maskery, R. Hague, M. Simonelli.

Table of contents

List of figures

List of tables

Abbreviations

3D	Three-dimensional
AM	Additive manufacturing
BC	Boundary condition
BCC	Body-centred cubic
BCM	Beam compensation
BCT	Body-centred tetragonal
BD	Build direction
BSE	Back-scattered electron
CAD	Computer aided design
EBSD	Electron backscattered electron
EDX	Energy-dispersive x-ray spectroscopy
FCC	Face-centred cubic
FEA	Finite element analysis
GB	Grain boundary
GND	Geometrically necessary dislocations
ICP-OES	Inductively coupled plasma - optical emission spectrometry
IPF	Inverse pole figure
J-C	Johnson-Cook
KAM	Kernel average misorientation
LED	Linear energy density
LOF	Lack of fusion
PBF-LB	Powder bed fusion – laser beam

PH	Precipitation hardening
RF	Reaction force
RP	Reference point
SEA	Specific energy absorption
SEM	Secondary electron microscopy
SFE	Stacking fault energy
SHR	Strain hardening rate
SIMT	Strain-induced martensitic transformation
Stl	Standard triangle language
TB	Twin boundary
TPMS	Triply periodic minimal surface
TRIP	Transformation-induced plasticity
TWIP	Twinning-induced plasticity
UC	Unit cell
UTS	Ultimate tensile strength
VED	Volumetric energy density
VF	Volume fraction
XRD	X-ray diffraction
XRF	X-ray fluorescence

Nomenclature

P	Laser power
v	Laser scan speed
$wt\%$	Element weight percentage
Cr_{eq}	Chromium equivalent
Ni_{eq}	Nickel equivalent
c_p	Specific heat capacity
ρ	Density
T_m	Melting temperature
h_d	Hatch distance
Te	Equilibrium temperature
γ	Austenite
α’	Martensite
α	Ferrite
σ_Y	Yield strength
ΔT	Undercooling
M_s	Martensite start temperature
M_f	Martensite finish temperature
$M_S{}^{\sigma}$	Stress-assisted martensitic transformation temperature
M_d	Upper limit of martensitic transformation
$M_{d30/50}$	Temperature for 50% martensitic transformation
σ	Stress
T	Temperature

θ	Incident and diffraction angle
d_{hkl}	Interplanar spacing
m_{SR}	Strain rate sensitivity
$\dot{\varepsilon}$	Strain rate
R	Solidification rate at the solid-liquid interface
G	Temperature gradient
ε	Strain
λ_1	Primary cell spacing
E^*	Relative elastic modulus
ρ^*	Relative density
σ^*	Relative collapse strength
U_G	TPMS gyroid equation
U_{hon}	TPMS honeycomb gyroid equation
η	Energy absorption efficiency
ε_D	Densification strain
σ_{peak}	Maximum transmissible stress
λ	X-ray wavelength
d-spacing	Minimum distance between two parallel planes of atoms
ε_f	Elongation at failure
L_T	Layer thickness
P_D	Point distance
E_T	Exposure time

1 Introduction

The focus of this chapter is to provide the background of additive manufacturing (AM) and the relevant framework for this thesis, with Section 1.1. In Section 1.2 the outline of the main aim and objectives of this work is presented, and finally Section 1.3 presents the structure of the present thesis.

1.1 Laser powder bed fusion and energy absorption applications

AM encompasses a range of techniques that build 3D parts by adding thin layers of materials through the input of a digital model, contrarily to subtractive manufacturing techniques[1]. This allows complex and customised parts without need for tooling thus smoothening the production steps with respect to conventional manufacturing processes. In addition, the part count to be realised and assemble is reduced. The technological improvements have made metal AM a new way to produce high performance components in different sectors, including aerospace, medical, energy and automotive [2–5]. The PBF-LB process has proven to be the most performing technique among the metal AM manufacturing processes, thanks to its ability to produce complicated geometries while keeping the highest resolution and precision [6].

The PBF-LB process consists of a laser source that selectively melts a powder bed made of metal powder, scanning with a specific set of process parameters to reach the targeted mechanical, microstructural properties and surface finish. This process is repeated layer-by-layer until the parts are printed in their entire height. The main advantage by using PBF-LB is the freedom of printing complex shapes which are able to accommodate additional requirements for designers in structural applications [3]. The printing process also enables the use of several materials, each showing distinct mechanical properties in terms of strength and ductility. The cause is the specific range of phase and microstructural content, depending on the production process parameters. The mechanical properties can be compared to select the most performing structure and materials for the specific application. All this has been found fundamental for the research of components used for energy absorption purposes, to improve the protection of components or persons [7]. The focus of this thesis is the PBF-LB technology with emphasis on strain hardening (or work hardening) stainless steels and lattice structures for energy absorption purposes.

The mechanical properties obtained with PBF-LB are numerous and are chosen according to the required application. Titanium alloys have the advantage of being lighter than steels and showing higher yield and ultimate tensile strength than most steels, with the high strength and subsequent hardness at the expense of ductility [8]. Considering crashworthy applications, titanium mechanical properties would allow an initial high response to the applied load, however the limited ductility impacts the extension of the deformation for the absorbing structure [9]. Aluminium alloys have the advantage of being lightweight materials as opposed to

titanium and steel alloys. High-strength aluminium alloys are characterised by low density, great strength and corrosion resistance, which makes them suitable for energy absorption applications [2]. However, the formation of hot cracks during the solidification process makes them difficult to process, particularly for PBF-LB technologies.

Stainless steels have been extensively studied and used thanks to the simplicity of processability and relatively competing price compared to titanium and aluminium alloys [10]. Stainless steels have limited defects during the manufacturing process compared to any other metal alloys. Another advantage of stainless steels in PBF-LB is the combination of resistance to corrosive environments and good mechanical properties, specifically for alloys that show work-hardening behaviour when they are deformed in the plastic regime, reaching similar strength as titanium alloys while keeping good ductility [11]. A class of stainless steels, being composed fully of austenite and therefore called austenitic stainless steels, presents a phenomenon called twinning-induced plasticity (TWIP). The latter creates bands in the microstructure and contributes to the increase of strength of the material, in particular to the high elongation at failure (ε_f) [12]. Another class of stainless steels, composed by a complexity of phases including austenite, martensite and ferrite, referred to as martensitic stainless steels, undergo a transformation-induced plasticity (TRIP). The latter causes a transformation of austenite into martensite [13]. High strength is reached, and the strengthening contributes to increase of ductility as well. These exceptional behaviours make strain hardening stainless steels suitable for applications where high strength and ductility are required, including crashworthy applications.

The challenge linked to PBF-LB is the thermal history during the manufacturing process as it contributes to different microstructures from conventionally made materials, even for strain-hardening stainless steels [14]. The large range of process parameters and energy densities demands deep investigation of the microstructural and phase features, to explain the onset of the strain hardening behaviour and how it affects the mechanical properties of the material. For this reason, crashworthy applications can benefit from unexplored as-built conditions for improvement of the absorption requirements.

Crashworthy applications require freedom of design, which is an advantage by PBF-LB. This allows the development of new design methods for AM. Of particular importance is the investigation and advancement of topologically optimised designs [15] or lattice structures with the target of keeping high mechanical properties while reducing weight and thus fuel consumption [16–18]. Furthermore, lattice structures for energy absorption have been deeply investigated with unit cells from the strut-based topology [19]. Strut-based lattices encompass a wide range of unit cell topologies, some of which have directional stiffness for energy absorption, while others demonstrate a homogeneous capacity to withstand external load [20]. The main disadvantage of these unit cells comes from the stress concentration at the nodes where struts connect, which is detrimental to the stability of the lattice structure and limits the capabilities in energy absorption applications. Hence, a new class of triply periodic minimal surface (TPMS) lattice structures has been considered as more performant. It is characterised by a significant reduction in stress concentration points thanks to the mean zero curvature on

each point of the unit cell [21]. Moreover, the mechanical properties of TPMS based lattices in different orientations are more homogeneous than strut-based lattices, or they are anisotropic but present higher directional stiffness. This makes them suitable for energy absorption applications. TPMS based lattices research is still open to improvements, in terms of configurations and materials, to increase the knowledge of optimal performance to reach for crashworthy applications. There is a new unit cell, the honeycomb gyroid, which shows the highest anisotropy among all lattice structure unit cells and favours exceptional absorption in the extrusion direction. However, the perpendicular direction results weak. By investigating the most appropriate application material along with process parameters, as well as the most appropriate geometrical configuration, the advancements in energy absorption would be dramatically increased.

Lattice structures have been printed, to explore the absorption capabilities, with different unit cells and materials including titanium, aluminium and stainless steel alloys. In view of the deviations derived from the unit cell topology, general observations were made. Aluminium alloys, such as AlSi10Mg, present the lowest compressive strength, accompanied though by the largest elongation at failure [22]. Titanium alloys, for example Ti6Al4V, depict high compressive strength with reduced extension [23]. The family of strain-hardening stainless steels, instead, shows a range of compressive strength and ductility depending on whether the alloy is austenitic, such as 316L, or martensitic, for instance 17-4 PH, which favour the ductility similarly to aluminium or strength likewise titanium, respectively [24,25]. Moreover, by using the proper range of process parameters, stainless steels lattice structures tune the as-built microstructure for a balanced combination of strength and ductility and subsequent improvement of crashworthy capabilities [26].

It is important to consider that strain rates determine different deformation behaviour of the lattice structures under compression with external loads. Low strain rates depend on the properties of the base material and the geometry of the lattices; conversely, high strain rates involve additional physical phenomena, including micro-inertia, trapped gas in the lattice structure and macro-inertia [27]. The literature has not investigated yet the entire range of capabilities of lattice structures printed with PBF-LB and performant metal alloys, at different strain rates. The potential of PBF-LB technology is to explore the process window for work hardening stainless steels, which show the best combination of strength and ductility as opposed to other steels and materials. Favourable microstructures can be determined and exploited for improved mechanical response under specific external loads. The second aspect that needs to be considered is the geometrical functional grading of the resulting lattice structure that responds to the applied load, to extend the elongation capacity while not transmitting excessive stress to the protected object or person for an efficient absorption. This must be made at different strain rates, to understand the capabilities of the lattice structures in different compression conditions. The outcome clarifies the role of maximising energy absorption by concurrent geometrical and microstructural optimisation.

1.2 Research aims and objectives

The aim of this research is to provide understanding of the deformation behaviour of two strain hardening stainless steels in the plastic regime produced with PBF-LB, 316L and 17-4 PH, defining methodologies that enable an extended knowledge of the strain hardening behaviour, to improve energy absorption applications through a combination of microstructure tailoring and cellular structure design. An investigation of the onset of the specific deformation behaviour of 316L and the microstructural control of 17-4 PH under different energy densities is carried out. The knowledge gained in this study is then exploited in the investigation of innovative lattice structures printed with PBF-LB, not yet fully inspected, to produce lightweight components that can absorb energy in automotive crashes under the application of external loads at dissimilar strain rates. Functional grading of the structure and process parameters variation are applied for comparison.

In order to fulfil the predetermined aim, the following objectives were addressed:

- **Stainless steels and lattice structures background.** The literature review was presented to point out methodologies for the investigation and quantification of the strain hardening behaviours of 316L (TWIP) and 17-4 PH (TRIP) as well as the design of crashworthy lattice structures. The review emphasised: the lack of understanding for the onset of TWIP and its interaction with deformation slip (or deformation glide, dislocation movement) in 316L; the lack of knowledge for the complex microstructures and properties through TRIP in 17-4 PH provided by laser processing parameters, due to homogenisation heat treatment processes; the weakness of traditional strut-based lattice structures to be used in lightweight crashworthy applications as opposed to TPMS based lattices or their derivation, for example the honeycomb gyroid unit cell, in particular stress concentration issues.

- **Quasi-static TWIP investigation.** Investigation on 316L stainless steel was performed to understand how TWIP affects the plastic regime of the material. The aim was to understand the onset of each deformation behaviour, between deformation slip and twinning, the onset of twinning and its evolution over plastic strain. A tapered specimen design was used to experimentally observe the onset and evolution of twinning along the axis of a specimen with decreasing cross-section, to explore different strain values, during quasi-static mechanical testing. A finite element analysis model was used to predict the deformation behaviour and extrapolate the stress and strain field over time. The synergistic interaction of deformation glide and twinning was pointed out.

- **Quasi-static TRIP investigation.** 17-4 PH was studied to control how energy density affects the complex microstructure and phase content of the as-printed condition. Moreover, the evolution of TRIP during deformation and at failure was evaluated too. In order to do so, in-situ x-ray diffraction analysis was performed during tensile testing on flat specimens. Post-processing of diffraction patterns and mechanical data allowed to extrapolate the evolution of retained austenite transforming into martensite. The resulting final microstructure and texture were discussed considering the phase content change.

- **Sheet-TPMS based lattice structures for energy absorption at different strain rates.** Design of an environment for sheet-TPMS based lattice structures made with PBF-LB metal alloy for energy absorption purposes. The objective was achieved by exploiting the TRIP effect of 17-4 PH, using the energy densities explored in the previous objective. The honeycomb gyroid was printed in different configurations, with uniform and graded unit cell (UC) and uniform and graded process parameters in the manufacturing process. Mechanical testing was performed in compression on the least stiff orientation at dissimilar strain rates. A finite element analysis was created to predict the deformation behaviour, so that future lattices configurations can be studied by means of simulations thus saving from the drawback of printing physical components. The analysis pointed out the configuration that provided the highest absorption of energy during an automotive crash.

1.3 Thesis outline

The present thesis is divided into 8 Chapters. The first Chapter has been a brief introduction to AM manufacturing process, its applications and advantages, the current drawbacks and the lack of knowledge in specific deformation behaviours that can be used in advanced protection applications. Chapter 2 presents the state of the art of AM of metal alloys, PBF-LB, the properties of stainless steels and a distinction between the two application materials. The Chapter also contains a description of lattice structures and their role into energy absorption in crash applications. Chapter 3 presents the methodology followed to undertake the materials investigation and the study of the lattice structures. The results obtained in this study are presented in Chapter 4 to Chapter 6.

Chapter 4 describes the twinning-induced plasticity shown by 316L stainless steel produced with PBF-LB, its onset and evolution over plastic strain, and how it affects the material deformation along with deformation glide.

Chapter 5 investigates the transformation-induced plasticity that PBF-LB 17-4 PH stainless steel undergoes when it is plastically deformed. Different energy densities were investigated to explain the complexity of the phase content and microstructure that can be obtained for this material, and their evolution.

Chapter 6 is a presentation of a specific lattice structure not fully investigated yet, and how applying a transformation-induced plasticity material with dissimilar configurations in terms of structure and material grading can be exploited for energy absorption purposes also on unit cells with low stiffness.

Chapter 7 presents a general discussion on the results obtained in the present work and their implication into the field of lightweight structures for energy absorption.

Chapter 8 is a summary of the work that has not been part of the present thesis, but it will help understanding more phenomena for the application of the studied lattice structures into the energy absorption for automotive crashes.

2 Literature review

The focal point of this Chapter is on the relevant literature required for the comprehension of PBF-LB of strain hardening stainless steels and lattice structures. At first, stainless steels are introduced, and the focus is given to austenitic and martensitic stainless steels. For each of the two classes, the two alloys used in this thesis are described when produced via PBF-LB. Microstructure, mechanical properties and the peculiar deformation behaviour, TWIP and TRIP, are investigated. Defects caused by the printing process are next discussed. Lastly, the implications on the strain rate applied during deformation of the application materials is introduced, to understand how this will affect the performance of lattice structures printed with the mentioned alloys. The focus will then be on lattice structures, with a classification of the two main kinds of lattice structures used in research and application context and the focal point on the TPMS derived unit cell used for this thesis. Finally, the focus will be on energy absorption performance with lattice structures.

2.1 Metal additive manufacturing

The typical workflow for the manufacturing of a part for any of the metal AM processes is depicted in Figure 2.1. The steps can be summarised in:

- **Design**: the physical object is designed into a CAD file with or without geometric features, if they are to be machined in a later step (i.e. threads, fillets).

- **Conversion**: the CAD file must be converted to data that can be understood by the metal AM printed and this is achieved with the standard triangulation language (.stl) format file.

- **File transfer and Configuration**: the .stl file is uploaded into a software so that the building environment can be created, and the part sliced into layers (conversion of 3D into 2D data). Moreover, the process parameters are set.

- **Print**: it is the activity that physically produces the object and generally the most time-consuming step.

- **Removal**: once produced, the part can be removed from the build chamber and the substrate. It can require, depending on the technology, additional steps, for example debinding for the BJ.

- **Machining**: this stage is used only if the application needs post-processing to meet specific tolerances or surface finishes.

- **Heat treatment**: it is another optional step and adopted if the part needs a relief of internal stresses generated by the printing process. Additionally, heat treatment can be targeted if specific mechanical properties need to be obtained or porosity has to be reduced (i.e. HIP, annealing, aging).

- **Inspection**: non-destructive tests can be utilised for a final check of the printed part, including surface roughness and dimensional accuracy.

- **Handover**: after the printed part has been checked, it is handed over to the final user.

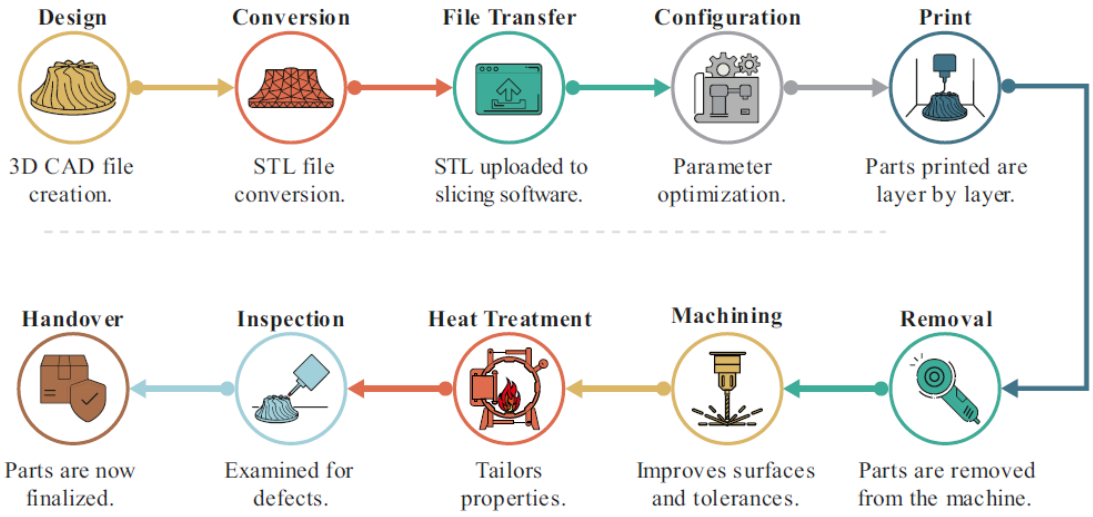

Figure 2.1. Workflow of a typical metal AM manufacturing process [28].

2.1.1 Powder Bed Fusion – Laser Beam

PBF-LB, also referred to as laser powder bed fusion (L-PBF) or selective laser melting (SLM), is a metal AM technique and one of the most widespread AM processes, thanks to the possibility of producing mechanical components with good levels of geometrical accuracy, surface quality and mechanical properties [29]. It involves a powder bed, scanned by a laser source on specific areas and moved by a chain of optical mirrors according to the input scanning path. The process takes place in an inert gas environment, the gas being argon (Ar) or nitrogen (N_2). The aim is to minimise the effects of high temperatures on the oxidation and reduce the impurities [30].

The variables involved are shown in Figure 2.2 and are referred to as process parameters [31]. The choice of the process parameter set to generate a part affects the final quality and mechanical properties of the part itself. In Figure 2.2(a) it is possible to see: the laser power (P) and laser scanning speed (v), which define at what rate the powder bed is scanned as well as the continuity of the track; the hatch distance (h_d), the distance between two adjacent scan lines; the layer thickness (L_T), the distance along the build direction (BD) perpendicular to

the scanning plane, that allows a layer-by-layer printing; roller speed, the speed at which the powder is spread onto the build plate; inert gas flow. The laser system can be programmed with a pulse width modulated (PWM) or continuous (CW) mode. In CW process, energy is continuously deposited to the material being scanned [32], while the former mode consists of a modulation of the laser emission by a fast switch of the electrical current that is provided to the pumping diodes. The result is a fast response of the fibre laser with pulse durations in the order of magnitude of microseconds [33]. As for the PWM, further variables to consider are the point distance (P_D), that is the gap between each scanned spot, and the exposure time (E_T), namely the time at which the laser is on, shown in Figure 2.2(b). Figure 2.2(c) provides an overview of the layer-by-layer process that defines PBF-LB, with laser scanning tracks that can change orientation to obtain specific properties on the final parts [34]. Two other important parameters, not shown in the figure, are the temperature at which the platform is held during the build and the O measure in the processing chamber. They affect the melting dynamics during the manufacturing process and therefore can be optimised for the required porosity level and mechanical properties.

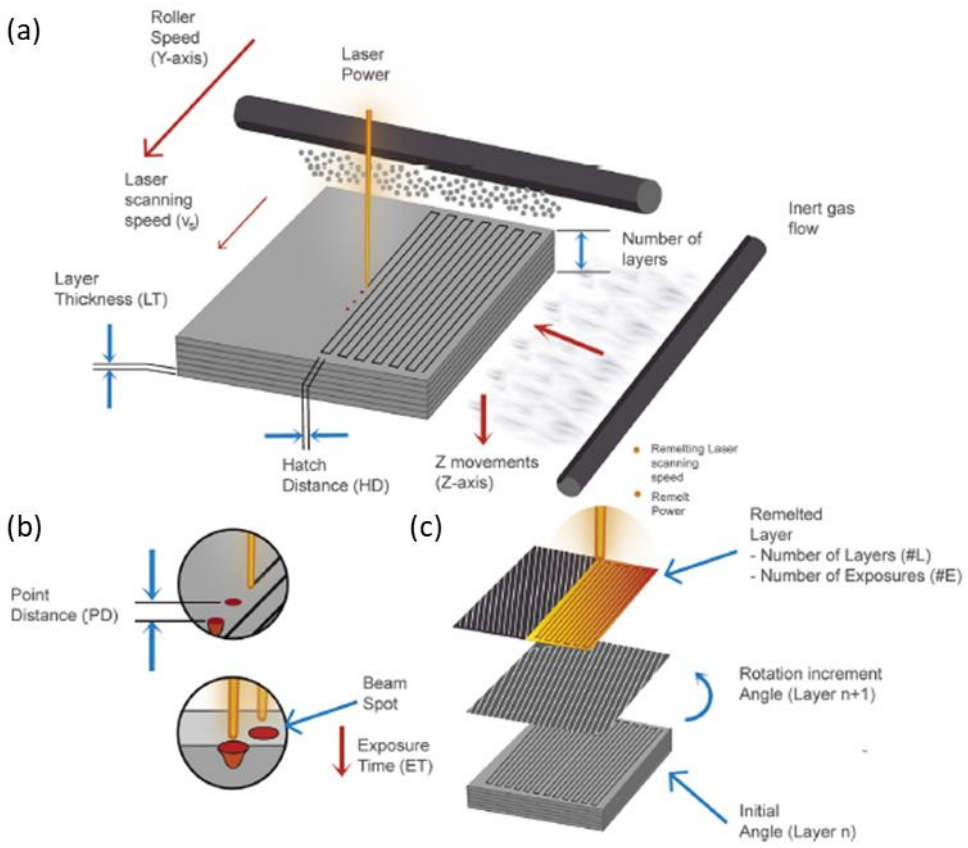

Figure 2.2. Set of process parameters related to PBF-LB: a) variables from the build chamber; b) modulated laser related parameters; c) melting history across layers [31].

In the process, the roller (or wiper) is fed with a quantity of powder coming from the doser (or hopper). The wiper moves from the feeding position to the opposite side, spreading the powder along its path on the build platform thus creating a new layer. The powder in excess is poured into an overflow, usually separated from

the build chamber, which allows to extract the powder at the end of the build for sieving and reuse. The wiper stops in the forward position to allow the laser to melt the powder according to the build file. Here, the process parameters inserted in the build file preparation software instruct the 3D printer how to scan the powder. Once the layer is melted, the build plate is lowered along the z-axis (BD) by a value corresponding to the L_T and the process is repeated. In the build chamber, throughout the entire job, the shielding gas flow is running perpendicular to the wiper movement.

The way the laser melts the layer is depending on the scan strategy used, that is the direction of the scanning lines. There are several strategies, with the most representative shown in Figure 2.3.

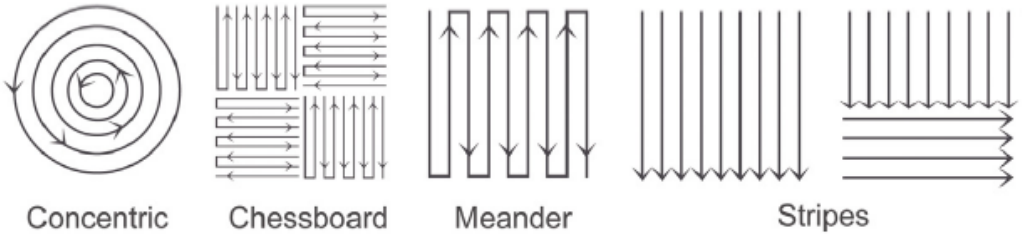

Figure 2.3 The most representative laser scanning strategies: concentric, chessboard, meander, stripes (from left to right) [34].

Concentric scan strategy was found useful for improvement of geometry in small struts, but at the same time it can leave residual compressive stress in the core and residual tensile stress on the edge [35]. Chessboard resulted a suitable scanning strategy to reduce residual stresses and increase relative density [36]. Meander strategy was found to be quick and provide good surface quality and mechanical properties to components, when each subsequent layer has an orientation (usually 67° or any other prime number) compared to the previous one as an isotropic heat distribution is provided to the layers [37]. Good mechanical properties are also caused by a reduction of porosity and residual stresses. All the mentioned scanning strategies overcame the original stripe technique, considered to be slow and causing issues such as delamination [37].

The PBF-LB process creates a thermal history through the energy transferred from the laser source to the powder. Therefore, choosing a distinct set of process parameters will provide specific mechanical properties, microstructure and surface quality. The most common energy density parameters are the linear energy density (*LED*) and volumetric energy density (VED), respectively defined as

$$LED = \frac{P}{v} \qquad \text{Equation 2.1}$$

and

$$VED = \frac{P}{v \cdot L_T \cdot h_d} \qquad \text{Equation 2.2}$$

where P, v, L_T and h_d are the power, scan speed, layer thickness and hatch distance, respectively. The parameters are widely used as an indicator to choose the optimum range of parameters, in particular to summarise process parameters or give a reference in porosity analysis, density measurements and tensile and hardness tests. These parameters are usually used to compare results between different PBF-LB systems. However, in case where functional materials are investigated, *LED* and *VED* do not provide information about the material and the main characteristics of the laser. Moreover, *VED* and *LED* are thermodynamic quantities which do not consider physical phenomena such as the Marangoni flow, hydrodynamic instabilities and the recoil pressure, which impact the consistency of the tracks. To have a more precise information, absorptivity of the powder related to the material printed should be considered.

According to this approach, normalised enthalpy has been introduced [38] to predict the melt pool depth other than the threshold for formation of keyhole during PBF-LB processes. Equation 2.3 defines the relationship

$$\frac{\Delta H}{h_s} = \frac{Abs \cdot P}{\pi \cdot h_s \cdot \sqrt{D \cdot v \cdot {d_{spot}}^3}} \qquad \text{Equation 2.3}$$

Where ΔH and h_s are the specific enthalpy and enthalpy of melting. *Abs*, *D* and h_s are the absorptivity, thermal diffusivity and enthalpy at melting of the material, respectively, while d_{spot} is the laser spot diameter. In turn, h_s is calculated as

$$h_s = c_p \cdot \rho \cdot (T_m - T_0) \qquad \text{Equation 2.4}$$

c_p, ρ, T_m and T_0 are the specific heat capacity, density, melting temperature and initial temperature prior to melting, respectively. Equation 2.3 can estimate the threshold for the switch from conduction mode to keyhole mode (see Section 2.4), according to Gan et al [39]

$$\frac{\Delta H}{h_s} > 6 \qquad \text{Equation 2.5}$$

2.2 Stainless steels

Steels are a class of materials widely used in many applications, thanks to their corrosion resistance, mechanical properties (strength, ductility, toughness), low price, wide range of microstructures, functionalities such as ferromagnetism or invar effects [40]. The range includes structural steels, such as A514, shock resisting steels, including type S1, and stainless steels, such as SAE 304.

Stainless steels are used when resistance to corrosive environments is needed, and subclasses are chosen according to the required mechanical properties. AISI 316L steel are generally used when parts must come into contact with corrosive media at moderate temperatures during service, and good strength and high ductility are required. When higher mechanical strength and hardness are required, precipitation-hardened martensitic stainless are adopted: these are often referred to as PH (precipitation hardened) and some examples include 17-4 PH and 15-5 PH [41].

Stainless steels are chromium-nickel steels with a presence of at least 10.5% of chromium. The presence of chromium forms a thin stable oxide film on the surface of the component when exposed to air thus making it resistant in a range of corrosive environments, at room and elevated temperatures [42].

The dissimilar content of nickel (Ni) and chromium (Cr), including their equivalent elements, affects the resulting phases in the microstructure thus generating subclasses, including austenitic and martensitic stainless steels. The final microstructure of a steel is the result of the cooling after a heat treatment has been accomplished. Cooling a steel from its liquid phase undergoes different processes based on the specific conditions at which it occurs. The driving force must be taken into consideration. This is proportional to ΔT, defined as the difference between the equilibrium temperature Te (between the two phases) and the value of T at which the material is cooled. It follows that, by applying a specific cooling rate, distinct microstructures are obtained which provide unique mechanical properties.

2.2.1 Thermally controlled transformations

Different phases can be found in stainless steels, and they are obtained in two specific ways: by solidification from the liquid phase and by solid-state transformation. The former experiences the formation of ferrite and austenite, the latter produces phases from ferrite and austenite, including pearlite, bainite and martensite. Theoretical thermally controlled transformations are described by equilibrium cooling diagrams. Cooling processes, that more properly describe manufacturing processes, adopt the time-temperature-transformation (TTT) diagrams. The cooling rate used in the thermally controlled transformation affects the phases that are obtained, up to the fastest cooling rate that leads to the quenching and produces martensite. Moreover, further transformations can take place by other means, for example martensitic transformation caused by deformation

(see Section 2.4.2). In this Section, the main and secondary phases for a stainless steel are considered, and a discussion on the effects of each alloying element on the microstructure is presented.

2.2.1.1 Austenite

Austenite, a face-centred cubic (FCC) phase, is present in pure iron at elevated temperatures, within a range of 912 °C to 1394 °C. The Fe-C equilibrium diagram can be used to explain the process of cooling from liquid and formation of austenite (γ), Figure 2.4. When such a transformation occurs, the atoms rearrange into a new pattern thus giving the name of reconstructive transformation. Carbon defines an interstitial solid solution in iron matrix because of the difference in the atomic value between the two elements (4.58 cm^3/mol for C, 7.1 cm^3/mol for Fe). Diffusion of atoms for the formation of austenite (and ferrite), in the case of C [42], is done in a way that only volume changes happen leaving no shear components so that a reduction in the overall free energy is observed. The solidification line that starts the formation of austenite is dependent on the content of C in the alloy.

Other alloying elements, such as manganese (Mn), Ni, cobalt (Co) and copper (Cu), tend to stabilise austenite [43]. As a result, the region of stability of austenite can be extended. The Fe-Ni phase diagram is used as an example in Figure 2.5 [44].

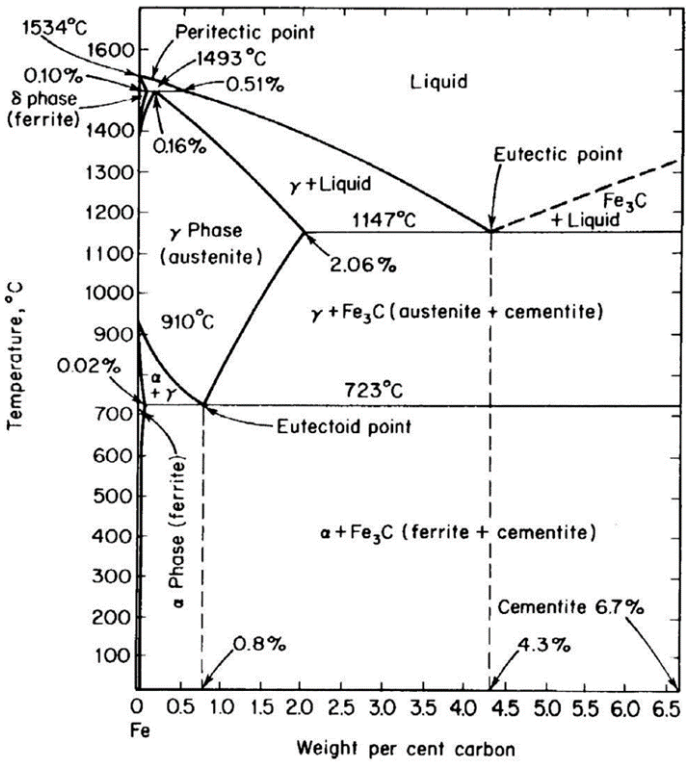

Figure 2.4. Iron-carbon phase diagram [45].

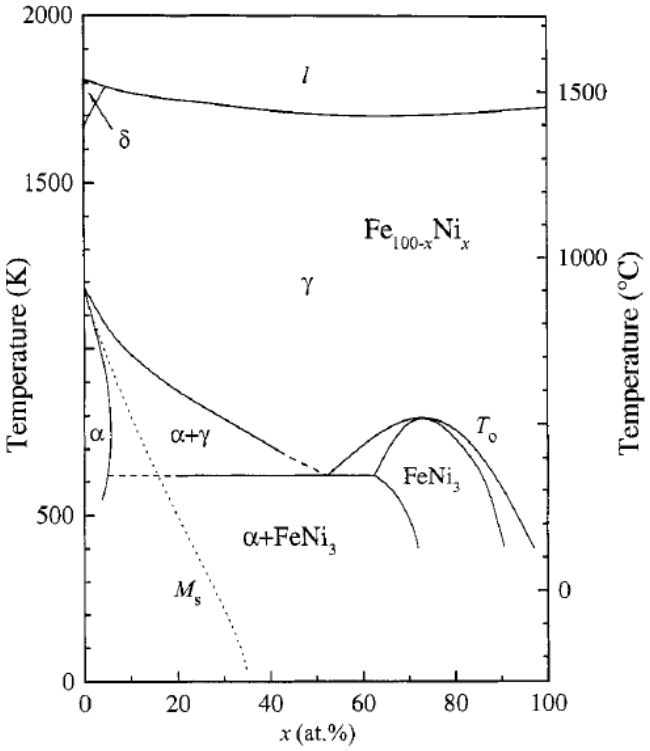

Figure 2.5 Phase diagram of Fe-Ni [44].

2.2.1.2 Ferrite

Ferrite is defined as a body-centred cubic (BCC) phase and forms by two mechanisms: directly from the liquid phase and it is referred to as δ ferrite, or from the austenite through a solid-state transformation and takes the name of *α* ferrite. The latter process is a diffusive process of C to the austenite, ferrite grows, and the maximum concentration allowed is reached, 0.02 *wt%*. The diffusion of C atoms into the adjacent austenite contributes to the nucleation of other phases.

For a stainless steel to reach the so-called passivation, the alloy must have a minimum content of around 10.50 *wt%* Cr. Good properties are reached with a content of around 17 *wt%* [42]. This content allows for the stabilisation of ferrite along with other alloying elements, such as tungsten (W), molybdenum (Mo), vanadium (V) and silicon (Si), because they have a BCC lattice. Those elements tend to be more soluble in the ferrite than austenite and diminish the quantity of C dissolved in the austenite by forming carbides [43]. As an example, the Fe-Cr binary system is displayed in Figure 2.6 [46]. Cr restricts the field of existence of austenite, and with Cr content of above 13 *wt%* the alloy only shows ferrite at the highest temperatures.

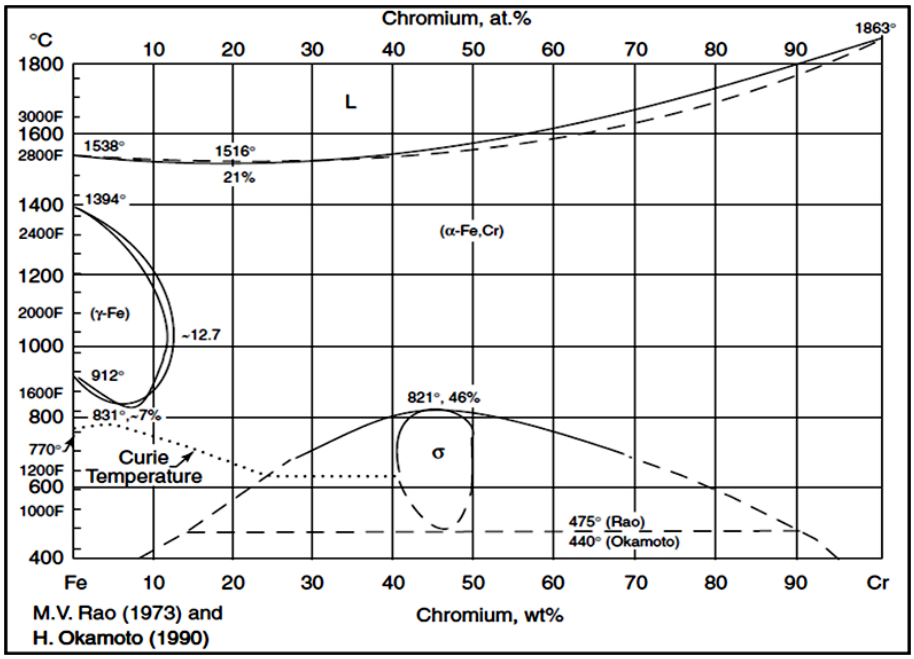

Figure 2.6 Binary Fe-Cr phase diagram [46].

2.2.1.3 Martensite

Martensite (α') is a metastable phase, body-centred tetragonal (BCT) or BCC when the content of C is low that cannot be distinguished from a BCC phase [47]. Martensite can be obtained by rapid cooling from the austenite phase or by deformation of austenite (see Section 2.4.2).

As for the former process, quench provides cooling rates up to 420 °C/s and high driving force [42]. The resulting large ΔT does not allow austenite to diffuse C atoms along the lattice (solute trapping). This causes a displacive transformation to occur, leading to the formation of martensite from the prior austenite composition.

M_s is the temperature at which martensite starts to transform, while M_f is the temperature at which 95% of austenite transforms into martensite, and both depend on the alloy. To represent the martensitic transformation, the TTT curve is adopted as shown in Figure 2.7 [48]. The martensitic transformation is not time dependent but only depends on M_s and M_f.

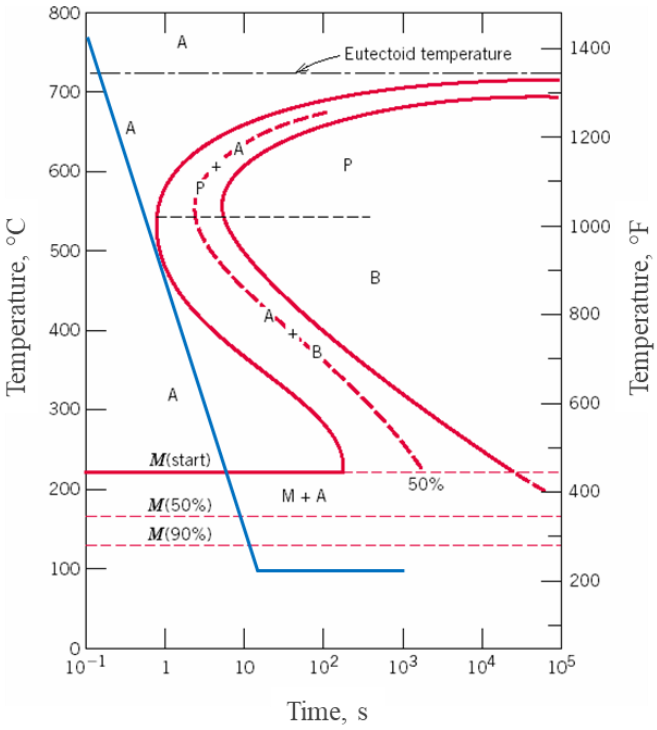

Figure 2.7 Time-Temperature Transformation diagram with example of transformation of austenite phase to martensite [48]. In the diagram, the letters A, B, P and M represent, respectively: austenite, bainite, pearlite and martensite.

The nature of the displacive transformation forces C to fit into the interstitial sites of the BCC lattice. Bain relationship is a simple description of martensite formation [49]. In this relationship, a supersaturated solid solution of C in ferritic iron forms, with the C atoms causing a tetragonal distortion into a BCT lattice (Figure 2.8). Since different outcomes were detected experimentally, further relationships which consider the complexity of the martensitic transformation were proposed. The main referred ones are the Kurdjumov-Sachs and Nishiyama-Wassermann. The former provides a crystallographic orientation relationship between FCC and BCC as follows

$$\{111\}_\gamma || \{110\}_\alpha \qquad \text{Equation 2.6}$$
$$< 110 >_\gamma \; || < 111 >_\alpha$$

The deformation of the lattice is supported by the movement of slip dislocations on parallel slip planes, causing a macroscopic shear. The resulting substructure in plates of martensite is formed by twins or slip steps, Figure 2.9. The consequent strain is a uniaxial dilatation and a shear, both normal to the invariant line.

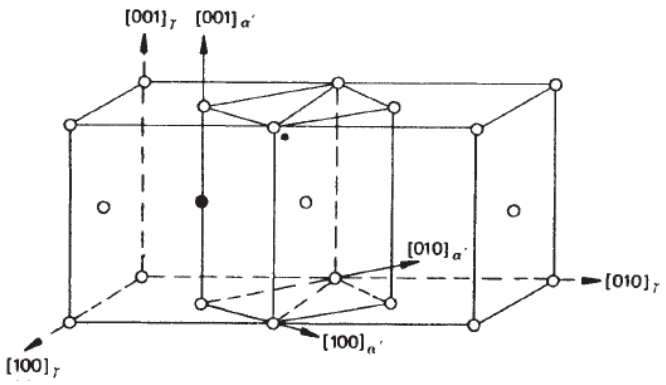

Figure 2.8 Transformation from FCC to BCT lattice [42].

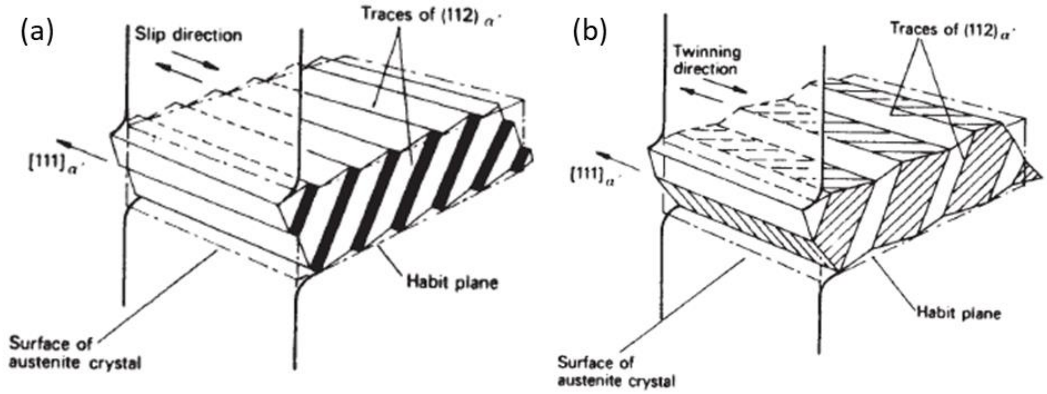

Figure 2.9 Slip (a) and twinning (b) in the formation of martensite plates [42].

The nucleation of martensite takes place heterogeneously on pre-existing embryos with a semi-coherent interface to the austenite. The formed martensitic plates have a lenticular shape because the matrix is trying to oppose to the shape change. Plates contain packets of laths and are long and narrow, in the order of some micrometres. Singular laths have a thickness of less than 1 μm. The resulting microstructure is complex, as in Figure 2.10 [50].

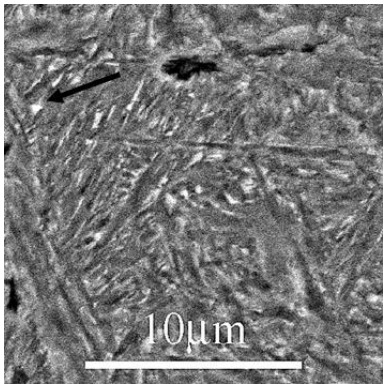

Figure 2.10 Micrograph of martensite formed by a Fe - 0.8 *wt%* C alloy [50]. The ferrite microstructure is dark coloured, while retained austenite is lighter (indicated by the arrow).

2.2.1.4 Other phases

A hexagonal close-packed (HCP) martensite, referred to as ε martensite, exist as opposed to the α' described earlier. It is considered to provide softening in the stress-strain behaviour of the material as well as improvement of damping capacity [51]. It is the nucleation site for the strain induced α' martensite.

Precipitates are sub-microscopic particles that form during the manufacturing process or subsequent heat treatment. They can be wanted, as in the case of precipitation hardening (PH) stainless steels, or unwanted when they are detrimental to the properties of the material. When they are designed to form, the reason is to increase hardness and strength [52]. One mechanism by which they do so, is by impeding the movement of dislocations in a crystal's lattice.

Stainless steels can have other phases, not considered in this work because not present in the materials investigated. They include pearlite, bainite and cementite. If the chemical composition allows for that, by looking at Figure 2.7 it is possible to understand that these phases are obtained according to the required cooling rate.

2.3 Types of stainless steels for energy absorption

Stainless steels contain alloying elements that determine the phase content at room temperature. Elements that allow austenite at room temperature are called γ stabilisers, while the elements that contrast the formation of austenite in favour of ferrite are referred to as α stabilisers [42,53]. Among the former group are Ni, Mn, C, Cu and nitrogen (N); the latter comprise Si, phosphorus (P), titanium (Ti), Mo, Cr and niobium (Nb). The main elements in the stainless steels object of this work are C, Cr, Ni, Cu, Mo, Mn, Si and Nb. The presence of certain alloying elements comes from the resulting mechanical properties that are needed for the energy absorption requirements. If extended ductility is needed, more γ stabilisers are present [54], while α stabilisers are used in larger quantities in the alloy in case higher strength is preferred [55].

To consider the effects deriving from the presence of different alloying elements in Cr-Ni stainless steels, the Schaeffler diagram is often adopted. It displays the compositional limits at room temperature of austenite, ferrite and martensite according to specific levels of nickel and chromium equivalents, Figure 2.11. The diagram was developed for non-equilibrium processing and therefore takes into account the cooling rate effects. Since metal AM is characterised by high cooling rates, it can be concluded that the Schaeffler diagram is suitable for the cooling rates occurring in PBF-LB [56].

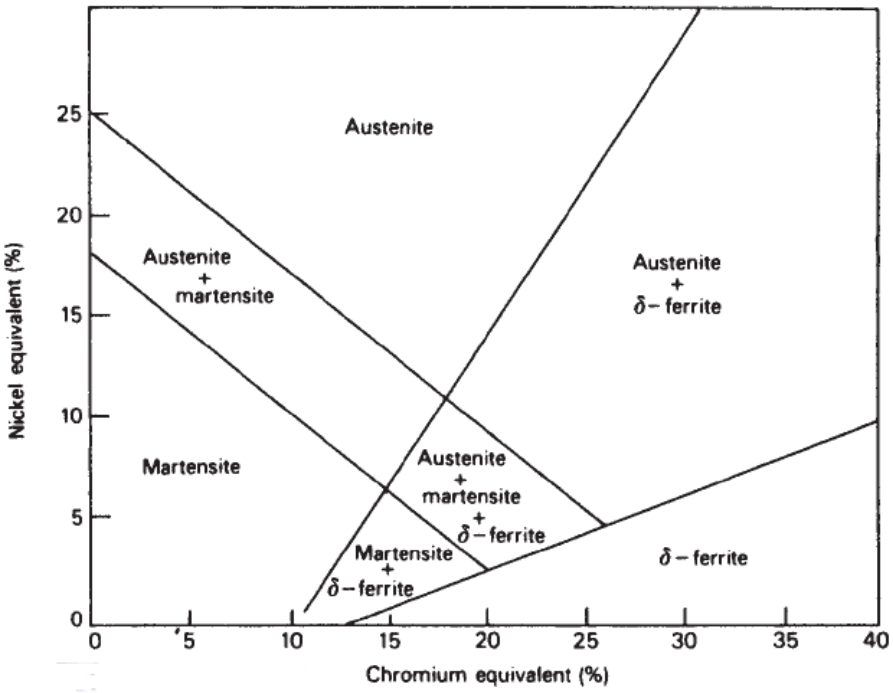

Figure 2.11 Schaeffler diagram. Effect on the phase composition of Cr-Ni stainless steels given by alloying elements [57].

Cr equivalent (Cr_{eq}) and *Ni equivalent* (Ni_{eq}) terms have been defined, since it was determined empirically that other alloying elements have the same effect in terms of resulting phases [58]. They are defined as follows (concentrations are expressed as *wt%*)

$$Cr_{eq} = (Cr) + 2(Si) + 1.5(Mo) + 5(V) + 5.5(Al) + 1.75(Nb) + 1.5(Ti) + 0.75(W) \quad \text{Equation 2.7}$$

$$Ni_{eq} = (Ni) + (Co) + 0.5(Mn) + 0.3(Cu) + 25(N) + 30(C) \quad \text{Equation 2.8}$$

The Cr_{eq}/Ni_{eq} ratio is adopted to describe if a material contains more γ or α stabilisers.

2.3.1 Austenitic stainless steels

Austenitic stainless steels contain high content of Ni and other alloying elements to retain austenite at room temperature, or FCC crystal structure. The resulting Cr_{eq}/Ni_{eq} ratio is lower than 2 [59]. Important properties are reached in austenitic stainless steels, which are useful for energy absorption structures: the presence of Cr improves the resistance to corrosion; they do not suffer from ductile/brittle transition, a detrimental effect on ferritic steels [42]; they possess good mechanical properties. Conventionally manufactured austenitic steels

possess a yield strength (σ_Y) of around 250 MPa and ultimate tensile strength of 500-600 MPa. Moreover, they have good ductility, with elongations around 50% in tensile tests [42].

Different austenitic stainless steels were investigated to determine energy absorption capabilities. AISI 304 steel was studied along with another austenitic steel, H400 [60,61]. The two materials showed strain hardening behaviour (see Section 2.4) and excellent gradual formability at the expense of strength level as opposed to dual-phase and TRIP steels. More recently, medium Mn austenitic steels have addressed requirements for high strength and ductility, for example the medium Mn Fe-C-Mn-Ni-Al alloy [62]. The latter was determined to have higher strength and lower ductility than typical austenitic steels, such as 304, that allows to absorb energy and reduce damage propagation. It was found the importance of reducing the presence of martensitic phase in the manufactured material for a performant deformation behaviour. AISI 304 steel has been extensively investigated, and the typical range of the Cr_{eq}/Ni_{eq} from 1.4 up to 2 [63]. AISI 316L stainless steel is another widely used steel in the industry, with an average Cr_{eq}/Ni_{eq} of 1.43 and typical chemical composition being shown in Table 2.1 [64]. The. One peculiar characteristic of 316L is a carbon content less than 0.04 *wt%* (which gives the 'L' in the name) to contrast weld-decay effect, an intergranular corrosion that causes precipitation of $Cr_{23}C_6$ on grain boundaries and reduced susceptibility to thermal stress driven micro-cracking. Moreover, the content of molybdenum provides better stress corrosion cracking and pitting resistance. The benefits of good mechanical properties and corrosion, oxidation and heat resistance, make 316L the perfect choice for applications in many industry fields, including crashworthy applications [65,66].

Table 2.1. Typical chemical composition of 316L stainless steel, in *wt%*.

Element (weight %)									
C	Cr	Ni	Fe	Mo	Mn	Si	N	S	P
0.03	16.50-18.50	10-13	Bal.	2-2.5	2	1	0.1	0.015	0.045

Compared to conventional manufacturing processes, 316L processed with PBF-LB possesses higher σ_Y and provides larger ductility [67]. This is the reason why the material has been heavily investigated for applications in energy absorption applications [66]. The explanation of the mechanical properties and issues of 316L manufactured with PBF-LB are described in Section 2.4.1.

2.3.2 Martensitic stainless steels

Martensitic stainless steels can show a BCT, BCC and FCC crystal structure upon production, and a BCT structure in the heat treated and hardened condition. The main alloying elements in the Fe matrix are Cr, C, Ni

and Mo [68]. The resulting properties are corrosion resistance, high tensile and fatigue strength, heat resistance. According to the alloying elements content, the σ_Y of conventionally manufactured martensitic steels is in the range of 500 and 800 MPa, with the ultimate tensile strength being 900 up to 1400 MPa. The elongation is up to 27%, lower than the austenitic stainless steels [69].

Various martensitic stainless steels were examined for their energy absorption properties. AISI 420 stainless steel, exhibiting a Cr_{eq}/Ni_{eq} of 2, was investigated at different retained austenite content in the as-built configuration [70]. It was found that increasing retained austenite induced a decrease in yield and ultimate tensile strength, whereas energy absorption increased up to 79%. The reason was ascribed to the TRIP effect of the material, and the increased retained austenite acted as soft phase for retardation of crack initiation and propagation. TRIP700 was considered in the study by Ratte et al [61] for a comparison with austenitic and dual phase steels. TRIP700 resulted being the material, along with 304 steel, that showed extended displacement before necking and failure during energy absorption tests. Ku et al compared lattice structures made of Corrax maraging stainless steel, Cr_{eq}/Ni_{eq} of 2.3, to the same structures manufactured with Ti6Al4V alloy [55]. The result was that Corrax outperformed Ti6Al4V alloy, both in the as-built and in the solution aging treatments. The reason is attributed to the superior strength and ductility of Corrax, where dislocation strengthening is the main deformation mechanism, along with precipitation hardening. Considering the improved mechanical properties given by the strain hardening of martensitic stainless steels with retained austenite, some studies focused on the energy absorption of other martensitic steels, such as 17-4 PH. Its average Cr_{eq}/Ni_{eq} ratio is 2.7, and the chemical composition of this alloy is represented in Table 2.2 [11]. The benefits of using 17-4 PH are: it has the highest strength of the martensitic steels, up to 1100-1300 MPa; it shows better weldability; it can withstand corrosive environments better; it possesses superior toughness and strength over a wide range of temperatures [11].

Table 2.2. Typical chemical composition of 17-4 PH stainless steel, in *wt%*.

Element (weight %)								
C	Cr	Ni	Fe	Cu	Mn	Si	Mo	Nb
Max 0.07	15-17	3-5	Bal.	3-5	Max 1.5	Max 0.7	Max 0.6	Max 0.45

When 17-4 PH is produced with conventional manufacturing processes, it undergoes heat treatment to obtain its martensitic microstructure and mechanical properties. The steps are generally a solution heat treatment (at 1050 °C), then quenching and finally aging at different temperatures. Materials processed with PBF-LB usually undergo the same heat treatments, to provide a uniform and reproducible microstructure. However, PBF-LB can give 17-4 PH a wide range of microstructure in the as-built condition, including a ferritic or austenitic microstructure, thus making it interesting to obtain a wide range of properties [71]. The improved mechanical

properties and disadvantages of 17-4 PH processed with PBF-LB compared to conventional manufacturing processes are presented in Section 2.4.2.

2.4 Physical phenomena in PBF-LB

PBF-LB involves several phenomena during the production process, including the interaction between the laser and the powder, the solidification of the melt pool and the surrounding affected zone, and finally the heat transfer across the layer and the build direction. A summary is shown in Figure 2.12 [72] (defects will be discussed in Section 2.5). Once the laser source irradiates the exposed layer, a series of heat transfer phenomena happen. Radiation of the powder bed, between the laser source and the powder particles, convection, between the powder bed and the surrounding environment in the build chamber, and heat conduction, between the molten layer and the underlying scanned layers, powder bed and substrate as well as the molten material and powder particles [73].

As for the radiation, the laser energy is high enough to melt locally the powder and form a so-called melt pool (or molten pool). The described heat phenomena imply that the molten powder enters a mushy zone that affects surrounding powder not supposed to be scanned, which contributes to the formation of the surface roughness typical of the PBF-LB process and that needs post processing (as described in Section 2.1). If O is in the build chamber, usually a few hundred of parts per million, it can interact with the melt pool thus creating an oxide layer which hinders the melting process and causes detrimental consequences on the mechanical properties of the material [74]. When the energy of the laser source is so high that a larger melt pool is generated, a temperature gradient between the hot centre of the melt pool and the colder surface can cause evaporation of some elements and generates Marangoni convection, which is a flow movement of fluid from the top region with high surface tension to the bottom of the melt pool. If the laser turns off but moves to the adjacent scanning spot, once it irradiates the exposed layer, an additional heat treatment onto the molten layer already scanned can occur. When the laser turns off, the temperature drops below the solidification temperature and the melt pool starts to solidify. As the melt pool has higher temperature than the surrounding environment, there is still a temperature gradient which causes an extremely rapid cooling down of the melt pool to generate the crystalline microstructure for metals and stainless steels, while amorphous structure for other materials (i.e. glass). The cooling rate reaches high values because the scanned powder that is molten is in low volume compared to solidified material where it is deposited onto. As a result, very fine microstructures are generated, and thermal stresses arise. Elevated thermal stresses are deleterious for the process stability of PBF-LB [75]. Therefore, to reduce them, the scanning of the layers is performed onto the substrate directly, or onto support structures that act as sacrificial material and removed after the printing process.

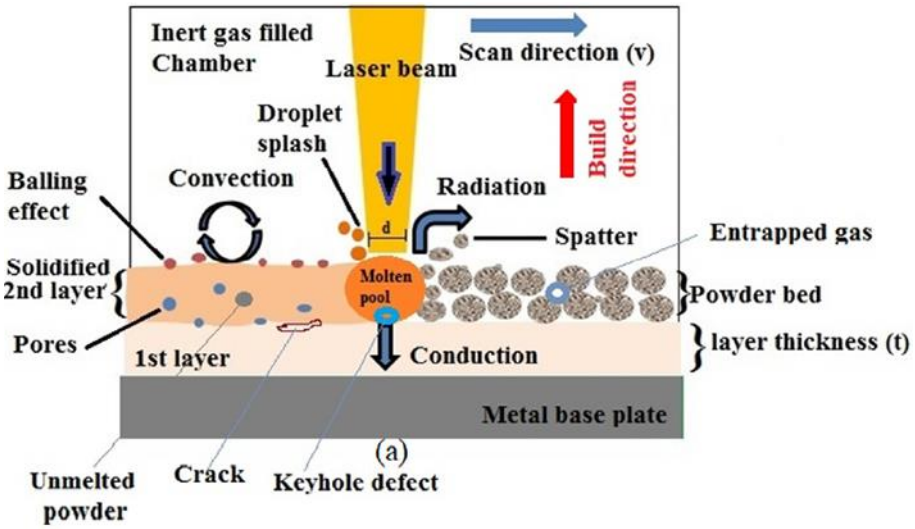

Figure 2.12. Schematic illustration of the thermophysical phenomena that take place during the PBF-LB process [72].

In case of a PWM mode for PBF-LB, the laser source irradiates the powder bed at several spots across the scanning track, melting the powder and generating a melt pool with a tear-drop shape [76]. The solidification of the melt pool, strictly linked to the process parameters used, influences the microstructure of the material. The mechanical properties will depend on the evolution of the grain structure, that is the grain size, morphology and orientation. As mentioned, the physical phenomena involved in the PBF-LB produce non-equilibrium conditions. In addition, the remelt of the underlying layers, that ensure components with high density, reduces if not deletes the energy barrier for nucleation. As a result, the same phenomena that are present in welding occur, so that the growth of the grains in PBF-LB is a localised solidification process [77]. This means that there is a competitive growth toward the centre of the melt pool. In particular, the partially melted grains solidify by means of an epitaxial growth from the layer previously scanned by the laser. The resulting grain morphology can be of different types: planar, cellular, columnar dendritic and equiaxed dendritic. The morphology is in turn affected by the temperature gradient G, the solidification rate at the solid-liquid interface R, the undercooling ΔT and the solute diffusion coefficient D_L, as displayed in Figure 2.13(a) [78]. The relationship between G and R is depicted in Equation 2.9

$$\varepsilon_{CR} = G \cdot R \qquad \text{Equation 2.9}$$

where ε_{CR} is the cooling rate. Furthermore, the ratio G/R predicts the solidification mode. Cooling rates can be in the order of 10^5-10^6 K/s, while temperature gradients can easily reach 10^6 K/m [79]. Reducing G results in equiaxed growth, and high cooling rates imply finer microstructure thus affecting the cell spacing and size of cell structures. This can be mathematically described by Equation 2.10

$$\lambda_1 \propto G^{-m} R^{-n} \qquad \text{Equation 2.10}$$

where λ_1 is the primary cell spacing (the average distance between centrelines of adjacent primary cells) and *m* and *n* are constants, respectively computed as 0.24-0.26 and 0.72 for steels [80]. For the general PBF-LB process, the relationship gives primary cell spacings in the order of magnitude of the micrometre, with values not greater than 9 µm.

The general solidification of PBF-LB is depicted in Figure 2.13(b), with the growth directions aligned in the thermal gradient direction, even if the initial solidification state is characterised by multiple orientations. Each grain grows along particular crystallographic orientations. Nonetheless, the grains with similar orientation as the temperature gradient will grow faster and stop the growth of the grains with divergent orientations. This is the reason why generally PBF-LB solidification generates unidirectional columnar grain structures with a preferential orientation.

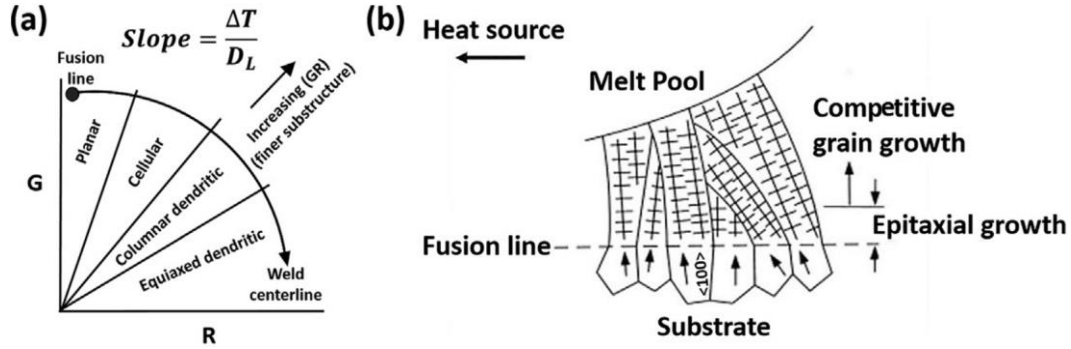

Figure 2.13. (a) Schematic of the grain morphology and the effects of *G* and *R*; (b) the growth of a grain in PBF-LB with the initial epitaxial growth and following competitive growth [78].

PBF-LB is defined by non-equilibrium microstructures as opposed to those from conventional manufacturing processes such as forging and rolling, because of the fast solidification rates and repeated heating-cooling cycles typical of the manufacturing process [81,82]. It is therefore important to characterise the main microstructural differences that explain the specific behaviour and mechanical properties of the materials manufactured and used in the present work (see Chapter 4, 5 and 6).

2.4.1 Microstructure, mechanical properties and TWIP behaviour of PBF-LB 316L

Conventionally manufactured 316L stainless steel shows a homogeneous microstructure, given by the manufacturing process with low solidification rates or homogeneous heat treatments. Figure 2.14 depicts a typical microstructure for a wrought processed 316L [83], extracted from an inverse pole figure (IPF), with an average grain size of 38 µm. The fully recrystallised austenite grains are strain-free as it can be noted from the kernel average misorientation (KAM) equals to 0.30°. KAM maps are employed to determine the misorientation between adjacent points, with growing values caused by the larger presence of defects in the structure and induced strains.

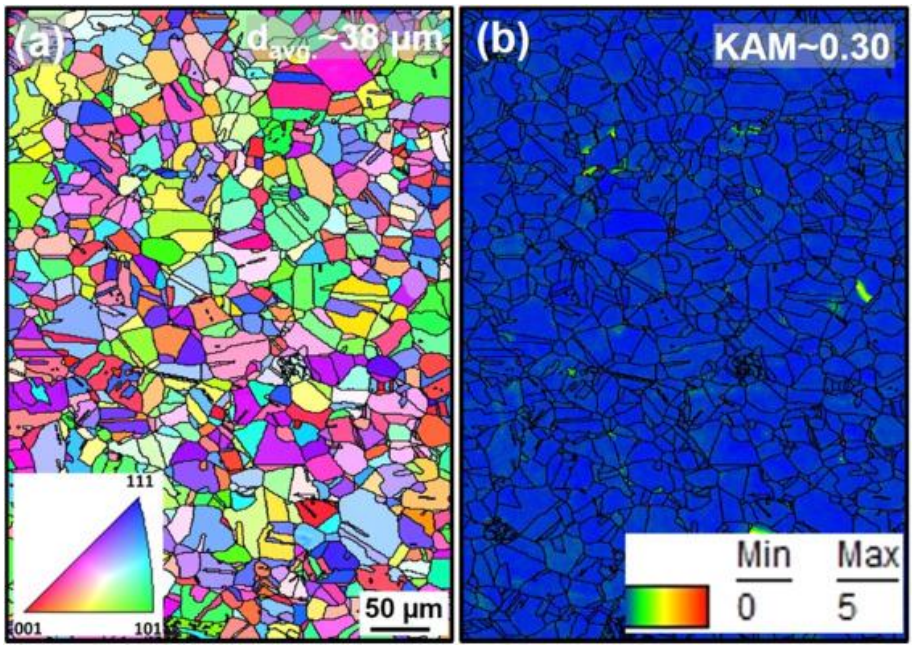

Figure 2.14. Microstructure of a wrought processed and annealed 316L sample , (a) is the electron backscattered diffraction (EBSD)-IPF and (b) shows the KAM map [83].

316L steel processed with PBF-LB is characterised by a completely different microstructure, as shown in Figure 2.15 [12]. First of all, the typical thin columnar grain morphology can be seen along the build direction, and a specific orientation of the grains is also present ([101] parallel to BD). The cross-section, instead, is defined by a checkerboard pattern with equiaxed grains. The size of the grains is more heterogeneous than the conventionally manufactured counterpart as well as the ratio of the grain dimensions, due to the presence of elongated grains. Moreover, the grain size distribution can be lower than the conventionally manufactured counterpart, and in the order of 27 µm for the section along the BD and 17 µm in the cross-section. As-built 316L produced with PBF-LB also tends to have higher residual stress in its microstructure, as found in previous studies KAM between 0.5° and 1° [84].

An advantage of 316L stainless steel produced with PBF-LB is better mechanical performance compared to the conventional manufacturing processes. As can be seen in Figure 2.16(a), 316L produced with PBF-LB shows higher σ_Y compared to the as-cast and as-wrought counterparts, a larger ultimate tensile strength (UTS) and higher tensile ε_f. Furthermore, additively manufactured 316L is also characterised by having a uniform tensile elongation, that exceeds the material produced with conventional techniques, as displayed in Figure 2.16(b). The exceptional mechanical properties of additively manufactured 316L stainless steel are the reasons why it is extensively investigated for several applications.

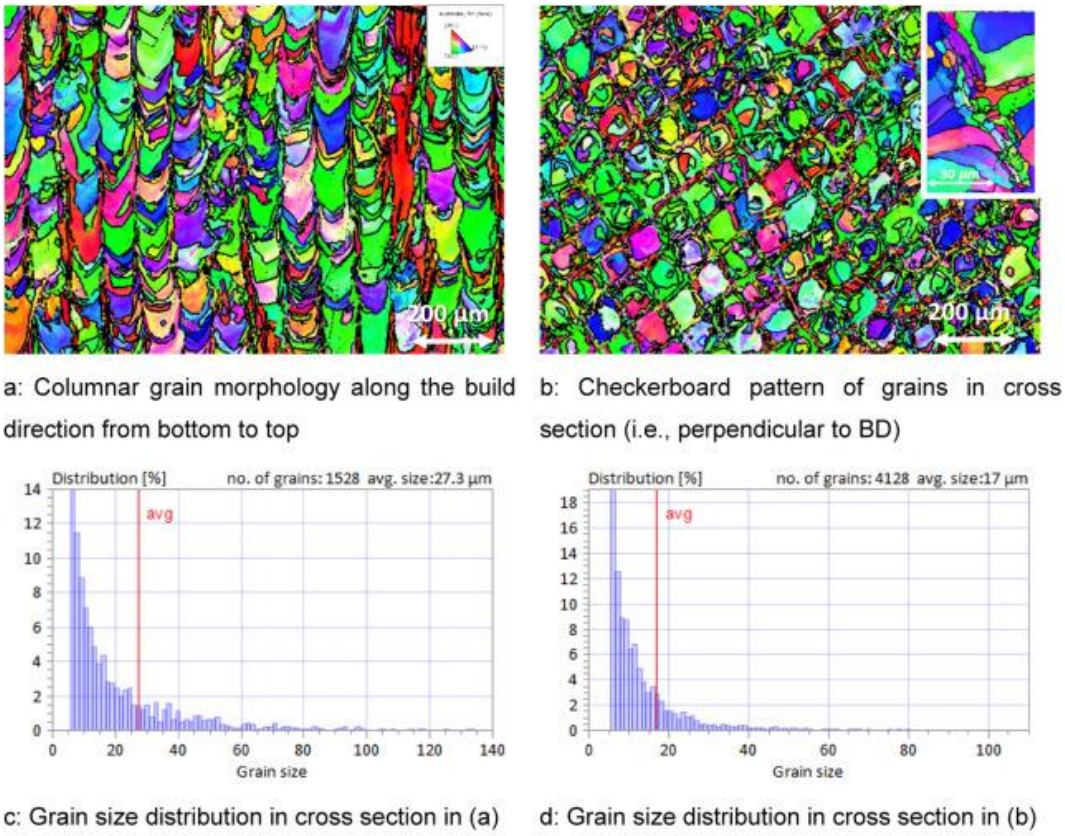

Figure 2.15. Typical microstructure of 316L produced with PBF-LB [12]. (a) is the columnar morphology along the build direction, (b) shows the equiaxed cross section, (c) depicts the grain size distribution along from (a) and (d) represents the grain size distribution from (b).

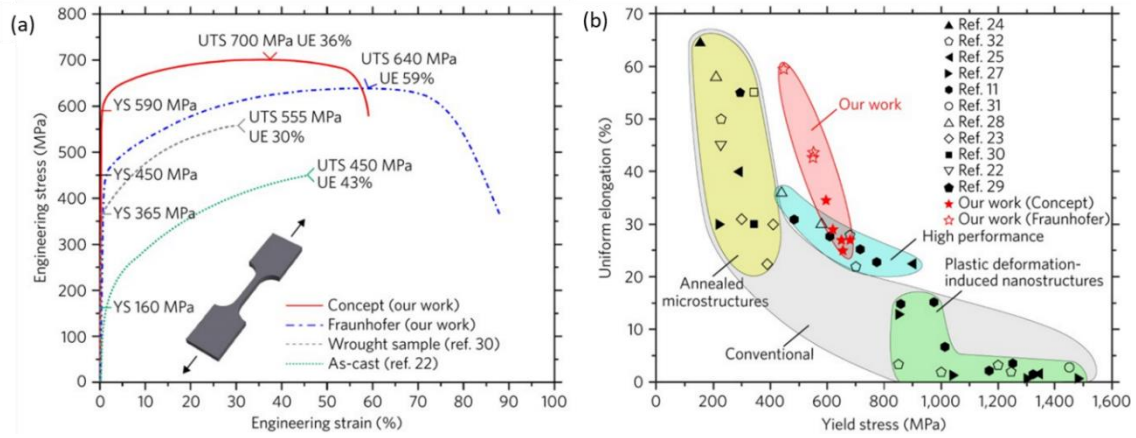

Figure 2.16. Mechanical properties of 316L stainless steel produced with PBF-LB [84]. (a) shows the tensile stress-strain curves of the investigated additively manufactured samples compared to as-cast and as-wrought parts. (b) depicts an overview of the uniform elongation versus σ_Y for 316L produced with conventionally manufacturing processes and PBF-LB. The label "our work" refers to the work by Wang et al [84].

The high strength of PBF-LB 316L is ascribed to the large dislocation density and finer grain size than conventionally manufactured material, thanks to the Hall-Petch effect [85,86]. The high ductility is associated

with a strain hardening mechanism [87]. The mechanism is called TWIP and is a fundamental deformation mode when the material is subjected to plastic regime. Slip and twinning enable a solid to change shape under the application of strain and are the major deformation mechanisms at temperatures below those that allow for atomic diffusion [88]. Deformation applied to single crystals showed that metals with FCC structure twin only after an appreciable amount of deformation slip has taken place [88]. The phenomenon is characterised by a rapid formation of twinned regions and is sensitive to the temperature of deformation as well as the strain rate (increase of contribution when the temperature is lower, or the strain rate is increased). It is defined by the shape change of the material's parent lattice when shear stress is applied, and a general definition was provided by Bilby and Crocker, reported in Figure 2.17(a). The invariant plane of the shear stress is called K_1 and the shear direction η_1. The second undistorted, or conjugate, plane is K_2 and the two normals to K_1 and K_2 is the plane of shear, called P_S. The intersection of K_2 and P_S is the conjugate shear direction η_2. Bullough provided a theory to describe the formation of a twin. The sequence is shown in Figure 2.17(b-d). There is a combination of the lattice invariant deformation, which is a shear on K_2 in the direction η_2, with the lattice deformation, which is a rotation about the direction in K_2 normal to η_2, that produces the shape deformation. The deformation is a shear on K_1 in the direction of η_1.

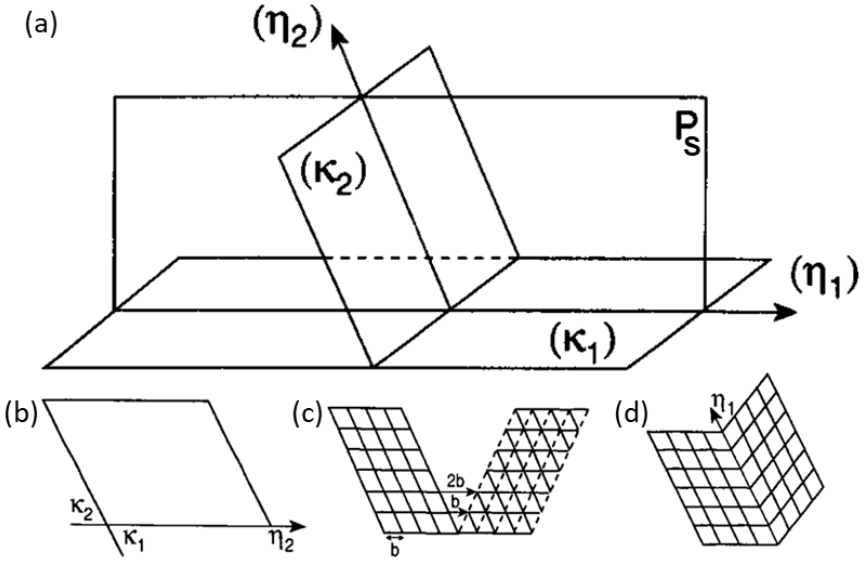

Figure 2.17. Schematic of the Bullough theory of twinning [88]. (a) shows the original parent lattice. (b) describes the homogeneous lattice invariant shear given to the parent lattice on the K_2 plane which is horizontal in the figure; as a result, a lattice dislocation of Burgers vector b starts to glide through each lattice on the K_2 plane (original unit cells are depicted with full lines, while dashed lines are used for the cells in the shear region). (c) shows the combination of the lattice invariant shear with a rotation about the normal to the plane of shear that gives as a result the twin.

In 316L stainless steel produced with PBF-LB, the strain hardening mechanism is regulated by the hierarchical microstructure that spans approximately six orders of magnitude due to its heterogeneous microstructure [84].

The length scales, in fact, range from the nanometre to the sub-millimetre, where the highest length is given by grains with length up to 0.2 mm. Cell diameters and wall thicknesses are in the order of the micrometre, while precipitates are as big as tens or hundreds 115metres. Finally, the lowest scale is reached with impurities such as N and H that are smaller than 1 nm in size. Of particular importance are the solidification cellular structures typical of PBF-LB process, whose size can be less than 1 μm. Along the walls of these solidification cellular structures and low-angle grain boundaries (LAGBs), solute segregation of Cr and Mo, as well as Mn, Si and O has been found [89]. In addition, cellular walls are characterised by a high density of dislocations. A study pointed out that the cell size is a major contribution to the strength of the material thanks to the Hall-Petch-type strengthening behaviour, while the high-angle grain boundaries (HAGBs) are not contributing to this [84]. The solute segregation at the cellular walls and the LAGBs have been found to increment dislocation pinning and favour twinning. It was also found that plastic deformation introduced back stresses into the material, which has been reported to help strain hardening [90]. Residual stress is another component for enhancing the σ_Y and the work-hardening behaviour of steels at the sub-grain level have an important role because of the heterogeneity in the microstructure and the dislocations induced during the manufacturing process.

As a consequence, upon deformation a reorientation of the grain occurs. In 316L, twin boundaries (TBs) are defined as $\Sigma 3$ coincidence site lattice boundaries with misorientation angle and axis of 60° and [111] respectively [91]. During the deformation, a strain value acts as the threshold above which deformation slip stops being the predominant deformation mechanism, and deformation twinning takes over, also referred to as onset of twinning. The number of twins forming increases and eventually reaches a plateau as the microstructure completely recrystallised.

Apart from the hierarchical microstructure, the formation of twins is also enabled by the low stacking fault energy (SFE) that characterises PBF-LB 316L. SFE values are found to be in the range of 40-60 mJ/m^2 according to the chemical composition, which brings it in the low end of the medium SFE category. As solute atoms diffuse into faulted areas, this reduces the SFE. As a result, dislocations are disassociated and form stacking faults that block the movement of cross slips and favouring the deformation twinning [92]. The advantage of twinning is dual, since the formation of twins prevents the motion of dislocations, giving an additional rise of strength [12,91].

2.4.2 Microstructure, mechanical properties and TRIP behaviour of PBF-LB 17-4 PH

Conventionally manufactured 17-4 PH stainless steel (e.g. wrought material) is characterised by having a typical microstructure of low-carbon martensitic steels [93]. Specifically, equiaxed grains that represent prior austenite grains, with dimensions of around 30 μm, where after the manufacturing process blocks of martensite form. The blocks are roughly equiaxed too and can exhibit a length similar to the grain size and a mean size

below 10 µm, as shown in Figure 2.18. It has also been found that fine inclusions, less than 100 nm, are present in the material. Moreover, the usual solution heat treatment, done in the industrial practice, does not change drastically the microstructure of the wrought material.

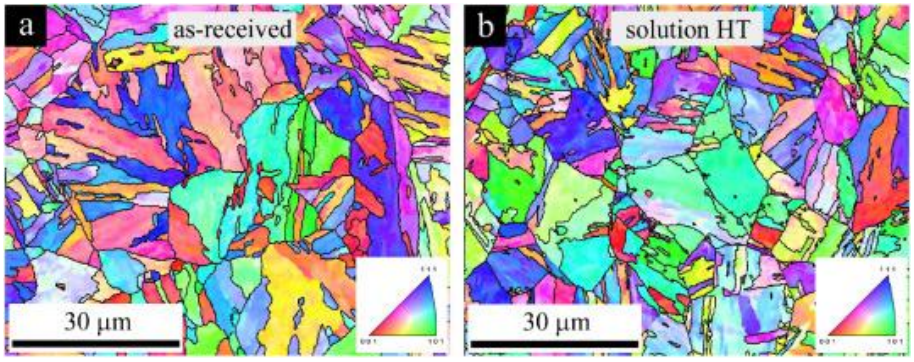

Figure 2.18. EBSD-IPF maps of (a) as-received and (b) solution heat treated wrought 17-4 PH steel [93].

Conversely, a 17-4 PH alloy produced with PBF-LB depicts a contrasting microstructure, and differences arise within material produced with the same technique due to dissimilar starting points. An overview of the complexity provided by PBF-LB is displayed in Figure 2.19 [94]. Divergent powder composition of the alloy results in different grains morphology and phase composition, shown in Table 2.3. The microstructure derived from PBF-LB can provide an epitaxial columnar structure, as in Figure 2.19(a-b), with length over 150 µm, interrupted by coarse semicircular grains with average grain diameter of the same order of magnitude. The alignment of the grains is towards the temperature gradient, the build direction. As opposed to what described for the previous two cases, an alternative microstructure is shown in Figure 2.19(c). It is much finer and more homogeneous. The mean grain size can be of just below 100 µm, as in Figure 2.19(a-b), or 10 µm and below similarly to Figure 2.19(c). The powder composition contributes to the Cr_{eq} / Ni_{eq} ratio for specific microstructure. It is known that the epitaxial growth typical of PBF-LB eliminates the nucleation barrier for solidification and favours the phase that grows at the highest temperature [95]. However, if the Cr_{eq}/Ni_{eq} ratio is higher than 2, the growth rate is not sufficient to have nucleation of austenite in the liquid. As a result, with high Cr_{eq}/Ni_{eq} ratios, ferrite and martensite form [96]. For the highest ratios, a prevalent ferritic mode of solidification is seen, Figure 2.19(a-b). Conversely, lower values of Cr_{eq}/Ni_{eq} ratio in the high range produce austenite and transformation to martensite can occur during the solidification, as in Figure 2.19(c). Finally, Cr_{eq}/Ni_{eq} ratios lower than 2 favour the nucleation of austenite from the liquid thus resulting in high content of retained austenite in the as-built material.

Table 2.3. Chemical composition of the three gas-atomised 17-4 PH stainless steel powders (Powder A, Powder B and Powder C) from [94].

	Element (weight %)									
Powder	C	Cr	Ni	Fe	Mo	Mn	Cu	N	Si	Nb+Ta
Powder A	0.02	16.12	4.15	Bal.	0.05	0.02	3.21	0.007	0.79	0.2
Powder B	0.01	16.7	4.29	Bal.	0.05	0.2	4.49	0.031	0.36	0.27
Powder C	0.01	15.6	4.7	Bal.	0.24	0.5	3.61	0.036	0.38	0.22

Investigations on the mechanical properties of as-built PBF-LB 17-4 PH stainless steel and a comparison with the corresponding conventionally produced counterpart were conducted. The variety of microstructures and phase composition, that 17-4 PH produced with PBF-LB can show, provided contrasting results when compared to the wrought counterpart. It was demonstrated that PBF-LB specimens can perform worse than wrought counterparts in terms of strength, with a reduction of 25% and 7% for the σ_Y and UTS respectively, and better for what concerns ε_f, up to 25% increase [8]. However, even if the displayed σ_Y of PBF-LB produced samples was lower than the wrought counterpart, around 28%, the UTS and ε_f experienced an increase for the additively manufactured specimens [97]. Finally, it was found that σ_Y can be even higher for PBF-LB 17-4 PH specimens [98]. The non uniformity of mechanical properties is ascribed to the different content of phases that 17-4 PH assumes during the AM process. The reason lies on the process parameters, printing conditions and powder. As a result, in the industrial practice components produced with 17-4 PH steel are heat treated so that homogeneous microstructure and phase distribution can be easily controlled for the required application. The lack of extensive research on the as-built PBF-LB 17-4 PH hindered the exploration of the exceptional mechanical properties that this technology gives to the material.

The peculiarity of PBF-LB as-built 17-4 PH is the in-situ aging treatment, dependent on the printing conditions, which enables superior properties than the wrought counterpart thanks to precipitation hardening and dislocation strengthening [99]. High dislocation density is the result of thermal strains during the repeated heating and cooling of PBF-LB, strains that are accommodated trough plastic deformation and affect the as-built microstructure and phase content [100].

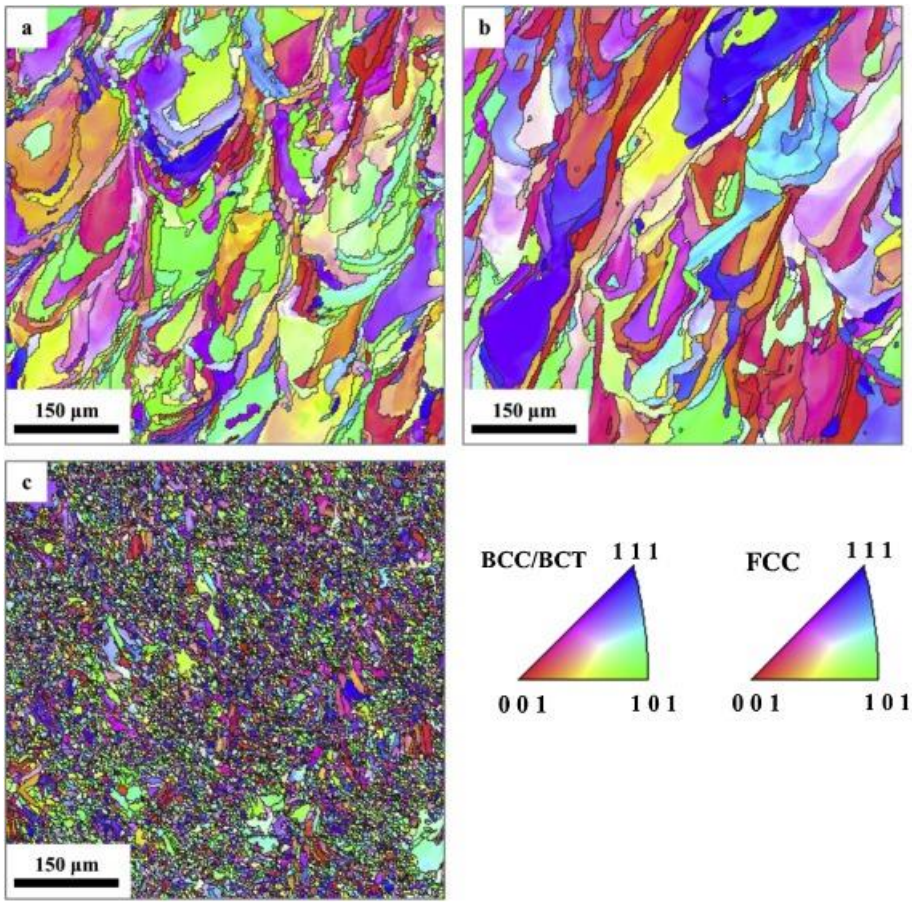

Figure 2.19. EBSD-IPF maps obtained through PBF-LB process with three different powders, referred to as (a) Powder A, (b) Powder B and (c) Powder C [94].

The reason why 17-4 PH processed with PBF-LB possesses high strength, even with high content of austenite, and at the same time extended ductility, is because of the TRIP nature of the material. The strain hardening phenomenon is described as the transformation of retained austenite to martensite during the plastic deformation for the enhancement of both strength and ductility [101]. The transformation that takes place helps the material by increasing the work hardening rate and the neck region is strengthened by hindering the further movement of the crack that initiated. Steels with this deformation behaviour include fully austenitic steels and steels that contain only a fraction of retained austenite, as 17-4 PH, and are referred to as TRIP-assisted steels. The TRIP effect happens when plastic deformation is applied to the material, and to understand the process that allows the transformation process, the chemical free energies of martensite and austenite versus temperature must be taken into account as depicted in Figure 2.20(a). When the material is at the temperature M_S, ${\Delta G_{Ms}}^{\gamma \to \alpha'}$ is the critical value for the beginning of the transformation to martensite. However, at a higher temperature, referred to as T_1, an additional value *U'*, called mechanical driving force due to the applied stress, needs to compensate the lower ${\Delta G_{T_1}}^{\gamma \to \alpha'}$ chemical driving force so that the stress-assisted martensitic transformation can start [102]. By considering Figure 2.20(b), it can be noticed that from M_S up to ${M_S}^{\sigma}$ a linear increase of stress is needed to activate the stress-assisted martensitic transformation. Between ${M_S}^{\sigma}$ and M_d

instead, where M_d is the upper limit of the martensitic transformation, plastic deformation takes place due to the lower stress needed to deform the material. However, the transformation of austenite to martensite can take place thanks to the strain-induced martensitic transformation (SIMT). If, for example, at the temperature T_1 austenite initiate plastic deformation with a stress of σ_a and then hardens when the stress σ_b is reached, SIMT can initiate directly thanks to the nucleation sites that form thanks to the plastic deformation, that lowers the energy of formation [103]. The phenomenon is favoured for alloys that have low SFE.

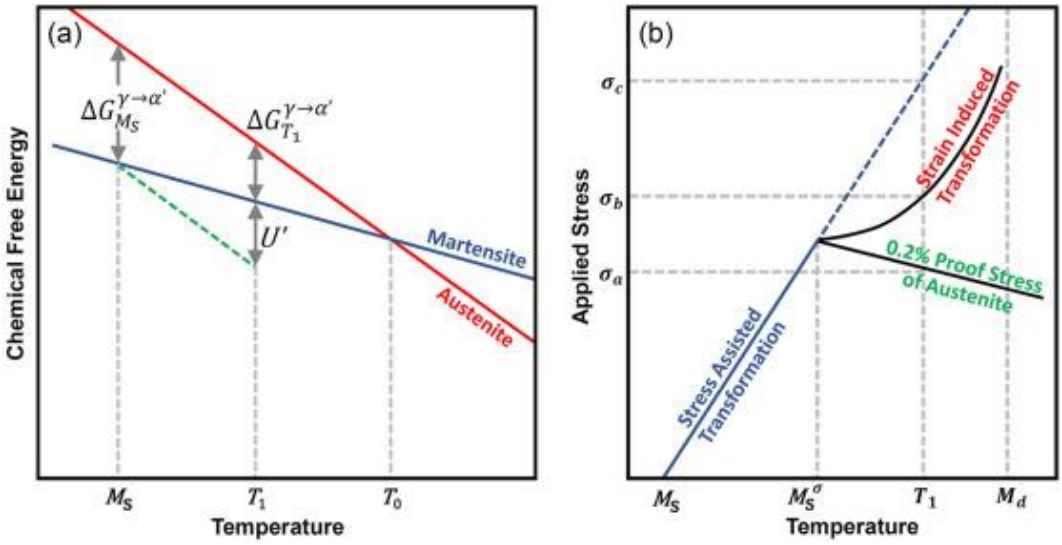

Figure 2.20. Graphs representing the (a) chemical free energies and (b) critical stress for the formation of martensite, versus temperature [101].

The kinetics of SIMT is defined by an empirical parameter that accounts for the effects of the chemical composition (in *wt%*) and the ASTM grain size number (G_S), which is the $M_{d30/50}$ and is described as the temperature corresponding to the formation of 50% of martensite (induced by plastic strain) when a 0.3 true tensile strain is reached [104]

$$M_{d30/50} = 551 - 462(C + N) - 9.2Si - 8.1Mn - 13.7Cr - 29(Ni + Cu) - 18.5Mo - 68Nb - 1.42(G_S - 8) \quad \text{Equation 2.11}$$

A low value for $M_{d30/50}$ results in higher stability of austenite as opposed to SIMT. This can be accomplished by increasing the alloying elements, as SFE is affected by their introduction. It was found [105] that three different ranges for SFE favour contrasting deformation mechanisms. In particular, SFE between 10 and 20 mJ/m^2 assists the SIMT, the range between 20 and 50 mJ/m^2 supports twinning induced plasticity, whereas values higher than 50 mJ/m^2 favour deformation glide. 17-4 PH has been found to possess an SFE between 15 and 20 mJ/m^2 and therefore SIMT is favoured in this alloy [14]. The formation of martensite can be however reduced if not suppressed by refining the austenite grain size, as small grains cause a lower *Ms* temperature and do not transform until a large deformation takes place [106]. The same effect is obtained at increasing temperature because the SFE grows, and the chemical driving force is reduced. A model was proposed by

Olson and Cohen [107] to describe the kinetics of SIMT. Specifically, the transformed fraction from austenite to martensite versus the equivalent plastic strain ε, considering two constants that depend on the temperature (α considers the rate of the shear band formation in the austenite, while β is the probability that martensite nucleates at a shear band intersection). The exponent n is a fixed value. The result is shown in Equation 2.12.

$$f_{\alpha'} = 1 - exp\{-\beta \cdot [1 - exp(-\alpha \cdot \varepsilon)]^n\} \qquad \text{Equation 2.12}$$

As described earlier, in TRIP-assisted steels the plastic deformation allows for the transformation of the retained austenite into martensite and this prevents the necking to advance, as shown in Figure 2.21.

17-4 PH contains several alloying elements, the weight percentage of each is dictated by a compromise between the benefits for the TRIP effect and the detrimental consequences of having those elements in the composition. Carbon is a strong austenite stabiliser but needs to be in a content below 0.3 *wt%* because it affects the weldability of the alloy. Manganese stabilises austenite as well, however it can segregate easily after the production process to provide detrimental mechanical properties and for this reason the content is usually lower than 2 *wt%*. Silicon restricts the precipitation of carbides during the production process to allow for partitioning of C; this means that the austenite that partially transforms into ferrite or martensite can be enriched in carbon and become more stable due to a decrease of *Ms* and *Mf*, thus leaving retained austenite in the as-printed material; nonetheless, high content can bring to the formation of an oxide layer and therefore the recommended maximum content is 2 *wt%*.

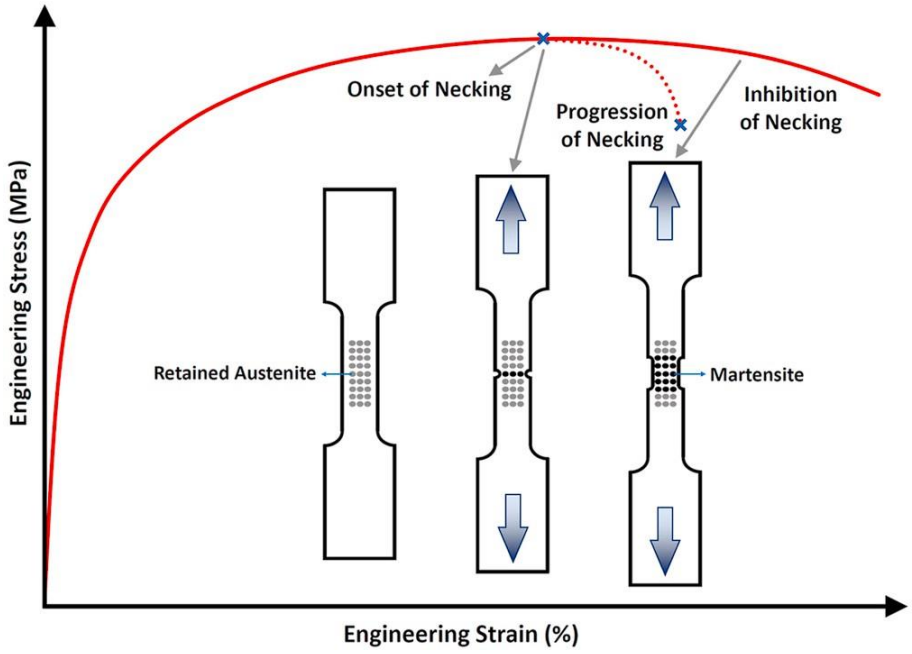

Figure 2.21. Stress-strain curve of a TRIP-assisted steel with the schematic of the transformation of the retained austenite into martensite [101].

2.5 Defects of stainless steel alloys processed by PBF-LB

PBF-LB technology suffers from a range of defects during the melting process, caused by the laser source and the powder interacting. The main defects that can be seen during the printing process are porosity, cracks, spatter and residual stress. The defects are caused by several reasons, which include the process parameters in terms of power, scan speed, hatch distance and layer thickness of the laser; the scan strategy and the gas flow. The main defects will be discussed in this section. Cracks is an important family of defects that can occur to metal alloys. However, the knowledge on stainless steels is so deep that cracks are easily avoided, and they were not encountered in the investigations performed in this work. Therefore, they are not discussed.

2.5.1 Porosity

The process map is a useful tool to describe how a PBF-LB alloy responds to process parameters and the formation of porosity [108]. A process map helps to determine the defect density variation in a graph where the axes are represented by the power *P* and laser scan speed *v*. Figure 2.22 represents the boundaries to obtain a defect free structure with only gas pores, which enclose a process window. Outside of these boundaries, lack of fusion, keyholes and other defects can be found.

Gas pores have a spherical shape, depicted as a circle in a micrograph, a size no larger than tens of microns and are distributed within the melt pool [109]. They are gas bubbles deriving from the evaporation of hydrogen in the molten metal. The high cooling rate that takes place in PBF-LB starts the solidification before the gas pores are able to escape the melt pool.

Lack of fusion (LOF) defects arise when low *P* and high *v* values are used in the PBF-LB process. This condition brings low energy density onto the substrate to scan thus causing lack of adhesion between adjacent layers. The size for such defects ranges between 10 μm and 1 mm and the resulting shape is irregular shape [110,111]. LOF defects can be defined as geometrical defects because they result from an incorrect superimposition of the melt pools generated by the laser thus leaving space between the melt pools [112]. Figure 2.23 shows morphology of LOF defects, both in the cross-section plane (perpendicular to the BD) and in the longitudinal plane (parallel to the BD). To ensure that a complete overlap is guaranteed when printing, Tang proposed an approach, according to which the quantity in Equation 2.13 must be lower or equal to 1 [113]

$$\left(\frac{h_d}{w_{MP}}\right)^2 + \left(\frac{L_T}{d_{MP}}\right)^2 \leq 1 \qquad \text{Equation 2.13}$$

Where h_d is the hatch distance, w_{MP} is the melt pool width, L_T is the layer thickness, and d_{MP} is the melt pool depth.

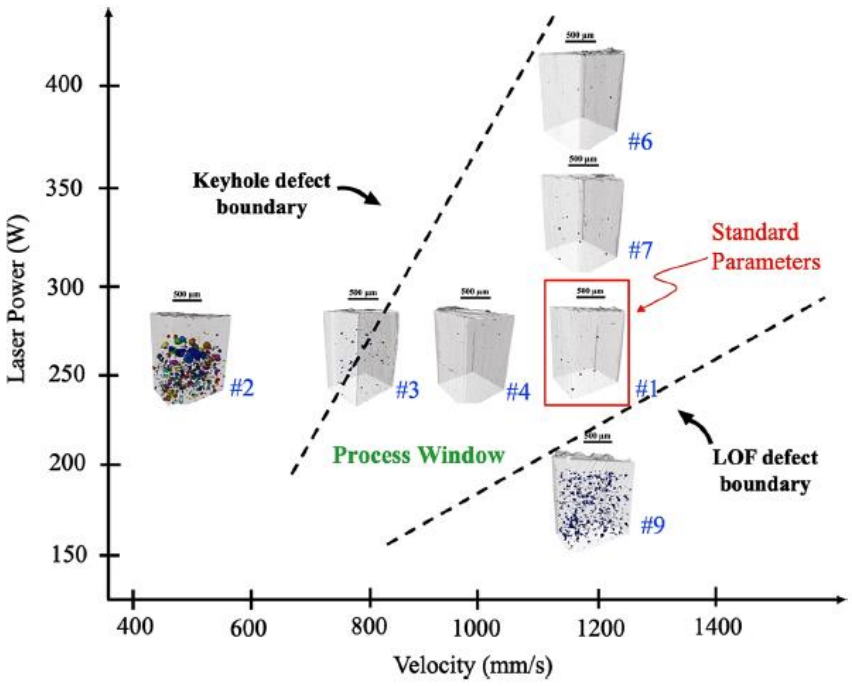

Figure 2.22. Process window for PBF-LB [108]. The process window guarantees a defect free structure with only gas pores. The window is separated by the keyhole defect and the LOF defect boundaries from areas where the density level drops.

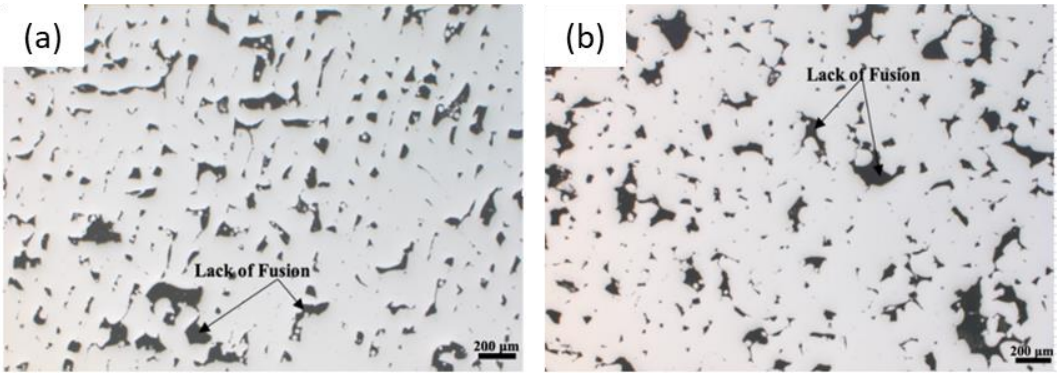

Figure 2.23. Lack of fusion defects for a 316L stainless steel component melted with a VED of 34.09 J/mm^3 with resulting density of 90.78% [111] ; (a) is a micrograph in the cross-section (perpendicular to the BD) while (b) is a graph from the longitudinal plane (parallel to the BD).

On the other boundary of the process window, keyhole defects can be encountered. Conversely to LOF defects, they form when high laser *P* and low *v* are used in the PBF-LB process. This phenomenon depends on the excessive energy density provided to the melted layer thus leading to the evaporation of the metallic powder and change in phase to plasma [108,114,115]. A variation from conduction mode to keyhole mode occurs, where the absorptivity increases to extremely high values because the beam reflects multiple times within the vapor cavity generated by the high energy density that is applied. As a result, the phenomenon causes spherical

defects, with sizes approximately between 35 and 60 μm [116]. Figure 2.24 shows keyhole defects at the bottom of melt pools in the longitudinal direction, parallel to the BD, for a sample printed with 17-4 PH.

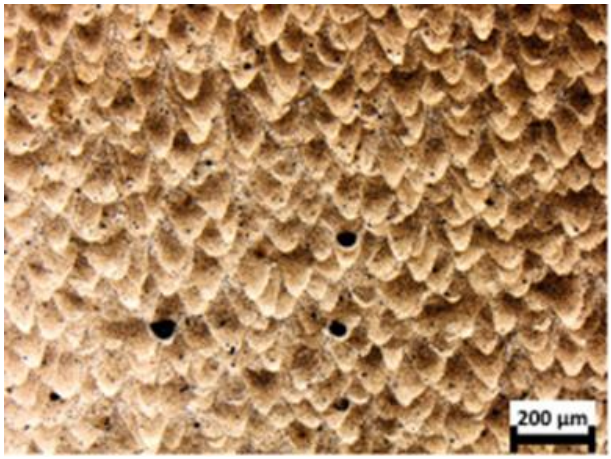

Figure 2.24. Micrograph along the BD showing keyhole defects at the bottom of melt pools for a sample printed with 17-4 PH and a VED of 125 J/mm^3 [117].

As there is a dependence of keyhole defects on the given VED, different values of h_d create specific process maps that can be used to predict the resulting defects on a material. Figure 2.25 displays two process maps for 316L for two dissimilar values of h_d.

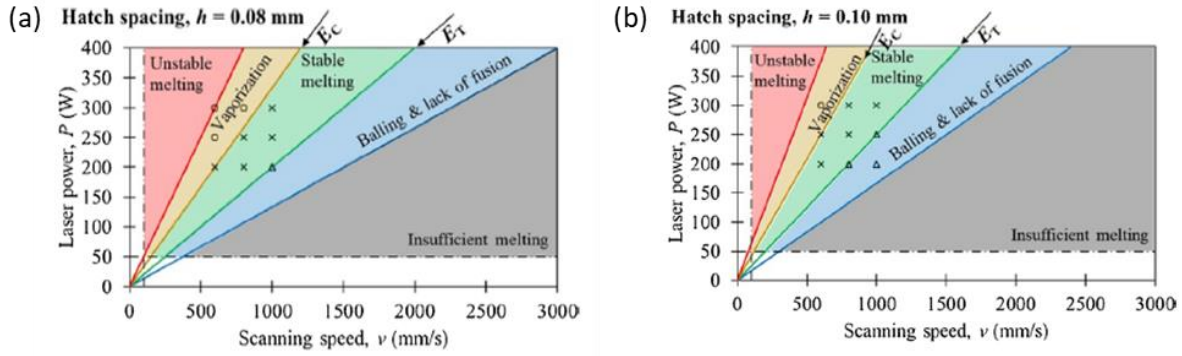

Figure 2.25. Process maps derived from two different h_d values for 316L [115] : (a) 0.08 mm and (b) 0.10 mm.

Balling is a phenomenon occurring during PBF-LB process as the laser molten track has a shrinking tendency to decrease the surface energy by surface tensions [118]. As a result, molten powder can solidify as spheres and pores can form between discontinuous metallic balls thus reducing the mechanical properties of the printed parts [119]. In general, balling is caused either by worsened wetting ability of the powder [120], or by high v values [118]. Decreasing the oxygen content in the build chamber to at least 0.1% helps addressing the phenomenon, which is why the phenomenon did not occur in this work.

Denudation is a phenomenon causing the depletion of the metal powder close to the laser scan path, and it results from an antagonism amid the metal vapour flux directing outwards off the scanned area and gas flow

induced in the build chamber [121]. When a high induced gas flow is acting on the powder bed, entrainment of powder particles occurs at the melt pool location. If low gas flow is present, the metal vapour flux can expand laterally thus pushing powder particles outward.

Spatter occurs during the melting process of PBF-LB when the laser beam provides such a high *VED* that the melted material is compressed, part is vaporised and some liquid material leaves the molten pool [122]. The reason is because high *VED* induces high temperature and strong temperature gradients, which enable temperature dependent surface tension (temperature expressed in K)

$$\sigma(T) = 3.282 - 8.9 \cdot 10^{-4} \cdot T \qquad \text{Equation 2.14}$$

Marangoni effects are generated which increase the depth of the melting area, with liquid metal that ejects away from the surface in the form of spherical particles [123,124]. There are three types of spatter. The first is called metal jet and is caused by the recoil pressure of gas phase formed due to vaporisation of the metal. The second is determined by the metal liquid flowing from the high temperature bottom of the hole to the walls on the sides and the back thus allowing low viscosity metal liquid to be jetted out under recoil pressure as droplets. The third type of spatter is determined by liquid metal squeezed by the beam to the front of the scanning direction, along with non-melted particles. Spatter particles will be entrapped onto the substrate they fall onto, thus deteriorating the mechanical properties of the material.

2.5.2 Residual stresses

The PBF-LB process of 316L and 17-4 PH undergoes phase changes upon melting of the powder and subsequent cooling, as well as high temperature gradient in the component along the build direction during manufacturing. As a consequence, residual stresses originate which are a fundamental aspect of the additive manufacturing technology.

The large thermal gradients that take place during the PBF-LB process are generated by the process parameters, including the part size, build time, build place temperature and atmosphere [125]. Different microstructural features can be obtained, with potential excess of dislocations formation and related stress fields. This causes localised deformation for a loss of the desired net shape, along with detachment from the support structures or even a failure of the printed part.

In the literature it is documented that residual stress values can be in the order of the σ_Y of the printed material or even higher [126]. As the high values are caused by the process parameters, most of the recent investigations focused on minimising residual stresses by means of tailored laser scanning strategies. It was found that it is important to avoid a longitudinal scanning in the direction of a long cross-section, and the reduction of residual stress can be of up to 75% when using an alternating longitudinal/transversal scanning, a transversal scan

strategy, or even an island scanning [127]. Considering island scanning strategy, a further decrease is reached by reducing the size of islands [128]. However, an island with excessively reduced size has a detrimental effect in that the area being melted is too small compared to the scanning layer. The result is more dispersive and random spots, thus causing excessive thermal gradient between the island and the rest of the printed part. As a consequence, residual stresses increase and result higher than those originated with a meander or stripe scan strategy [129]. A meander strategy is generally the most used strategy, which provides a random and homogeneous heat distribution throughout the layers. Additional laser scan strategies were studied to determine how they were affecting, among the others, mechanical properties, geometrical and dimensional quality and surface finish [34]. For instance, hexagonal improved porosity, while normal (a linear pattern with an orientation continuously changing from 45° to −45° on each layer) and hexagonal improved the mechanical properties. Ductility and low roughness on the faces were instead favoured by the concentric strategy.

Another remark on residual stress is related to the laser scanning mode. Pulsed laser, used in this work, increases the cooling rate of the PBF-LB process as opposed to a continuous mode. Consequently it allows, for 316L, a cooling process that retains the same austenitic phase upon cooling, by-passing the austenitic to ferritic transformation. This solves the issues related to phase change and difference in coefficient of thermal expansions during the process [129].

An additional fundamental aspect is the preheat of the substrate, or build plate, where the part is printed onto [130]. The rational for using it is to reduce the residual stresses, enabling a proper thermal gradient between the printed layer and the colder build plate. Further effective solutions to the residual stress issue are the remelting of the melt pools and the ex-situ heat treatments, such as annealing.

2.6 Strain rate of strain hardening steels under deformation

The strain rate, at which mechanical tensile or compression tests are conducted, strongly affects the mechanical properties of most materials. This includes the strain hardening steels investigated in this thesis. Hence, a distinction must be made between tests conducted at low and tests conducted at high strain rates. In addition, the production process for the stainless steels affects the strain rate sensitivity. The strain rate sensitivity is used to evaluate the dependence of stress on the strain rate and is expressed in terms of the parameter m_{SR}, that is determined at a given strain and temperature with Equation 2.15

$$m_{SR} = \frac{\partial \ln \sigma}{\partial \ln \dot{\varepsilon}} \qquad \text{Equation 2.15}$$

Where σ is the applied stress and $\dot{\varepsilon}$ is the strain rate.

2.6.1 Strain rate sensitivity of 316L

Strain rate sensitivity of 316L stainless steel produced with PBF-LB has been determined to be slightly higher than the conventionally manufactured counterpart in the quasi-static strain rate range (between 1 x 10^{-4} and 1 x 10^{-2} s^{-1}). At higher strain rates up to ~ 2800 s^{-1}, there is a similarity in terms of sensitivity until 11% strain, while the sensitivity becomes again higher for additively manufactured 316L at strains higher than 11% [131,132]. The literature explained that the phenomenon was the result of the higher dislocation density in additively manufactured material, dislocations promoting a strengthening effect at increasing strain. As for PBF-LB 316L steel, twinning formation was detected in higher quantity when dynamic tests were performed, up to 22% strain. After that threshold, it has been revealed that adiabatic heating is a factor that decreases the twin formation at growing strain values. In Figure 2.26 is a visual representation of the trend for the stress and work hardening, versus strain, at different strain rates.

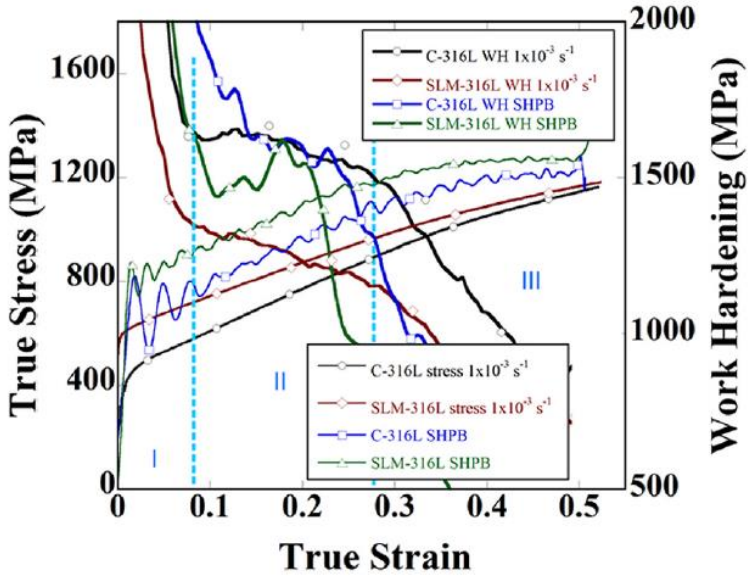

Figure 2.26. Graph showing the stress-strain and work hardening-strain curves of 316L specimens produced with PBF-LB and conventional manufacturing, at quasi-static and dynamic strain rate [131].

The stress for twinning onset was instead detected not be dependent on temperature or strain rate [132,133]. The higher strength of dynamically tested specimens is explained with an initial increase of twin formation at low strain values due to the increased critical stress needed to initiate deformation by slip. However, when adiabatic heating takes over there is a decrease of twin formation, deformation by dislocation glide is the preponderant mechanism and can keep the strength of the material tested dynamically higher than the quasi-static counterpart[134]. The higher work-hardening rate extracted from dynamically tested specimens, caused by higher formation of twins at low strain values, can generate up to 1.5 times more twin boundary fraction than quasi-static mechanical tests at 11% strain [135]. This demonstrates that quasi-statically tested specimens are deformed more by deformation glide than twinning, compared to dynamically tested specimens.

2.6.2 Strain rate sensitivity of 17-4 PH

Strain rate is an essential factor in determining the SIMT behaviour of 17-4 PH stainless steel. Taking into account that at high temperature, i.e. M_d, the SIMT is not taking place because the formation of martensite is not favoured, at high strain rates stacking faults form along with ε-martensite in both PBF-LB and conventionally made 17-4 PH, and α' martensite formation is suppressed [101]. The phenomenon occurs due to the adiabatic heating which decreases the chemical driving force of the martensitic transformation [136]. Previous studies compared PBF-LB and conventionally made 17-4 PH specimens at a range of strain rates between 1 x 10^{-3} and 1 x 10^{3} s^{-1} [137]. It was found that σ_Y and UTS are higher for the PBF-LB specimens than the conventionally manufactured parts, for all types of thermal processing history and orientations of additively manufactured specimens. Furthermore, higher mechanical strength across the entire range of strain rates for both technologies took place, meaning the strain rate sensitivity changed similarly. In Figure 2.27 is a visual representation of the trend for the stress and mechanical properties (UTS and σ_Y), versus strain, at different strain rates.

The higher UTS of PBF-LB specimens (as high as 12.4%) were attributed to the microstructural refinement coming from the AM process and subsequent heat treatment, since the strain rate sensitivity was detected similar for PBF-LB and conventionally manufactured specimens, at each strain rate. The lower ε_f for PBF-LB specimens compared to conventional counterpart was, instead, attributed to the higher porosity present inside the printed materials. Increasing the strain rate has positive effects for parts produced with all technologies. These results were confirmed with a focus on as-built and annealed specimens printed with PBF-LB (strain rates between 1 x 10^{-2} and 10 s^{-1}) [138]. The main difference between as-built and annealed specimens is in the phase transformation enabled by annealing. The as-built material contains larger fraction of retained austenite that can transform into martensite during plastic deformation for a larger contribution of the TRIP effect [138,139]. However, the strain rate sensitivity at the same strain rate also depends on the microstructural grain size, with finer grain size increasing the strain rate sensitivity of materials [139]. It was also revealed that increasing the strain rate can diminish the quantity of martensite phase forming. This seems to contradict the increase in strength with strain rate. Nonetheless, high strain rates generate more dislocations, and deformation glide plays an important role in strengthening the material over TRIP [140]. In fact, dynamic loading was found to be beneficial to the dislocation motion along multi-slip systems and the development of additional dislocation nucleation. Moreover, dynamic loading allows the formation of precipitates that results fundamental for the strengthening and detrimental for the ductility of the material.

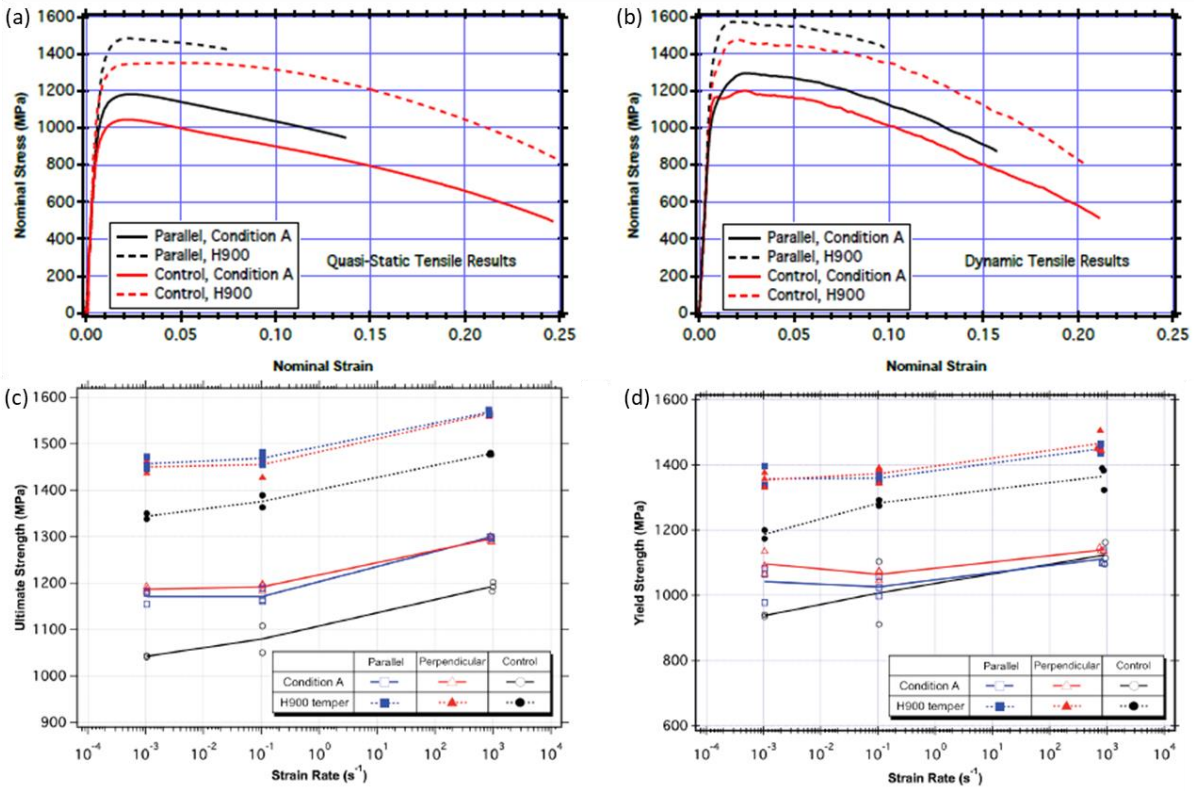

Figure 2.27. Graphs comparing the stress-strain curves of 17-4 PH specimens produced with PBF-LB (referred to as *Parallel* or *Perpendicular*) and conventional manufacturing (named *Control*), at (a) quasi-static and (b) dynamic strain rate; the figure also shows the similar evolution of (c) UTS and (d) σ_Y over strain rate [137]. *Condition A* and *H900* are two heat treatments considered in the referenced study.

2.7 Lattice structures

Additive Manufacturing enables the redesign of components for lightweight applications. This aim can be reached by adopting topology optimisation (TO), which generates an optimised shape for a specific case load. If the loading conditions are unknown, lattice materials, also referred to as lattice structures, lattices, metamaterials or architected materials, offer good mechanical properties in multiple directions [141]. Lattice structures comprise repeating unit cells made of interconnected struts, plates or shells at the unit length scales less than 10 mm [142]. The main reference design theory for lattice structures has been the Gibson-Ashby model [143], which links several key performance metrics, like stiffness and strength, to the mass density. Lattice structures do not require high computational resources from iterative resolution of the TO problem and they absorb deformation energy in a predictable manner. Two main classes of lattice structures are presented in Section 2.7.1.

2.7.1 Typologies of lattice structures

Lattice structures include two main classes, strut-based and TPMS based lattices [7,27]. Strut-based lattices are defined by straight struts interconnected at their vertices (referred to as nodes) to form a unit cell. They are mainly characterised by an elementary cubic cell with a modulation of the number and the size of struts, to obtain the required density and mechanical properties. The most common unit cells are reported in Figure 2.28.

The second class of lattices, the TPMS, are a subset of the constant mean curvature surfaces and have been introduced more recently into the AM field [144]. TPMS lattices have a zero mean surface curvature at each point and are created by mathematical formulations. Two different strategies generate two sub-classes [145]. The first approach consists of filling the volume separated by the TPMS, to create a solid structure referred to as "skeletal" TPMS, Figure 2.28(B). The second one creates a solid structure by thickening the surface obtained through the mathematical formula, and this solid structure is called "sheet" TPMS, Figure 2.28(C). Compared to strut-based lattices, TPMS offer a good combination of specific stiffness and axisymmetric stiffness, high surface-to-volume ratio and pore connectivity, application of functional grading [146]. In addition, a reduction in stress concentration occurs thanks to the lack of nodes and points of curvature and discontinuity, which enhance the fatigue strength [21].

The general behaviour of lattices depends on the applied stress on the struts, according to the Maxwell criterion [147]. If bending stress acts on the struts, they are referred to as bending-dominated structures; if axial stress applies, stretch-dominated lattices are generated. Stretch-dominated lattices are stronger and stiffer than bending-dominated structures.

The mechanical behaviour of the lattice structures is displayed in Figure 2.29 for (a) stretch-dominated and (b) bending-dominated lattices considered with the same quantity of material (relative density or volume fraction, VF). Both curves can be divided into three phases of lattice deformation. (1) linear elastic region until the yield point, (2) plateau regime where the unit cells sequentially collapse because they buckle, crush or yield according to the material and the morphology, (3) the densification phase with collapse of the cells reaching contact. The stretch-dominated lattices possess a higher initial stiffness and σ_Y than a bending-dominated lattice structures. In addition, a post yield softening is detected and caused by the buckling or brittle crush of a unit cells layer. The representative stress-strain curve is defined by peaks and valleys depicting the progressive failure of the layers. As opposed to stretch-dominated lattice structures, bending-dominated lattices are more suitable for energy absorption application. In fact, they are not susceptible to important post-yield softening with high peak stress and subsequent lower plateau stress [148], as well as they show an extended stress plateau under deformation [149].

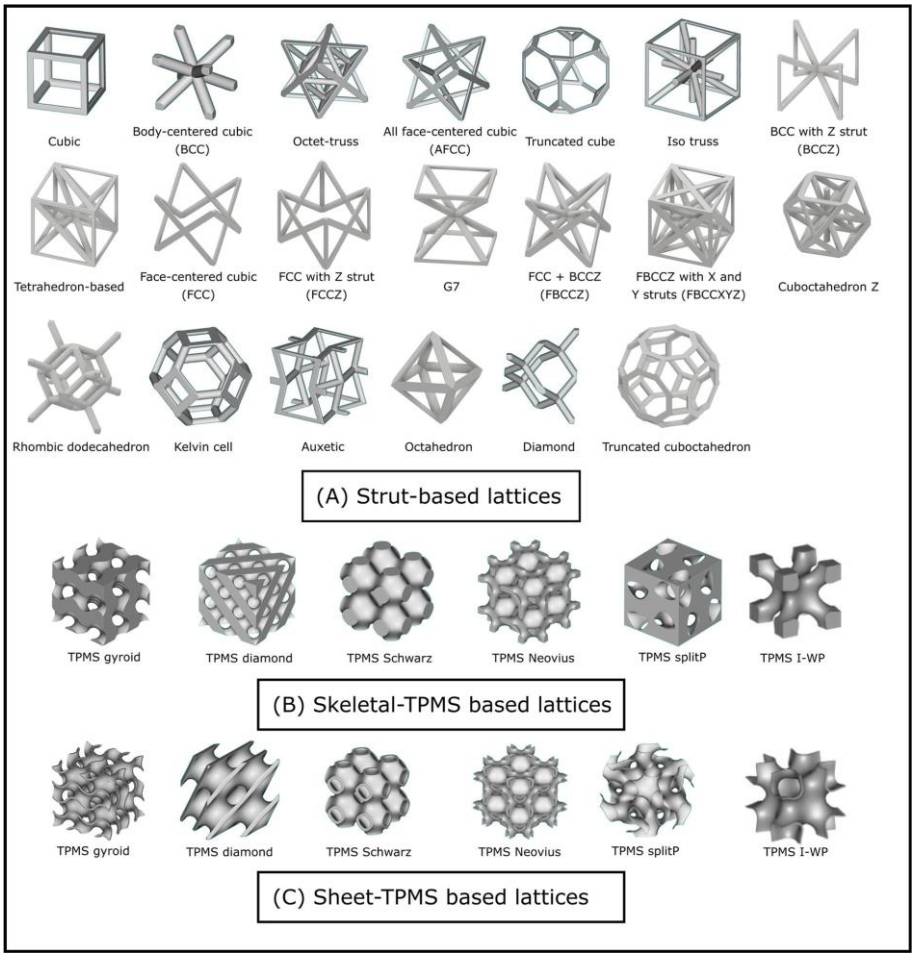

Figure 2.28. Architectures of lattice structures according to the main classification : (A) strut-based lattices; (B) skeletal-TPMS and (C) sheet-TPMS based lattice structures [27].

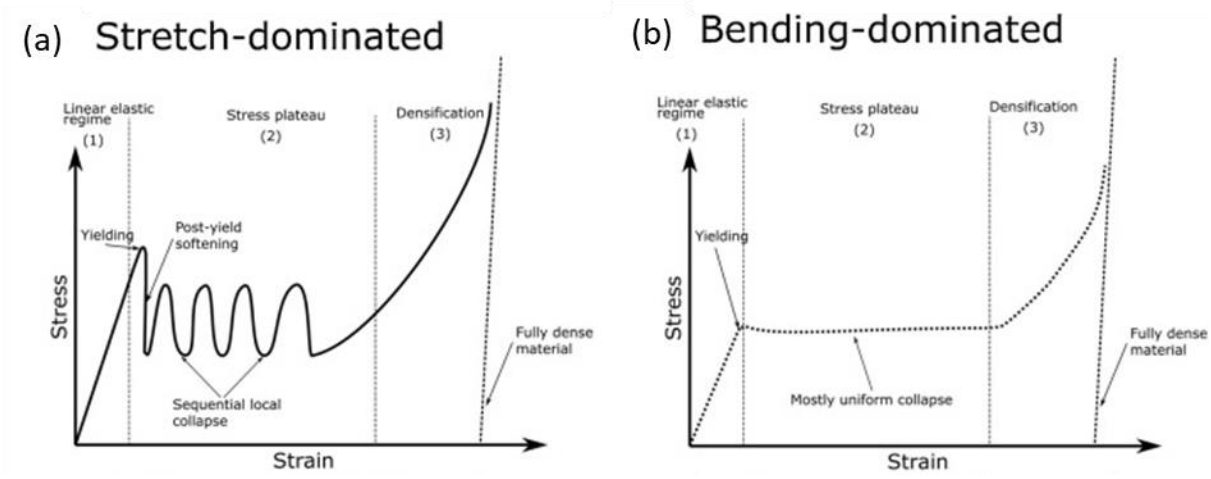

Figure 2.29. Stress-strain curves for (a) stretch-dominated and (b) bending-dominated lattice structures, considered with the same relative density [7].

One of the most studied lattice structures is based on the gyroid surface, defined by Schoen [150], and is shown in Figure 2.30.

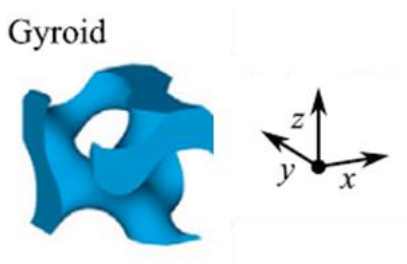

Figure 2.30. Representation of the gyroid unit cell [150].

Gibson and Ashby determined the characteristics of cellular solids, such as density and pore size, and their physical properties. Therefore, their findings are used when approaching the study of lattice structures [151]. The most important relationships, for materials having a plastic yield point, are:

$$E^* = C_1 \cdot \rho^{*n} \quad \text{Equation 2.16}$$

$$\sigma^* = C_5 \cdot \rho^{*m} \quad \text{Equation 2.17}$$

where

$$\rho^* = \frac{\rho_{latt}}{\rho_{sol}} \quad \text{Equation 2.18}$$

$$E^* = \frac{E_{latt}}{E_{sol}} \quad \text{Equation 2.19}$$

$$\sigma^* = \frac{\sigma_{pl.latt}}{\sigma_{y\ sol}} \quad \text{Equation 2.20}$$

C_1 includes the geometric constants of proportionality, and the range value is 0.1 – 4

C_5 includes the geometric constants of proportionality, and its range value is 0.1 – 1

n is ~ 2 when deformation occurs by bending

m equals to around 3/2 when deformation occurs by bending

ρ_{latt} is the density of the lattice structure

ρ_{sol} is the density of the constituent material

ρ^* (also referred to as VF in this thesis) is defined as relative density or volume fraction of the lattice

E_{latt} is the elastic modulus of the lattice structure

E_{sol} is the elastic modulus of the constituent material

E^* is referred to as relative elastic modulus of the lattice

$\sigma_{pl.latt}$ is the compressive strength of the lattice structure

$\sigma_{y\,sol}$ refers to the yield strength of the constitutive material

σ^* defines the relative collapse strength of the lattice

A sheet-based TPMS lattice is generated by finding the $U = 0$ iso-surface of the TPMS equation and specifying the cell repetitions and volume fractions. The gyroid (G) equation

$$U_G = (sin(k_x x)cos(k_y y) + sin(k_y y)cos(k_z z) + sin(k_z z)cos(k_x x))^n - t^n \quad \text{Equation 2.21}$$

Where

$$k_i = 2\pi \cdot \frac{n_i}{L_i}, (\mathrm{i} = \mathrm{x, y, z}) \quad \text{Equation 2.22}$$

n_i are the numbers of cell repetitions in the x, y and z directions; L_i are the sizes of the structure in the same three directions.

The iso-surface is treated as a boundary between solid and void. Moreover, *t* is used as a variable to control ρ^* in Equation 2.21, and ρ^* increases with *t*. When creating a lattice structure, solid and void regions must be defined. In particular, the solid is determined for $U \leq 0$, while void is described by $U > 0$ [152].

Equation 2.21 can describe different gyroid TPMS lattices. When *n* is selected as 1, it describes the network structure, while to define the matrix structure *n* must be set as 2. A modification of the equation, where the terms periodic in *z* are removed and *n* equals 2, generates a new unit cell, referred to as honeycomb gyroid

$$U_{hon} = (sin(k_x x) \cdot cos(k_y y) + sin(k_y y) + cos(k_x x))^n - t^n \quad \text{Equation 2.23}$$

Therefore, the honeycomb gyroid unit cell is considered to be a derivation of a TPMS structure. The resulting unit cell geometries for the network, matrix and honeycomb lattice structures are shown in Figure 2.31.

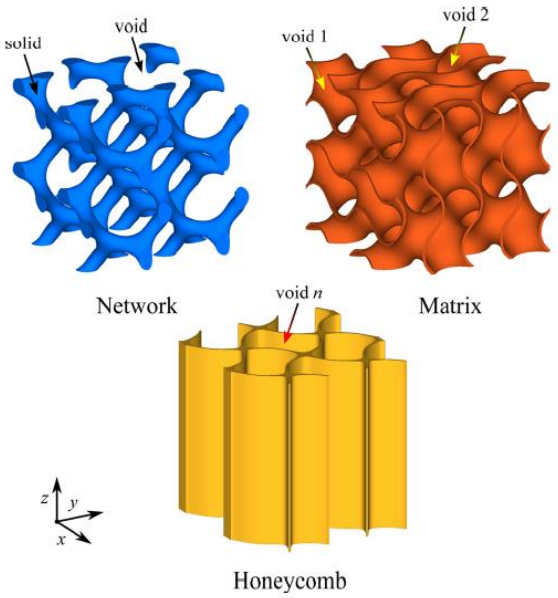

Figure 2.31 Gyroid lattice structures based on the network, matrix and honeycomb unit cells [151]. The configuration is 2x2x2 for the network and matrix, 2x2 for the honeycomb cell.

By applying the homogenisation code on these three lattice structures (see Section 3.6), it has been determined that the matrix gyroid is almost isotropic. The honeycomb gyroid is the most anisotropic, with the ratio $\frac{E^*_{max}}{E^*_{min}}$ (E^*_{max} being the relative elastic modulus in the *z* direction, E^*_{min} the value in the *x*-*y* plane) is close to 250. In Figure 2.32, the results of the investigation for a volume fraction of 0.2 can be seen for a polymer material [151].

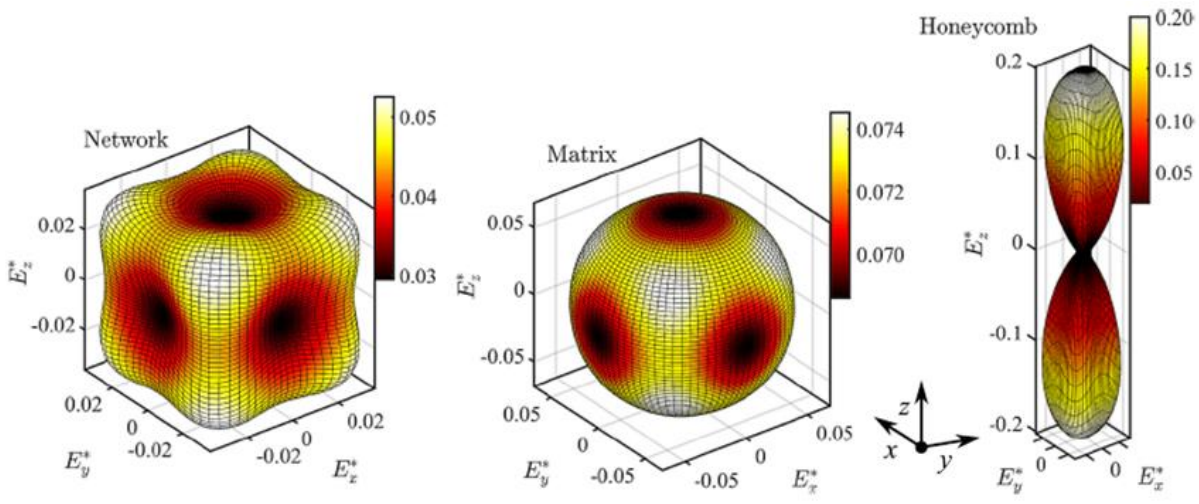

Figure 2.32 Relative elastic moduli determined on the network, matrix and honeycomb gyroid unit cells (from left to right) for a volume fraction of 0.2 and a polymer material [151].

2.7.2 Lattice structures produced via PBF-LB for energy absorption

Lattice structures have complex shapes, that PBF-LB allows to produce, and a large surface area to volume ratio. Moreover, PBF-LB provides higher surface roughness, for an increased available surface area as opposed to the CAD model [7,27]. This can be beneficial in applications such as implants for osseointegration. However, for crashworthy applications, increased roughness is detrimental to performance because it creates additional crack initiation sites to the deforming structure. Therefore, surface accuracy is a factor to consider for printed lattices. Lattice structures have small features compared to bulk parts, and same process parameters can result in microstructural deviation. Other challenges for energy absorption applications are linked to the scan strategy, that can produce excessive or insufficient melting on the scanned layer, for increased porosity defects. Likewise, the smaller scanned wall thickness decreases the thermal conductivity for the heat dissipation away from the melt pool thus causing higher residual stress and bending of thin features. As a result, printed parts must be checked for geometrical and microstructural conformance. Furthermore, orientation of the printed part is important to consider, as more self-supporting surfaces will reduce the thermal conductivity which is instead provided by the supports.

The current research on strut-based lattices focuses on microstructural changes obtained with different printing conditions or post-processing heat treatments, for diverse mechanical response under deformation including crashworthy application [153]. Moreover, rotating the topology, modifying it or adding infills can enhance the mechanical behaviour by efficiently redistributing the applied stress [9,154]. An example is shown in Figure 2.33, where the volume fractions of the lattice structures without (HSL) and with (TP-HSL) the integrated thin plate are the same for each of the three cases.

The investigation of TPMS lattice structures printed with PBF-LB is more recent and has become preponderant because of the enhanced mechanical properties compared to traditional strut-based lattices for energy absorption purposes. Several materials have been used, including titanium [23] and stainless steels, especially 316L for its extended ductility before collapse of the structure [24,149]. The limitations of PBF-LB in terms of printing time and build platform size, along with the cost requirements, has made it necessary to invest into prediction tools for compressive behaviour of lattice structures. Therefore, FEA has proved to match with reliable results the experimental deformation, supporting the research on energy absorption (see Section 2.7.4) [149].

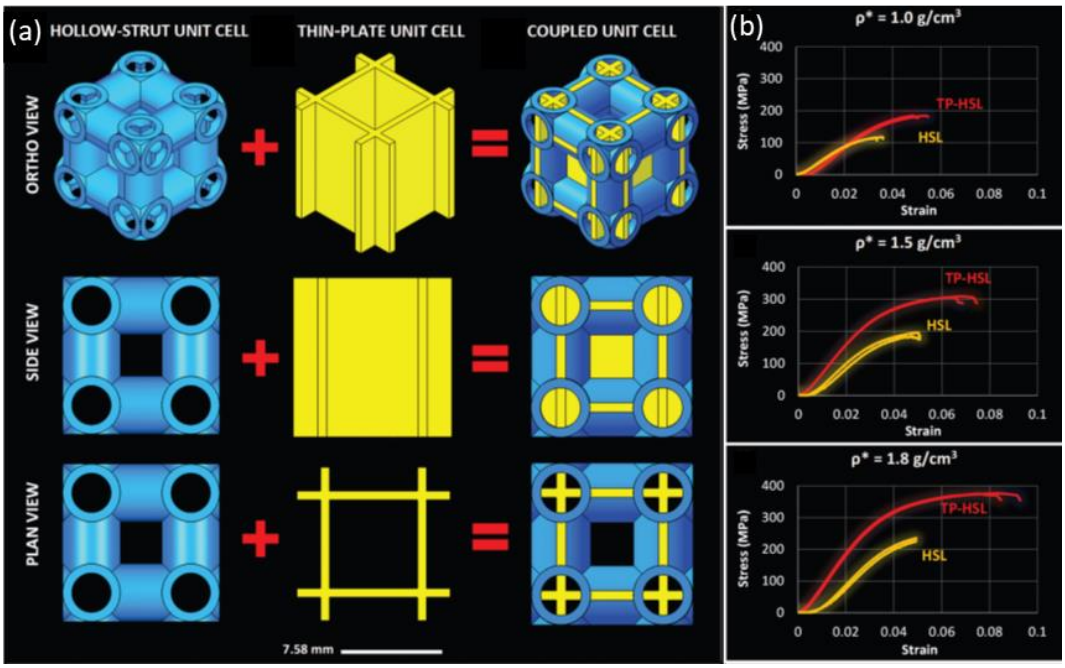

Figure 2.33. Overview of the investigation performed in [9]. (a) is the CAD model of the lattice structure integrated with a cubic thin plate; (b) shows the compression response at three different volume fractions for the HSL and TP-HSL lattice structures.

Early studies on strut-based lattices printed with 17-4 PH started focusing on process parameters for the printability and geometrical accuracy of lattices, to provide performing compression behaviour [155]. More recent studies analysed the as-built microstructure, how the energy density affects the initial phase content and the thermal strain, since these have a fundamental contribution on the TRIP effect during deformation of the structures [25]. It was found that low energy density caused lower thermal strain and martensite phase fraction for a bend-dominated compression response, whereas high energy density increased the thermal strain and martensite content, changing the compression response to a stretch-dominated.

2.7.3 The Johnson-Cook damage model for lattice structures

The Johnson-Cook (J-C) damage model is a widely spread constitutive model for the description of damage in lattice structures deformation at different strain rates [156,157]. It was proposed by Johson and Cook in 1983 to describe the characterisation of yield stress and failure strain of materials during deformation [158]. The importance of the model is given by the three key factors that are considered when investigating materials, typically metals, which are strain, strain rate and temperature. By including them, the model enables a reliable description of the material's behaviour under different conditions that affect strain, when large strains, strain rates and temperatures apply.

Mechanical properties of the material are affected by strain hardening, strain rate hardening and temperature softening in agreement with Equation 2.24

$$\sigma_e = (A + B \cdot \varepsilon_{e,p}^{n}) \cdot (1 + C \cdot \ln \frac{\dot{\varepsilon_{e,p}}}{\dot{\varepsilon_0}}) \cdot \left[1 - \left(\frac{T - T_r}{T_m - T_r}\right)^m\right] \quad \text{Equation 2.24}$$

where σ_e represents the flow stress, $\varepsilon_{e,p}$ indicates the effective plastic strain, $\dot{\varepsilon_{e,p}}$ and $\dot{\varepsilon_0}$ represent the effective plastic strain rate and the reference strain rate. T, T_r, and T_m denote, respectively, the temperature of the test, the reference temperature, and the melting point of the material. The properties of the material are represented by A, B, C, n, and m. A is the yield strength under a reference temperature and reference strain rate; B and n denote the strain hardening coefficients; C represent the strain rate sensitivity coefficient; m is the temperature sensitivity coefficient.

In addition to this, in 1985 Johnson and Cook introduced the J-C failure model [159], which additionally takes into account the effects of stress triaxiality, strain rate, and temperature on the failure of the material, according to Equation 2.25

$$\varepsilon_f = [D1 + D2 \cdot exp(D3 \cdot \sigma^*)] \cdot (1 + D4 \cdot \ln \frac{\dot{\varepsilon_{e,p}}}{\dot{\varepsilon_0}}) \cdot \left[1 + D5 \cdot \left(\frac{T - T_r}{T_m - T_r}\right)\right] \quad \text{Equation 2.25}$$

where ε_f denotes the failure strain; D1, D2, D3, D4, D5 represent the failure parameters of the material. In the equation there is a dimensionless compressive stress ratio σ^*, obtained by

$$\sigma^* = \frac{p}{\bar{\sigma}} = -\eta \quad \text{Equation 2.26}$$

Where p denotes the hydrostatic pressure, $\bar{\sigma}$ is the equivalent stress, and η represents the stress triaxial degree.

The J-C model requires determination of several parameters, which are extracted from different mechanical tests. A, B, and n are determined by quasi-static experiments; C is extracted from dynamic tests; N is took through compression testing at high-temperature; D1, D2 and D3 are achieved by notch tensile tests; D4 is obtained by quasi-static tensile experiments; D5 is extracted via tensile testing at high-temperature.

2.7.4 Lattice structures and energy absorption

Regarding the deformation behaviour of lattice structures, a distinction between energy and impact absorption must be made. Energy absorption is linked to the capability of a material to withstand loads at low strain rates without a catastrophic failure, whereas impact absorption refers to the same definition but at high strain rates. For fields where high performance is required, such as automotive and aerospace, metal-based lattices are preferred to polymers due to the durability of metals and the higher achievable impact strength.

The energy absorption, in quasi-static compression, depends on the properties of the base material, the volume fraction of the lattice structure and the geometry of the unit cells. The typical response of a lattice structure is displayed in Figure 2.29. The ideal energy absorber has a long and flat plateau with stress lower than the peak stress detrimental to the protected object, and it must absorb all the energy requested before densification. Several metrics from a stress-strain curve enable a comparison between different lattice structures. The average stress that the structure undergoes in the plateau is the average plateau stress σ_{pl}, and its value increases with the volume fraction of the lattice. A drop in the plateau stress, described by undulations, is caused by buckling, folding or a fracture event in the lattice. The most used metric to compare different lattices is the specific energy absorption (SEA), which measures the amount of absorbed energy per unit mass (unit being J/g)

$$SEA = \frac{\int_0^{\varepsilon_D} \sigma \, d\varepsilon}{\rho_{latt}}$$ Equation 2.27

The specific energy absorption corresponds to the area under the curve in the stress-strain response for a lattice structure, as presented in Figure 2.34.

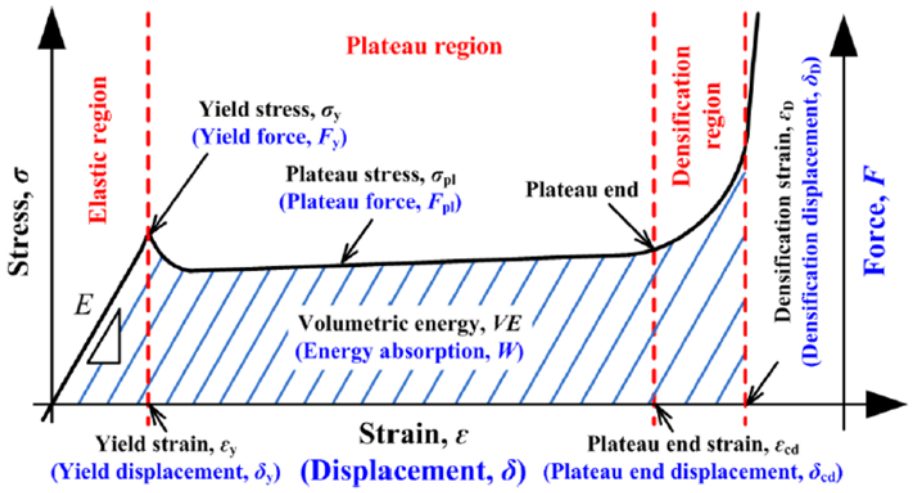

Figure 2.34. Overview of the stress-strain response of a lattice structure with the highlighted region comprised between the origin and the densification strain being the specific energy absorption [160].

Likewise, the energy absorption efficiency η can be used, which compares the energy absorption of a lattice structure to an ideal energy absorber for the maximum transmissible stress σ_{peak}

$$\eta = \frac{\int_0^{\varepsilon_D} \sigma \, d\varepsilon}{\sigma_{peak} \cdot 100\%}$$ Equation 2.28

Where ε_D is the densification strain and defines the maximum strain that can be reached during the deformation for energy absorption. The approach used in this thesis for the ε_D is based on the intersection of the σ_{pl} and the tangent line to the stress-strain curve when all unit cells go into compaction.

Conversely, high strain rate impacts involve different properties affecting the deformation behaviour. The properties are the rate dependence of the base materials, the micro-inertia, the trapped and flowing gases in the lattice structure, the macro-inertia and the wave transmission properties [27]. The impact tests at high strain rates for lattice structures are performed with a split Hopkinson pressure bar (SHPB) or direct impact Hopkinson bar (DIHB) technique [161,162]. They show limitations in the analysis of lattice structures, primarily because the diameter of the pressure bar is limited compared to the dimension of the lattices required to avoid size effects. Moreover, it has been found that SHPB is not able to deform the structure throughout the entire plateau. However, the more challenges of alternative testing techniques make SHPB and DIHB the best approaches when investigating the dynamic behaviour of lattice structures.

It is widely accepted that quasi-static testing is a reasonable way to compare dissimilar lattice structure topologies, although the reliability of energy absorption can only be obtained when dynamic testing is performed, as higher impact velocities cause higher peak stresses before densification.

Crashworthiness applications are dependent on the strain rates and use cases, which will affect the absorbed energy. The aim of the current research is to provide lightweight structures that are able to absorb high amount of energy in crashes in different fields, supplying the required mechanical properties in place of bulk components [163], specifically in dynamic conditions [66]. The fields that are mainly focusing on energy absorption are aerospace, railways [65], automotive [164]. A key field is the automotive, to provide passengers and components protection in casualties of all severity [165]. Different speeds are usually driven on the road, which must be taken into account to supply protection at the different allowed limits. In the UK, two common speed limits are 30 mph, on built-up areas, and 70 mph, the highest limit on motorways. The corresponding values translate into 58 km/h and 115 km/h. Converting speed into strain rates for the structures presented in Section 3.5, it is then clear how, in energy absorption applications, values between 1000 s^{-1} and 2000 s^{-1} need to be investigated. Impact energy in automotive crashes is in the order of 100 kJ [166,167], and highly performing lattice structure were found to withstand the required energy absorption of the impacting vehicle by reaching a SEA of 40.2 J/g [166]. It is then critical for an energy absorption related unit cell to satisfy such an order of magnitude of SEA in each direction, given the unpredictability of direction when crashes occur.

Computational modelling of lattice structures is a solution already adopted in research and industrial contexts to predict the quasi-static and dynamic behaviour of lattice structures under compression. The state-of-the-art provides a range of different unit cells and materials [23,24,55], as well as mesh elements for a prediction of the mechanical properties variation during compression at different strain rates [65,168]. However, challenges are still to be solved. Firstly, accuracy issues of the physical printing of lattices causes the dimensions of printed parts to deviate from the intended designed lattices used in the meshing [169]. This leads to a

divergence between the experimental and computational stress-strain curves. A second challenge relates to the unpredictability of defects from the PBF-LB process of physical parts, although almost full density is approached when considering the resulting porosity. The presence of pores or surface roughness in different spots represents initiation for cracks that causes unexpected failures as opposed to computational modelling, which relies upon a damage model with no defects as in the physical experiments [153,170]. An additional issue is the different physical problem implemented in the computational solver, when considering the quasi-static or dynamic configuration. The inserted values are derived from previous physical experiments on standard experiments, which are likely to be affected by experiment-related and geometry-dependent issues [66]. Finally, the right choice of meshing must be made when creating the computational environment for the simulated lattices. The proper elements are needed to accurately predict the deformation behaviour and the mechanical properties of the lattices [171,172]. Moreover, refined meshes or adaptive meshes can be used to allow for a better prediction of the stress variations on the unit cell upon deformation, but this causes in turn excessively high computational times [66].

2.8 Summary and research gap

The development of crashworthy applications is hindered by the technical knowledge of metallic materials and the components design. Specifically, PBF-LB has been found to be an effective manufacturing technology to provide tailored microstructural and mechanical properties to the material, as well as to produce complex shapes that are not possible to realise through conventional processes. As a result, lightweight components made of lattice structures with stainless steels showing strain hardening behaviour is currently possible.

Strain hardening stainless steels 316L and 17-4 PH are alloys that can be produced by means of PBF-LB with reduced presence of microstructural defects through the right process parameter sets and printing environment. 316L shows a fully austenitic and hierarchical microstructure that provides TWIP behaviour for good strength and improved ductility. 17-4 PH contains martensite, ferrite and retained austenite in its as-built condition, contributing to high strength and good ductility thanks to its TRIP behaviour. Advancements in the design of TPMS lattice structures leads to the creation of new unit cells, including the high anisotropic honeycomb gyroid that can absorb unprecedented energy in the stiffer, out-of-plane direction.

In the literature are studies that exploit PBF-LB to produce steels lattice structures for energy absorption purposes. Nevertheless, some gaps in the research must be addressed:

- The onset of the deformation behaviour for PBF-LB 316L is still under discussion. Quantification of twinning formed during plastic deformation needs at the same time an understanding of the concurrent deformation mechanisms, twinning and deformation glide, and a modelling on how to predict when each behaviour takes place.

- PBF-LB 17-4 PH is generally heat treated to homogenise the microstructure, enable precipitation hardening and improve the σ_Y and UTS. This leaves the as-built condition not fully explored. Sensitivity of microstructure and phase content to energy density requires examination to determine the subsequent plastic deformation, mechanical properties and TRIP activity.

- Lattice structures are studied mainly experimentally with different materials and configurations to provide high crashworthy capabilities in all directions. The newly designed honeycomb gyroid has high stiffness in the out-of-plane but low in the in-plane direction. It is of interest to investigate, experimentally and computationally, the latter direction for high performance at different strain rates.

The aim of this thesis is at first to investigate PBF-LB of 316L and 17-4 PH strain hardening steels, to understand the corresponding TWIP and TRIP deformation behaviour onset and development. 17-4 PH is then applied to the newly designed honeycomb gyroid unit cell in different configurations, made of uniform as well as grading energy densities and/or volume fractions. The energy absorption capability in quasi-static and dynamic conditions is addressed by means of finite element analysis and experimental investigation, for a synergistic behaviour in the study of lattice structures.

3 Methods and materials

The aim of this chapter is to provide information about the materials analysed in this work, as well as the experimental techniques and methods used to prepare the samples. Sections 3.1, 3.2 and 3.3 present the materials and their specifications, the PBF-LB equipment adopted and the process parameters used in the manufacturing of the samples. Sections 3.4, 3.5, 3.6, 3.7 and 3.8 outline the software used for designing the samples used in this work, the modelling of the specimens and the sample preparation to execute the experimental activities needed for the present study. Sections 3.9, 3.10, 3.11, 3.12, 3.13, 3.14 and 3.15 offer the experimental activities utilised to obtain information about the presence of defects, mechanical properties, chemical composition, phase analysis and microstructure of the specimens produced with the investigated materials. Finally, Section 3.16 depicts the software adopted to describe the behaviour of the lattice structures modelled in the present work.

3.1 PBF-LB system used to produce the samples

In this thesis, all the investigated samples were manufactured through a Renishaw SLM125 (Renishaw PLC, UK) [173]. Renishaw SLM 125, represented in Figure 3.1, is a system that uses a 200W fibre laser to process metallic powdered feedstock within a purged argon atmosphere. The laser spot diameter is reported to be 40 µm, and the machine is supplied with a modulated Yb doped fibre-laser at an approximate wavelength of 1070 ± 10 nm. The build chamber has a maximum part building area of 120 mm x 120 mm, and the maximum building height is 125 mm. The allowable range of the scanning speed is up to 2 m/s, whereas the positioning speed is 7 m/s. The building rate ranges from 5 to 20 cm^3/hour. The layer thickness that can be scanned ranges between 20 and 100 µm. The SLM125 features the heating of the build platform throughout the entire building process up to a temperature of 170 °C, and the value kept during all the manufacturing processes for both 316L and 17-4PH was 80 °C. All printing operations were conducted with the building chamber maintained at low vacuum via an inert gas flow of Ar atmosphere, the target of oxygen level being 500 ppm to minimise oxidation. The machine is powered by a power supply with the following specifications: 230V, 1PH, 16A.

Figure 3.1. Renishaw SLM 125 [173].

The Renishaw SLM125 is an additive manufacturing system with a PWM laser, in that each applied scan track is composed of several single static exposure. Conversely to a laser system with continuous wave, the scan speed v is defined by additional parameters. The spatial-temporal evolution, linked to the optical chain, is depicted in Figure 3.2 [174]. One single scan track can be seen as a sequence of pulses, i.e. various segments, spaced by the point distance (P_D). Temporally, a pulse is on for a sufficient time to irradiate the powder bed, and in second instance it goes off to be moved to the next scanning spot. Respectively, they are referred to as exposure time (E_T) and delay time (D_T). Therefore, the formula that defines the v of the laser needs to consider the aforementioned parameters P_D, E_T and D_T. The laser scan speed v is expressed as:

$$v = \frac{P_D}{E_T + D_T} \qquad \text{Equation 3.1}$$

The consequence of using a PWM laser affects the effective power as opposed to a CW mode. This because the temporal distribution of the laser beam heat source, and consequently the available power, will drastically change the heating and cooling rates applied, for a different thermal history of the laser emission [32]. The main reason is the application of laser power under a duty cycle, for a continuous ramp up of laser power up to the maximum value with a subsequent decrease. Conversely, a CW emission keeps the same laser power over the entire scanning on the scan track after the initial ramp up. This must be taken into account when comparing results between the two emission modes.

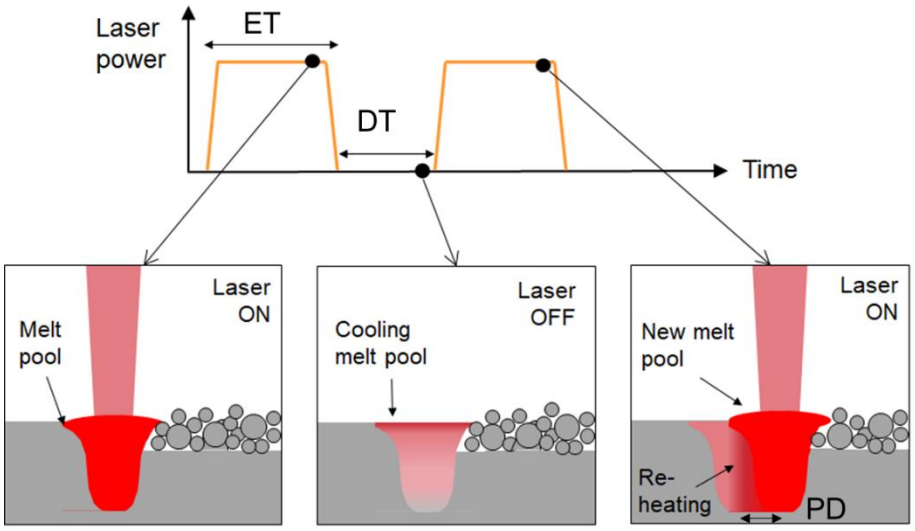

Figure 3.2. Renishaw SLM125 laser spatio-temporal evolution [174].

3.1.1 Build file creation

PBF-LB works by inputting a build file consisting of a slicing of the required part to be printed. After the .stl file is obtained from the CAD file or FLatt Pack (see Section 3.5), it is imported into QuantAM, the software provided by Renishaw. The part, represented by the .stl file, is positioned onto a virtual build platform that reproduces the Renishaw SLM 125 build plate in the needed location and with eventual supports to sustain the part on its bottom surface and overhangs, if the part is not printed directly onto the substrate. The software also allows to select the process parameters needed to scan each layer. For all the builds of this thesis, some parameters were kept fixed: layer thickness (30 µm), point distance (50 µm) laser focus offset (-1.5 mm).

Beam compensation (BCM) is defined as the offset of the laser beam from the edge of the .stl boundary to the core of the printed part. It considers for the laser beam radius, as it can be seen in Figure 3.3, and avoids the scanning of a stock to be removed afterwards. The default value, 50 µm, was used for all builds until Section 6.1.3, where it was changed to 100 µm to solve wall thickness issues presented in Section 6.1.3.

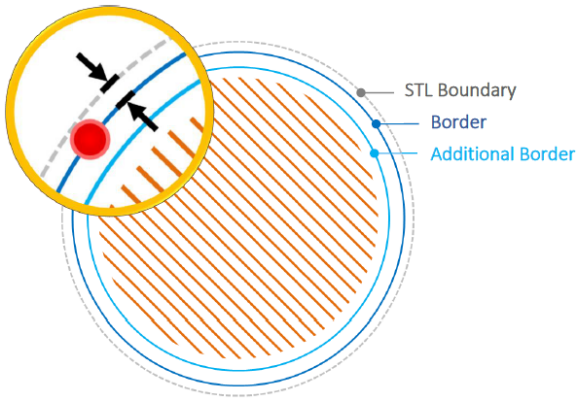

Figure 3.3. Graphical display of the beam compensation [175].

Once the process parameters are updated and slicing of the part is checked, the build file is generated by exporting the .mtt file which is imported into the Renishaw SLM 125 by means of WinSCP.

3.2 Production of specimens with PBF-LB 316L for TWIP investigation

The powder used in Chapter 4 for the twinning investigation was 316L stainless steel provided by LPW Ltd, UK [176]. The feedstock was produced from bulk 316L using an Ar gas atomisation process. The composition of the manufactured metal powder is reported in Table 3.1. The lab used different techniques to determine the chemical composition of the alloy: Laboratory Equipment Corporation (LECO) inert gas for O, N and H; infrared absorption and thermal conductivity, which measures combustion gases in the metallic sample, for C and S; inductively coupled plasma-optical emission spectrometry (ICP-OES) for the other elements. The resulting particle size of the atomised powder is within the range of 15 μm and 45 μm, as reported by Laser PSD by Volume technique. The Cr_{eq} and Ni_{eq} for such an alloy are 23.25 *wt%* and 17.55 *wt%*, respectively, with a Cr_{eq}/Ni_{eq} ratio of 1.32 thus inserting it into the austenitic phase field.

Table 3.1. Elemental analysis of 316L powder feedstock, supplied by LPW, ltd.

Element (weight %)											
C	Cr	Ni	Fe	Mo	Mn	Cu	N	O	P	S	Si
0.02	17.8	12.7	Bal.	2.3	0.8	0.02	0.09	0.03	0.008	0.005	0.65

The process map to determine the processability area of fully dense material was performed by printing cubes with an edge of 10 mm. The fixed parameters are the L_T of 30 μm, the P_D of 50 μm, the D_T of 20 μs, the h_d of 50 μm and the meander scan strategy with a rotation angle of 67° at each layer to randomise the average scan vector lengths per cross-sections. The scan strategy did not include a contour. The only parameters to vary were P and E_T, the latter affecting the v of the scanning laser. Overall, 35 combinations of P and E_T were adopted to manufacture samples each with a different process parameter. The process parameters are reported in Table 3.2.

Table 3.2. List with the variable parameters, power and exposure time, utilised to determine the process window of the 316L stainless steel powder in Chapter 4.

Parameters	Values
P [W]	75, 100, 125, 150, 175, 200
E_T [µs]	35.7, 41.7, 50, 62.5, 83.3, 125

The cylindrical standard and tapered specimens were manufactured with one of the examined process parameter sets, as will be explained later in Chapter 4. A recap of the parameters is presented in Table 3.3. The resulting v was therefore ~ 0.72 m/s.

Table 3.3. Process parameters for the production of 316L stainless steel.

P (W)	E_T (µs)	v [m/s]	LED (J/mm)
160	50	0.72	0.16

3.3 Production of specimens with PBF-LB 17-4 PH for TRIP investigation

The powder used in Chapter 5 and 6 for the investigation on TRIP behaviour and its application into the energy absorption of TPMS lattice structures was 17-4PH stainless steel provided by Globus Metal Powders Ltd, UK. The feedstock was produced from bulk 17-4PH using an Ar gas atomisation process. The composition of the manufactured metal powder, as provided by the powder supplier, is reported in Table 3.4. The lab used different techniques to determine the chemical composition of the alloy: ICP-OES (to detect Cr, Cu, Fe, Mn, Mo, Nb+Ta, Ni, P and Si), combustion (for C and S) and fusion (N and O). The manufacturer powder size analysis, through Laser Diffraction Technique, provided values for *D10*, *D50* and *D90* of 22.2 µm, 32.0 µm and 45.7 µm, respectively.

Table 3.4. Chemical composition of gas-atomised 17-4PH powder feedstock, as provider by Liberty Steel Group Holdings UK Ltd.

Element (weight %)												
C	Cr	Ni	Fe	Mo	Mn	Cu	N	O	P	S	Si	Nb+Ta
0.02	13.6	3.99	Bal.	0.05	0.3	5.3	0.022	0.029	0.01	<0.003	0.69	0.48

A process window was obtained to extract the area in which the processability of the powder could provide fully dense material. The process was performed by printing cubes with an edge of 10 mm. All process parameters were kept fixed except for two. The fixed parameters are the L_T of 30 μm, the P_D of 50 μm, the D_T of 20 μs, the h_d of 75 μm and the meander scan strategy with a rotation angle of 67° at each layer to randomise the average scan vector lengths per cross-sections. The scan strategy did not include a contour. The only parameters to vary were P and E_T (different values of E_T imply changing v of the laser during its processing of the powder layer to scan the required area). A combination of 10 values for the P and E_T were used to process the samples, each with a different process parameter. The processing conditions are reported in Table 3.5.

Table 3.5. List with the variable parameters, power and exposure time, utilised to determine the process window for the 17-4PH stainless steel powder in Chapter 5 and 6.

Parameters	Values
P [W]	100, 120, 140, 160, 180, 200
E_T [μs]	71.4, 100, 166.7, 500

The flat specimens, tested during the in-situ characterisation at the synchrotron facility to study the TRIP behaviour, as described later in Chapter 5, were produced with a set of two different process parameters. A description is depicted in Table 3.6. The resulting v were ~ 0.42 m/s and ~ 0.27 m/s.

The TPMS derived structures printed and tested, as described in Chapter 6, were produced with Set 1 and Set 3 as shown in Table 3.6.

Table 3.6. Process parameters adopted for manufacturing PBF-LB 17-4 PH stainless steel.

Set	***P* [W]**	***E_T* [µs]**	***v* [m/s]**	***LED* [J/mm]**
Set 1	180	167	0.27	0.67
Set 3	120	100	0.42	0.29

In Figure 3.4 is a Schaeffler diagram representing where the alloys used in this work, 316L and 17-4 PH, are located. The diagram points out the different phases that are obtained for each of these alloys, when produced with PBF-LB. For the 17-4 PH alloy, the standard alloy composition is included for comparison.

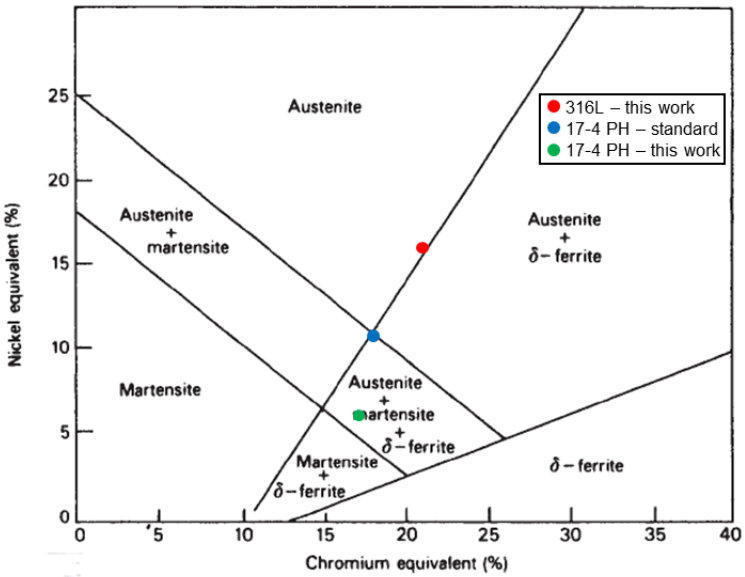

Figure 3.4. Schaeffler diagram from Figure 2.11, showing location of the 316L alloy used in this work (red marker), the 17-4 PH standard alloy composition (blue marker) and the 17-4 PH alloy used in this work (green marker).

The 17-4 PH alloy investigated in this work, represented by Table 3.4, is lower in Cr, conversely to standard 17-4 PH alloys shown in Table 2.2. The main detrimental consequence is an overall decrease of the Cr_{eq}, for a reduction of BCC phase stability. A potential result is undesirable phases forming, such as carbide precipitates or sigma phase, thus worsening mechanical properties and leading to embrittlement.

Although the 316L and 17-4 PH alloys are fairly similar, in Table 3.2 and Table 3.5 it can be seen that the parameter space analysed is different. The rationale for this is the non-standard 17-4 PH utilised, which showed printability issues with standardised process parameters and led to the process parameters presented in this thesis.

3.4 Modelling – Fusion 360

The specimens manufactured via PBF-LB in this work, except for the lattice structures generated in FLatt Pack as described in section 3.5, were designed in Fusion 360 (Autodesk, CA, USA). It is a software package that combines CAD, CAM and CAE tools in a single cloud-based platform [177]. Solid modelling was the process used.

3.5 Flatt Pack

FLatt Pack (Functional Lattice Package) is a software created to address the design requirements of creating lattice structures in a research environment. The coding environment is MATLAB. It enables the design of several lattice cell types which provide different connectivity, structural anisotropy and surface area. Moreover, it offers a GUI guiding through all the steps from the definition of dimensions to the creation of different format files of the lattice designs through the definition of the lattice shape, including functional grading and mesh [171]. The flow is shown in Figure 3.5.

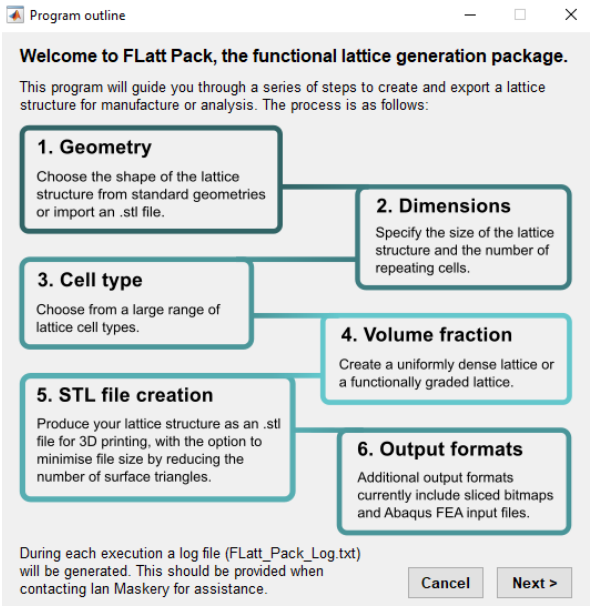

Figure 3.5. FLatt Pack flow to produce lattice structures.

Among the features, the geometry can be defined by choosing a predefined shape or importing .stl files to optimise with lattice structures. Different lattice cell types are allowed that are strut-based, TPMS-based and 2D honeycombs based on reduced-periodicity TPMS equations (including the honeycomb gyroid investigated

in this study). The lattice structure must be assigned a VF, which can be uniform or graded. The user can then choose the type of output files needed, the ones used in this work being:

- .stl → the standard format for AM designs to print.

- .mat → it is a MATLAB logical array where solid and void are represented by 1 and 0 respectively (used for the homogenisation code, Section 3.6).

- .inp → selecting this type format, a mesh composed by hexahedral elements is written to be inputted in Abaqus. A simulation environment can be generated, as was the case for this thesis.

For the present work, the source code was used and modified from the original version to adapt it to the required needs of elastic-plastic behaviour of the lattice structures when compressed. Cubes were generated with different dimensions. To validate the FEA model with PA2200 against the experimental counterpart [151], 50 x 50 x 5 mm^3 cubes with 5 x 5 cell repetitions and 10 mm UC length were obtained as .inp file, to exploit the periodic behaviour of the structures in a direction perpendicular to the load direction. A lattice structure with 4 x 4 cell repetition or higher is effective against boundary effects on the deformation results [150]. For an initial investigation via FEA with 17-4PH stainless steel, 30 x 30 x 5 mm^3 homogeneous cubes with 5 x 5 cell repetitions were generated as .inp file to predict the deformation behaviour under specific variables, as specified in Table 3.7. The corresponding UC length is 6 mm. Three VFs were used for each of the two investigated sets. The experimental counterparts were conducted with 30 x 30 x 30 mm^3 cubes with 5 x 5 cell repetitions extracted as .stl files from FLatt Pack. The uniform cube with 0.2 VF is represented in Figure 3.6(a) in isometric view, and Figure 3.6(b) in top view.

Table 3.7. Variables used to generate homogeneous and hybrid lattice structures with 30 mm x 30 mm x 5 mm size for FEA investigations.

Type	**Variables**	**UC size [mm]**	**Samples size [mm^3]**	**UC repetition [-]**
Homogeneous	VFs: 0.20, 0.30, 0.40	6	30 x 30 x 5	5 x 5
Homogeneous	Process parameter sets: Set 1, Set 3	6	30 x 30 x 5	5 x 5

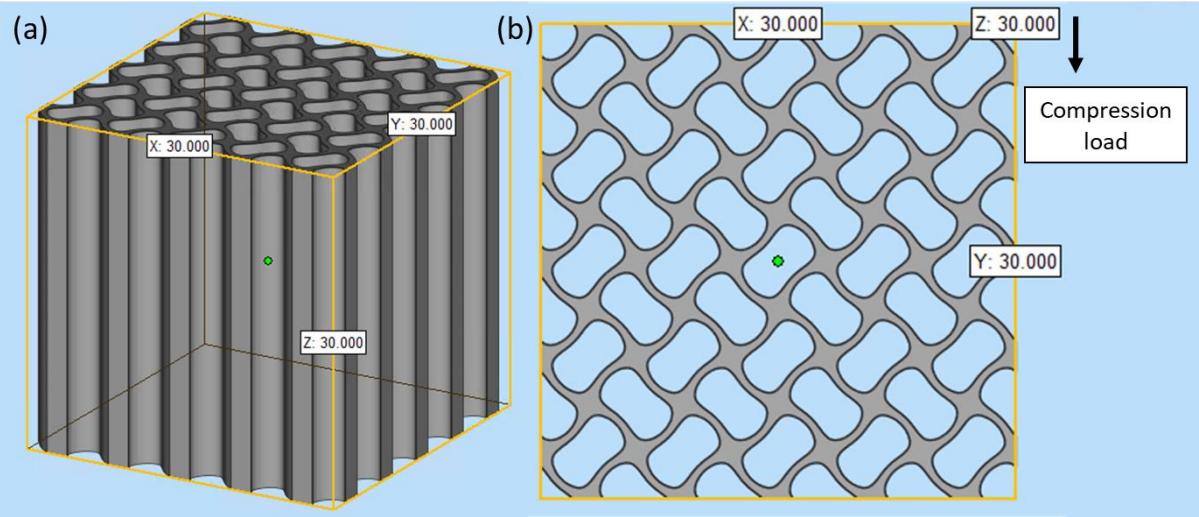

Figure 3.6. Cubes extracted from FLatt Pack: uniform lattice structure (a) isometric view and (b) front view with indication of the compression load direction.

The previous investigation pointed out challenges in printing two different process parameter sets, which required a study on the wall thickness that is presented in Section 6.1.3. The outcome proved that the minimum UC length, that could avoid excessive deviation for the printed lattices due to low thickness along the UC, is 8 mm. 32 x 32 x 5 mm^3 homogeneous cubes with 4 x 4 cell repetitions were generated as .inp file to predict the deformation behaviour under specific variables via FEA, as specified in Table 3.8. The reason for these dimensions is to satisfy geometrical requirements for the dynamic investigation, as explained in next paragraph. Two VFs, 0.4 and 0.45, were used for each of the two sets (Set 1 and Set 3) on the uniform lattice, and 0.45 VF was investigated with grading of process parameter sets (Set 1 at the bottom and Set 3 at the top or vice versa); three different VF gradings (between 0.5 and 0.4, 0.6 and 0.3, 0.7 and 0.2) were adopted for the graded structures, either with a uniform process parameter or with a grading of the two process parameter sets (Set 1 at the bottom and Set 3 at the top or vice versa). The experimental samples were performed on 32 x 32 x 32 mm^3 homogeneous and graded cubes with 4 x 4 cell repetitions, extracted as .stl files from FLatt Pack. The considered structures are a subset of the computational one, specifically homogeneous with 0.4 VF and single process parameter sets; hybrid with VF grading of 0.5 to 0.4 and single process parameter sets; hybrid with VF grading of 0.5 to 0.4 and process parameters grading.

For the purpose of investigating dynamic conditions with high strain rates, due to limitations on the testing equipment, a further and reduced configuration was considered. FEA and experimental investigations were conducted in quasi-static conditions on 16 x 16 x 5 mm^3 homogeneous and graded cubes with 2 x 2 cell repetitions, with 8 mm UC length. The dynamic studies were performed on the FEA samples only. The variables are in Table 3.9.

It must be noted that the "No skin" option was chosen for the contact surfaces when generating the lattice structures, leaving the latter unmodified. As a consequence, cell walls or struts exposed to the acting load can be sensitive to damage. Nonetheless, in the literature the recommendation is to not include an exterior skin on the contact surfaces, if the goal is to extract bulk properties of the lattice structure, as it can be mechanical properties [171]. The reason lies in the modification of the lattice's properties due to increase of mass, material connectivity and stiffness.

Table 3.8. Variables used to generate homogeneous and hybrid lattice structures with 32 mm x 32 mm x 5 mm size for FEA investigations, with 4 x 4 UC repetition and 8 mm UC length.

Type	**Variables**	**UC size [mm]**	**Samples size [mm^3]**	**UC repetition [-]**
Homogeneous	VF: 0.40, 0.45 + single process parameter set (Set 1 or Set 3)	8	32 x 32 x 5	4 x 4
Hybrid	VF: 0.45 + Set 1 in the bottom half and Set 3 in the top half (and vice versa)	8	32 x 32 x 5	4 x 4
Hybrid	VF grading from 0.40 to 0.50, 0.60 to 0.30, 0.70 to 0.20 + single process parameter set (Set 1 or Set 3)	8	32 x 32 x 5	4 x 4
Hybrid	VF grading from 0.40 to 0.50, 0.60 to 0.30, 0.70 to 0.20 + Set 1 in the bottom half and Set 3 in the top half (and vice versa)	8	32 x 32 x 5	4 x 4

Table 3.9. Variables used to generate homogeneous and hybrid lattice structures with 16 mm x 16 mm x 5 mm size for FEA investigations, with 2 x 2 UC repetition and 8 mm UC length.

Type	Variables	UC size [mm]	Samples size [mm^3]	UC repetition [-]
Homogeneous	VF: 0.40 + single process parameter set (Set 1 or Set 3)	8	16 x 16 x 5	2 x 2
Hybrid	VF grading from 0.40 to 0.50 + single process parameter set (Set 1 or Set 3)	8	16 x 16 x 5	2 x 2
Hybrid	VF grading from 0.40 to 0.50 + Set 1 in the bottom half and Set 3 in the top half (and vice versa)	8	16 x 16 x 5	2 x 2

3.6 Homogenisation code

A MATLAB code can be used to test the different cellular structures through numerical homogenisation method and avoid the expensive computational cost linked to traditional finite element analysis (FEA) techniques [20]. The steps involved are the following.

1) The coordinate of nodes and struts of the strut-based lattice are defined into a .txt file, and the voxel model is generated in a dimensionless space of a cube with a unit length. The voxel logical matrix contains 1 for material, 0 for void.

2) Geometrical inputs to provide to the MATLAB code include: the length of the unit cell along *x*, *y* and *z* axes; the Lamé's first and second parameter of the lattice structure solid material (λ and μ); the voxel; the element stiffness matrix

$$\mathbf{K}^{(e)} = \int_{\Omega^{(e)}} \boldsymbol{B}^T \cdot \boldsymbol{C}^{(e)} \cdot \boldsymbol{B}\, d\boldsymbol{\Omega}^{(e)} \qquad \text{Equation 3.2}$$

Where **B** is the strain-displacement matrix and **C** is the constitutive matrix for the element (constant over the element); the material is assumed to be isotropic. **C** is expressed in terms of the Lamé's parameters λ and μ

$$\mathbf{C}^{(e)} = \lambda^{(e)} \begin{bmatrix} 1 & 1 & 1 & 0 & 0 & 0 \\ 1 & 1 & 1 & 0 & 0 & 0 \\ 1 & 1 & 1 & 0 & 0 & 0 \\ 0 & 0 & 0 & 0 & 0 & 0 \\ 0 & 0 & 0 & 0 & 0 & 0 \\ 0 & 0 & 0 & 0 & 0 & 0 \end{bmatrix} + \mu^{(e)} \begin{bmatrix} 2 & 0 & 0 & 0 & 0 & 0 \\ 0 & 2 & 0 & 0 & 0 & 0 \\ 0 & 0 & 2 & 0 & 0 & 0 \\ 0 & 0 & 0 & 1 & 0 & 0 \\ 0 & 0 & 0 & 0 & 1 & 0 \\ 0 & 0 & 0 & 0 & 0 & 1 \end{bmatrix} \quad \text{Equation 3.3}$$

The load vector is defined in terms of the macroscopic volumetric strain and can be described as

$$\boldsymbol{f}^{i}{}_{(e)} = \lambda^{(e)} \cdot \boldsymbol{f}^{\boldsymbol{i}}{}_{\lambda} + \mu^{(e)} \cdot \boldsymbol{f}^{\boldsymbol{i}}{}_{\mu} \quad \text{Equation 3.4}$$

The unit cell is meshed and the stiffness matrix for each element is made. It is then possible to assemble the sparse global stiffness matrix.

3) The MATLAB code proceeds by calculating the homogenised constitutive matrix C^H

$$C^H{}_{ij} = \frac{1}{|\boldsymbol{\Omega}|} \cdot \sum_{(e)} \int_{\Omega^{(e)}} (\chi_{(e)}^{0(i)} - \chi_{(e)}^{(i)})^T \cdot k_e \cdot (\chi_{(e)}^{0(j)} - \chi_{(e)}^{(j)})\, d\boldsymbol{\Omega}^{(e)} \quad \text{Equation 3.5}$$

Where $\chi_{(e)}^{0(i)}$ is the element displacement related to the *i*th unit strain; $\chi_{(e)}^{(i)}$ is the displacement field computed from the global stiffness equation; Ω is the volume of the unit cell. C^H can be used to generate the homogenised compliance matrix S^H, its inverse, which in turns allows to calculate the Young's modulus

$$S_{11}^H = \frac{1}{E_x}, S_{22}^H = \frac{1}{E_y}, S_{33}^H = \frac{1}{E_z} \quad \text{Equation 3.6}$$

In case of a TPMS based lattice structure, generated through FLatt Pack (see Section 3.5), the .mat file of the unit cell can be used instead of the .txt file.

In Figure 3.7 is an overview of the elastic modulus obtained from strut-based and TPMS based gyroid lattice structures, determined from the homogenisation code with the material model of a generic steel and for the same 0.3 volume fraction. The strut-based BCC and octet, and the TPMS based matrix and network are the most homogeneous lattices in all directions. The strut-based lattices mainly show anisotropy in the property, as well as the honeycomb gyroid. The latter displays the highest value of elastic modulus along the z direction.

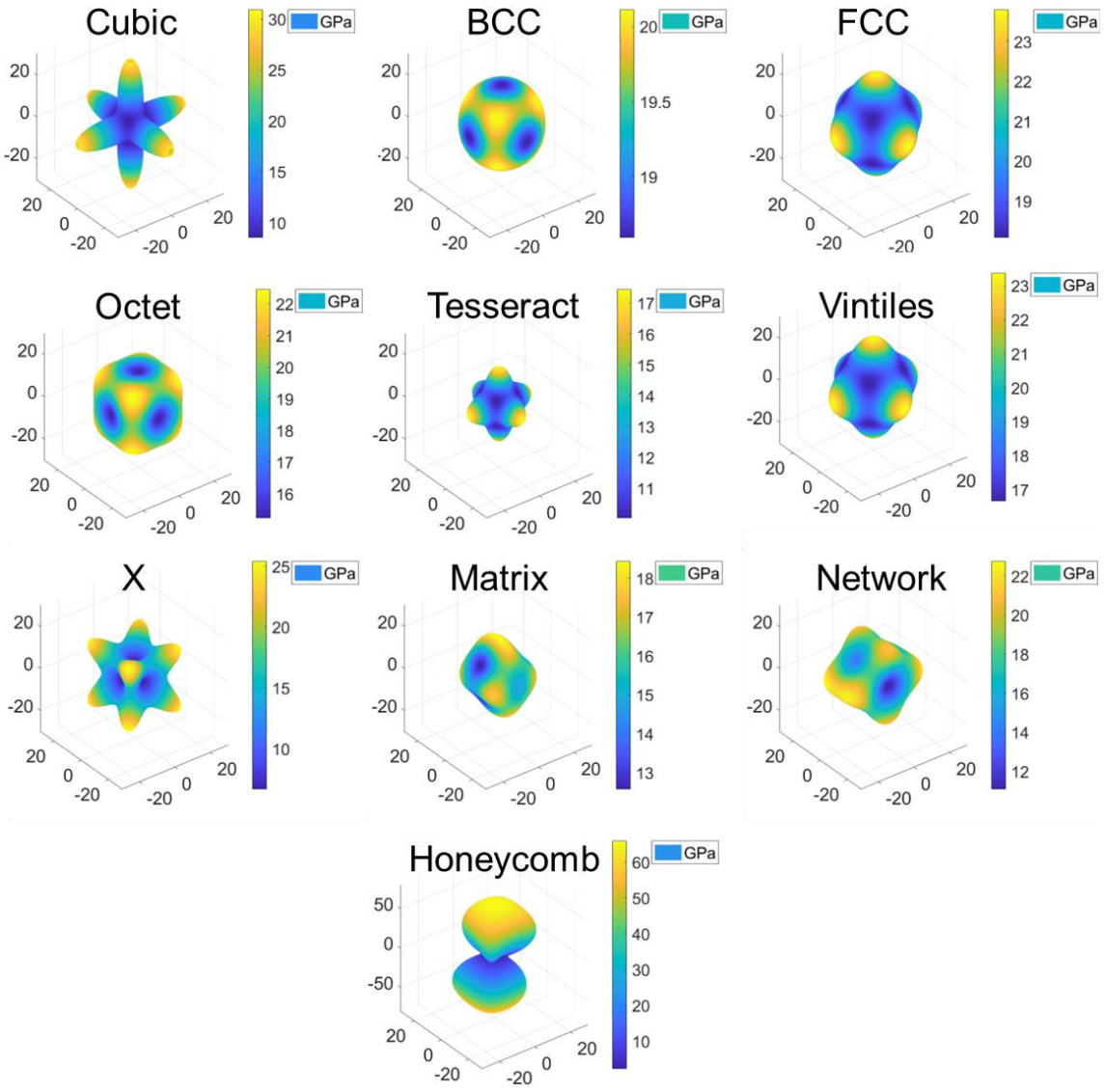

Figure 3.7. Overview of the elastic moduli obtained from the homogenisation code for some strut-based and TPMS based lattice structures.

3.7 Samples design

Cubes with dimensions of 10 × 10 × 10 mm^3 were printed with both 316L and 17-4PH for the purpose of density check, microstructural analysis and hardness measurement on the selected process parameter sets.

Tensile specimens, cylindrical standard with 4 mm gauge diameter and 20.4 mm gauge length, and tapered with diameter decreasing from 5 mm to 4 mm and a gauge length of 20.9 mm) were manufactured with 316L. The geometry of the tapered tensile specimen was utilised to allow a decrease in load-bearing area along the gauge section of 36 % [178]. A single experiment could extrapolate all required features of twinning, as a

variation of the local stress and strain along the length of the sample occurred. The reason for the choice of a small angle of taper was to preserve the stress system as simple and as near to a conventional tensile test as possible. The geometries are depicted in Figure 3.8.

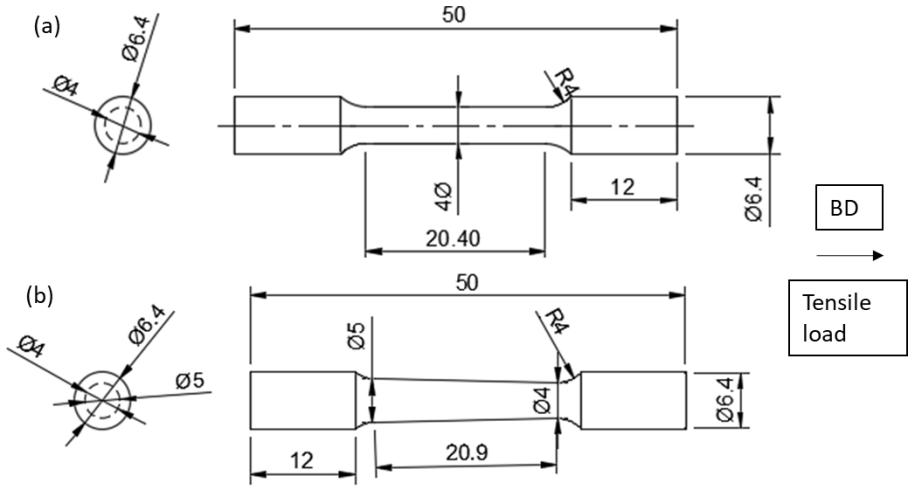

Figure 3.8. Technical drawing of the (a) standard and (b) tapered geometry used for the tensile tests on specimens printed with 316L. All dimensions are given in millimetres.

Flat specimens were printed with 17-4PH according to the Subsize Specimen dimensions, and the length of grip section was increased to 35 mm to enhance the grip into the testing equipment for the in-situ characterisation at the synchrotron facility. The thickness of 1.5 mm was opted for due to the need of the transmission mode of the x-ray source during the in-situ monitoring of the specimens. The samples were printed as rectangular thin walls (112 x 14 x 1.5 mm^3) with the build direction (BD) as displayed in the figure, milled to provide the ASTM standard dog-bone shape and finally polished on their flat surfaces to provide a roughness of 7.8 µm. The polishing procedure on the specimens might have caused superficial martensitic transformation due to induced plastic deformation during the manual preparation. As a result, the reported phase fraction coming from an XRD analysis, which has a penetration depth of tens of µm, would be affected by such transformation. The *in situ* XRD analysis performed in this study, in transmission mode as explained in Section 3.14, aimed at reducing the effect of increased superficial martensitic content by extracting the phase fraction of the analysed 17-4 PH samples across the entire thickness.

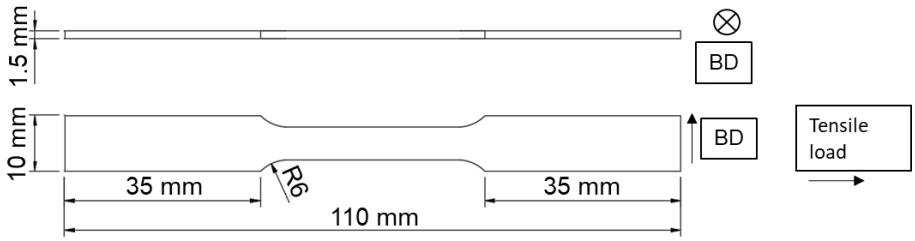

Figure 3.9. Technical drawing of the specimen designed for the in-situ characterisation and manufactured with 17-4PH. All dimensions are given in millimetres.

The cylindrical and flat specimens were manufactured following the ASTM E8M for tension testing of metallic materials [179].

3.8 Sample preparation

The specimens from this work were prepared in the *Sample Preparation Lab* in Wolfson Building, University Park (University of Nottingham, Nottingham, UK), for porosity, microstructural and hardness analysis.

The samples were cut by means of an ATA cutting machine (ATA Group, Ireland). Cubes printed for porosity checks and microstructure analysis were cut along a plane that encloses the build direction (BD). Following fracture, the tapered specimens manufactured with 316L stainless steel were cut longitudinally. The fractured samples produced with 17-4PH stainless steel were cut transversely to the gauge length. The cut samples were mounted in a hot mounting machine by means of a conducto-mount resin. A grinding step was executed with a *Struers LaboPol-21* equipment according to standard practice. The last steps consisted of polishing with colloidal silica. The aim is to obtain mirror-like surfaces for analysis under the optical microscope, the SEM, or the hardness testing machine.

To reveal grain boundaries, melt pools and microstructure dendrites, chemical etching was executed. For 316L stainless steel, a solution of three parts of HCl and one part of HNO_3, in volume, diluted with a part of distilled water, was used for approximately 20 s. 17-4PH stainless steel was etched with Kalling's No. 2 reagent, for approximately 10 s.

3.9 Hardness test

The hardness of the samples printed with both 316L and 17-4PH stainless steel powders were obtained by means of micro-hardness measurements. The equipment used to carry out the investigation was a Wilson VH3100 Automatic Knoop/Vickers equipment (Bühler Ltd, UK), according to the Test Method for Micro Indentation Hardness of Materials with designation ASTM E384-08 [180]. For each sample, a force of 5 kg was applied onto the samples' surface to create the required indentation, performed with a 10 s dwell time.

The cubes produced with 316L were investigated for as-printed hardness with an array of 10 x 10 indents, to produce an aerial hardness map. The tapered specimens were tested to determine the change in hardness along the build direction (the symmetry axis) by means of an array of 2 x 960 indentations, where the 2 indents were

applied to each cross-section and the 960 indents were applied to along the build direction. The 2 indents were distanced by 100 μm, while the 960 indents by a value of 200 μm. An average of the values was performed for each cross-section.

The cubes produced with 17-4PH were investigated for as-built hardness values with an array of 10 x 10 indents, to produce an aerial hardness map.

3.10 Tensile testing

The cylindrical standard and tapered specimens, as well as the flat specimens described in Section 3.7, were examined until failure by means of an Instron 5969 universal testing machine with a 50 kN load cell (Instron, MA, USA). Room temperature and 10^{-3} s^{-1} strain rate were adopted. A video gauge supported the collection of the stress-strain curves during the tests.

As for the cylindrical samples produced by PBF-LB with 316L stainless steel, described in Chapter 4, the direction of the tensile load was aligned with the PBF-LB build direction. The surfaces of the specimens, standard and tapered, were kept in their as-fabricated condition.

The flat samples manufactured by PBF-LB with 17-4PH stainless steel, whose results are in Chapter 5, were investigated using the tensile load with an orientation perpendicular to the PBF-LB build direction. The printed samples were machined according to the Test Methods for Tension Testing of Metallic Materials with designation ASTM E8/E8M [179].

3.11 Compression testing

Compression testing was used to analyse the mechanical response of the TPMS structures presented in Section 3.5, and their energy absorption capabilities. The results are described in Chapter 6.

To obtain stress–strain curves and investigate the failure modes, the fabricated honeycomb gyroid lattice specimens were firstly subject to quasi-static compressive mechanical testing with an Instron 5985 universal testing machine (Instron, MA, USA), equipped with a 250 kN load cell. The printed samples were tested statically in their as-built conditions at room temperature, according to the Standard Test Methods of Compression Testing of Metallic Materials at Room Temperature ASTM E9 [181]. The strain rate used was 10^{-3} s^{-1}. A video gauge was adopted for the collection of the stress-strain curves during the tests.

Dynamic tests were planned to investigate the strain rate sensitivity of the lattice structures at different rates, by applying two sets of velocities for the configurations investigated, and make a comparison with the quasi-static case. In section 2.7.4 it was explained that the ideal equipment for dynamic tests is a DIHB, which can apply strain rates between 1000 s^{-1} and 2000 s^{-1}. The applied strain rates in this work are 1000 s^{-1} and 2000 s^{-1} for the 16 mm x 16 mm x 16 mm lattices configuration. The corresponding speeds are 58 km/h and 115 km/h, respectively. The rationale is to provide absorption performance at increasing speed and understand if the lattice structure is suitable at any strain rate. The TPMS structures were only tested, in their in-plane direction, through FEA simulations, whose setup is in Section 3.16.

3.12 X-ray diffraction

The solid phases, in the microstructures of 316L and 17-4PH, were identified by means of x-ray diffraction (XRD). XRD uses a reflection geometry method with an x-ray source, the crystalline sample and a detector [182]. The x-ray source is a Cu cathode tube with a wavelength of 1.542 Å. The x-rays are directed from the source onto the surface of the sample with a specific wavelength and collimation. The scatter, at various angles, comes from the interaction of the x-rays with the atomic planes of the sample. The Bragg-Brentano law is used to decipher the diffracted x-rays, each having a specific pattern given by the distinct crystal structure of every phase.

In this study, a Bruker D8 Advance Da Vinci diffractometer with a Lynxeye 1D detector (Siemens, Munich, Germany) was adopted. All the samples were tested in their cube form, adopting 0.02° as step size along with 0.2 seconds as step time. The scan was between $2\theta = 20°$ and $2\theta = 100°$. The commercial software from the same company Bruker, Diffract.EVA, was used to extract information about the collected peaks by means of the PDF-2 2021 database from the International Centre for Diffraction Data – ICDD [183].

3.13 Microscopy techniques

An optical microscope (OM) was used to obtain images of polished samples for porosity analysis or etched samples to extract information about melt pool boundaries and grain morphology. The equipment used for the purpose of this work was the optical microscope Nikon Eclipse LV100ND.

As for the porosity analysis, existence of defects (LOFs, keyholes, gas pores) was determined by importing the optical micrographs into the open-source software ImageJ (National Institutes of Health – NIH, MD, USA).

The output from the analysis with this software is a list of geometrical features of the defects, including the area of the detected defects inside the printed sample.

The repeatability of the fully dense cubes' production with 316L PBF-LB was performed with the Archimede's analyses. The equipment used for the purpose was a Kern ABT-100-5NM analytical scale (Kern & Sohn, Germany). Two series of weight measurements are recorded for the printed samples in air and in a selected fluid. Averaging the two weights, and knowing the density of the aid liquid, the density of the material is determined as:

$$\rho = \frac{w_A}{w_A - w_B} \cdot \rho_0 \qquad \text{Equation 3.7}$$

Where w_A is the weight of the sample in the air, w_B is the weight of the sample in the aid liquid (Isopropyl alcohol) and ρ_0 is the density of the aid liquid.

Scanning electron microscopy (SEM) is a technique that uses a focused electron beam to investigate a conductive sample. The electron beam interacts with the surface of the specimen thus creating an interaction zone where the electrons have such high energy that they can penetrate the specimen. The energy of the focused electron beam determines the penetration depth. In Figure 3.10, a schematic of the phenomenon is represented [184]. The focus of this work is on the emitted signals only, and the three emission signals that are considered are [185]: secondary electrons, utilised for extracting images and performing studies on the surface; backscattered electrons, important to retrieve information about sample surface, as well as to perform chemical and crystallographic studies; x-ray photons, utilised for chemical investigations.

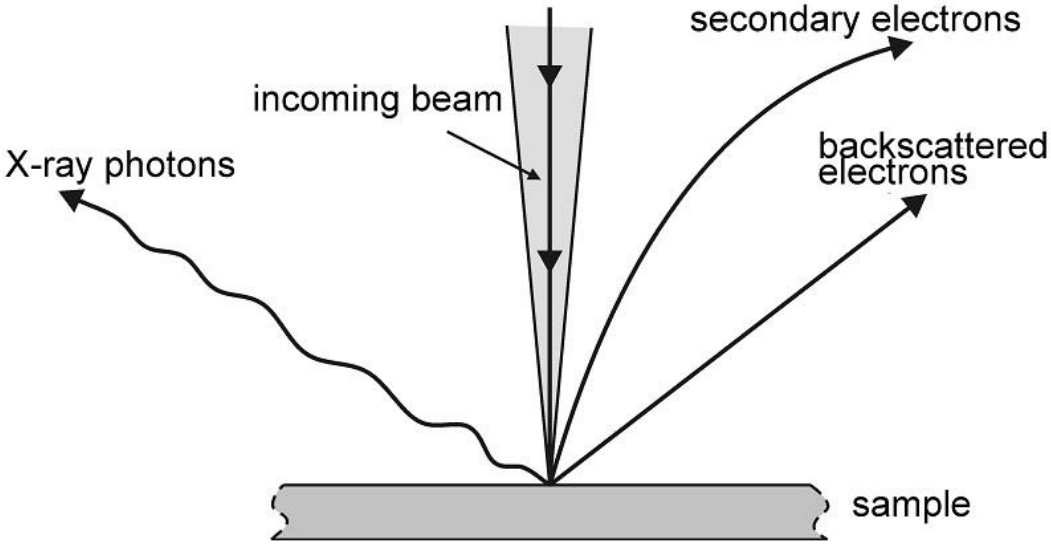

Figure 3.10. Representation of the schematic of the interaction between the focused electron beam and the sample during SEM [184].

Secondary electron imaging (SEI) was employed to extract topographic micrographs of the microstructure from the samples investigated in this study. The specific quantity of colloidal silica used during the polishing process affects the quantity of material removed. Larger concentration of silica removes more material, thus being suitable for surface topography in case this is required. SEI is more effective for topography information than optical microscopy, even on etched samples, as larger resolution and depth of field can be obtained through a focused electron beam on a smaller area. However, an excess of material removal would alter the surface flatness so that topographical investigations are not reliable.

Backscattered electrons (BSE) are electrons of the focused electron beam that undergo an orbital motion around the atoms' nuclei of the material and, because of the specific angle they are moving towards the material, they come back out of the sample without slowing down. Thanks to their high speed, BSE travel in straight lines. A detector is placed in their path to form an image. Each element possesses a specific size for its nuclei and, as the size of the atom nucleus increases, the number of BSE increases. Therefore, BSE is used when it is important to differentiate between different elements in a sample.

EBSD uses BSEs to extrapolate crystallographic orientation information by considering a small area of the sample under a SEM. BSEs are utilised because they do not suffer from reduction of energy during the scattering [186]. The software AZtec (Oxford Instruments PLC, UK) was used to collect the data, while AZtecCrystal was used to post-process the acquisition, especially the samples produced with 17-4PH. Average misorientation, grain size, grain orientation and crystallographic texture were extracted. To determine grains size in vertical planes, enclosing the BD, ellipse fitting was used, and the equivalent circle diameter was adopted. The MATLAB toolbox, MTEX, provided the post-process for the raw EBSD data [187] on the samples printed with 316L powder, because of the embedded functions to analyse the TWIP behaviour of the tapered specimens. In both tools, the legend was defined so that the EBSD maps had the family of crystallographic directions {100}, for the Fe-FCC matrix, parallel to the BD.

Energy-Dispersive X-ray Spectroscopy (EDS, EDX, or XEDS), also known as Energy Dispersive X-ray Analysis (EDXA), is an analytical SEM technique to perform elemental analysis or chemical characterization of a sample. The x-ray radiation spectrum is categorised by a semiconductor detector, allowing the EDS analysis to determine the elemental composition of individual points or to map out the lateral distribution of elements from the imaged area [188]. The data that is returned after the processing is in terms of total of counts linked to every energy level thus making possible to visualise the collected spectrum. The peak positions are compared against the nominal ones for the pure elements, enabling the understanding of the material composition.

This thesis was defined by use of various scanning electron microscopes. The JEOL 7000F SEM and the JEOL 7100F field emission gun (FEG)-SEM were used to conduct imaging on the samples manufactured with 316L (Chapter 4). An accelerating voltage of 11 kV and a current of 8 nA were used, with a working distance (WD)

of 10 mm. The JEOL IT-200 SEM was used for imaging and EDX on the samples produced with 17-4PH (Chapter 5 and 6). An accelerating voltage of 11 kV and a current of 8 nA were used, with a WD of 10 mm.

The microstructure of the standard cube and the tapered specimen printed with 316L was characterised with EBSD by means of a ZEISS Crossbeam 550 focused ion beam (FIB)-SEM. The step size of the EBSD analysis was 0.25 μm, and the build direction of the PBF-LB process was parallel to the EBSD Z direction. The post-processing of the EBSD data was conducted on the MATLAB toolbox, MTEX, to determine the crystallographic phases and texture. The established threshold for the grain boundaries was 5º. TBs were defined as *Σ3* coincidence site lattice boundaries with a misorientation angle of 60º and rotational axis of <111>. To utilise Brandon's criterion, that considers a deviation from the angular misorientation for exact lattice coincidence due to a network of dislocations superimposed on the coincidence boundary, a slight angular deviation from the nominal misorientation ($15°/\sqrt{3} = 8.66°$) was considered [189]. Twin concentration was extracted as areal fraction of the micrographs. KAM and Schmid factor maps were adopted to determine the existence of defects in the material in the plastic field. KAM maps were employed to lay out the average misorientation between each measurement point and the nearest neighbours, with growing values caused by the larger presence of defects in the structure. In a previous research by Gussev et al [190], it was disclosed that KAM maps are utilised to extract a portrayal of the distribution of the geometrically necessary dislocations (GNDs) in the structure at different strain values. The calculation considered as negligible misorientations larger than a critical value of 5°.

The microstructure of the as-built (at the grip end) and fractured cross-sections (at the fracture side) of the specimens printed with 17-4PH powder were studied through EBSD technique by using a ZEISS Crossbeam 550 FIB-SEM as well. The settings to perform the analysis were: accelerating voltage of 15 kV, probe current 5 nA, tilt angle 70º, working distance 15 mm, step size 1 μm for large areas and 0.25 μm for detailed mappings. EBSD data were post-processed with the commercial software AZtecCrystal (Oxford Instrument PLC, UK) to evaluate crystallographic phases and texture for the as-built and the fractured cross-sections for the two sets used in the investigation. Grain boundaries were defined using a threshold of 5º.

3.14 In-situ synchrotron investigation for PBF-LB 17-4 PH specimens

Diamond Light Source is the national synchrotron facility of the United Kingdom. I12 is the Joint Engineering, Environmental and Processing (JEEP) beamline, which uses high energy x-rays to penetrate through large dense samples of engineering materials including steel [191]. It is the facility used to conduct the experiment depicted in Chapter 5, and it contains two experimental hutches, EH1 and EH2. The investigation presented in this work was conducted in the EH1 of the I12 beamline, the hutch at closer distance from the source which is

used for experiments on small samples and sample environments. The overview of the EH1 is shown in Figure 3.11.

Figure 3.11. Overview of the EH1 in the I12 beamline at the Diamond Light Source facility. The x-ray source is provided into the hutch by the source indicated by the dash-dot arrow; the table with the testing machine, for the tensile test, is pointed out by the dash arrow; the data obtained during the mechanical testing were collected by the computer indicated by the continuous arrow, and transmitted to a computer into the control room so that data could be monitored and analysed in real time

Figure 3.12 shows the details of the experimental setup adopted for the in-situ x-ray diffraction tensile experiment at the synchrotron facility. A monochromatic beam of 100.096 keV, represented by the horizontal red dash arrow in the left of Figure 3.12(a), with a wavelength of λ of 0.12386 Å, was used in transmission geometry. The incident beam on the tested samples was a 0.5 x 0.5 mm^2 square, and the test was conducted with an exposure of 2 s per frame. The x-ray beam was diffracted through the dog-bone shaped specimens, while the latter were loaded for a tensile experiment to failure. The direction of the tensile testing is indicated by the vertical red continuous arrows from Figure 3.12(a) which are perpendicular to the build direction at which the production of the specimens was done. The diffracted x-ray beam, represented by the horizontal red dash-dot arrows in the right of Figure 3.12(b), were continuously collected on a 2D Pilatus 2M CdTe area detector [192]. The tensile tests were done using an Instron 100 kN uniaxial servo-hydraulic mechanical test rig (Instron, MA, USA) with a nominal strain rate of 1.33 x 10^{-5} s^{-1}, following the indications of the ASTM E8M for tension testing of metallic materials [179]. The geometrical calibration of the detector was performed using a CeO_2 standard sample [193]. The in-situ investigation was performed to evaluate the phase content evolution caused by the application of external source of stress, which affects the intensity count of XRD pattern, as well as the lattice strain, indicated by a shift in *d-spacing* and broadening of the peaks. The 2D diffraction data was integrated along an azimuthal range of 360º, to account for any change in the

microstructure of the tested samples, thus being reduced to 1D data. DAWN was used as a software for the purpose [194], as well as for the extraction of load and displacement data for mechanical properties.

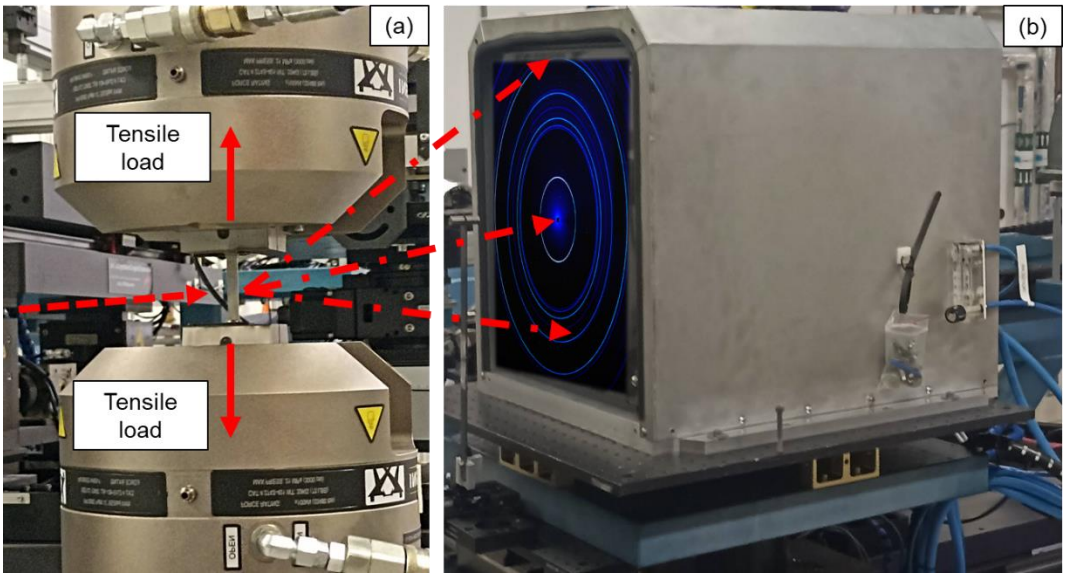

Figure 3.12. Experimental setup of the experiment performed at the Diamond I12 beamline : (a) incident high energy source (dashed arrow) on the tensile loaded specimen (continuous arrows); (b) Pilatus 2M detector with sample diffraction patterns obtained through transmission of the monochromatic beam (dash-dotted arrows).

MATLAB was used to post process the data obtained during the x-ray diffraction measurements, by importing the .dat format files containing both the tensile tests (load and displacement) and XRD patterns (*d-spacing* and intensity count) information for each time frame. Load and displacement files were processed to extract the stress-strain curves and mechanical properties (elastic modulus E, σ_Y, UTS and ε_f). The XRD pattern files were binned in groups of 10 frames each to reduce the amount of data to process, and the resulting averaged patterns were analysed to determine the position of the peaks for each of the two phases investigated (BCC and FCC) by means of the PDF-2 2021 database from the International Centre for Diffraction Data – ICDD [183]. The identification was performed by using ICCD card n. 00-006-0696 and 01-071-4407 for the BCC and FCC phase, respectively. Only BCC phase was considered for ferrite and martensite, as for low C concentration the BCT structure is not extensively distorted and cannot be distinguish from a BCC structure, as described in [47]. The binned patterns were fitted using a Gaussian function with a linear background and the fitted peak areas were utilised to obtain the phase VF (*vol%*) for each of the two phases, to monitor the trend over strain according to what was formerly executed by Church et al [195]. The accuracy in calculating the phase fractions is ± 0.1%.

3.15 XRF

X-ray fluorescence (XRF) spectrometry is an analytical technique that belongs to the family of atomic spectrometry techniques such as ICP-OES [196]. The technique enables to extract most of the elements in the periodic table. The detection limits are in the order of the parts per million (ppm). The technique investigates samples in their solid form. In this work, 17-4PH alloy was analysed via XRF. The powder was tested in its original form by investigating 1 g. Conversely to ICP, XRF does not allow to determine with accuracy the low concentration of elements with high atomic number. Nonetheless, ICP experiences issues caused by the interference of elements having lower atomic number. Therefore, for a comprehensive multielement analysis, ICP and XRF are complementary techniques.

The technique uses an analytical crystal of known composition to differentiate the x-rays diverted by the sample's surface. It provides fixed interplanar spacing between planes of atoms within the crystal that allows to differentiate the x-rays emitted from the analysed sample [197].

Both quantitative and qualitative analysis for elemental identification through XRF utilises Bragg's law of diffraction, given by:

$$n \cdot \lambda = 2d_{hkl} \cdot \sin\theta \qquad \text{Equation 3.8}$$

Where n is the order of diffraction, λ is the wavelength of the x-ray, d_{hkl} is the interplanar spacing and θ is the incident and diffraction angle.

3.16 Numerical simulation of deformation behaviour – Abaqus

Abaqus (Dassault Systèmes, France) is the software suite adopted for FEA analysis in this thesis, and includes Abaqus/Standard and Abaqus Explicit [198].

Abaqus/Standard allows to solve both static (or quasi-static) and dynamic problems. Abaqus/Standard solves a system of equations implicitly at each step of the analysis, referred to as solution *increment*. The module works by solving incremental-iterative solution technique based on the Newton-Rapson method. The stiffness is determined in the initial and final state, after breaking in small increment the load (static problems) or total time (dynamic analysis). The residual force is also calculated and, if it is not zero (in static analysis) or equal to the inertial force (dynamic problems), the increment size is reduced. Conversely, the convergence is met for the next increment.

In contrast, Abaqus/Explicit solves problems through time by introducing small time increments without solving a coupled system of equations at each increment. The kinematic state is advanced from the previous increment and the solution is determined without the Newton-Rapson method and each increment results less expensive. Abaqus/Explicit is suitable for modelling dynamic events and contact problems involving collision between multiple bodies and self-contact.

Some additional differences between Abaqus/Standard and Abaqus/Explicit are highlighted as follows.

- Refining the mesh affects linearly the computational cost of the Explicit analysis. Moreover, a uniform mesh makes Explicit perform better when reducing the time increment. Conversely, in Abaqus/Standard a localised mesh refinement is possible, however it will increase the computational cost in an exponential manner.

- Contact is a severe discontinuity, and Abaqus/Explicit analyses better the problem in terms of discontinuous nonlinearity. Abaqus/Explicit must be chosen when multiple independent bodies and self-contact are involved.

- Abaqus/Explicit performs better in handling discontinuities such as material failure where material stiffness can suddenly turn negative or ductile failure where material stiffness gradually decreases to zero, causing instead convergence issues in Abaqus/Standard.

- Sudden change in stiffness as loads are applied are also dealt with better in Abaqus/Explicit, for example in phenomena such as buckling, where stiffness changes drastically.

- Abaqus/Explicit has a limit library of mesh elements, a subset of the Abaqus/Standard one.

Therefore, Abaqus/Standard was used to simulate the static analysis representing the tensile testing on the cylindrical standard and tapered specimens used in Chapter 4 for the investigation of the twinning in 316L. The aim was to extract the resulting local stresses and strains under tensile loading via FEA. The simulation on the standard specimen was performed to validate the FEA model, by importing the material properties collected from the corresponding geometry produced with PBF-LB (obtained and presented in Chapter 4) as the homogeneous material model, including the post-yield behaviour. Once validated, the model was used to predict the behaviour under tensile loading of different designs of tapered specimen, to choose the one with an extended and uniform grading of stress and strain along the axis of the specimen. For both specimen designs, the top grip end surface was coupled with a Reference Point (RP), offset from the planar top surface and on the specimen's axis, as a coupling constraint (Figure 3.13). The boundary conditions (BCs) applied were: encastre on the bottom grip end, movement locked on the top grip end in translation and rotation apart from the loading direction (parallel to the BD) and the displacement to simulate the tensile testing was applied to the RP. A recap of the BCs applied is represented in Table 3.10. The environment was entirely generated in Abaqus through the graphical user interface (GUI). The specimens were meshed by means of quadratic tetrahedral elements (C3*D10*), a general-purpose tetrahedral element with 10 nodes and 4 integration points.

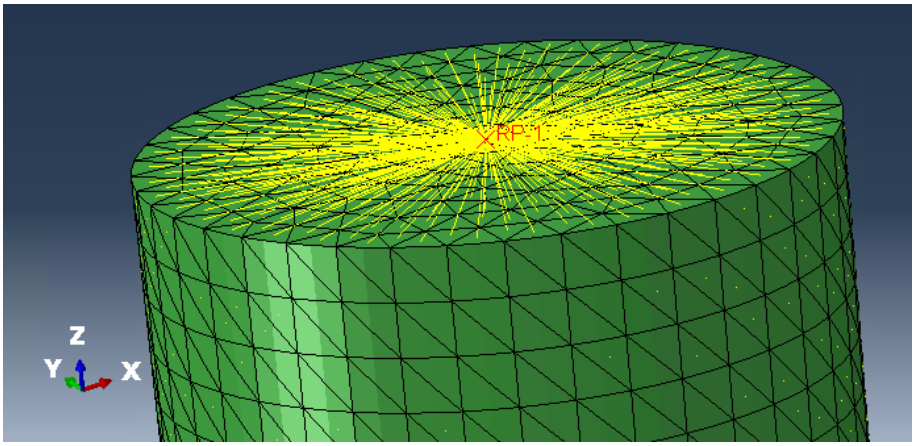

Figure 3.13. Coupling constraint of the top grip end surface to a Reference Point.

Table 3.10. Boundary Conditions applied to the standard and tapered specimens, simulated with 316L stainless steel material properties. U is the translational BC, while U_R is the rotational BC applied to the specimen.

Location	Boundary Conditions
Bottom grip end	Encastre: $U_X = U_Y = U_Z = U_{RX} = U_{RY} = U_{RZ} = 0$
Top grip end	$U_X = U_Y = U_{RX} = U_{RY} = U_{RZ} = 0$
Reference Point	Displacement along U_Z

Conversely, Abaqus/Explicit was adopted to investigate the honeycomb gyroids presented in Chapter 6. The issue related to the simulation of lattice structures is that the component is made of complex geometry and surfaces, external or internal. In this study, the contact between the lattice walls had to be tested. Therefore, contact options different than the surface-to-surface or the slave/master methodology [199] had to be applied. A general self-contact was used for all internal and external surfaces [200]. This avoids penetration and a hierarchy between the walls of the UCs.

The Explicit analysis included the quasi-static validation against the experiments from [151] as well as the quasi-static and dynamic analysis of lattices with 17-4 PH as material model (whose specific geometries are described in Section 3.5). As for the validation of the FEA model, the aim was to extract the resulting stress-strain curve applied onto the top surface of the lattice structure, to match the experimental curve. The simulation was performed by importing the material model collected from the bulk specimen as determined by Maskery et al [146], as detailed in Table 3.11, and considered as homogeneous material model, including the post-yield behaviour.

Table 3.11. Material properties of PA2200 used to validate the FEA model on the honeycomb gyroid lattice structure.

Property	Value
Density	960 kg/m^3
E	1.695 GPa
σ_Y	29.7 MPa
Poisson's ratio	0.3
Tangential behaviour	Friction coefficient: 0.32
Normal behaviour	Hard contact
Contact	General contact
Linear bulk viscosity parameter	0.06 (default value)
Quadratic bulk viscosity parameter	1.2 (default value)

The simulation environment was created in MATLAB through FLatt Pack, as explained in Section 3.5, through one of the scripts embedded in the software and modified for the intended purpose. The material properties and the boundary conditions were introduced in the script. The latter generated the required meshed lattice structures, for the mesh convergence study, and the two rigid bodies used to simulate the top and bottom heads of the testing machine. The schematic of the Abaqus environment is presented in Figure 3.14.

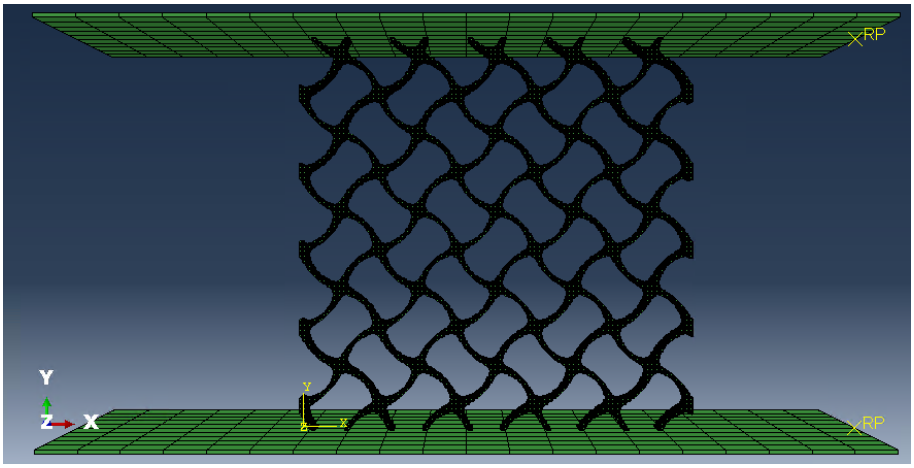

Figure 3.14. Abaqus environment for the simulation of the lattice structures, both validation with PA2200 and prediction of the energy absorption with 17-4PH.

The top and bottom grips of the compression testing machine were created as rigid bodies with inertia of 600 kg, to act as undeformed during the compression of the lattice structures. Two RPs, one per rigid body, were generated to apply the BCs and extract the information of the simulated testing, reaction force (RF) and displacement (*U*) to convert into stress and strain values. A recap of the BCs and predefined fields applied is represented in Table 3.12. The rigid bodies were meshed with *R3D4* rigid elements, that are used in Abaqus to define master surfaces for contact applications. The lattice structures were meshed with *C3D8R* element type, a general-purpose linear brick element, with reduced integration (8 nodes and 1 integration point), used for its higher accuracy [201]. It has the same shape functions as the *C3D8* element [202] and has been often used in the literature because of its capability of reporting with good accuracy the stress and strains in its integration point, when contact is involved.

Table 3.12. Boundary Conditions (BCs) applied to the bodies used to simulate the compression testing with honeycomb gyroid lattice structures, with both PA2200 for the FEA validation and 17-4PH for the prediction of energy absorption.

Location	**Boundary condition (BC) and predefined fields**
RP on bottom rigid body	Encastre: $U_X = U_Y = U_Z = U_{RX} = U_{RY} = U_{RZ} = 0$
RP on top rigid body	$U_{RX} = U_{RY} = U_{RZ} = 0$
RP on top rigid body	Velocity in compression of 2×10^{-8} m/s
RP on top rigid body	Displacement of 24 mm in compression

Once the FEA model was validated against the experimental results with PA2200, it was used for the description of deformation behaviour with 17-4PH alloy. Therefore, the only geometrical difference was the size of the lattices, as explained in Section 3.5. Two process parameter sets were used for the analysis, that is Set 1 and Set 3 as called in Section 3.3. For every simulation, the related material properties collected from Chapter 5 were imported, following the combinations explained in Table 3.7, as the homogeneous material model, including the post-yield behaviour. The only difference from the contact properties in Table 3.11, was the friction coefficient, 0.6. The same conditions as the validation applied to the top and bottom grips. For what concerns the BCs, the same velocity was kept for quasi-static analysis as in the validation model, while changed to the correspondent values (see Section 3.11) for the dynamic cases. Moreover, only the displacement (in terms of 80 % of the total height of the lattice structure, in the compression direction) was applied to the RP on the top rigid body. The same meshing elements were utilised for the rigid elements and the lattice structures.

The input files for the simulations were loaded into the High Performance Computer (HPC) provided by University of Nottingham, and the output files were downloaded to be analysed into Abaqus. The post-processing was performed in MATLAB.

4 On the development of twinning-induced plasticity in additively manufactured 316L

316L austenitic stainless steel produced with PBF-LB is characterised by increased mechanical properties compared to the conventionally manufactured counterpart. These increased properties rely on the strain hardening behaviour of 316L, referred to as TWIP, that occurs in the plastic regime. The advantages linked to PBF-LB relies on the hierarchical microstructure of the material that spans nearly six orders of magnitude due to its heterogeneous microstructure. However, there is still a debate on the onset of TWIP, its evolution over plastic strain and the interaction with deformation slip.

In this Chapter, the reasons for the onset of TWIP and the synergistic effect with deformation slip across the plastic regime are studied. First, an optimised process window for low porosity is determined by means of the Renishaw SLM 125, and the process parameter set with the highest density is selected. Subsequently, the as-printed properties of the chosen parameter set are investigated (phase content, microstructure and texture, residual stresses and mechanical properties), showing high strength and ductility as well as lack of twinning activity. The main technologies used are XRD, EBSD and tensile testing. Cubes and standard specimens are used for this initial investigation.

The results on the as-printed condition are employed to explain the following analysis on TWIP behaviour. To investigate the onset of TWIP, a tapered specimen was adopted, to extract all information about onset and evolution of twinning along an axis with decreasing cross-section. FEA, by means of Abaqus software, is used to support the design choice to extract a range of changing properties along the axis, in particular stress and plastic strain.

The selected tapered design is then mechanically tested with tensile testing at different final strain values, to detect the testing configuration that could provide the more comprehensive set of mechanical properties. The ε_f is chosen because of the largest range of hardness obtained, and further studied. The longitudinal section of the tested tapered specimen is analysed with SEM and EBSD to extract the microstructure, residual stress and twinning evolution in the plastic regime. FEA is used as support to quantify the stress and plastic strain values at each considered cross-section. The results allow to understand the reasons that activate TWIP in specific areas of the printed material, the onset of twinning and its interaction with deformation glide, and the evolution of the phenomenon explained at microstructural level.

4.1 Results

4.1.1 Optimal process window of as-printed 316L

The investigation started with the understanding of the process window, represented as a v (in terms of E_T) versus P, while keeping the other process parameters fixed. Figure 4.1 shows the experimental study on printed cubes, processed as described in Section 3.13. The green dots, that generate the so-called process window, were characterised by a density higher than 99.9%, that makes them fully dense material. Above them, with high v and/or extremely low P, an area defined by low density is present, seen as yellow dots of Figure 4.1. The value of the density varied between a minimum of 98.9% and a maximum of 99.7% density. On the bottom of the process map, a region of red dots can be noted. The density that defines that region ranges between 99.6% down to a detrimental 91% value.

The distinction between the 3 regions can be understood better by considering micrographs of the specimens, Figure 4.2. The green processability region is characterised by areas that lack pores or show a small amount, that is gas pores, inclusion or random LOFs. The last two occasionally occur because of the presence of faults during the PBF-LB process, such as spatter as discussed in Section 2.5.1. The yellow region is defined by LOF pores, typical for low energy densities, and showed the characteristic geometrical irregularity [110]. They are present in larger amount for lower values of v, while higher P values tend to recover the porosity. The red area, instead, is expressed by the presence of keyhole pores and gas pores, defining the switch from the conduction mode to the keyhole mode that has negative consequences in terms of stability of the melt pool [123]. A process parameter set was selected from the processability region and used for the remainder of the investigation on 316L stainless steel, as already specified in Table 3.3. The rationale for the selected process parameter set was to have a fully dense material, as it locates itself in the middle of the processability region. The values of the singular process parameters are comparable to those used in past literature investigation, including the 67 degrees layer rotation meander scan strategy [12,89,203].

The density for the chosen process parameter set was found to be 99.90 ± 0.06 % through the software ImageJ. To confirm the validity of the used density investigation, Archimede's principle was used for this process parameter set. The results provided a density of 99.94 ± 0.03 %.

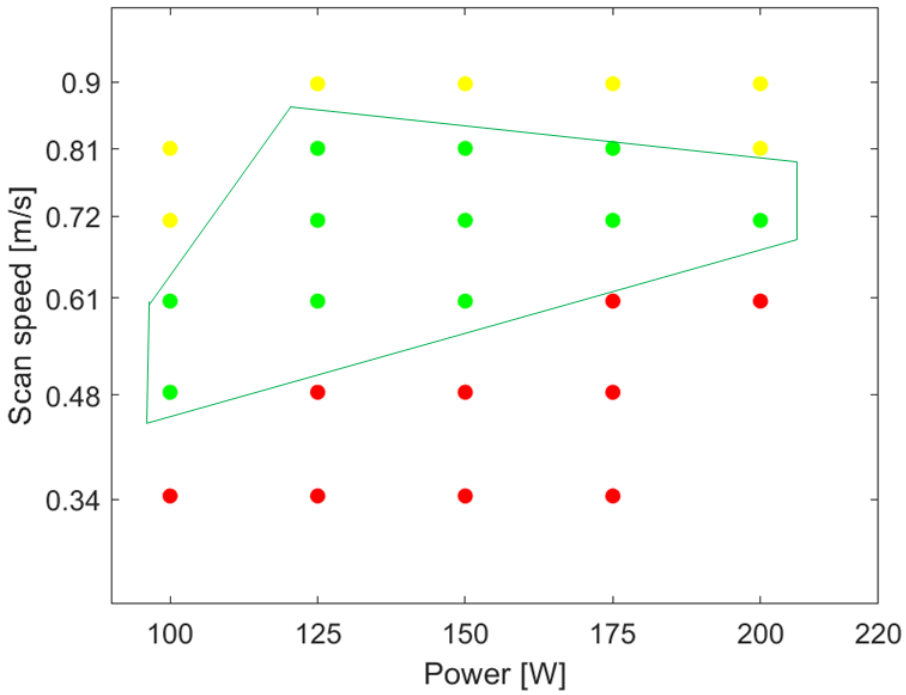

Figure 4.1. Plot of the process map, *v* as a function of *P*, extracted for 316L stainless steel. The green dots represent the processability region. Yellow dots show the LOF region, while the red dots display the keyhole area.

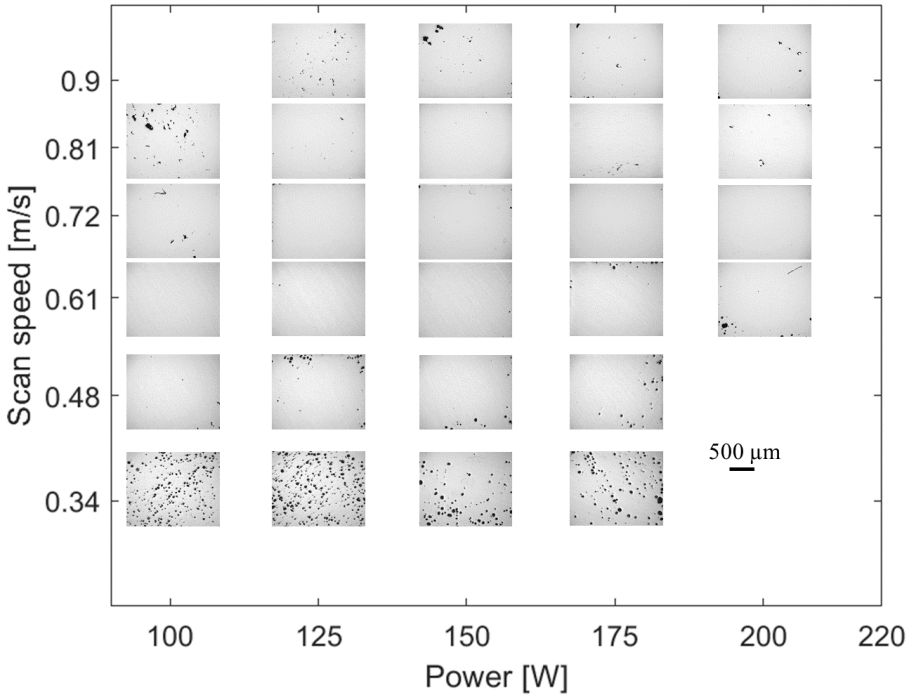

Figure 4.2. Process map with combinations of *v* and *P*, represented with optical micrographs of vertically cut (along BD) density samples.

4.1.2 Hardness and phase characterisation of the as-fabricated material

Different characterisation techniques were employed on the process parameter, including hardness and phase content of the as-printed material. The hardness map obtained from the cross-sections of printed cubes provided as a result 200 ± 10 HV. The average value is in agreement with the literature for 316L processed with PBF-LB, where the main contribution is given by the FCC lattice itself [204].

XRD analysis was performed on the same cube printed for the hardness map computation. The result can be seen in Figure 4.3. The spectrum of the scanned specimen shows 5 peaks corresponding to the FCC phase that characterise 316L. Every peak corresponds to one family of planes of the material, and each single peak lies at the theoretical value of 2θ, for the considered range between 20 and 100°.

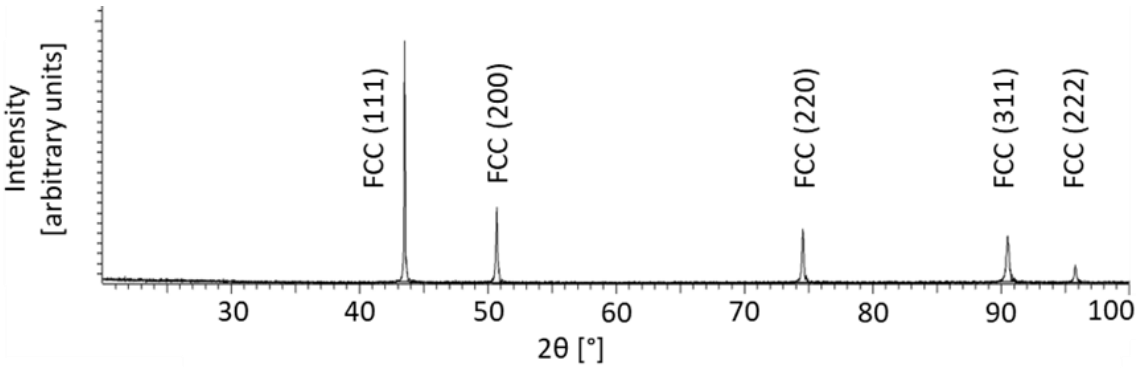

Figure 4.3. XRD plot obtained from the scan of the surface of 316L cubes printed with PBF-LB. Y axis has arbitrary units.

4.1.3 Microstructure and texture investigation analysis

PBF-LB processing of 316L generates a wide range of grain size, and the grains are either columnar or equiaxed [87]. EBSD and optical microscopy were used to extrapolate the as-printed microstructural information, to compare with the corresponding outcomes after deformation.

By means of EBSD technique, the grain morphology and orientation were retrieved, as well as the texture of the crystallites. The result is displayed in Figure 4.4(a) for an IPF map considered perpendicular to the printing layer and parallel to the BD. It can be noticed that most of the microstructure is characterised by columnar grains, with the longest dimension almost aligned with the vertical direction. The grains show a zig-zag growth. In addition, it is possible to see that some small equiaxed grains formed during the process. They are located in random spots of the area map with no precise alternation pattern with the columnar grains. Finally, a minor preferential orientation of [001] is the characteristic of the grains with respect to the BD. In Figure 4.4(b) a general lack of defects, mainly GND, in the as-built condition was revealed by considering the KAM map, conversely to what was noticed in other as-built studies, such as Kale et al [205].

The pole figures extracted from the same area scanned for the IPF are represented in Figure 4.5. The BD corresponds to the Z_0 axis of the coordinate used for the depiction of the texture. The image in the centre showed a preferential {101} fibre texture perpendicular to the BD. Conversely, the left and right images are defined by a weak {001} and {111} cubic texture, where [001] is aligned with the BD.

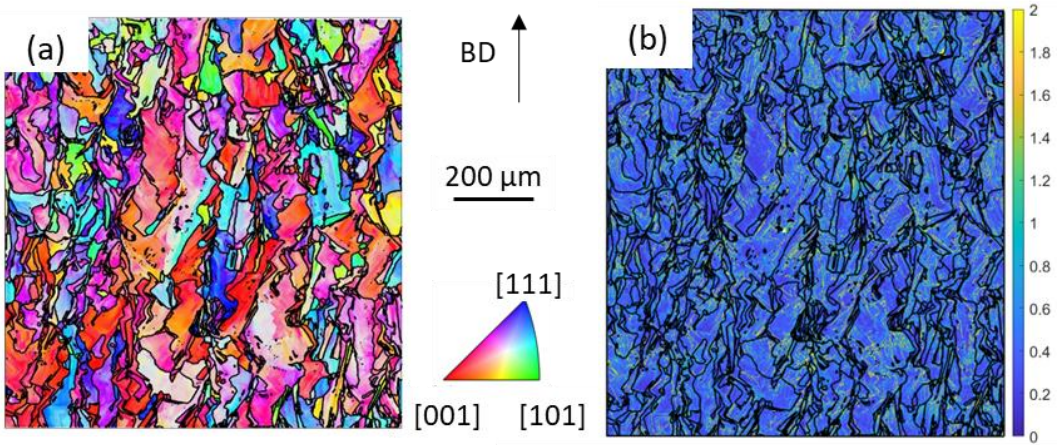

Figure 4.4. (a) IPF map of the as-printed condition for the 316L sample printed with the optimal process parameter set, aligned with the BD as shown in the figure. The IPF colour key has the [001] direction parallel to the BD. (b) KAM map of the same longitudinal section.

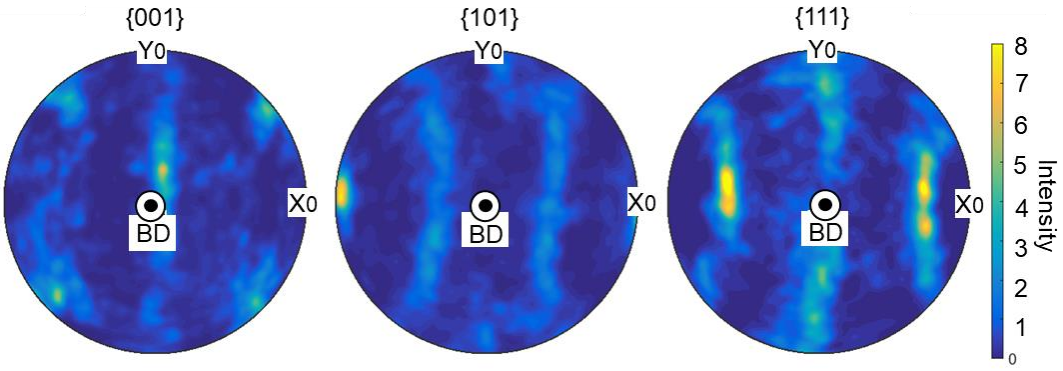

Figure 4.5. Pole figures of as-printed PBF-LB 316L processed with the optimal process parameter set, extrapolated in the plane parallel to the BD. The material displayed a fibre texture as well as a weak cubic texture.

Figure 4.6(a) depicts the etched microstructure of the cubic sample, imaged in the plane parallel to the BD. The meander strategy provided a random heat distribution throughout the layers, causing a non-uniform geometry of the melt pools in the cross-section. The calculated melt pool width was found not to exceed 181 ± 0.6 µm. The direction of laser travel that has been accounted for, when measuring maximum melt pool width, was perpendicular to the surface of the mounted sample. Figure 4.6(b) is a detailed image of the etched microstructure, which demonstrates that the grains are formed by dendrites with random orientation. Dendrites

along the BD were measured to extract the width that they show in the as-fabricated condition. The outcome gave an average of 0.57 ± 0.07 μm.

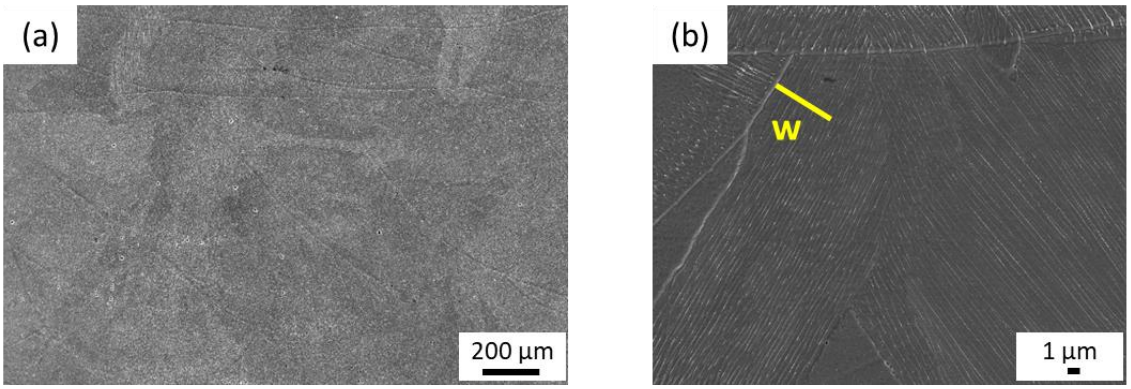

Figure 4.6. Etched imaging of the as-printed PBF-LB specimen, printed with the optimal process parameter set. (a) large area map showing the irregular size of the melt pools, caused by the PBF-LB process; (b) inset of the etched microstructure, depicting the dendritic with random orientation.

4.1.4 Mechanical testing of additively manufactured standard specimens

Five standard specimens, with the dimensions given in Section 3.7, were printed and tested to failure to obtain information about the mechanical properties of the as-printed PBF-LB 316L. Figure 4.7 provides a stress-strain plot obtained from the components, with the load applied along the BD. The resulting mechanical properties are given in Table 4.1. The average σ_Y and ductility resulted 485 MPa and 55% respectively. Two samples suffered from an earlier failure than the other three, below 50%. Given that the sample with ε_f of 54% engineering strain resulted to have the median curve among the five specimens that were tested, this material model was used for the remainder of the analysis, both computational and experimental. From it, the resulting stress and strain values were used to extrapolate more information regarding the TWIP behaviour of the material. The mechanical properties obtained from the tensile testing lie within the range of properties available in the literature [84,206]. The range of mechanical properties for PBF-LB 316L is wide due to dissimilar process parameters and parts orientations affecting microstructural features. The presence of porosity, as explained in Section 4.2.2, is the cause for variability of elongation at failure, also found by Sames et al [207].

The selected material model was investigated in further detail to understand the strain-induced capability of the PBF-LB processed 316L steel. The investigation was accomplished by the extrapolation of the strain hardening rate (SHR) from the mechanical stress-strain curve in Figure 4.7. The SHR curve for the tested standard specimen is shown in Figure 4.8. This SHR is consistent to previous studies that show presence of twinning, as obtained by Karthik et al [83]. This result confirmed the application material to be a suitable candidate for the remainder of the investigation on the onset and development of twinning-induced plasticity and its interaction with deformation glide behaviour.

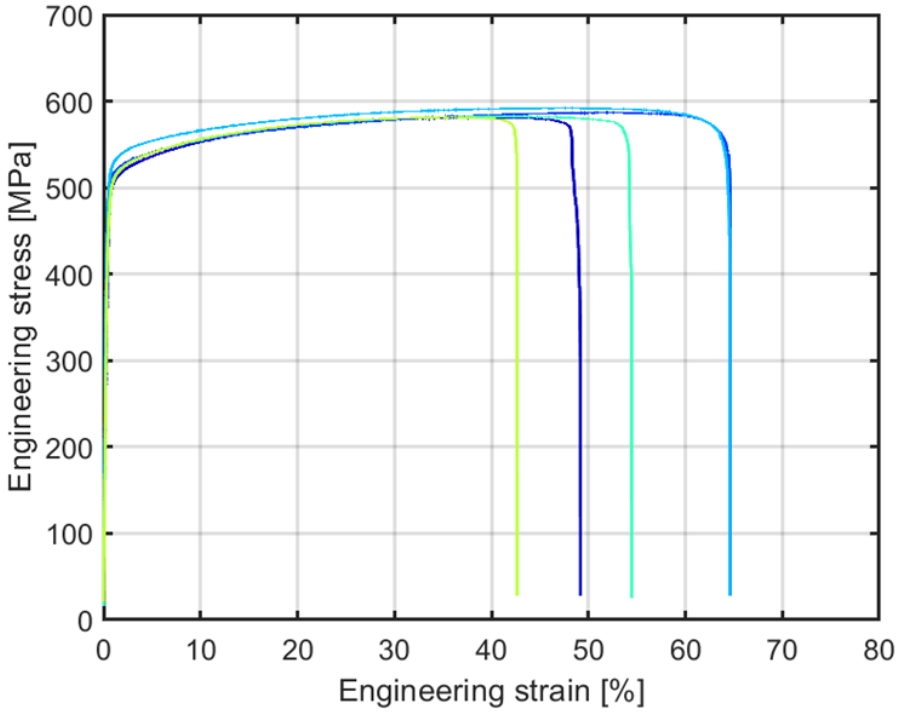

Figure 4.7. Tensile mechanical curve for the PBF-LB printed sample with the optimal process parameter set.

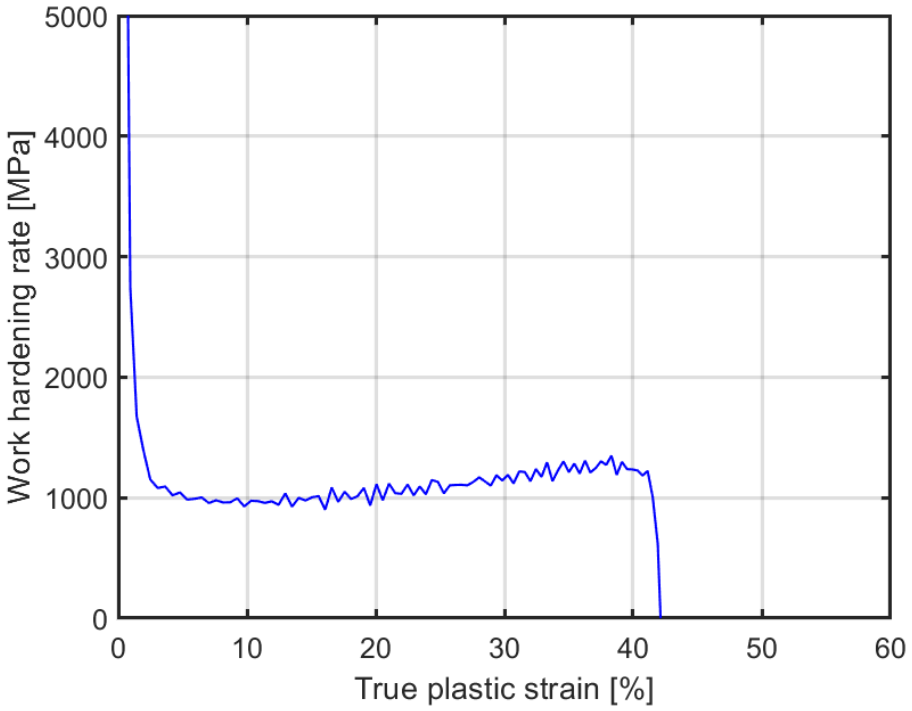

Figure 4.8. Strain hardening rate versus true plastic strain plot for the standard specimens tested. The material model is the median stress-strain curve from Figure 4.7 with average material properties as in Table 4.1, taken as a reference for the mechanical properties of PBF-LB 316L stainless steel.

Table 4.1. Mechanical properties of 316L stainless steel obtained from standard tensile specimens. The quoted error is the standard deviation.

E (GPa)	σ_Y (MPa)	UTS (MPa)	ε_f (%)
179 ± 11	485 ± 12	585 ± 5	55 ± 9

4.1.5 Design of a tapered specimen for twinning investigation

It is known the importance of computational modelling to support experimental investigations when some mechanical properties cannot be extracted due to limitation to experimental techniques. Therefore, an FEA model was created in Abaqus in support of the experimental results for the investigation on the TWIP behaviour of 316L printed with PBF-LB.

The first step for such a model was its validation with results determined from the standard tensile specimen geometry. As already mentioned in Section 4.1.4, the material model of the median tensile stress-strain curve was taken as a reference, also for the FEA model. A testing environment was generated as described in Section 3.16. Simulations were run with different mesh element size. The reason for that was a sensitivity analysis to obtain the mesh element size of the FEA model that contributes to a convergence on the experimental counterpart. The mesh element size for the considered element ranged between 1 mm down to 0.1 mm. Figure 4.9 provides a summary of the stress-strain curves obtained from the experimental investigation and the FEA model, considering the cross-section interested in the necking and failure of the standard tensile specimen. Figure 4.9(a) shows the stress-strain curves for the highest mesh element size of 1 mm. There is a mismatch between the FEA and experimental curves up to 8.6%, both in the elastic region and in the plastic regime, which is the focus of the present thesis. By reducing the mesh size of the C3*D10* element, the convergence of the modelling tensile curve approached the experimental curve with decreasing error throughout the entire strain range of the mechanical testing. Figure 4.9(b) depicts the results obtained with element size of 0.2 mm. The error curve showed the highest deviation of the FEA curve to the experimental testing of up to 2.1%. However, the mismatch between the curves decreased at the beginning of the plastic regime so that an accuracy of more than 99% was achieved and almost 100% was reached past the 8% true strain. Decreasing the mesh size to 0.1 mm provided a similar convergence of the FEA model to the experimental curve, at the expense of the simulation time. Therefore, 0.2 mm was used for the next simulations on the tapered investigation.

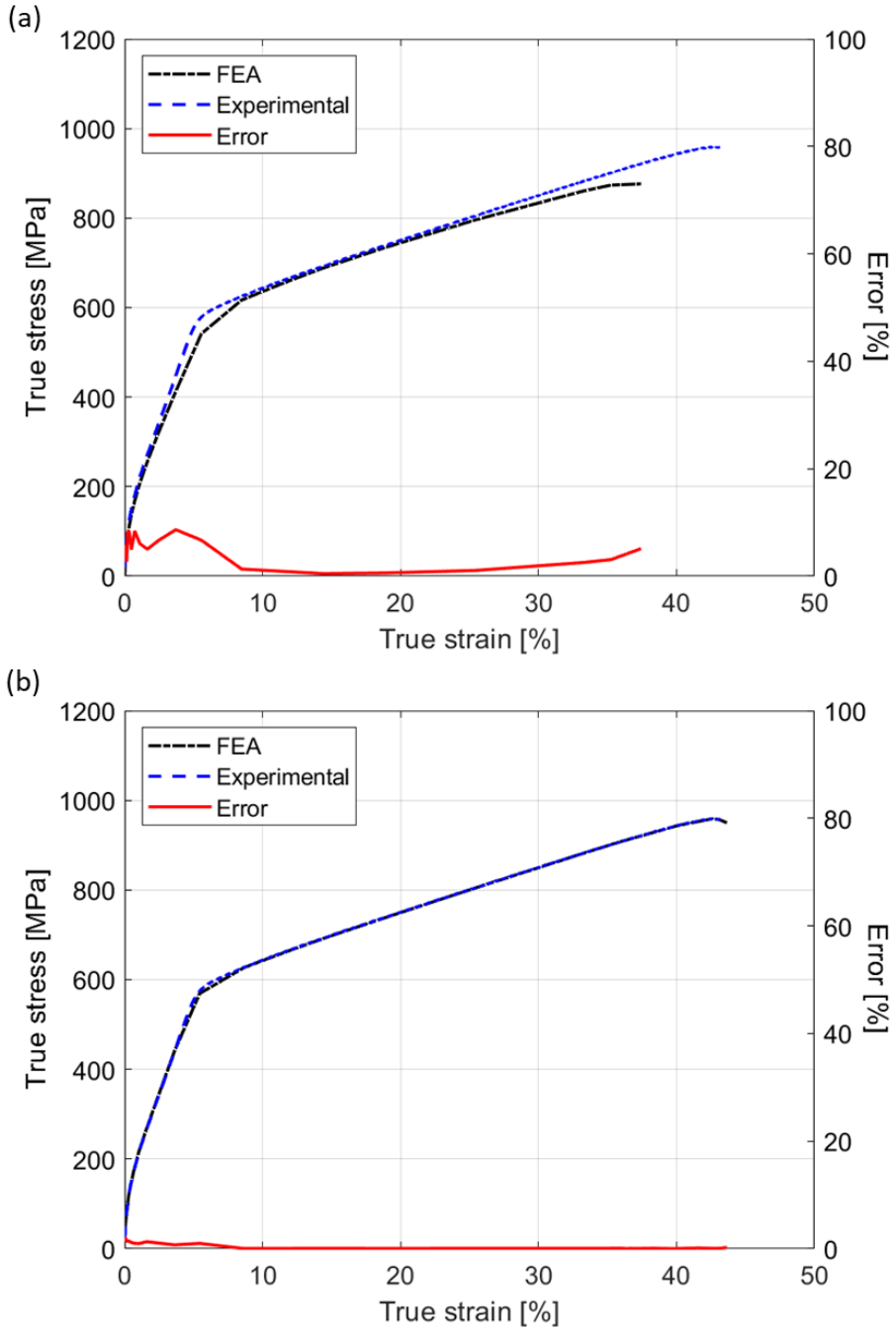

Figure 4.9. Stress strain curves of the standard tensile specimen geometry, each showing a comparison between the experimental behaviour of the printed samples and the FEA results from the Abaqus simulations at (a) 1 mm element mesh size and (b) 0.2 mm element mesh size. Error representing the deviation is also presented.

The validated FEA model was adopted to create a simulation environment for several configurations of tapered specimens. The aim of this task was to extract the tapered geometry that could provide a wide range of mechanical properties on the same specimen when undergoing plastic deformation, as done previously by Bhadeshia [178] and discussed in Section 3.7, that could then be printed and physically tested. The six generated designs are shown in Figure 4.10. It can be noted that the grading occurs from the bottom to the top

of the gauge section. This induced the failure, at the shoulder of the different configurations, on the side with the lowest diameter of the conical cross-section.

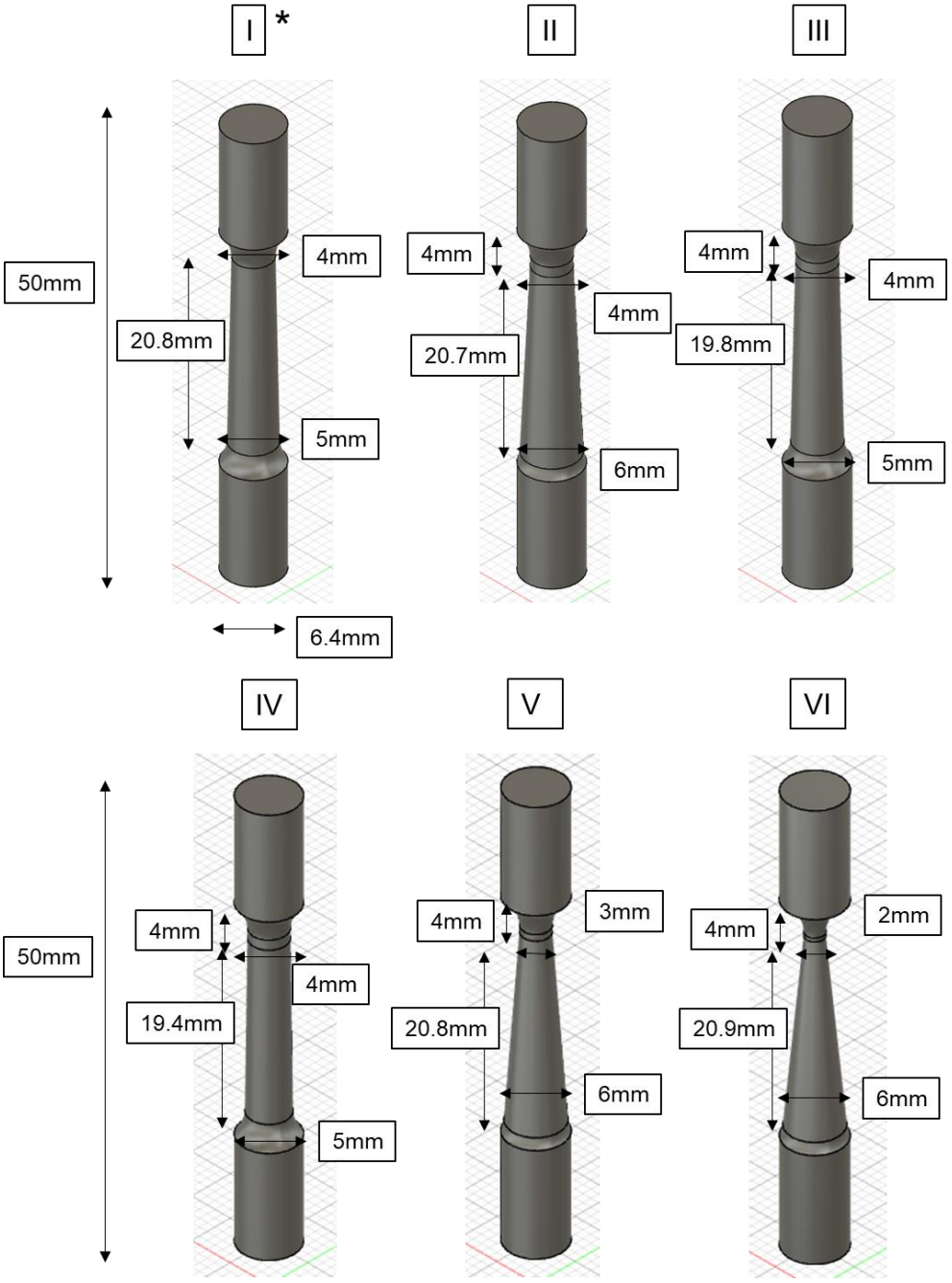

Figure 4.10. Isometric view of the drawing for the six different configurations of tapered specimen investigated to obtain a wide range of mechanical properties for PBF-LB 316L steel. The selected configuration, referred to as *I*, is pointed out by a star.

The six tapered models were imported into Abaqus and simulations were run with the same test environment as the standard specimen geometry. Table 4.2 contains the combination of maximum stress and displacement that is met for each configuration at the necking of each specimen, in terms of true stress which is the quantity

that Abaqus works with. Each configuration starts the necking at different elongation values, which implies a dissimilar grading of the mechanical properties as well. The least graded configuration, referred to as *I*, was characterised by a reduction in load-bearing area across the gauge section of 36 % and resulted in the highest ε_f, to provide a uniform grading of the mechanical properties. Therefore, it was selected for the experimental work.

Table 4.2. True stress and displacement required to reach the true stress values for the designs used in the FEA modelling to obtain a tapered specimen with high range of mechanical properties.

Design number	**I**	**II**	**III**	**IV**	**V**	**VI**
True stress [MPa]	900	900	900	900	900	900
Displacement [mm]	5.4	4.3	5	5.2	3.1	2.8

4.1.6 Mechanical testing and hardness characterisation of the tapered geometry

The selected design for the tapered specimen was studied with tensile mechanical testing, following the reasoning that a range of mechanical properties could be extracted along the axis of the specimen (corresponding to the BD of the PBF-LB printing process) across the cross-sections. The mechanical testing was characterised by 4 different tests. The tapered specimen was investigated until the failure extension along with interrupted tests at different elongation steps. In Figure 4.11 the outcome of the tensile testing can be appreciated. In order of displacement, the tapered specimens were elongated at 2.5 mm, 3.5 mm and 4 mm before each test was interrupted and the specimens could be removed with no further extension applied. The fourth and last specimen, instead, was brought to failure and reached a final elongation of 5.5 mm at the end of the tensile test. A maximum load of 8430N was applied by the equipment jaws. The aim of the study was to accomplish different stages of the deformation, from a region without necking formation up to a complete detachment of the tested sample, to understand the condition that could supply the most information to the twinning investigation.

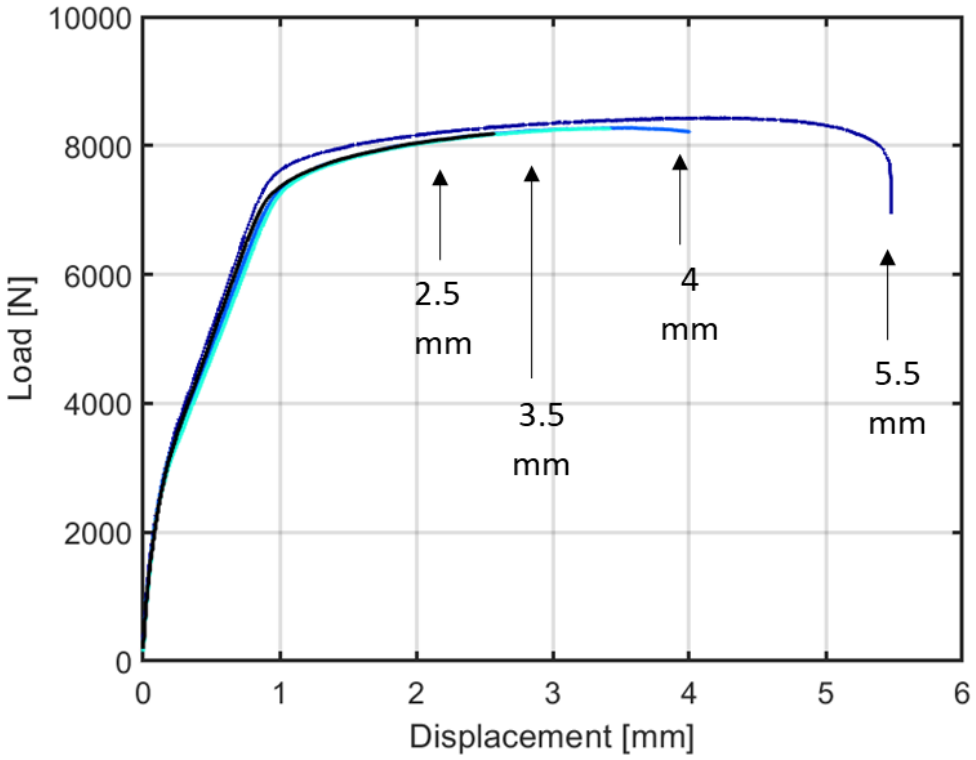

Figure 4.11. Load displacement curves for the selected tapered specimen design. Each curve represents an individual tensile test. The investigation was characterised by three interrupted tests at 2.5, 3.5 and 4 mm, plus a test to failure of the tapered specimen.

The outcome of the tensile testing showed in Figure 4.11 can be inferred in Figure 4.12. The samples were longitudinally cut and prepared for further analysis as described in Section 3.8. The first step was to infer the distribution of the hardness of the four different configurations, along the axis of the specimens. From the figure, it can be first seen that each specimen is characterised by a different behaviour at the lowest value of the cross-section, after the tensile test. In particular, the specimen brought to failure had a complete necking with the detachment of the two parts of the gauge section that was stressed during the tensile examination. The specimen with a 4 mm elongation had a necking that is almost half-way through the cross section where it was originated. The specimen elongated at 3.5 mm displayed the beginning of the necking on the specimen. Finally, the last specimen was not characterised by the onset of the failure of the cross-section. A dissimilar range of hardness was obtained. The mentioned range, moreover, interested only part of the gauge section. Specifically, the specimen tested to failure was defined by having the largest length of interested cross-sections in hardness change from the minimum value that defines the as-printed condition. The length was determined to be of 10.7 mm. In addition, the highest hardness value was found for this configuration, and reported to be 380 ± 10 HV. The remaining interrupted tests did not show the same outcome as the specimen tested to failure; therefore, the latter was considered for the next steps of the investigation.

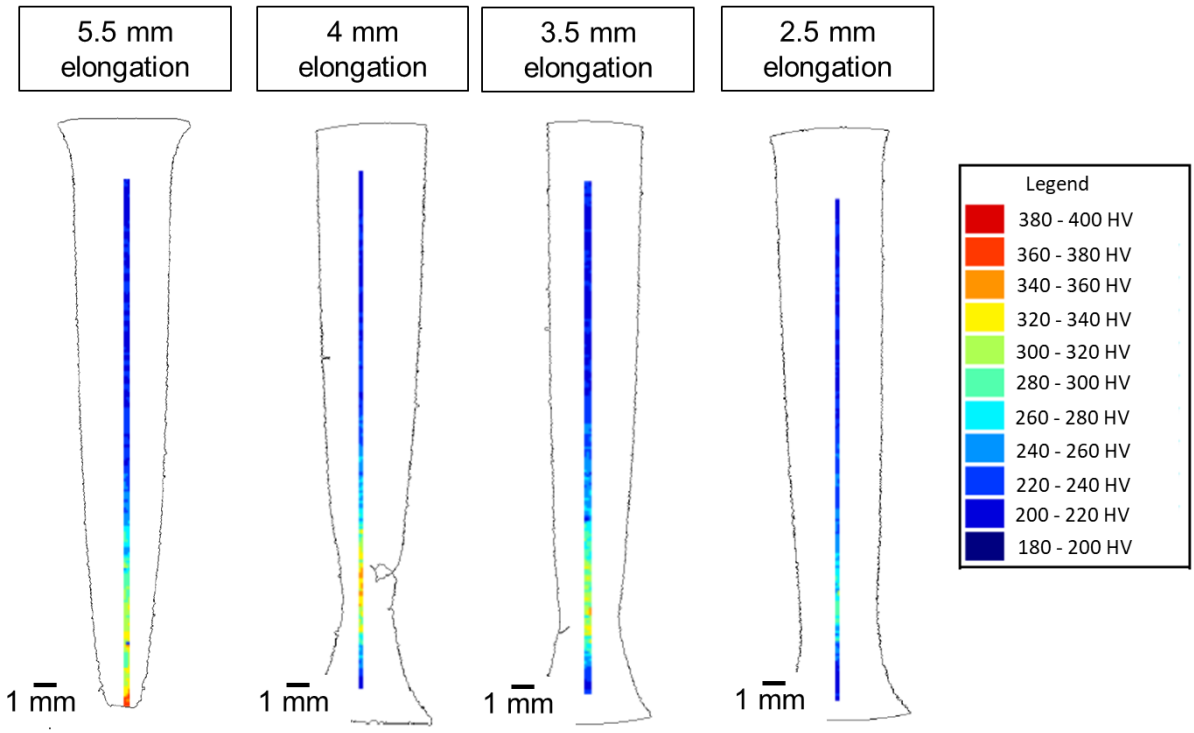

Figure 4.12. Hardness maps obtained from the series of tensile testing on the tapered specimen design. The specimens were longitudinally cut, mounted and polished for the purpose. From left to right: the 5.5 mm elongation specimen is the one brought to failure, the other maps are for decreasing interrupted tensile displacement at 4, 3.5 and 2.5 mm respectively.

4.1.7 Microstructural characterisation of tapered specimen

Microstructural characterisation of the tapered specimen tested to failure was executed to focus on the plastic regime and the differences between the as-printed conditions and the areas interested by plastic strain, and also between the different areas that are affected by deformation of the plastic strain. Figure 4.13 displays the drawing of the tapered specimen in its deformed condition and the five selected areas that are presented in this thesis. Each area corresponded to different levels of hardness, higher than the unstressed value. The plastic strain values contemplated in the figure are 9%, 15%, 26%, 44% and 60% respectively. In the same order as the mentioned values, Figure 4.13(a-e) reveal the BSE images of the five areas. In Figure 4.13(a) is the BSE result that 9% plastic strain caused to the microstructure of the tapered specimen. The grains are well defined, with only sporadic areas with brighter bands (i.e. the twin bands) that interrupted the growth of the columnar grains. Increasing the plastic strain to 15%, 26% and 44% provided the images in Figure 4.13(b-d) where the density of the mentioned twin bands became predominant compared to the 9% plastic strain induced. Finally, Figure 4.13(e) represents the necking cross-section, which was characterised by not having a recognised microstructure compared to the as-built condition. Figure 4.13(f-j) show EBSD results with IPFs at the same corresponding cross-sections Figure 4.13(a-e), aligned with the BD and load direction. The purpose of these

images was to reveal the properties of the bands forming along the axis of the tapered specimen and confirm the presence of twinning [89]. Figure 4.13(f) is the IPF for a plastic strain of 9%, and it can be perceived that the grains were interrupted by a few twin bands that assumed a specific orientation, as pointed by the two arrows. The increase of plastic strain affected the density of the twin bands, with a rise of the latter from Figure 4.13(g) to Figure 4.13(j), where the grains cannot be distinguished between each other. Specific orientations of the grains seemed to be more favourable to the formation of the twin bands than others.

Morphology of the tapered specimens in the five investigated cross-sections was carried out. In Figure 4.14(a-e) is an inset of the five areas, at increasing plastic strain from 9% to 60%, whereas in Figure 4.14(f-j) are the low magnification images of the cross-sections, in the same order of plastic strain of the insets. The yellow lines, referred to as *w* in each of the 5 images, contain a group of dendrites of the microstructure of the material, considered along the BD. With the increment of the plastic strain from 9% to 60%, it is possible to notice that there was a constant decrease in size of the cell size in the specimen. Computation of the average cell size provided the following result, in order of increasing plastic strain: 0.51 ± 0.07 μm, 0.48 ± 0.08 μm, 0.45 ± 0.03 μm, 0.39 ± 0.06 μm and 0.26 ± 0.04 μm. A visual inspection that describes the stretching of the dendrites can be appreciated at lower magnification, in Figure 4.14(f-j) with the same order of the previous images. In Figure 4.14(f) the depth of the melt pools was near to the value of the as-built condition, down to 35 μm, while a substantial increase of depth occurred up to 60% plastic strain, where Figure 4.14(j) shows a stretched melt pool that takes in depth the entire height of the image, 95 μm.

In Figure 4.15 are the Schmid factor maps for two cross-sections of the tested tapered specimen, the region at 15%, Figure 4.15(a), and 26% plastic strain, Figure 4.15(b). The two values were chosen to provide a distinction between an area with lower deformation as well as concentration of twin bands, and an area with larger deformation where the density of twin bands was suddenly higher and homogeneously distributed into the microstructure. The grain orientation is defined with the same convention as the IPFs data from Figure 4.13. In the two areas, both small and large grains were present. The average value of the Schmid factor increased by the input of higher plastic strain, that is 26%, to the tapered specimen.

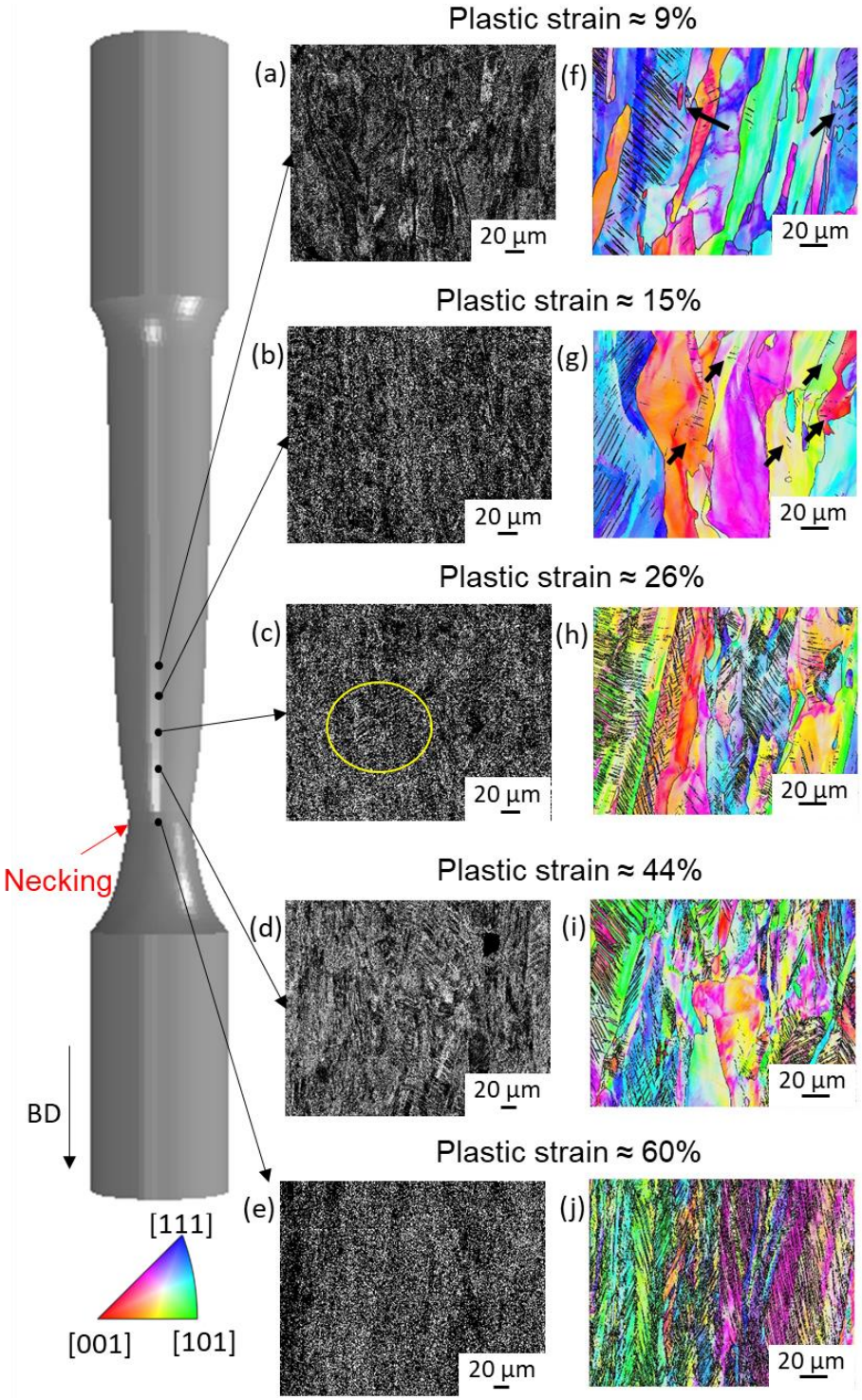

Figure 4.13. Evolution of the microstructure at distinct strain levels along the axis of the tapered sample. (a-e) BSE pictures of chosen areas of the sectioned tapered specimen considering a range of plastic strain; twins are detectable as striations, as circled in (c). (f-j) EBSD maps in the same areas; black arrows point out grains where twinning is detected.

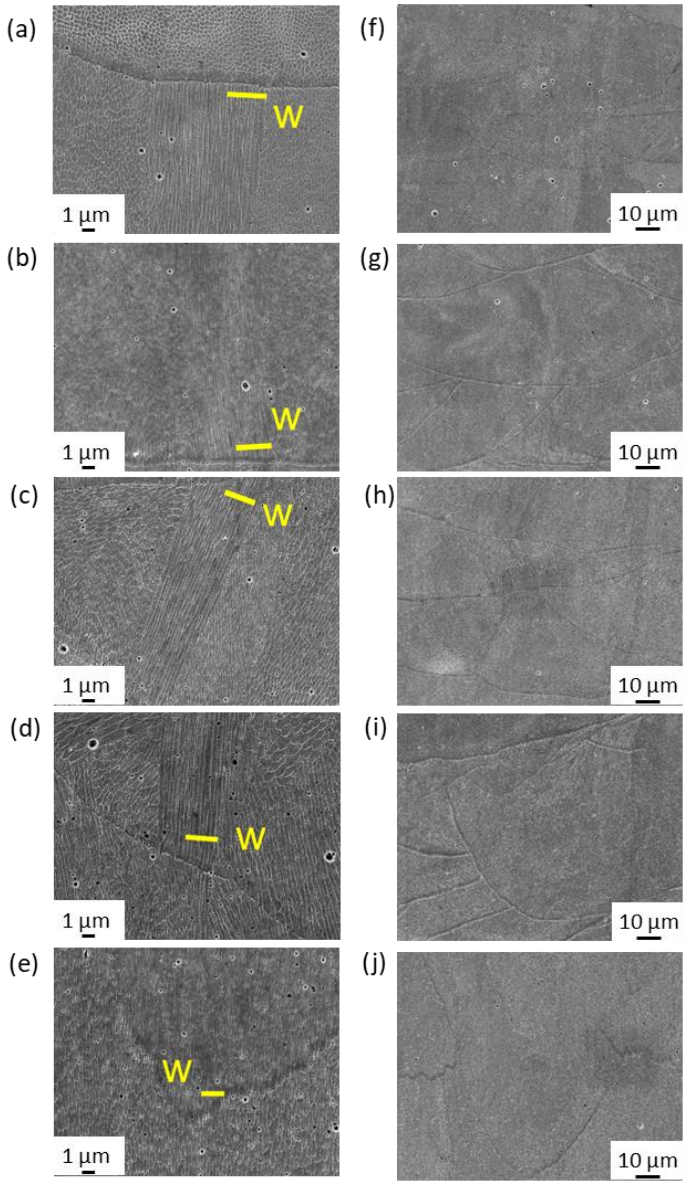

Figure 4.14. Morphology of the investigated areas on the tested tapered specimen. (a-e) SE imaging of the same areas as in Figure 4.13, focusing on the cells size; the average widths of the dendrites are: (a) 0.26 µm; (b) 0.39 µm; (c) 0.45 µm; (d) 0.48 µm; (e) 0.51 µm. (f-j) SE imaging at lower magnification of (a-e) to show the melt pools size along the axis of the tapered specimen.

KAM maps were extrapolated and reported for the cross-section at plastic strain of 15% from the insets drawn in Figure 4.15(a) and revealed in Figure 4.15(c-d). Figure 4.15(c) is the image of a large grain, whereas Figure 4.15(d) contains information about a small grain from the cross-section. The relationship between the twin bands as well as the dislocations and the size of the grains where they are present, can explain the evolution of the twinning behaviour over plastic strain. It can be noted that small grains were characterised by low presence of twin bands and high density of dislocations, and the general KAM value of the large grains was lower than that of smaller grains.

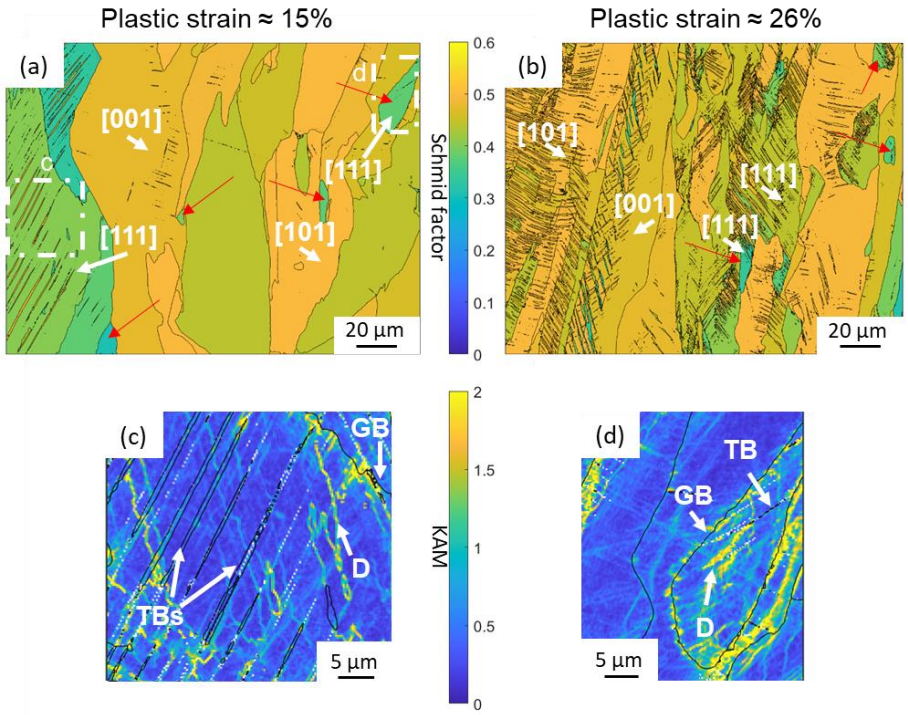

Figure 4.15. Schmid factor and KAM maps at growing plastic strain. (a, b) Schmid factor map for the regions where twinning becomes the prevalent deformation mechanism; small grains that do not present twinning are signalled by red arrows. (c, d) KAM maps of two areas emphasised by the dashed boxes in (a), extracted from grains with [111] orientation; TBs, dislocations (D) and grain boundaries (GB) are pointed out. (c) is the inset of a large grain, (d) is the inset of a smaller grain.

4.1.8 Computational mode in support to experimental results

The computational model and the experimental investigation were used in synergy, to link the properties that can be extracted from the FEA model, true stress and plastic strain evolution, with the hardness, twin concentration and position along the axis of the physically tested geometry.

Figure 4.16 represents the true stress, hardness and twin concentration with reference to the position from the fracture point of the specimen. In Figure 4.16(a) is the evolution of the true stress along the axis of the tested tapered specimen, where zero is the fracture point. The increasing trend of the stress can be divided into three phases. The first phase saw an increase in stress from 436 MPa at the farthest point from the fracture point up to 537 MPa at 5.8 mm from the zero. The second phase was defined by a rise from 537 MPa to 873 MPa. Finally, in the last phase a trend from 873 MPa to the UTS occurred. Figure 4.16(b) depicts the hardness and twin concentration evolution along the axis of the tapered specimen. Hardness increased along the axis towards the fracture tip, with the highest value being 380 HV. A similar tendency can be described for the concentration of twins. To provide a visual overview of the trend on the tapered specimen up to the UTS, in Figure 4.16(c) is the FEA prediction of the true stress depicted at the necking frame of the FEA.

In Figure 4.17 hardness and twin concentration are presented with reference to the local plastic strain as predicted by the computational model. Below 15% plastic strain, the twin concentration was steady. Between 15% and 26% plastic strain, there was a significant increase in the twin concentration from around 2% to 11% of the cross-sections considered in the analysis. Finally, at 44% and 60% strain, the twin concentration increased to 15% and 28%, respectively. The relationship between hardness and plastic strain was also characterised by a rise with strain. However, for this property there is an initial rapid increase in the region up to 15% strain, from 230 HV to 300 HV. The rate of increment of the hardness was then more modest once the activation of twinning was reached, with the fracture point expressed by a value of 380 ± 10 HV. Linking the localised true stress in the regions between 15% and 26% strain, the FEA model predicted a gain from 544 MPa to 694 MPa.

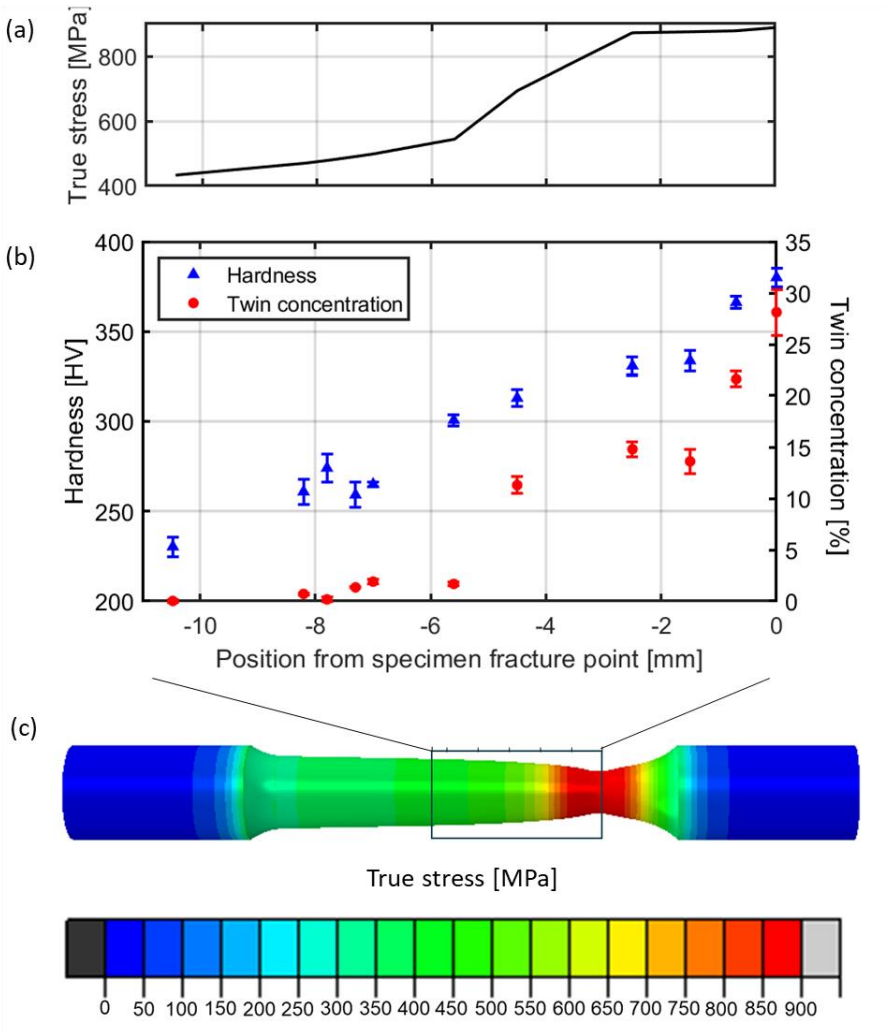

Figure 4.16. Stress, hardness and twin concentration in the tapered tensile sample brought to failure. (a) true stress line profile data from the FEA; (b) hardness and twin concentration, on the tapered sample from the breakage point for the region emphasised in (c); (c) Stress distribution in the tapered specimen predicted by FEA at the point of failure.

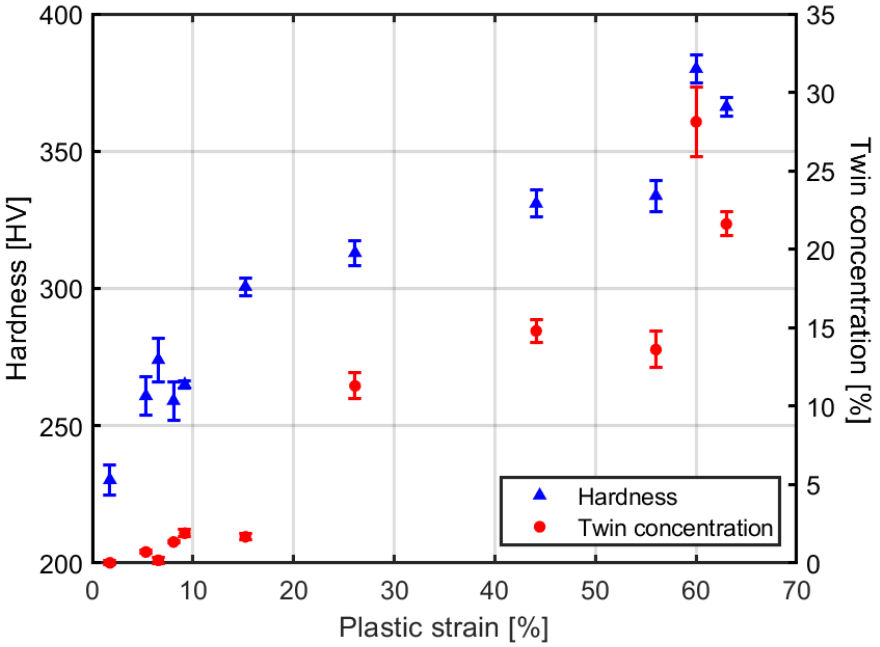

Figure 4.17. Hardness and twin concentration versus plastic strain in the tapered tensile specimen tested to failure.

4.2 Discussion

This Section discusses the most important features that emerged during the twinning-induced plasticity study on PBF-LB 316L. They are considerations on the as-built conditions and related mechanical properties, and examinations on the onset and development of twinning under deformation.

4.2.1 The investigation of the as-printed conditions for PBF-LB 316L stainless steel

The initial investigations performed in Sections 4.1.1, 4.1.2, 4.1.3 and 4.1.4 aimed at extrapolating the as-built properties of PBF-LB 316L stainless steel and confirming the improved performance with respect to conventional manufacturing processes.

The process map, whose plot is reported in Figure 4.2, was extrapolated to determine and select a process parameter with high density. The presence of defects, namely LOFs or keyholes, are detrimental to the mechanical properties of a material processed with PBF-LB and can cause, for example, early failure to printed specimen, as discussed by Pham et al [12]. In this study, a lack of defects was revealed in the central region of the process map. The porosity was characterised by a porosity of 0.1% as the highest value. Such an outcome

can be appreciated in other previous works on the same material processed with PBF-LB, as obtained by Hajnys et al [114]. This assures that no early failures were affecting the mechanical properties.

The XRD in Figure 4.3 supported the presence of a single FCC phase across the entire scanned section. This result is in agreement with the research done by Pham et al [12]. It is a confirmation that the as-printed 316L steel with PBF-LB did not contain secondary phases that would affect the behaviour of the material under deformation, including the TWIP activity as determined by Wang et al [84]. Moreover, the process parameter chosen for the investigation did not influence the printed material with lattice strain for any of the family planes. Such a consequence is represented, in a XRD spectrum, by mean of a shift of the peaks from the theoretical values 2θ. This because of the deformation of the lattice of the FCC phase, as investigated when thermal stresses are introduced on the printed material by Ding et al [208].

From the IPF map in Figure 4.4(a), it can be noticed that the majority of the microstructure was characterised by columnar grains, with the longest dimension that tended to align with the vertical direction, the BD. The latter is the direction of heat transfer through the printed material, down to the supports and the build platform. This consequence of laser processing was described by the research of Ma et al [209]. The grains also show a zig-zag growth, already found in investigations done on PBF-LB process. In particular, FCC metal alloys that are manufactured by means of alternating scanning strategies unveil such a growth, as in the work by Wei et al [210]. In addition, small equiaxed grains formed during the manufacturing process. Their presence in the as-printed condition of 316L illustrates the phenomenon of the high cooling rate from PBF-LB that faces issues in providing a homogeneous morphology, due to no sufficient time for some grains to grow in the direction of the heat dissipation. Finally, the [001] minor preferential orientation of the grains along the BD direction is an outcome revealed in past investigations on the same material [87].

The lack of defects extrapolated from the KAM map, Figure 4.4(b), highlights the difference in process parameters used between this study and the results provided by Kale et al [205]. Specific process parameter sets, defined by low energy density, can leave the as-fabricated specimen with a not negligible KAM distribution. The reason for such high presence of defects is linked to residual stresses due to the thermal contraction during the rapid cooling of the PBF-LB process, more extreme than the cooling rate undergone by the specimen analysed in this thesis.

The texture of the as-printed material, displayed in Figure 4.5, brings important information about the process parameter used and its influence on the orientation of the crystallites in the material. The presence of a preferential {101} fibre texture perpendicular to the BD, and two weak {001} and {111} cubic textures, confirms that the process parameter set used for the investigation of twinning in 316L steel is such that it affected the orientation of the crystallites due to its rapid cooling rate. However, it does not intrinsically contain high energy density to assign a strong texture, as can be seen in case of a multiple of uniform density (mud) larger than 20 [206].

The solidification dendrites, analysed via BSE imaging, and reported in Figure 4.6, display random orientation across the entire section. The dendrites considered along the BD gave an average width of 0.57 μm. A similar order of magnitude was previously reported for this material by Dépinoy [211], where the reported dimension in the literature was 0.6 ± 0.16 μm. The differences in the absolute values are given by the specific process parameters used to print the specimens. From the BSE images, it can be noted that some dendrites were able to grow across grain boundaries, and in addition no secondary branches formed during the PBF-LB process. This can be still explained by the rapid cooling and fast solidification process [212].

4.2.2 Mechanical properties for standard PBF-LB specimens

The stress-strain curves in Figure 4.7 and the mechanical properties in Table 4.1 provide information about the exceptional outcomes that can be obtained with 316L stainless steel printed with PBF-LB.

The exceptional maximum ε_f that was reached, namely 65%, is ascribed to the TWIP behaviour of the material in the plastic regime, generating twin bands that oppose to the movement of dislocations and the corresponding onset of the necking that brings the material to failure [91]. Some of the tested standard specimens were failing at lower engineering strain, approximately 43%. The reason is in the presence of porosity, which created initiations of cracking at earlier failure points, given by four main causes. The first is entrapped gas in the powder particles, that results in random entrapment of inert gas in the printed specimens during PBF-LB process. The second cause is different particles size, having a diameter larger than the produced layer thickness. Incomplete flow of metal powder onto the required scanning area has an additional impact to porosity. Finally, the fourth reason is spatter [207,213]. Overall, the σ_Y and ductility are in good agreement with previous investigations on 316L produced with PBF-LB [85]. In addition, the properties are found to be most performant than the corresponding annealed 316L counterpart [214].

The SHR curve presented in Figure 4.8 for the standard specimen confirmed that the as-printed PBF-LB 316L was produced to have the proper microstructural as-built properties to show twinning behaviour when deformed due to the application of plastic strain. As found by Karthik et al [83], a continuous drop of SHR has been observed to be associated with materials or production processes that do not produce twin bands under deformation, as in the case of wrought 316L that produced significant amount of twin bands past 40% strain. Conversely, metal AM manufacturing processes show a more or less steady SHR versus plastic strain after an initial sudden drop, with small differences due to the process parameters and orientation of the realised parts [83]. The drop is caused by the response of the material before the twin bands formed, after which the work hardening rate kept maintaining the same value throughout the deformation process until the failure of the specimen.

4.2.3 Onset and development of twinning in PBF-LB 316L stainless steel

The interrupted mechanical tests on the tapered geometry, presented in Figure 4.11, provided precious information about the properties of each configuration, for the investigation of the TWIP behaviour of 316L steel produced with PBF-LB.

The first output from the interrupted tests was the hardness of the longitudinal cross-sections, with the overview reported in Figure 4.12. It could be appreciated that each step of the interrupted test displayed a specific range of hardness, from the lowest value in the unstressed area to the highest value of hardness at the location where the largest elongation was reached. The reason that caused such a varied hardness values along the axis of the tapered specimen has to be found in the fact that, a decreasing cross-section of the tensile specimen under deformation, gradually reduced the surface area of the material that could oppose to the external load. The decrease of material rose the local stress on the specific cross-section. Therefore, along the axis of the tapered specimens, the deformation took place leaving a gradual strain value towards the tip. As a result, the TWIP behaviour occurred in each section differently, and caused dissimilar concentrations of twin bands, incrementing towards the necking region. It was believed that higher amount of twin bands was causing higher hardness because of the hindering of the movement of dislocations that caused local increase of strength, as outlined by Agrawal et al [215]. Overall, the interested area affected by the increase of hardness for the specimen brought to failure resulted into 10.7 mm length along the axis. As the hardness around the tip resulted extremely high, approaching 400HV, it can be demonstrated that strain hardening behaviour was occurring during the deformation due to the plastic strain applied to the specimen.

The role of plastic strain acting on the microstructure could be appreciated with BSE imaging and IPFs from EBSD, Figure 4.13(a-e) and Figure 4.13(f-j) respectively. As plastic strain is provided to an austenitic stainless steel, such as PBF-LB 316L, other phenomena than deformation glide take place as opposed to standard materials. As for BSE imaging, the initial strain at 9% was such that a clear microstructure could still be seen, Figure 4.13(a). Contrariwise, at increasing deformation the amount of twin bands rose and at the failure strain, Figure 4.13(e), no microstructure could be further noticed, but only bright twin bands permeated the microstructure. Those results are in accordance with previous research by Wang et al and Gao et al [84,91], where similar behaviour was detected by interrupted tests. The only difference that can be detected, in both tensile and compression behaviour, is the percentage of strain at which the twin bands were detected. This can be explained by dissimilar cooling rates in the specific printing process parameters with PBF-LB, that results in divergent grains size, shape (columnar or equiaxed) and residual stress. In the work by Wang et al [84], a low amount of twin bands was already found at tensile strain of 3%, that could be activated at such a low strain value, and a higher number was then extracted at 12% strain during the tensile test. The study performed by Gao et al, instead, showed that a compressive strain of 2.7% did not contribute to a change of microstructure for the tested specimen, including the absence of twin bands. The micrographs changed, instead, at 7.7% strain, where grains started to become less clear and brighter spots spread over the analysed section, similarly to what

occurred in this study in Figure 4.13(b). In the cited literature, these outcomes were explained as plastic strain, that caused the activation of TWIP behaviour. The latter is confirmed to be responsible for the formation of twin bands. Moreover, the difficulty in detection of the grains is related to specific misorientation in the microstructure driven by the deformation.

EBSD mapping performed at the same distance along the axis confirmed the presence of deformation twinning and revealed more information about the twin bands forming at increasing strain values. At low strain, twinning is activated only in a subset of grain orientations, in which it is possible to reach the critical shear stress needed to move partial dislocations. For example, it is seen in Figure 4.13(f) that grains with the [111] direction parallel to the BD were the first to activate twinning. It is thought that these grains do not re-orient during tensile loading, and therefore the accumulated strain contributes to reaching the critical shear stress necessary for twin activation. Specifically, the grains already had that orientation, or the external load was able to stretch the specimen and re-orient some of the grains. Afterwards, once the [111] orientation was reached, due to the related low SFE of the twin bands, twinning was activated. When the strain increased, more grains showed twinning activity, as illustrated with arrows in Figure 4.13(g). As described by Güden et al [216], the origin of twins in these grains might be due to a lattice rotation that aligns the [111] crystal orientation to the loading axis, as the tensile load is increased. Below around 15% strain, it is believed that grains with orientations other than [111] mainly experienced dislocation slip, as they possessed slip systems favourably oriented to the stress state. Finally, as the plastic strain reached the highest levels, up to ~60% (Figure 4.13(h-j)), the critical shear stress was reached in almost all the grains and peak twin concentration was achieved, as previously identified by Sun et al [217].

The SEM results on the etched specimen are shown in Figure 4.14. A consideration can be made for the as-fabricated microstructure in Figure 4.14(a). Firstly, a dendritic microstructure was found in the analysed material in all micrographs. Secondly, the dendrites assumed a random orientation within each melt pool. These characteristics are typical of a fully austenitic stainless steel as 316L, printed with PBF-LB, and were previously found in the literature [87,135,218]. The presence of random dendrites is attributed to the rapid cooling rate of the PBF-LB that does not provide sufficient time for the grains to be formed with a specific orientation of the dendrites. Considering increasing strain, from Figure 4.14(a) to (e) and Figure 4.14(f) to (j), both dendrites and melt pools were stretched. This is a natural consequence of the deformation occurring during the tensile test. However, as it can be seen, at the area where the failure occurred, Figure 4.14(j), the melt pools resulted less distinct than the micrographs at lower strain, Figure 4.14(f-i). The stretch of a melt pool was found to be as high as 70% in other studies, such as Güden et al [216].

As described in Section 4.1.7, the Schmid factor maps were obtained for two plastic strains, namely ~ 15%, Figure 4.15(a), and ~ 26%, Figure 4.15(b). The factor gives a deeper understanding of the shear stress of the material and in what configurations the latter is resolved to specify the deformation behaviour of the stretched 316L steel. First of all, a consideration on the spot at ~ 15% can be made. As observed by Bean et al [219],

grains with a low Schmid factor (up to 0.4) presented deformation twins. However, this was true only for grains with [111] parallel to the BD. In this work, smaller grains (indicated by red arrows in Figure 4.15(a)) and the same low Schmid factor showed no noticeable twinning. It was demonstrated that the stress at which local yielding occurs increases with decreasing grain size [220]. This means that, in the smallest grains, deformation slip acted instead of twinning. To confirm this experimentally, KAM maps with overlap of the twin boundaries were obtained in this work. The KAM maps are shown in Figure 4.15(c) and Figure 4.15(d) for the 15% plastic strain value. Figure 4.15(c) represents a large grain, with [111] orientation, where many twins formed in areas with low KAM values and lower geometrically necessary dislocation distribution. The average KAM in that area was lower than that determined in a smaller grain, with same orientation, displayed in Figure 4.15(d). In the smaller grain, deformation slip was the predominant deformation mechanism, as confirmed by the presence of only one twin and many GNDs within the grain. The map also revealed that, if the average KAM value is high in specific grains, the presence of defects is important and prevents the formations of the twin bands. The Schmid factor map at ~ 26% plastic strain, given in Figure 4.15(b), shows that the average Schmid factor increased from the ~ 15% plastic strain state, and produced a far greater quantity of twins. Figure 4.15(b) confirms that, as the strain increased, the next favourable orientations for deformation twinning were [101] followed by [001]. The plastic strain managed to resolve the critical shear stress at different orientations of the grains, causing twinning to take over on the specimen at that strain value. This is consistent with the observation from Pham et al [12], that the [001] grains are the last to form twins because these grains are preferably oriented for dislocation slips. Moreover, as in Figure 4.15(a), Figure 4.15(b) reveals that small grains with [111] orientation did not form twins, thus confirming the importance of grain size in the activation of twinning. Those grains, in fact, offered the same higher concentration of defects as the ones at 15% strain, Figure 4.15(a).

In Figure 4.16 a recap of the trend for the physical properties extrapolated in this work can be appreciated. All figures show a trend that corresponds to an increase from the unstressed areas, located at the larger cross-section of the tapered tensile geometry, up to the necking region. Noticeably, the evolution of the quantities along the axis of the specimen seemed to be interconnected. In particular, the twin concentration was not substantially present until a distance from the specimen necking corresponding to 5.6 mm. From that point, the twin concentration changed with a sudden increase, to a maximum value at the failure of the specimen. Likewise, the true stress developed with a low slope until the 5.6 mm distance to the fracture point, to then sudden rise and finally reach a steady plateau value. As for the hardness, instead, a rather steady growth was experienced along the entire gauge length, meaning that another deformation mechanism other than the TWIP was occurring to provide the computed increment of hardness up to 380 HV.

A better understanding of the evolution of the physical quantities along the tapered specimen derives from Figure 4.17, where hardness and twin concentration are represented with respect to the local plastic strain from the computational model. It can be noticed that, below 15% plastic strain, the twin concentration is quite stable and not exceeding 1.9%. In this strain region, twins are believed to occur only within grains where the [111]

direction is favourably oriented with the loading direction, meaning the Schmid factor is sufficiently low to produce local twinning [221]. This was previously reported when describing the results shown in Figure 4.15. The subsequent trend was a significant increase between 15% and 26% strain, and then the additional rise up to 28%. Such a behaviour, a region at low strain with low twin concentration, replaced by a sudden increment in the twin band amount, that finally reached a plateau, has been previously found in the literature. Gao et al [91] conducted tests in compression on PBF-LB 316L steel, obtaining an analogous outcome. Mentioning the results presented for the localised true stress in Section 4.1.8, between 15% and 26% strain values, the FEA model reported an increase from 544 MPa to 694 MPa. These results are in good agreement with the conclusion from the investigation performed by Güden et al on additively manufactured 316L, tested under tensile loading [216]. As a consequence, it can be inferred that, in this work, the strain hardening took place on the tapered specimen after the yield point. Up to that condition, slip motion was found to be the responsible mechanism. This follows previous studies where, between the yield point and the critical shear stress that defines the onset of twinning, the dominant deformation mechanism is dislocation slip [84,88,91]. Therefore, the main finding of this study is that twinning-induced plasticity acted as the prevailing deformation mechanism only past a specific strain value that acted as a threshold. This result follows the theoretical concept of twinning activation in strain hardening materials that was theorised by Christian et al [88].

4.3 Summary

In this Chapter, the aim was to understand the twinning-induced plasticity of 316L stainless steel produced by PBF-LB process, how it develops over the application of plastic strain. First of all, standard specimens were investigated to extract the as-fabricated conditions of the material processed with this metal AM technique. Second, experiments on a tapered specimen were carried out to provide observations of the microstructural evolution of 316L and evolution of hardness, stress and plastic strain along the loading axis. The main findings of this study are:

(1) Standard specimens were printed with a fully austenitic 316L stainless steel with PBF-LB. A process parameter with a density higher than 99.9% was found. The specimens did not show presence of twin bands, thus meaning lack of residual stress.

(2) The as-fabricated material presented a preferential orientation of the grains following the PBF-LB cooling rate, and a dendritic microstructure with random orientation.

(3) The standard specimens provided good levels of stress (UTS of 585 MPa and σ_Y of 485 MPa), extended ductility (55%) and a steady work hardening rate that is symptom of TWIP in the material.

(4) A tapered geometry was designed and chosen with the help of finite element analysis. The FEA model predicted a range of physical properties along the axis of the specimen.

(5) Twin concentration was quantified from the tapered specimen, as a function of the plastic strain. The strain levels obtained ranged between 0% and 60%.

(6) Dislocation movement was the principal deformation mechanism of 316L stainless steel printed with PBF-LB, for plastic strain levels lower than 15%. Above the threshold, a combination of slip motion and twinning occurred. Twinning happened firstly in grains with the [111] orientation preferentially aligned with the BD. At a later stage, a progressive activation of twins took place in grains oriented otherwise. Specifically, [101] orientation higher than 26% strain, while [001] was the last orientation to show twinning.

(7) Grain size is another factor that regulated the onset of twinning. Even among the grains having the preferential [111] orientation, the smallest ones developed low twins concentration.

(8) Finally, hardness increased as a function of strain. A larger increase took place until 15% plastic strain. Afterwards, a less pronounced increase rate can be noticed once twinning was activated.

5 Microstructure and crystallographic phases sensitivity to process parameters in a bespoke PBF-LB 17-4 PH alloy

17-4 PH is a martensitic stainless steel, that shows better mechanical properties in terms of strength and ductility with respect to its conventionally manufactured counterpart, when produced with PBF-LB. The reasons are to be found in the strain hardening behaviour of the material, called transformation-induced plasticity, that happens in the plastic regime. The difference relies on the dissimilar initial phase content, characterised by higher retained austenite for PBF-LB, that transforms into martensite. To date heat treatments, typical after production of a component, have hindered the opportunity to monitor the microstructure evolution derived from different PBF-LB process parameters, and therefore control the mechanical properties.

The present Chapter focuses on how different linear energy densities affect the TRIP activity of as-printed PBF-LB 17-4 PH alloy. Firstly, process parameter sets, fully dense, are extracted from the process map. The as-printed conditions are studied to infer differences in the mechanical properties. Cubes and standard round and flat specimens are adopted for this section. The results demonstrated divergent starting points.

These parameter sets, characterised by dissimilar linear energy density, are then used to explain the following analysis on TRIP activity. For the study, flat specimens are utilised, with uniform cross-section. An in-situ XRD analysis during mechanical tensile testing is performed for the purpose, for a synergistic investigation of the phases' evolution, FCC and BCC, over plastic strain. The resulting stress strain curves and XRD patterns over strain are extrapolated and post-processed through a MATLAB code to quantify the amount of FCC transforming into BCC for each process parameter set and predict the evolution of the phases to the stress and strain acting. EBSD analysis is conducted on the microstructure and texture of the different process parameters, in the as-printed and tested condition, to point out the effect of linear energy density on the TRIP activity.

5.1 Results

5.1.1 Process window and processability region of as-fabricated 17-4 PH stainless steel

Firstly, the process map of the material was investigated by keeping all process parameter fixed but P and v (in terms of E_T), as described in Table 3.5. The results were then represented in Figure 5.1. The preparation and analysis followed what described in Section 3.8 and 3.13. The processability region is defined by green dots, having a density higher than or equal to 99.4%. In the area with low *LED*, yellow dots are present, defined

by low density. Specifically, the density ranged from a minimum of 87% up to the highest value of 95.8%. The lowest row of the process map, characterised by a *v* of 0.1 m/s, was defined by high *LED* and density varying from 97.7 to 99%. They are represented as red dots.

Figure 5.2 shows the micrographs from the previous investigation. The processability region is the central area, which is characterised by small gas pores or isolated bigger pores, and only three process parameters (0.42 m/s *v* and 180/200 W *P*, and 0.27 m/s *v* and 200 W *P*) have a small cluster of large defects. The top row and left column (but the lowest micrograph) represent the LOF defects. The most affected process parameter has a *v* of 0.55 m/s a *P* of 100 W, for a density of 87%. The keyhole mode that characterised the lowest *v* and a *P* ranging from 120 W to 200 W, provided gas pores as well as large and rounded pores, typical of the printing mode [222]. The porosity increased with the *P*, up to 2.3% with 200 W. A set of four process parameters was picked from the process window, to choose two sets that could provide the most different microstructure for the remainder of the investigation. They are circled in green in Figure 5.2. The process window considers a range of values that was previously investigated and applied to the present non-standard alloy, whose composition is shown in Table 3.4. In particular, process parameters with similar high *P* and low *v* values, providing high energy density, led to an almost fully martensitic composition with low FCC content [223]. Conversely, using comparable low *P* and high *v* values, for a lower energy density, proved to retain an increased quantity of retained FCC [224].

The selected process parameter sets had the following densities. Set 1: 99.90 ± 0.08 %; Set 2: 99.90 ± 0.06 %; Set 3: 99.80 ± 0.16 %; Set 4: 99.70 ± 0.19 %.

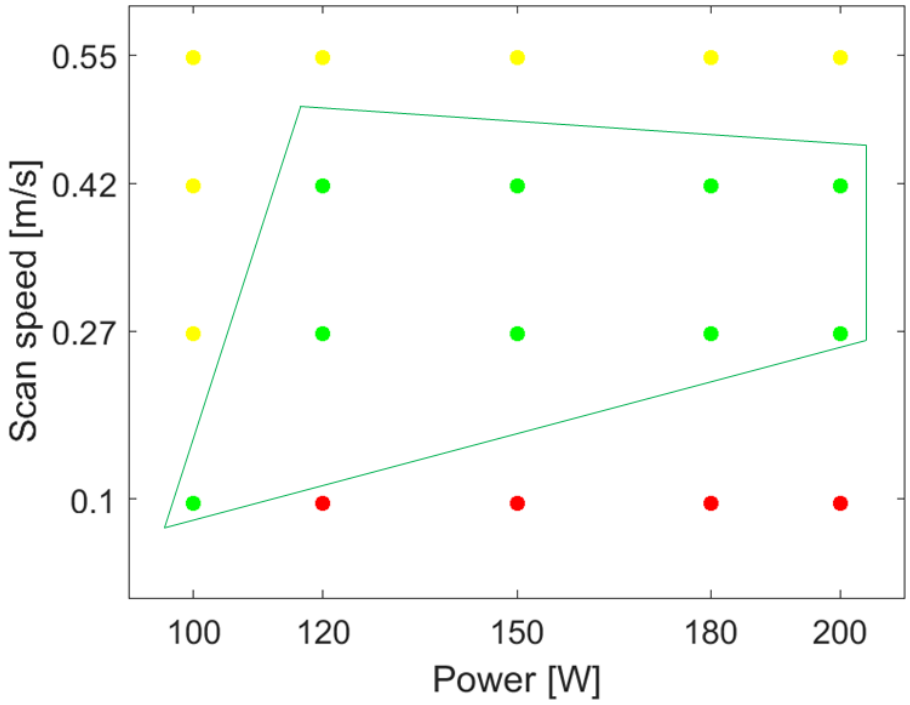

Figure 5.1. Graph reporting the analysis of the process map, with *v* as a function of *P*, carried out for the PBF-LB 17-4 PH stainless steel. The processability region is displayed by the green dots, where the material had a density of at least 99.8%. The yellow dots at high *v* or lowest *P* represent the LOF region, whereas the red dots are characterised by keyhole mode.

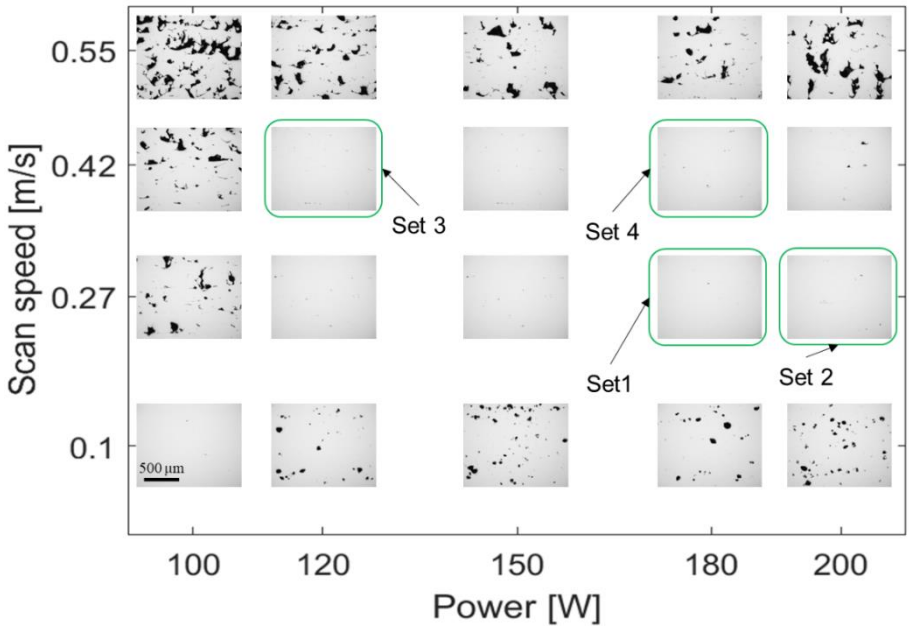

Figure 5.2. Optical micrographs of cubes used for the density check, obtained by cutting vertically (along the BD) the samples. The micrographs represent the same combination of v and *P*, as shown in Figure 5.1. The circled and labelled micrographs represent the process parameters chosen for the next investigation.

5.1.2 Hardness and phase characterisation of as-printed configurations

The four process parameter sets were tested with regards to their hardness. A different value of hardness would imply dissimilarity in the content of BCC and FCC, other than the content of residual stress on each sample, as presented by Hsiao et al [41]. The hardness maps are displayed in Figure 5.3. Different average values were extracted. They are the following: Set 1, 425 ± 10 HV; Set 2, 400 ± 10 HV; Set 3, 360 ± 10 HV; Set 4, 380 ± 10 HV. The two sets that showed the largest difference, Set 1 and Set 3, were selected for the following analyses and were labelled *high-LED* and *low-LED* respectively, as *high-LED* was defined by having a higher *LED* than *low-LED*.

Each of the two process parameter sets was characterised in terms of chemical composition. As *high-LED* is defined by a higher *LED* for the manufacturing process, the possibility of element volatility needed to be considered [225]. Table 3.4 presents the weight percentage of the elements by means of ICP, as provided by the powder supplier. In this investigation EDX was used, therefore it was necessary to determine how accurate the EDX characterisation technique was as compared to ICP or XRF. The results are displayed in Table 5.1, where a comparison between ICP, XRF and EDX are presented in *wt%*. Neither XRF nor EDX could detect presence of C, P, N, O, S. XRF was able to detect only a small number of elements, that is Fe, Cr, Cu, Ni, Nb. EDX could additionally identify Mn, Si and Mo. Overall, given the same number of elements that could be detected, and the similar values of ratio to Fe, as with ICP, the level of accuracy of EDX for the 17-4 PH powder resulted good enough to adopt this technique.

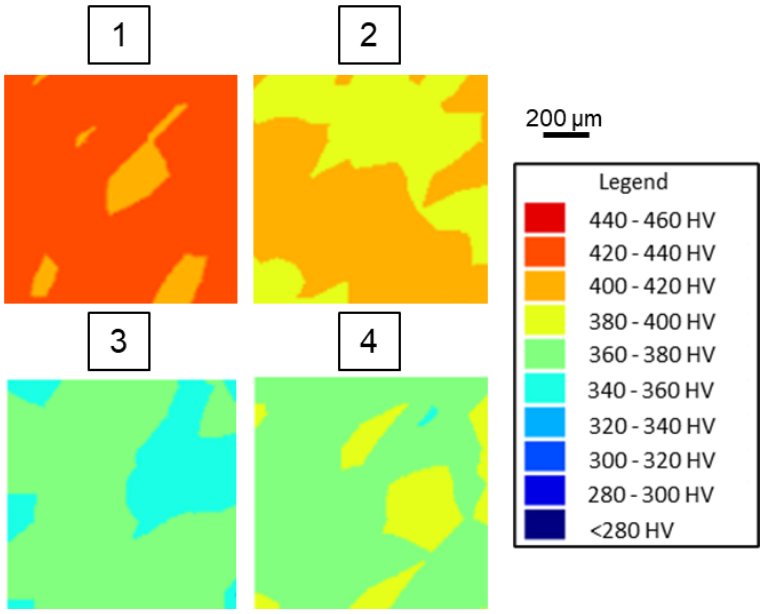

Figure 5.3. Hardness map of the four process parameter sets selected for the PBF-LB 17-4 PH after the process window analysis.

Table 5.2 shows the chemical composition of *high-LED* and *low-LED* as collected by EDX on the PBF-LB as-built samples. *Low-LED* was found to have a chemical composition with a weight percentage, for each element, equal or close to what is reported in Table 5.1 for the alloy powder. *High-LED*, conversely, presented lower content of some elements compared to the corresponding EDX on the powder. The affected elements are Cu, Nb, Mn and Mo. The most noticeable difference in concentration occurred for Cu and Mn, the former reducing by 15.9% and the latter by 27.2% with respect to the *wt%* element detection on the powder from Table 5.1.

Table 5.1. Chemical composition (*wt%*) of the PBF-LB powder for 17-4 PH stainless steel. From left to right, the values reported by the powder supplier with ICP, the values reported by Sheffield Assay Office with XRF, the values obtained with EDX at University of Nottingham facilities. The analysed area is 260 x 200 μm^2, and the reported error is the standard deviation.

ICP			**XRF**			**EDX**			
Element	***wt%***	**Ratio to Fe [%]**	**Element**	***wt%***	**Ratio to Fe [%]**	**Element**	***wt%***	**StDev**	**Ratio to Fe [%]**
Fe	75.506	100	Fe	76.7	100	Fe	74.79	0.06	100
Cr	13.6	18.01	Cr	13.9	18.4	Cr	14.31	0.03	19.1
Cu	5.3	7.02	Cu	5.5	7.3	Cu	5.18	0.04	6.9
Ni	3.99	5.28	Ni	3.4	4.5	Ni	3.9	0.03	5.2
Nb	0.48	0.64	Nb	0.5	0.7	Nb	0.62	0.03	0.8
Mn	0.3	0.40	Mn	0	0	Mn	0.38	0.02	0.5
Si	0.69	0.91	Si	0	0	Si	0.75	0.01	1.0
Mo	0.05	0.07	Mo	0	0	Mo	0.08	0.03	0.1

Table 5.2. Chemical composition (in *wt%*) of the PBF-LB 17-4 PH with *high-LED* (left) and *low-LED* (right). The results are provided by EDX analysis. The analysed area is 260 x 200 μm^2, and the reported error is the standard deviation.

EDX *high-LED*					**EDX *low-LED***				
Element	***wt%***	**StDev**	**Ratio to Fe [%]**	**Ratio to EDX powder [%]**	**Element**	***wt%***	**StDev**	**Ratio to Fe [%]**	**Ratio to EDX powder [%]**
Fe	75.74	0.06	100	100	Fe	74.77	0.06	100	100
Cr	14.16	0.03	18.70	97.71	Cr	14.31	0.03	19.14	100.03
Cu	4.41	0.04	5.82	84.07	Cu	5.17	0.04	6.92	99.83
Ni	4.04	0.03	5.33	102.29	Ni	3.92	0.03	5.24	100.54
Nb	0.59	0.03	0.78	93.97	Nb	0.63	0.03	0.84	101.64
Mn	0.28	0.02	0.37	72.76	Mn	0.38	0.02	0.51	100.03
Si	0.77	0.01	1.02	101.38	Si	0.75	0.01	1.00	100.03
Mo	0.02	0.03	0.03	24.69	Mo	0.08	0.03	0.11	100.03

The samples, printed with *high-LED* and *low-LED*, were then prepared for chemical etching. An analysis of the melt pool can provide information about the formation of the grains and phases, since two different process parameter sets can bring divergence as shown by Moyle et al [226]. Figure 5.4 displays the two resulting microstructures. Figure 5.4(a) is the micrograph for *high-LED*. It presents three main areas, along the vertical direction, parallel to the BD. The top and bottom regions are defined by several melt pools stacked one on top of the other, with a small layer thickness. The middle area, conversely, contains more isolated melt pools. A parameter helpful to describe the effect of higher LED on the melt pools is the minimum width, calculated on melt pools scanned with a laser orientation perpendicular to the section displayed in Figure 5.4. The minimum value was determined as 134 μm, Figure 5.4(a), for *high-LED*. The melt pools for *low-LED* are in Figure 5.4(b), the red arrow indicating the melt pool with the minimum width of 97 μm.

A qualitative phase content characterisation is depicted in Figure 5.5 and Figure 5.6, obtained from the flat sample presented in Section 3.7 (where the sample preparation is also presented along) at the beginning of the *in situ* XRD analysis performed in transmission mode. Figure 5.5 presents the XRD pattern for the *high-LED*, with intensity of the peaks as a function of the *d-spacing* of the material's crystals (accuracy of ± 0.1). A total of 11 peaks were detected, of which 6 for the BCC phase and 5 for the FCC phase. The overall intensity of the

family of planes for the BCC phase resulted higher than the FCC. In addition, the FCC(111) is present as a shoulder on the peak from BCC(110). In Figure 5.6 is the XRD pattern for *low-LED*, with the same peaks for the two phases. However, the ratio of the intensity of the FCC to BCC peaks resulted higher than *high-LED*, suggesting a different content of the crystal phases for the two process parameter sets.

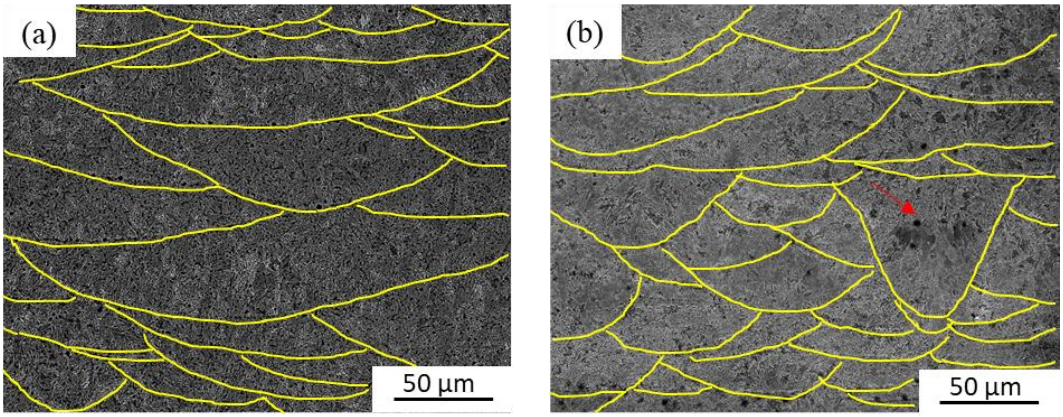

Figure 5.4. Micrographs of the etched surfaces for (a) *high-LED* and (b) *low-LED* obtained from the process window of PBF-LB 17-4 PH. The red arrow points at a deep melt pool with minimum width, obtained with the *low-LED*.

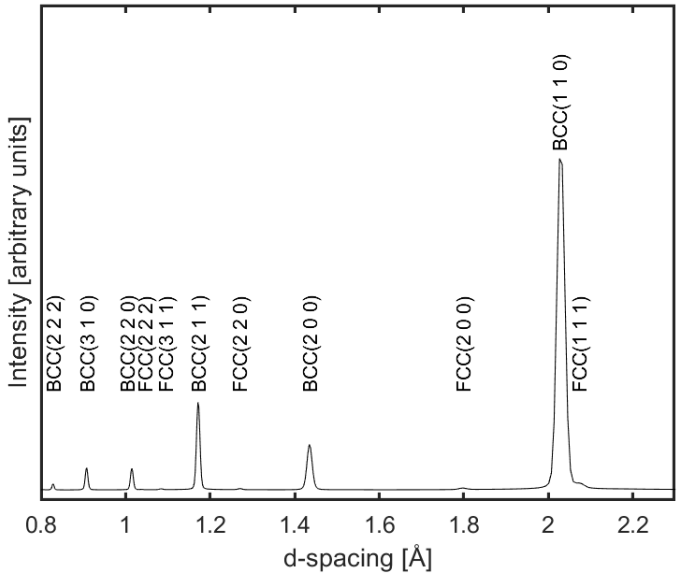

Figure 5.5. XRD pattern condition versus *d-spacing*, in the as-built condition for the *high-LED* sample printed with 17-4 PH steel.

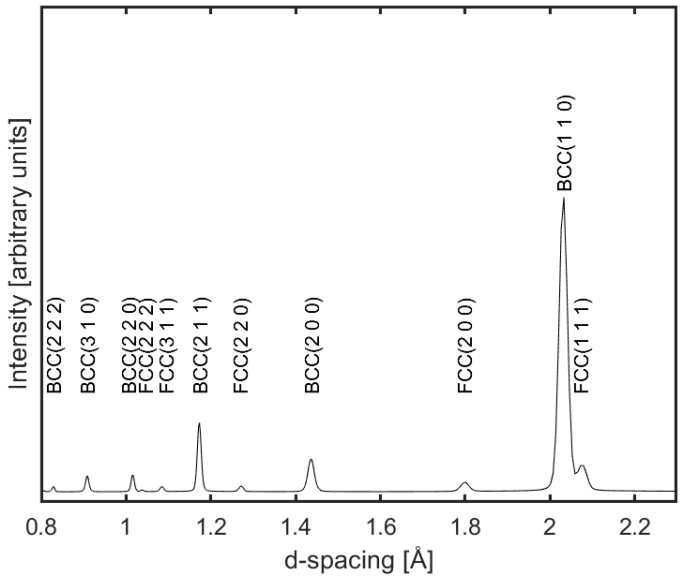

Figure 5.6. XRD pattern condition versus *d-spacing*, in the as-built condition for the *low-LED* sample printed with 17-4 PH steel.

5.1.3 Microstructure and texture of printed specimens

The undeformed microstructure was investigated for *high-LED* and *low-LED*, for a comparison. A microstructural analysis was carried out by means of EBSD maps. In Figure 5.7 are the IPFs considered with respect to direction Z_0 parallel to BD. Figure 5.7(a) provides the results on the grains from *high-LED*, which resulted to have a minor preferential orientation of [111] parallel to the BD. The dimension of the grains ranged from small to large scale, creating a bimodal microstructure. A layer with very fine grains (top, centre and bottom zone obtained by separating the map with dashed lines) was characterised by equiaxed grains within columnar grains. This layer alternated with a region where mostly elongated grains were present along the BD (second and fourth zone in the map), and there was only a small number of grains that showed an equiaxed compared to a columnar shape. Figure 5.7(c) depicts the grain size distribution for *high-LED*, where a prevalence of small grains up to 15 μm in equivalent circle diameter were present; however, coarser grains with an equivalent circle diameter up to 33μm defined the process parameter set as well. The IPF for *low-LED* is shown in Figure 5.7(b). A microstructure made of fine grains was predominant. The grains were randomly oriented and did not provide any preferential orientation. In Figure 5.7(c) is the grain size distribution for this process parameter set, with grains that presented a less wide range of the equivalent circle diameter, with dimensions between 0.7 μm and 17 μm. Specifically, most of the grains could be detected in the range of equivalent circle diameter up to 6 μm. Columnar grains were revealed, which mainly showed an orientation of [111] parallel to the BD.

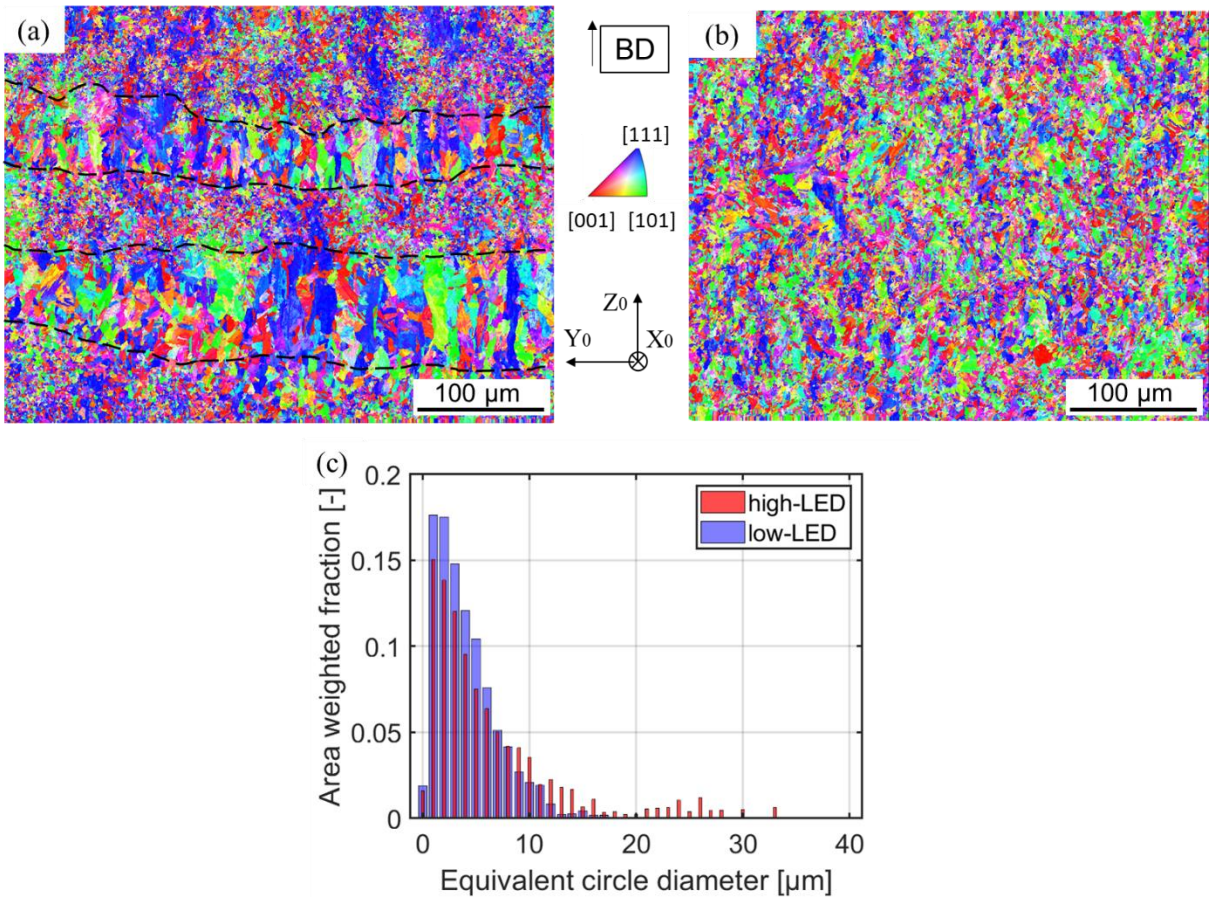

Figure 5.7. Detail of the microstructure for the as-built condition of 17-4 PH. Z_0-IPF colour map for (a) *high-LED*, where a bimodal microstructure is revealed and (b) *low-LED*; (c) grain size distribution for the as-built condition for *high-LED* and *low-LED* described by a plot where the area weighted fraction is represented versus equivalent circled diameter.

The texture for *high-LED*, Figure 5.8(a), and *low-LED*, Figure 5.8(b), can be observed for the as-built and undeformed configuration. As for *high-LED*, it can be noted that the process parameter set contributed to the formation of two different fibre textures. The first texture is a <111> // Z_0 fibre texture where a spot at high intensity of {111} density can be located near Z_0 (where Z_0 is defined as the build direction of the specimen); moreover, the ring of {111} density is characterised by a radius of approximately 70º, which is in agreement with the angle between (111) and $(1\bar{1}1)$, $(11\bar{1})$ and $(\bar{1}11)$ which is 70.53º for a cubic structure. There is consistency for the ring of {101} density around Z_0 with the <111> // Z_0 fibre texture, due to the angle between (111) and (110), (101) and (011) that is 35.26º. The third consideration is the ring of {001} density, which has a radius of ~ 55º and is a confirm of the mentioned texture as the angle between (111) and (100), (010) and (001) is 54.74º. In the pole figure, a spot of {001} density near Z_0 is a sign that *high-LED* caused some <100> // Z_0 fibre texture as well. The explanation to this is that there is lower intensity of the latter spot compared to the one corresponding to the <111> // Z_0 fibre texture, respectively 2.3 mud and 1.5 mud. Figure 5.8(b) represents the texture for *low-LED*. It can be seen as similar to the texture from *high-LED*, as both <100> // Z_0 and <111> // Z_0 fibre textures are present. There is, however, a deviation for what concerns the intensity of the

spots of {001} and {111} density near Z_0, that are less intense than the values obtained for *high-LED* and are similar between each other, 1.4 and 1.5 mud respectively. The weaker texture for *low-LED* is confirmed by the lower intensity of the rings of {001}, {101} and {111} density, which provided an increased randomness for the crystallites orientation in the PBF-LB 17-4 PH.

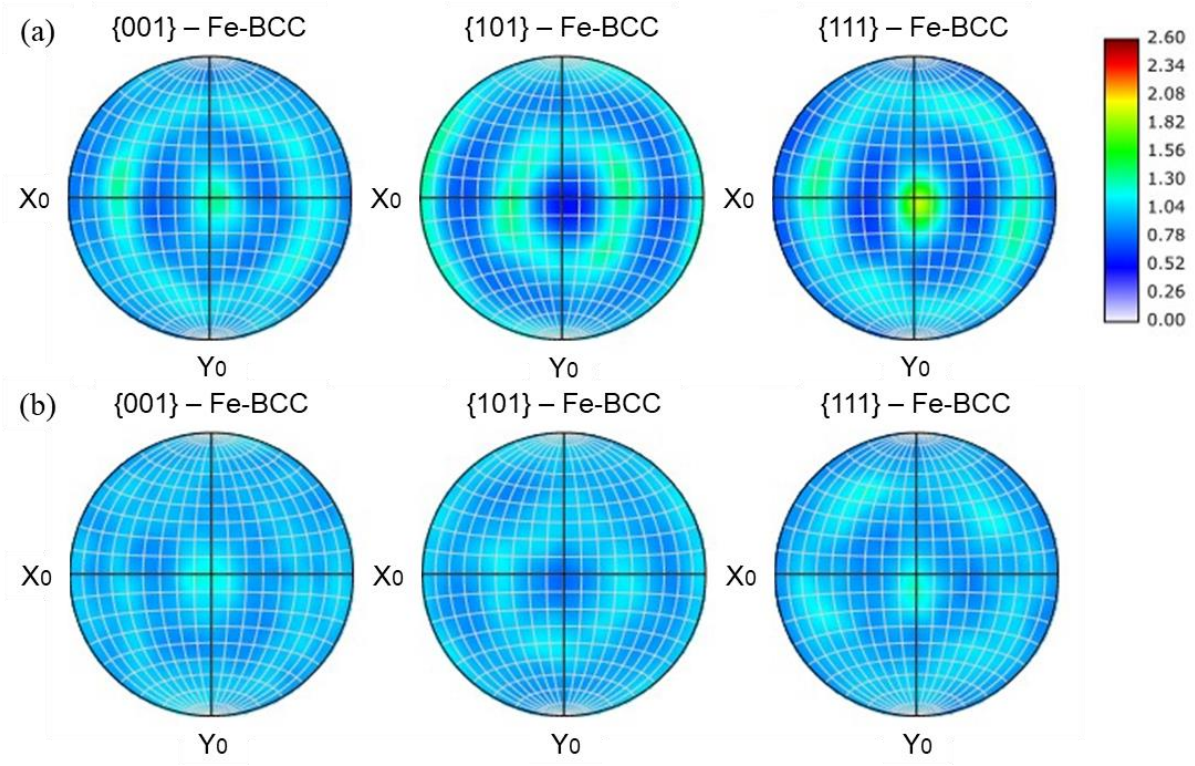

Figure 5.8. Texture of the as-built 17-4 PH printed with PBF-LB. Contour pole figures for (a) *high-LED* and (b) *low-LED*. The Z_0 direction is parallel to the BD.

5.1.4 In-situ x-ray diffraction analysis during mechanical testing for TRIP investigation

Mechanical tensile testing was carried out on the standard flat specimens printed with *high-LED* and *low-LED*, and the determined stress-strain curves are reported in Figure 5.9, with the average tensile properties presented in Table 5.3. The two process parameter sets were identified with almost identical *E*. A discrepancy of only 1 GPa was calculated, thus suggesting that two *LED*s did not affect the initial elastic behaviour of 17-4 PH. On the other hand, the mechanical curves in correspondence of the plastic regime and after the yield point showed completely divergent properties between the two *LED*s applied. The results are defined by respective average σ_Y of 1095 MPa and 607 MPa for *high-LED* and *low-LED*. *High-LED* reached the smaller average UTS at 1230 MPa, compared to 1279 MPa for *low-LED*. *High-LED* extended to a higher strain before failing, ε_f being of 20% higher than what obtained by *low-LED*.

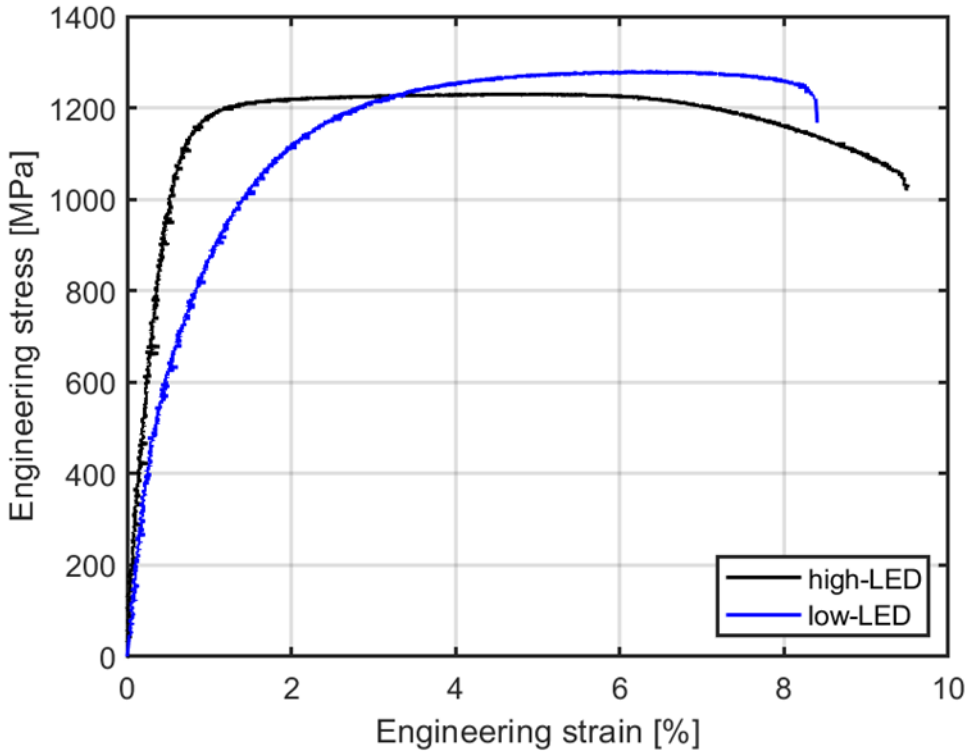

Figure 5.9. Plot of the engineering stress-strain curves for the specimens produced with PBF-LB, where the two sets are *high-LED* and *low-LED*, during the in-situ investigation at Diamond Light Source. The zoom-in shows the initial segment of the linear elastic response for both *high-LED* and *low-LED*.

Table 5.3. Mechanical properties for the standard flat specimens printed with *high-LED* and *low-LED*. The quoted error considers the accuracy of the testing machine.

Set	***E* [GPa]**	**σ_Y [MPa]**	**UTS [MPa]**	**ε_f [%]**
high-LED	184 ± 1	1095 ± 2	1230 ± 2	9.5 ± 0.2
low-LED	185 ± 1	607 ± 1	1279 ± 2	8.4 ± 0.2

The fracture surfaces of the tested samples are shown in Figure 5.10. *High-LED*, Figure 5.10(a), shows a cup and cone feature. In particular, the sides are generally more elongated with an orientation of 45º to the load direction (the direction of maximum shear stress), as displayed by the inset in Figure 5.10(b). The central area is instead characterised by a brittle fracture, as in the inset in Figure 5.10(c), where the fractured surface has an orientation that approximates 0º. Conversely, *low-LED* (Figure 5.10(d)) is distinguished on the entire cross-section by an elongated fracture described only by a shear acting along a plane with a normal oriented 45º to

the load direction as highlighted in Figure 5.10(e). This suggests that the material printed with *low-LED* was more ductile in the undeformed condition before the tensile testing was performed and before the transformation to martensite reached a similar final value at the failure of the specimen. For both sets, it is possible to notice the presence of defects, and in particular microporosities, contributors to the origination of the fracture surface.

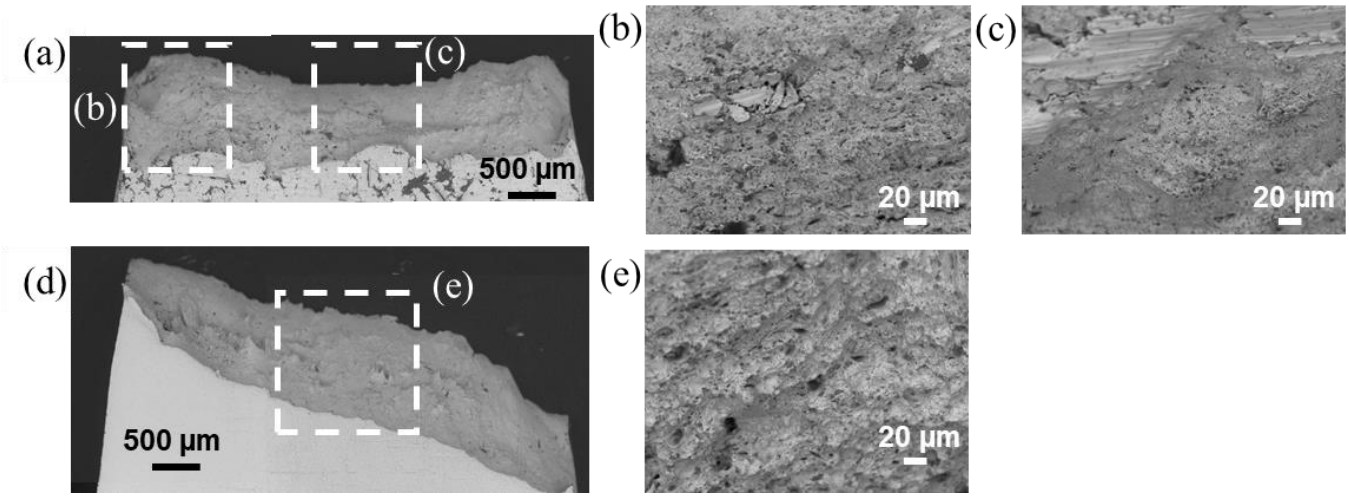

Figure 5.10. The fractured surfaces of the tested specimens. (a) front view of *high-LED*; (b-c) insets of top view for *high-LED*; (d) front view of *low-LED*; (e) inset of top view for *low-LED*.

In-situ x-ray diffraction revealed the XRD patterns that the specimens experienced during the deformation of the samples. The patterns are in Figure 5.11 and Figure 5.12 for *high-LED* and *low-LED*, respectively. The intensity of the counts, originated from the transmission analysis, are depicted versus the *d-spacing* (accuracy of ± 0.1). The patterns that are shown for the two process parameter sets are considered at four specific points of the stress-strain curves. From top to bottom: the beginning of the test, the yield point, the UTS, the final elongation. Figure 5.11 points out that *high-LED* has more pronounced peaks for the BCC phases, with the highest populated family of planes being the BCC(1 1 0). As the strain increased during the tensile testing, the BCC peaks underwent a reduction in intensity count, as well as a shift in *d-spacing* and a broadening of the peaks. The evolution of the FCC phase was distinguished by a constant loss of intensity until the failure point where they cannot be visually detected. In Figure 5.12 is the evolution of *low-LED* at the same strain values. The BCC phase peaks were still more pronounced compared to the FCC peaks. The latter could be easily detected at the beginning of the tensile experiment, and a decrease in the intensity took place over strain. The FCC(2 0 0) peak in Figure 5.12, indicated by a star, points at the evolution of the phase content of *low-LED* with increasing strain. *Low-LED* suffered from a shift of the peaks for both phases along the *d-spacing* axis and a broadening as well.

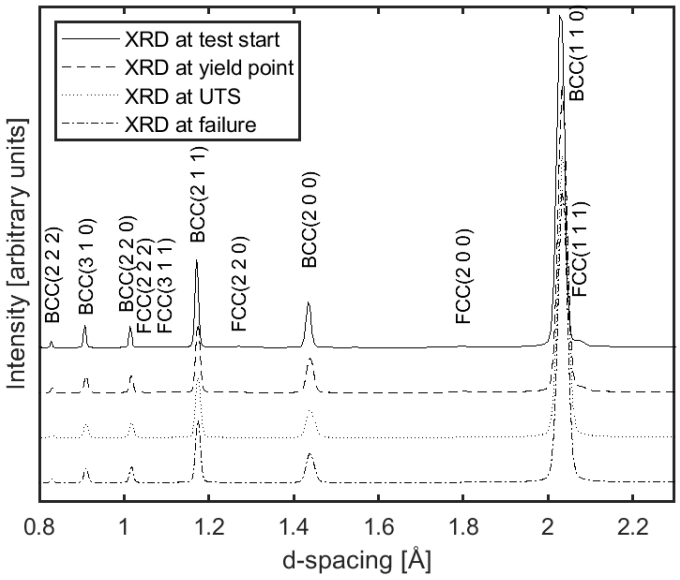

Figure 5.11. Plot depicting the XRD patterns versus *d-spacing* for the *high-LED* sample, at different strain levels. The beginning of the test, the yield point, the UTS and the failure of the specimen are present, and the increasing strain is from top to bottom.

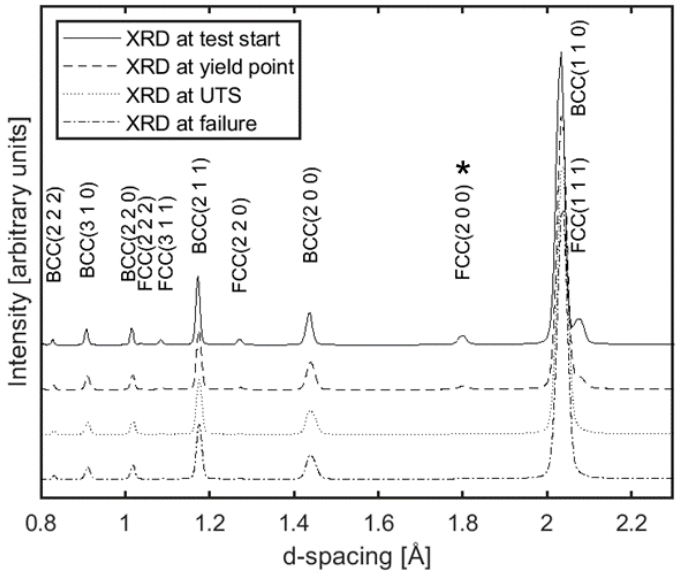

Figure 5.12. Plot depicting the XRD patterns versus *d-spacing* for the *low-LED* sample, at different strain levels. The beginning of the test, the yield point, the UTS and the failure of the specimen are present, and the increasing strain is from top to bottom. The start points out at the FCC(200) peak which experienced a decrease in intensity over strain.

The evolution of BCC and FCC were quantified over strain. The results are presented in Figure 5.13. Specifically, in the figure are the FCC phase *vol%* evolution for both *high-LED* and *low-LED* (accuracy of ± 0.1%). The initial phase content of BCC and FCC for *high-LED* is 96.2% and 3.8%, respectively. A loss to 3.7% for FCC was experienced by the process parameter set with an increase of strain to 0.46%. When the

deformation reached 0.79% strain, the curve of the phase content turned into being steeper and hit 3.2%. The FCC percentage constantly decreased further with strain, to become 2.4% and 2.1%, at 1.82% and 3.67% strain, respectively. The BCC phase content was subjected to a specular change than FCC, with absolute values that increased to the complement of 100% to the corresponding reduction of the FCC phase volume fractions. As the strain increased from 3.67%, no significant reduction of FCC or growth of BCC phases could be detected. Overall, from the beginning of the tensile testing to the failure, the FCC phase VF content reduced by 44.7% at the final elongation. Conversely, BCC phase VF rose by 1.7% from its initial value. The evolution of the phases for *low-LED* underwent a similar trend. The starting values for BCC and FCC VFs were 88.9% and 11.1%, respectively. A loss to 10.4% for FCC occurred at 0.35% strain to the undeformed configuration. 7.5%, 5.5% and 3.5% of FCC content were reached at 0.8%, 1.41% and 2.87% strain. When the specimen was brought to failure, the BCC and FCC VF contents were 97.7% and 2.3%, respectively. A decline of 79.3% took place for what concerns the FCC phase VF in relation to the beginning of the test, whereas the BCC VF experienced an increment of 9.9%.

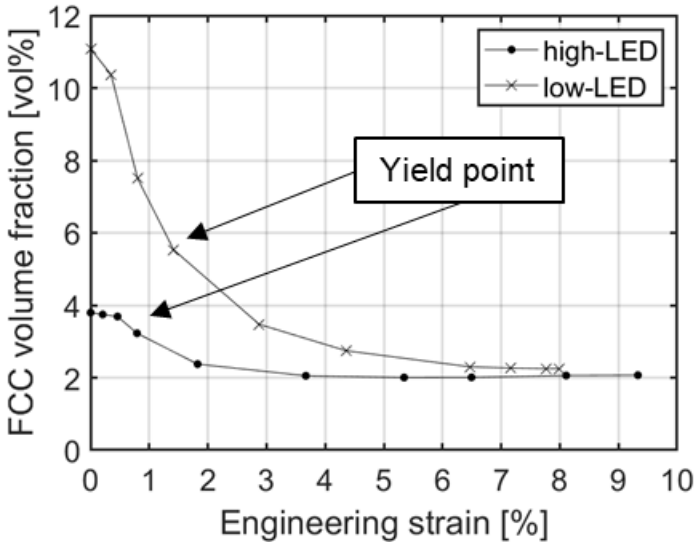

Figure 5.13. Evolution of the FCC phase volume fraction over the induced strain on *high-LED* and *low-LED*. The arrows point at the yield strain.

5.1.5 Microstructure and texture of 17-4 PH affected by TRIP

The deformed specimens were analysed by means of EBSD maps, at the failure tip. The aim was to compare the microstructure at the failure point with the as-built configuration, and comprehend the evolution upon deformation. Figure 5.14 shows the IPFs extracted along Z_0 direction parallel to BD. In Figure 5.14(a) is the microstructure for *high-LED*, where it is possible to see that the grains presented a random orientation in relation to the BD. There are, however, groups of grains which exhibited a preferential orientation. Moreover, the grain size was reduced at the highest values from the undeformed condition, Figure 5.7. Noticeably, for

high-LED the bimodal microstructure could not be distinguished. The grain size was defined by most grains with an equivalent circle diameter up to 12 μm, and the bigger grains did not exceed 22 μm, as depicted in Figure 5.14(c). The orientation of the elongated grains was varied, even if the preponderance of them was the [111] and [001], considered parallel to the BD. In Figure 5.14(b) the IPF for the deformed *low-LED* is revealed. As for the undeformed configuration, the grains in the tested condition displayed a random orientation. There is a good matching between the dimension of the grains in the undeformed and in the deformed condition for *low-LED*. The dimension of the grains ranged from 0.7 μm to 16 μm. The *low-LED* also showed a comparable orientation of the grains as for *high-LED*, with the most elongated grains that assumed a preferred [111] and [001] orientation parallel to the BD and perpendicular to the load direction.

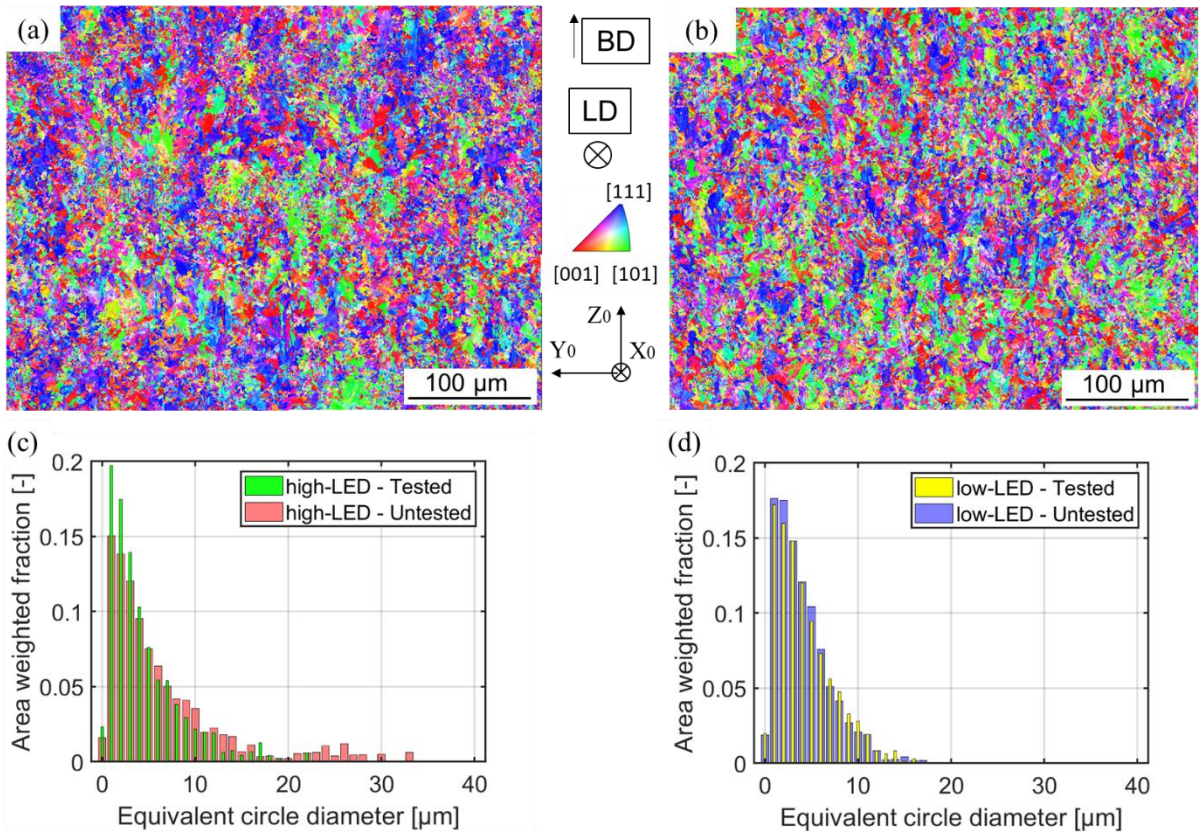

Figure 5.14. Detail of the microstructure for the deformed 17-4 PH, at its failure point. Y-IPF colour map for (a) *high-LED* and (b) *low-LED*. Grain size distribution represented by the area weighted fraction plotted versus the equivalent circled diameter, extrapolated for the untested and tested conditions for (c) *high-LED* and (d) *low-LED*.

Figure 5.15 presents the texture for *high-LED* and *low-LED* at the failure tip. The Z_0 is coincident with the BD of the PBF-LB production process. The texture for *high-LED* is in Figure 5.15 (a). It is possible to notice that the previous two fibre textures, detected for the as-built configuration as shown in Figure 5.8, are still present. However, the spots of {001} density and {111} density near Z_0 have larger intensity corresponding to 2 mud and 2.6 mud, respectively. In addition, the tensile testing modified the irregularity of the rings of {001} density

at around 55º and {111} density at around 70º, by introducing a more fixed orientation to the crystallites. The tensile test induced a further spot of {101} density near X_0, in particular introducing a new <101> // X_0 fibre texture to the tested material, where X_0 is the load direction. The main difference in the texture after the deformation were experienced by the *low-LED*. The results are in Figure 5.15(b). The deformed material with this process parameter set is characterised by a <101> // X_0 fibre texture determined by a high intensity spot of {101} density near X_0; the confirmation derives from the ring of {101} density with a radius of around 60º, other than the ring of {001} density around X_0 with an angle of 45º and the ring of {111} density with a radius of approximately 30º. *Low-LED* almost lost its original as-built texture, that is the rings linked to the <111> // Z_0 and <100> // Z_0 fibre textures, as those rings faded in their respective plots, and in addition are represented as isolated fainted spots.

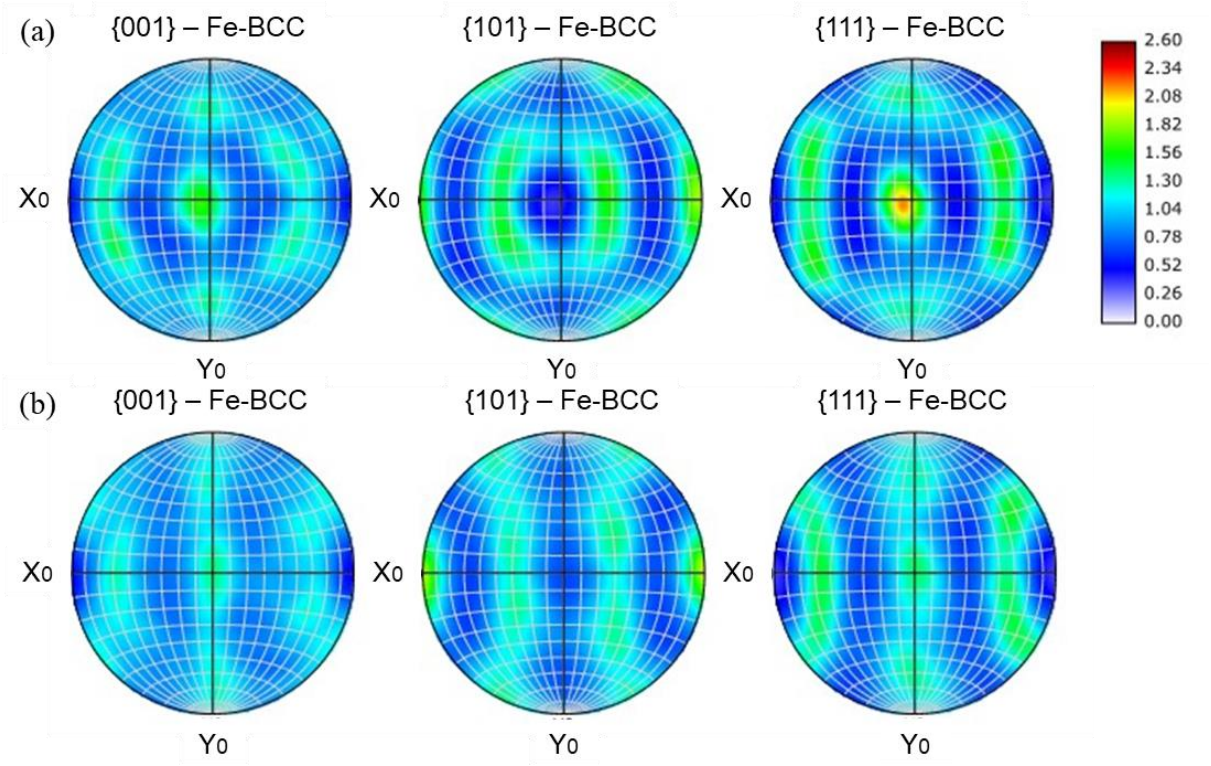

Figure 5.15. Texture of the deformed 17-4 PH printed with PBF-LB. Contour pole figures for (a) *high-LED* and (b) *low-LED*. Z_0 is parallel to the BD, whereas the load direction is parallel to X_0.

In Figure 5.16 are the KAM maps for *high-LED* in the (a) undeformed and (c) deformed condition, and for *low-LED* in the (b) undeformed and (d) deformed condition. *High-LED* presented an average KAM of 1.5° in the undeformed condition, and larger misorientation was found in layers with refined microstructure. Conversely, *low-LED* was defined by a lower average KAM, 1.3°. In the deformed material, the average KAM increased for both *high-LED* and *low-LED*, 1.6° and 2.0° respectively. In the order presented, geometrically necessary dislocations (GNDs) were also calculated and are reported as $1.3 \times 10^{15}\,m^{-2}$, $1.2 \times 10^{15}\,m^{-2}$, 1.5×10^{15}

m^{-2} and 1.8 x 10^{15} m^{-2}, in agreement with the order of magnitude for dislocation density reported for PBF-LB in the literature [99].

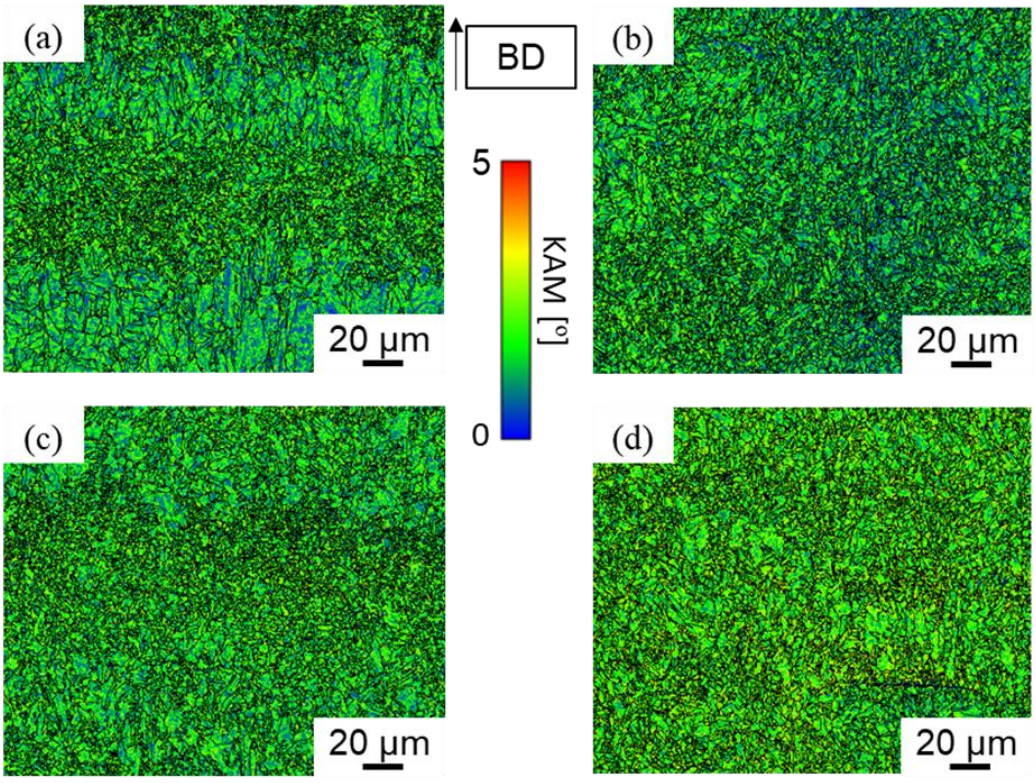

Figure 5.16. KAM maps of *high-LED* in (a) undeformed and (c) deformed conditions; KAM maps of *low-LED* in (b) undeformed and (d) deformed conditions. The maps are extracted from the central IPFs of Figure 5.7 and Figure 5.14.

A visual microstructural characterisation was conducted along the BD direction to distinguish between the two phases referred to as BCC, martensite and ferrite. The results are reported in Figure 5.17. The content of retained austenite did not exceed 11.1% in any of the four different configurations considered in this study (*high-LED* undeformed and tested, *low-LED* undeformed and tested). It was previously found that, with such low amount, the retained austenite is found as fine and dispersed equiaxed grains [227,228]. As for the undeformed conditions of *high-LED* and *low-LED*, the microstructure is mainly represented by a matrix of martensite, as indicated by the laths present in Figure 5.17(a) and Figure 5.17(c), respectively. The microstructure contains a grain of ferrite, as shown by the black arrow for both sets. Figure 5.17(b) and Figure 5.17(d) display a homogeneous martensitic matrix for both *high-LED* and *low-LED* respectively, describing a recrystallised microstructure. If grains of ferrite are still present, they would not be recognisable due to the large deformation occurring on the necking region, as it can be seen in the region highlighted by the black arrow in Figure 5.17(d).

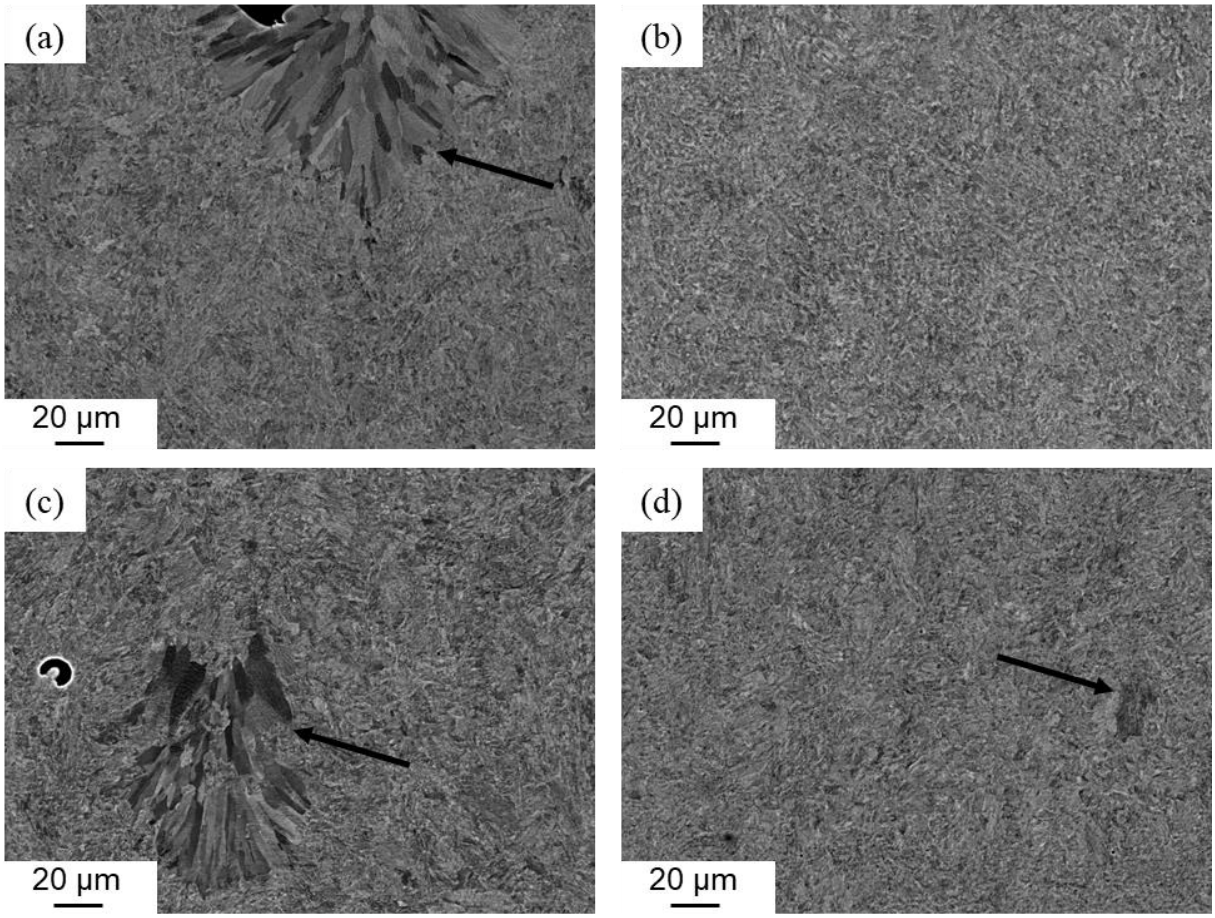

Figure 5.17. Backscattered images of *high-LED* for the (a) undeformed and (b) deformed conditions, and of *low-LED* for the (c) undeformed and (d) deformed conditions. The arrows indicate the presence of ferrite.

5.2 Discussion

This Section examines the most important aspects that derived from the investigation of PBF-LB 17-4 PH for the tailoring of microstructures and mechanical properties through energy density. They are the control of the as-built configurations, the TRIP activity, the microstructures and mechanical properties linked to the TRIP activity, and the effects of thermal strain on the resulting microstructures.

5.2.1 Control of the as-printed PBF-LB 17-4 PH at different linear energy densities

In Sections 5.1.1, 5.1.2 and 5.1.3, the as-fabricated conditions of 17-4 PH stainless steel produced with PBF-LB were determined to accomplish a control over the process parameters.

In Figure 5.2 are the micrographs of the process map for the as-printed samples. Following the work performed in Chapter 4, it is necessary to operate in the processability region. Control of the response of a material under deformation is only possible if no defects are present in large amount, because LOFs or keyholes are detrimental to the mechanical properties of the material processed with PBF-LB and cause a not predictable behaviour, thus reducing the chance of control over the material [225]. At *v* of 0.1 m/s and a *P* higher than 100 W, the formation of keyhole defects in the microstructure was found because of the larger *LED*, as found by Matilainen et al [229]. Conversely, an increase in *v* to 0.55 m/s resulted in LOF for all *P* values, because of a decreased *LED* by 86% compared to the lowest *v* analysed, as described by Steponavičiūtė et al [230]. Likewise, a progressive formation of LOF took place for *v* larger than 0.1 m/s and a *P* fixed at 100 W. The choice was on *high-LED* and *low-LED* because of the highest densities, that is 99.9% and 99.8% respectively. For this inspection, fully dense material, defined by a porosity of as high as 0.2%, was determined for the processability area and led to the choice of the *high-LED* and the *low-LED*. For additively manufactured 17-4 PH, other studies confirmed the possibility to print material with such high density and lack of defects [223,227].

The hardness test, whose results are presented in Figure 5.3, provided a range of hardness that spanned, for the average values, between 360 HV and 425 HV. The difference of 65 HV between the *high-LED* and *low-LED* is explained by the presence of different phase content, caused by the different *LED*s utilised. In fact, it is known from the literature that austenite is a soft phase compared to ferrite, which in turn results as less hard than martensite [231,232]. The choice of *high-LED* and *low-LED* was coherent with the purpose of this study. Consequently, it was to expect that twice as a value of *LED* for *high-LED* provides a different microstructure, texture and phases distribution than *low-LED*, which in turn affects mechanical properties [230,233,234]. The following quantification of the phases showed that *high-LED* has a larger fraction of BCC than *low-LED*, which results in higher hardness than the FCC phase, as already demonstrated by Hu et al [235].

Chemical analysis was necessary for this investigation on the printed and tested samples, because the elemental composition for the powder can be modified by the PBF-LB process. It is known that some elements are more volatile than others. Among the elements that characterise 17-4 PH alloy, for example, Nb and Mo are the most volatile, followed by Si. Instead, the most difficult elements to disappear are, in order, Mn, Cr, Cu and Ni. The most used techniques for chemical elements detection are, in order of accuracy, ICP, XRF and EDX, as presented in Sections 3.13 and 3.15. The powder analysis, supplied by the powder manufacturer, was performed with ICP except for elements such as C, P, N, O and S. However, in this study the other two techniques were used. The outcome from Table 5.1 confirmed that both XRF and EDX were delivering results in agreement with the ICP method. Moreover, XRF could not supply information regarding Mn, Si and Mo. Therefore, as previously done in other studies, EDX, that allowed to determine all the relevant elements, was used for the remaining of the investigation on the chemical content of the alloy in the process parameter sets considered, *high-LED* and *low-LED* [236].

Table 5.2 reported that *low-LED* experienced no substantial change of element composition from EDX on the powder, in the column referred to as *Ratio to EDX powder*. Conversely, *high-LED* induced a reduction in some of the elements. Specifically, Cu reduced its content ratio by 15.9% with respect to the powder, while Mn lost 27.2%. The loss of elements is caused by the high *LED* that is applied to the material [225]. The melting point of Cu and Mn is the lowest among the elements present in the alloy's composition, therefore it is most likely that they were lost from the melt pool during the PBF-LB process. Cu is an important element for 17-4 PH as it forms Cu-rich precipitates during the PBF-LB process, which contribute to the hardening of the steel [235]. *High-LED*, instead, caused Cu to evaporate and the coarsening of the grains, including precipitates, due to the higher energy input. As a result, the linked hardness decreases for components having the same phase content. In this work, the phase content between *high-LED* and *low-LED* is dissimilar, and the dislocation density is higher for *high-LED*. Therefore, the presence of higher martensitic and dislocation density content caused larger hardness for *high-LED*. Even Mn is an alloying element selected due to its hardness and brittleness. However the as-built condition contains a low amount of the element for both *high-LED* and *low-LED* than Cu. The same reasoning for what concerns the phase content and dislocation density applied for the resulting hardness. Finally, the loss of both Cu and Mn could impact the phase stability of the material, as they are both contributors to the increase of Ni_{eq}, that is they are γ stabilisers.

The discussed chemical composition resulted, for the Cr_{eq}/Ni_{eq} in this study, into a restriction of the ferritic to austenitic transformation during the application of energy density as opposed to alloys with lower Cr_{eq}/Ni_{eq} ratio compositions, favouring ferritic resulting microstructures [237]. A second factor to consider in PBF-LB process, for the resulting melt pool and microstructural features, is the LED applied onto the scanned layer. Chemical etching informed on the formation of the melt pools of the two process parameter sets. From Figure 5.4, a distinction can be found in the size of the melt pools between *high-LED* and *low-LED*, but also within the same process parameters. *High-LED* resulted as the process parameter with the largest melt pools and the deepest overlapping overall, although the latter was not uniform across the BD. Moreover, the process parameter also showed the most inhomogeneous etched microstructure. The central area is characterised by wide and distinctive melt pools. The top and bottom regions, instead, are defined by the presence of more overlapped melt pools. Shallower overlapping of the melt pools was instead detected for *low-LED*, which was also more homogeneous than *high-LED*.

Details of the microstructural features of 17-4 PH printed with different *LEDs* is depicted in the IPFs from Figure 5.7. As explained in Figure 5.7(a), the grain size for *high-LED* spanned a wide range, and a resulting bimodal microstructure can be appreciated. At raising LEDs with the same Cr_{eq}/Ni_{eq} ratio, a shift of the cooling

curve to the right of the CCT diagram occurs [237]. With higher energy density, *high-LED* from this study caused an extended duration of exposure within the temperature range that allows the phase transformation to FCC and subsequent martensitic transformation upon solidification. Conversely to *low-LED*, the overlapping of the melt pools is deeper for *high-LED*, and two regions must be considered during the PBF-LB process of each layer. In the first region, the fusion zone, which is not involved in the overlapping of melt pools, a coarsening of the grains occurred, as displayed in Figure 5.7(a). The fusion zone is only influenced by the actual scanning process and the resulting cooling curve, which is lower than *low-LED*. Consequently, larger grains are present which are characterised by lower dislocation density, Figure 5.16, than the refined subjacent HAZ. The decreased presence of strain as driving force locally reduced the thermally driven martensitic transformation, as explained by *Freeman et al.* [100], and promoted epitaxial grain growth, as demonstrated by *Liu et al.* [238]. The resulting microstructure is interested by predominantly ferritic microstructure and lower content of austenitic and martensitic phases. The coarse grains layers with lower dislocation density indicate lower driving force for precipitation. The second region, the remelted HAZ due to deep overlapping of melt pools, led to the formation of higher dislocation density than the fusion zone, as shown in Figure 5.16, dislocations that are accommodated by plastic deformation with following martensitic transformation as explained by *Hsu et al.* [239]. The increasing martensitic phase content in refined grains was found, in the HAZ, as the result of reheating of the subjacent region upon scanning of newly spread powder, local transformation and recrystallisation due to temperature excursion above the eutectoid point in the HAZ [240–242]. The microstructure has a higher stored energy and higher driving force for precipitation. Conversely to *high-LED*, *low-LED* showed columnar grains. However, most grains were found in the range of equivalent circle diameter up to 6 µm. With *low-LED*, the reason why a bimodal microstructure is not present is that the overlapping of melt pools is shallower. This was found to reduce the degree of epitaxial grain growth during part production due to the competitive growth of grains in other directions other than the vertical one (the direction of the highest thermal gradient) [243]. *Low-LED* is characterised by lower energy than *high-LED*, although higher than the critical value for ferritic to austenitic transformation. Therefore, *low-LED* still enabled the phase transformation to FCC, which then transformed into martensitic microstructure. Conversely to *high-LED*, the retained FCC transforms in lower percentage to BCC because it has less time for a full martensitic transformation upon solidification, the phenomenon being referred to as by-passing of martensitic transformation [237,244]. The result is a homogenous microstructure, as in Figure 5.7(b), and a decrease in the *in situ* thermal strain for a diminish of the thermally driven martensitic transformation. The subsequent higher content of retained FCC was pointed out, in Figure 5.16, by lower KAM values than *high-LED*. An additional reason for increased FCC content by *low-LED* is the smaller interdendritic spacing and the formation of small grains [245].

The XRD results depicted in Figure 5.5 and Figure 5.6 supported the choice of the two process parameter sets, *high-LED* and *low-LED*. In particular, the plots confirmed that both *LED*s produced microstructures with two phases, BCC and FCC. 17-4 PH stainless steel produced with PBF-LB can be comprised of both ferrite and

martensite depending on the process parameters used. In the work by Nezhadfar et al [246], presence of both phases was found. The SE imaging in Figure 5.4 and the BSE images in Figure 5.17 show an overall full martensitic microstructure for both *high-LED* and *low-LED*. In addition, large grains of ferrite were detected in some areas of the microstructures, as pointed out by the arrow in Figure 5.4(b) and Figure 5.17(a), (c) and (d). However, as already discussed in Section 2.2.1.3, when martensite has a low content of C, as is the case for the 17-4 PH alloy used in this work, XRD cannot distinguish a BCT from a BCC phase. Therefore, BCC was used to indicate both phases. Furthermore, from Figure 5.5 and Figure 5.6 it can be deduced that the content of FCC for *low-LED* is higher than *high-LED*. This is an important outcome for the control of the microstructure and mechanical properties of PBF-LB 17-4 PH steel, as the *LED* in the printing process has a direct implication of the content of BCC and FCC of the as-fabricated condition. Lashgari et al [224] determined that low values of *LED* can leave a high content of FCC, whereas increasing the *LED* can produce an almost fully microstructure with BCC phase, such as the components in the work of Alnajjar et al [247]. It can then be deduced that the influence of LED on the volume phase fraction from this work is in agreement with previous studies reported in the literature.

The investigation of the textures of the as-fabricated material shows that *high-LED* caused the same texture than *low-LED*. However, the intensity of the resulting fibre textures resulted higher for *high-LED*. Example in the literature that caused a stronger texture with increasing *LED* is the investigation from Moyle et al [226]. This result provides information about the control of microstructure given a specific linear energy density.

5.2.2 Understanding the TRIP activity of PBF-LB 17-4 PH

As determined in Figure 5.10, the two *LED*s determined different starting conditions of the microstructure and therefore the behaviour of the necking regions, during the mechanical testing at the failure of the specimens, resulted divergent. Figure 5.10(a), shows a cup and cone feature for *high-LED*. Noticeably, in both the sides and the centre of the cross section, large areas of brittle fracture, defined by the flat surface without micro dimples, are found. This can further confirm the presence of lower content of retained austenite for the *high-LED* compared to *low-LED*, as found by Eskandari et al [248]. *Low-LED* (Figure 5.10(d)) is conversely distinguished on the entire cross-section by an elongated fracture. Li et al [249] precedently discovered a similar behaviour for specimens printed with PBF-LB and 17-4 PH, where a shear labial region was present and showed a ductile fracture.

The XRD patterns, obtained during the in-situ XRD lattice strain analysis, allowed to carry out a control of the phase content evolution over strain for the two energy densities inputted on the 17-4 PH alloy. Four key strain values were selected, the beginning of the experiment, the yield point, the UTS and the failure of the sample. From Section 5.1.2 and 5.2.1, it was stated that the FCC content was higher for *low-LED* than *high-LED*. In this work, for the purpose of quantification, the method of the area under the curve of the XRD pattern was

adopted, as pointed out by Church et al in their research [195]. In the results section, it was already noted that the BCC phase decreased with shift and broadening of the peaks, while FCC phase constantly decreased until they could not be visually detected at the failure of the specimen. The explanation for such a behaviour is found in the literature. During plastic deformation of the tensile testing, the TRIP effect started taking place and the consequence was the transformation of FCC into the BCC phase, as described previously in the study by LeBrun et al [250]. A characteristic of 17-4 PH is the strain hardening at early plastic strain values, which can be understood by looking, in Figure 5.11 and Figure 5.12, at how the FCC peaks for both sets at the yield point of the mechanical testing had already diminished in intensity. The XRD patterns provided an explanation for the onset and development of the TRIP mechanism. The standard flat specimens suffered a local plasticity in the regions where the necking occurred at early strain values. Hence, work hardening applied on the specimens and continued until the failure occurred. As the specimens were tested at strains higher than the yield point, the strain hardening kept on acting on the material, with further reduction of the FCC phase in favour of the BCC phase. Eventually, at the end of the tests, correspondent to the failure, the FCC peaks cannot be visually detected further. This suggests that the work hardening rapidly acted for the phase transformation until a plateau was reached.

As mentioned, it was detected that the peaks of each phase, for both *high-LED* and *low-LED*, suffered from a shifting of *d-spacing* and broadening. The shift of the peaks appeared as a slight change of *d-spacing* to the right. Such a result implied that a minor lattice strain was induced by the tensile deformation, as found by Ahadi et al and Li et al [251,252]. Concurrently, the intensity of the peaks for both FCC and BCC diminished for both sets over strain, but the peaks became broader as the strain increased. This is a symptom of increase stress and lattice defects into the matrix. In fact, during a tensile test the material needs to accommodate for the internal stresses generated by the deformation and the transformation of retained austenite into martensite due to the TRIP [253–255]. Moreover, the residual stresses induced by the PBF-LB process affect the intensity of the shift and broadening of the phase peaks as well, if the magnitude is relevant. For this study, the slight shift changes mean that the applied *LED*s did not cause excessive distortion and residual stresses at each strain values due to the transformation.

From Figure 5.13 it can be noted that the FCC content for the as-fabricated conditions of the *high-LED* resulted 3.8% at the initial value and 3.2% at the yield point as opposed to 11.1% and 5.5% for *low-LED*, at the same checkpoints. Towards the failure of the specimen, as the work hardening enabled the transformation of most of the FCC, the ratio between the two sets for this phase approached a match. Both process parameter sets, in fact, were affected by a sudden decrease in FCC content after the yield point, when plastic deformation took place and the macroscopic effect of TRIP became evident. Moreover, an earlier transformation of FCC to BCC before the yield point occurred for both sets, which can be explained by local instability happening in the material during the deformation in the testing. The literature presented studies to explain this study, where a higher fraction of retained austenite favoured the formation of strain-induced martensite and improved the mechanical properties although reduced σ_Y was present. Moreover, a delay for the onset of localised plastic

deformation along can occur [13,250,256]. In this work, the end of the experiment for each set, caused by the failure of the specimens, caused a decrease in FCC content down to a similar value. *High-LED* resulted to have a final amount of 2.2%, lower than the 2.3% extracted with *low-LED*. This suggests that the final conditions for the two sets is similar. Considering the grain size distribution from Figure 5.14, the microstructures changed over strain to an extent that the two sets presented an equivalent microstructure at the end of the tests. A progressive reduction in the grain size for both *high-LED* and *low-LED* is visible. This is in accordance with Eskandari et al [248], who proved that performing a deformation testing causes a diminishing of grain size distribution over strain.

5.2.3 Microstructure and mechanical properties of tested PBF-LB 17-4 PH

The mechanical properties of the specimens printed with the two *LED*s and represented by *high-LED* and *low-LED*, resulted different between each other because of the dissimilar morphologies and content of retained austenite in their as-fabricated conditions. The results were appreciated with the plots in Figure 5.9 and quantification in Table 5.3. *High-LED* had a lower FCC/BCC ratio in the as-printed configuration, and that implied a higher σ_Y value than *low-LED* by 80%. Although retained FCC underwent martensitic transformation upon deformation, the transformation mainly took place in the first 5% of applied strain for both sets. *Aripin et al.* determined that the strain induced martensitic transformation in TRIP steels has a negligible autocatalytic effect [257]. This, because of the small austenite particles within the BCC matrix, that severely limits the autocatalytic propagation. The result is a uniform induced martensitic transformation, and *low-LED* reaches the yield point with higher FCC content than *high-LED*. Therefore, the yield point was determined by the initial microstructure. Generally, yield strength increases for refined grain size in metallic materials due to the Hall-Petch effect [258]. The refinement lowers M_S and leaves untransformed austenite until it is subject to deformation [259]. However, during the processing of PBF-LB 17-4 PH of *low-LED*, the process parameters homogenised the microstructure and decreased the dislocation density, for a decrease in yield strength. Therefore, in this study the refined grain effect on *low-LED* is overcome by the larger content of retained FCC and yield strength is higher for *high-LED*. The UTS reached an analogous value for *high-LED* and *low-LED* (even though larger for *low-LED*), and the elongation at failure grew higher for *high-LED*. The mentioned uniform induced martensitic transformation caused a work hardening for *low-LED*, due to the phase evolution, that led to an increase in stress up to the UTS. The change in mechanical behaviour for the two sets is further ascribed to additional reasons.

The grain size is the first argumentation. Figure 5.7 presented a wider grain size distribution for *high-LED*, with a few grains that resulted coarser than *low-LED*. The more than double *LED* favoured the discrepancy in grain size distribution. Therefore, although the σ_Y was higher for *high-LED*, a specimen produced with this *LED* that enters the plastic regime undergoes a phase of recrystallisation that results larger than *low-LED*. The consequence can be seen in Figure 5.14, where a microstructure that is finer than its untested condition and

overall smaller than *low-LED* can be appreciated, with larger presence of grains of equivalent circle diameter below 5 μm. Conversely, the finer morphology of *low-LED* in the as-printed configuration served to diminishing the fracture toughness and create an early crack nucleation and propagation for ductility failure compared to *high-LED.*

Another reason for this outcome is provided by the role of precipitates and carbides in the microstructures, in terms of size and content. Regarding precipitates, and specifically Cu precipitates, if they are present in fine size they can contribute to a rise of hardness in the material. Contrarily, the presence of coarse precipitates will produce a reduction in the hardness of the material, for the benefit of higher ductility [235,249,260,261]. Furthermore, a larger amount of carbides and inclusions contributes to the increment of sites from which cavitation can initiate, thus accelerating the generation of the necking of the specimen that undergoes deformation, for an earlier failure of the material [236,262]. The described role of precipitates and carbides is presented as a further mechanism to explain the difference in mechanical properties behaviour between *high-LED* and *low-LED,* and would need a focus as stated in Section 7.2.

A final consideration on the conditions at the end of the tensile testing for the specimens printed with two different *LED*s is in relation to the change in texture. Figure 5.8 presented the as-fabricated texture for *high-LED* and *low-LED,* defined by the same fibre textures and slight difference in intensity. The divergent textures in the deformed condition, as displayed in Figure 5.15, is interpreted as the result of different starting FCC/BCC ratio of the as-printed configurations. The presence of larger amount of BCC phase for *high-LED* at the beginning of the test implied the challenge for the crystallites in the {001} and {111} fibre textures to assume different orientations. The only possibility was to realign only along the Z_0 direction (i.e., the BD) to assume a more defined and less random orientation. A similar outcome was reported in past research by Pirgazi et al [263]. This well organised reorientation of the crystallites determined an additional {101} fibre texture parallel to the load direction, X_0. As for *low-LED,* there was a redistribution of the orientation for the crystallites, after the tensile testing ended, such that a random orientation occurred to cancel the previous {001} and {111} fibre textures aligned with the BD. The reason is the highest strain hardening due to TRIP effect than *high-LED.* The transformation of FCC into BCC favoured the reorientation of the crystallites, thanks to the ductility of the retained austenite, as described by previous authors [264,265]. Simultaneously, following the same outcome from *high-LED,* the {101} fibre texture was obtained. This was caused by the preferred orientation of this family of planes due to the load acting to deform the specimen.

5.2.4 Effects of thermal strain on undeformed and deformed microstructures

The effect of the two in-situ treatments during PBF-LB on the as-built microstructure was dealt with in Figure 5.16. The higher KAM and dislocation density for *high-LED,* 8.5% larger as opposed to *low-LED,* is linked to the higher content of BCC in the matrix than retained FCC conversely to *low-LED,* as demonstrated by Sabooni

et al [13]. It can be deduced that the higher thermal strains obtained during the PBF-LB process and remelting by *high-LED* contributed to plastic deformation that accommodated the internal generated strains, favouring the martensitic transformation as examined by Freeman et al [100]. Higher dislocation density was found in refined grains layers, due to Hall-Petch effect [266], compared to coarse grains layers which showed lower dislocation density. *Low-LED* did not show similar features, given the higher cooling rate that reduced remelting on the layers beneath, refined homogeneously the microstructure and decreased the in situ thermal strain thus diminishing the thermally driven martensitic transformation during the PBF-LB process, as determined in [100]. As a result, higher content of retained FCC was found and pointed out by lower KAM values than *high-LED*.

After deformation, the dislocation density was higher for *low-LED* than *high-LED*, by 23.8%. This implies that, during deformation, two factors determined the increase of dislocations. The first is related to the Hall-Petch effect [266]. In this study, low-LED led to stronger interaction of dislocation gliding with close grain boundaries, for subsequent dislocation multiplication and hindering of their motion. The second concurrent factor is linked to the TRIP behaviour that occurred during the tensile testing. The retained FCC transformed into martensite adding matrix distortion due to the displacive transformation in addition to the dislocation growth.

5.3 Summary

This study investigates how to control the as-built microstructural features and retained austenite content, as well as the TRIP activity in a strain hardening 17-4 PH stainless steel, made with PBF-LB with different linear energy densities. Mechanical tensile testing with in-situ x-ray diffraction experiment were carried out as well as ex-situ microstructural analysis. The main findings are summarised below:

(1) Two process parameters were picked from the processability region because at extremes of the hardness range, chemical composition due to volatility by different *LED*s, and different melt pool generation.

(2) Using different *LED*s, 0.67 J/mm for *high-LED* and 0.29 J/mm for *low-LED*, provided substantial dissimilar starting microstructure. High energy density caused a layered bimodal microstructure. The regions where melt pools overlapped to less extent, underwent a reduced thermally driven martensitic transformation and coarsening of the grains; the melt pools that overlapped more, increased dislocations, accommodated by martensitic transformation. Lower energy density caused shallower melt pools overlapping and faster cooling, for more homogeneous microstructure. A high value of *LED* also favoured a wider range grain size distribution. No substantial difference in the resulting fibre texture was noted between the two parameter sets.

(3) *high-LED* showed a σ_Y 80% higher than *low-LED* thanks to its lower FCC/BCC ratio. However, UTS resulted similar and ε_f was higher, 9.5% instead of 8.4%. This was because *high-LED* had a wider grain size in the undeformed condition and a lower porosity than *low-LED*.

(4) The *LED*s for *high-LED* and *low-LED* produced different phase contents in the undeformed condition. Quantification showed that high values of *LED* are linked to lower starting FCC than lower *LED*s. Consequently, during plastic deformation the TRIP activity acted differently. Overall, *high-LED* experienced a decrease of FCC of 44.7% during the tensile test. Conversely, *low-LED* was characterised by a reduction in FCC of 79.3%.

(5) The higher content of BCC for larger *LED*, in the as-printed condition, explained the dissimilar average hardness. This is particularly important for the design of structures that need resistance to wear.

(6) Plastic deformation caused a recrystallisation of the *high-LED* microstructure, for a smaller grain size distribution than *low-LED*. As a result, an improvement in ductility was seen. TRIP activity affected the texture of the two microstructures, with the introduction of a new <101> // X_0 fibre texture in both, but the disappearance of the as-printed fibre textures in *low-LED*.

6 On the energy absorption of additively manufactured honeycomb gyroid lattice structures with 17-4 PH

PBF-LB enables the manufacturing of complex shape TPMS based lattice structures for energy absorption in compressive applications, with improved mechanical properties and energy absorption from functional grading or different energy densities when printing lattices [25,170]. The newly designed honeycomb gyroid unit cell (UC), described in Section 2.7.1, possesses high anisotropy between its in-plane and out-of-plane direction.

The aim of this Chapter is to investigate the honeycomb gyroid in its weakest in-plane direction and processed by PBF-LB, for improvements on the energy absorption of the studied topology. For this purpose, the 17-4 PH strain hardening stainless steel, described in Section 3.3, is going to be implemented. In particular, the strain hardening properties of the materials when processed with PBF-LB, and specifically the microstructure tailoring when using different laser process parameters for subsequent dissimilar mechanical properties as investigated in Chapter 5. With the synergistic effect given by the combination of the in-plane orientation and 17-4 PH, and the exploitation of volume fraction (VF) and energy density (process parameters) grading in the loading direction, new absorption capabilities are disclosed that are comparable to the established state-of-the-art of crashworthy lattices. This Chapter also focuses on creating a computational modelling to predict the energy absorption capabilities of honeycomb gyroid lattices. The working environment was created in Abaqus and validated with experimental data obtained from the research of Maskery et al [151], in quasi-static conditions. The foreseen advantage is prediction of the deformation behaviour of lattice structures, to reduce the extensive physical production and testing of lattices. The methodology can be implemented to any lattice structure topology, for the purpose of enhancing mechanical properties, as explained in Section 2.7.

Lattice structures are manufactured with the energy densities from Chapter 5. Initial research is executed on quasi-static compression testing on lattices at different uniform VFs, with uniform energy densities. Deviation between the UCs thickness of the printed lattices and the CAD models emerges. Therefore, investigations on the manufacturability of the UCs to avoid excessive dissimilarity is performed. Two additional sets of lattice structures are then produced, to investigate quasi-static conditions as well as dynamic strain rates for energy absorption. Each of these sets has the same number of uniform and graded lattices. The effects of each configuration are compared to highlight the benefits of grading the honeycomb lattice structures on the energy absorption, both in quasi-static and in dynamic conditions.

6.1 Results

6.1.1 Validation of the FEA model with PA2200

A finite element analysis model, in order to be useful for making predications, must be validated against real observations [267]. In this study, the validation was carried out with the reference data of PA2200 from a previous study [151], and friction coefficient from [268] . The chosen element type was *C3D8R*, previously reported to provide a better contact prediction in general engineering problems [269] or for the contact analysis and prediction on lattice structures [270]. The honeycomb gyroid in Figure 3.14, whose .stl file is depicted in Figure 6.1, was meshed with different resolution values in FLatt Pack for the sensitivity study. In Table 6.1 is a recap of the resolution, number of elements and corresponding element size.

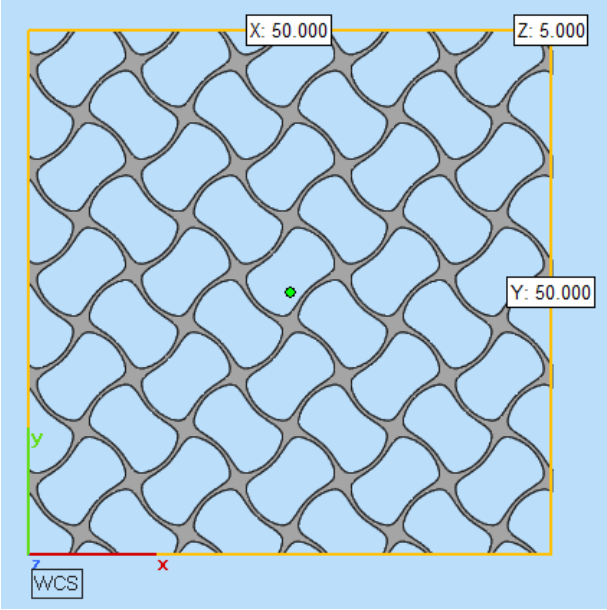

Figure 6.1. Schematic of the 5 x 5 UC repetition geometry used to validate the FEA model, with size 50 x 50 x 5 mm^3 and uniform VF.Focusing on three mesh resolutions, 39, 60 and 80, in Table 6.2 are the elements' volumes and surfaces, along with the deviation to the UC .stl. There is no exact matching between the generated meshes and the .stl. 60 resolution provided the lowest volume deviation of 2.6%, required to approximate the experimental results. Instead, the surface increased with larger resolutions.

In Figure 6.2 is an explanation for Table 6.2. The mesh is a combination of linear brick elements that split the lattice structure in the 3D space. The fixed size of the mesh elements caused a deviation of the external shape of the UCs in relation to the .stl file. Figure 6.2(a) displays a coarse mesh, not able to replicate the isosurface of the honeycomb gyroid UC. As the mesh element size decreased, a lower deviation of the overall volume occurred down to 60 resolution. Noticeably, by reducing further the size of the mesh elements, i.e. by increasing the resolution, the volume deviation of the meshed structure started to increase again, contributing

to a staircase effect for a shape mismatch. This leaves inaccuracy in the representation of the UC, affecting the contact problem.

Table 6.1. Sensitivity analysis in terms of the resolution for the *C3D8R* element type used. The geometry considered is a 5 x 5 cell repetition.

Mesh resolution	**Number of mesh elements [x 10^3]**	**Mesh element size [µm]**
39	33.8	125
50	60.5	100
55	91.1	91
60	108.6	83
80	252.3	63
100	479.1	50

Table 6.2. Detail of the .stl volume and surface, in comparison to three mesh element sizes from FLatt Pack considered for the mesh sensitivity study.

Part	**Volume [mm³]**	**Deviation Volume to .stl [%]**	**Surface [mm²]**	**Deviation Surface to .stl [%]**
.stl	1226.4	/	4704.5	/
Mesh – 33.8K elements	1321.7	7.7	5968.7	26.9
Mesh – 108.6K elements	1258	2.6	6115.2	30
Mesh – 252.3K elements	1277.9	4.2	6023.2	28

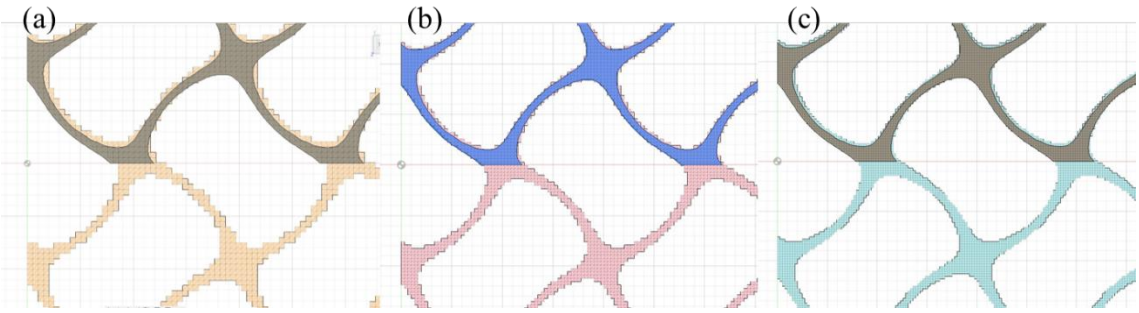

Figure 6.2. Visual representation, in the in-plane direction, of (a) 39 (orange), (b) 60 (magenta) and (c) 80 (cyan) mesh resolutions to explain Table 6.2. On the top figures is the linked .stl.

Simulating a single UC with a 60 resolution, the *E* was extracted and compared to the value obtained from the homogenisation code presented in Section 3.6. The FEA modulus provided 1.69 MPa, whereas the homogenisation code a value of 1.7 MPa, for a deviation of 0.6% for the computational model. The resolutions were used to generate the lattice meshes for compression tests as presented in Figure 3.14. The outcomes of the simulations are in Figure 6.3. Figure 6.3(a) presents the overview of the compression behaviours. In Figure 6.3(b), instead, is a detail up to densification of the lattice structure. The lowest resolutions, that is between 39 and 55, were underestimating the experimental stresses. Conversely, the higher resolutions, 80 and 100, provided too high computational time, limited by the HPC; furthermore, the higher deviation to the .stl volume increased the stiffness of the mechanical curves. For this reason, a mesh generated with the 60 resolution was determined as the best match against the experimental result, and chosen for the remainder of the validation process.

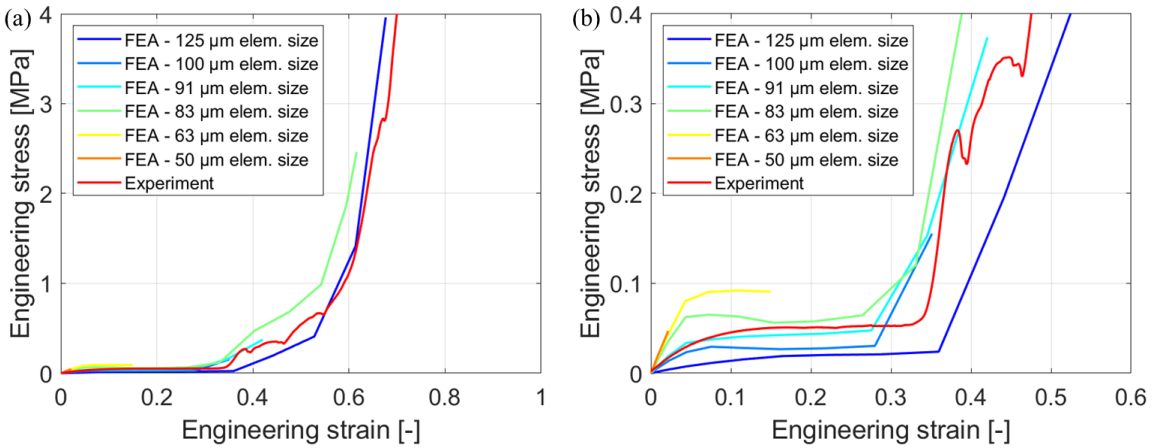

Figure 6.3. Stress-strain curves for the mesh sensitivity analysis of the FEA validation model for the honeycomb gyroid with PA2200 as material model. (a) Overview, (b) Detail. 39, 50, 55, 60, 80 and 100 resolutions correspond to 125 µm, 100 µm, 91 µm, 83 µm, 63 µm and 50 µm mesh element size, respectively.

The validation of the FEA model required to understand the reasons for the deviations to the experimental curve. During physical experiments, lower stiffness and large stress drops due to the printing process occurred,

which are detrimental to the response of the structure to the external load. In particular, the issues are caused by presence of defects such as pores or surface roughness, complex geometries that the scan strategy cannot follow, increased thermal concentration in regions with high curvature for excessive powder melting and subsequent crack initiation [271]. This explains the mismatch between the curves. Four modifications to the material model were considered by changing the σ_Y, the true stress (following σ_Y) or the friction coefficient, and are reported in Table 6.3 with a plot detail of the modified material models. The stress-strain curves for the honeycomb gyroid lattices are in Figure 6.4. The original material model, referred to as *FEA - unmodified*, overestimated the mechanical response of the lattice structure. Conversely, modified material models, that incorporated information related to the local onset of plastic regime, allowed to extrapolate stress-strain curves that could match the experimental results. From Figure 6.4 it can be noted that the curve *FEA – modified 2* is a reasonable match with the deformation behaviour of the honeycomb gyroid structure printed with SLS process. Specifically, the elastic region is overestimated with E being almost double. However, the σ_Y results 12.1% lower and the average plateau strength 7.9% higher than the experimental data.

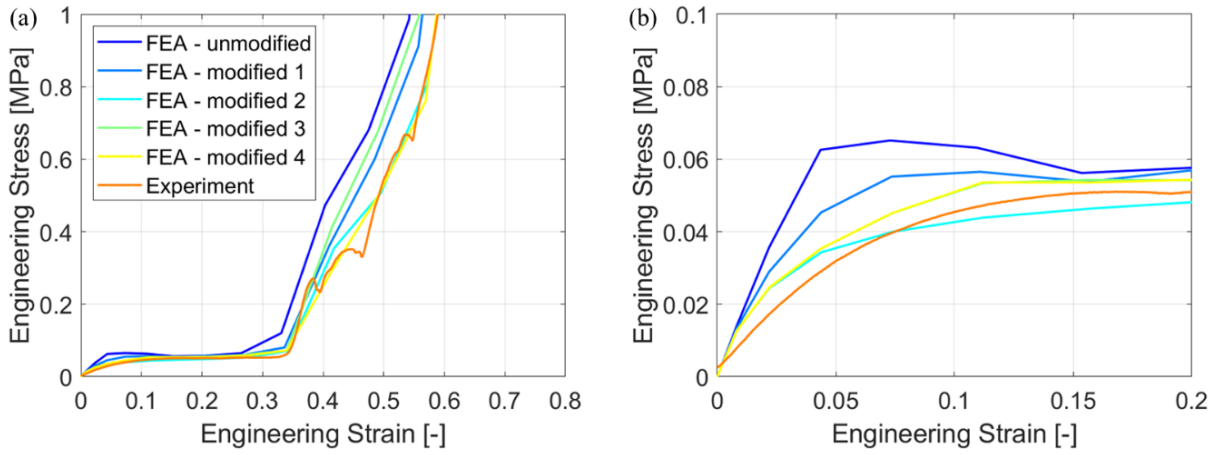

Figure 6.4. Stress-strain curves obtained from the FEA model with 60 resolution, for the honeycomb gyroid with modified material model as specified in Table 6.3.

The mesh study was also conducted on the *C3D8* element type. *C3D8* differs from the *C3D8R* element in having 2 x 2 x 2 integration points, as opposed to one only integration point of the latter [201]. The computational time for solving the compression problem was drastically increased, and the limit imposed by the HPC, 100 hours for a simulation to run, were not sufficient for the completion of the linear elastic regime.

Table 6.3. Material properties changed for the matching of the stress-strain curves of the validation FEA model with the experimental curve obtained in [151]. The modified material models *FEA – modified 3* and *FEA – modified 4* only differ by the friction coefficient (FC).

Material model	**True σ_Y [MPa]**	**FC [-]**
Unmodified	29.7	0.32
Modified 1	20	0.32
Modified 2	20	0.32
Modified 3	20	0.32
Modified 4	20	0.15

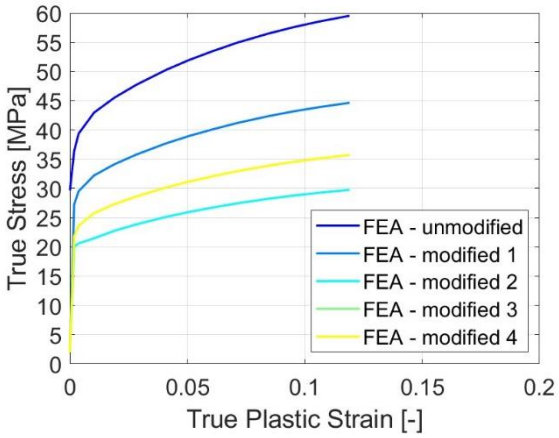

6.1.2 Computational and experimental quasi-static mechanical tests with 5 x 5 cell repetition

Six different configurations were printed for quasi-static analysis on honeycomb gyroid lattice structures produced with PBF-LB of 17-4 PH, presented in Table 6.4. The structures were uniform in material model and VF. The UC had a 6 mm length and the element mesh size, 83 µm, was decided based on the study in Figure. A.1. The resulting analysed configurations for the FEA investigation are depicted in Figure 6.5, where the minimum and maximum thickness of the UC for each VF are: 0.28 mm and 1.23 for 0.2 VF; 0.50 mm and 1.65 mm for 0.3 VF; 0.72 mm and 1.98 mm for 0.4 VF. The table shows the intended and the experimental VFs, where the VF of the latter was calculated from the actual weight of the printed components. The table reveals that the manufacturing process caused large deviation on the geometry of the UCs. The percentage decreased from 40% with the lowest VF and *high-LED*, to the lowest value of 15% with 0.4 VF and *low-LED*. The bigger melt pools, generated with *high-LED*, have a higher contribution to the resulting UCs thickness. Moreover, the influence of the meander scan strategy, which does not follow the contour of the scanned layer, must be considered. These considerations are discussed in Section 6.2.1.

Table 6.4. Printing parameters and geometrical deviations for the 17-4 PH lattices to the .stl files. The geometry considered is 5 x 5 cell repetition.

Process parameter set	Theoretical VF [-]	Experimental VF [-]	Deviation [%]
high-LED	0.2	0.28	40
	0.3	0.39	30
	0.4	0.48	20
low-LED	0.2	0.24	20
	0.3	0.36	20
	0.4	0.46	15

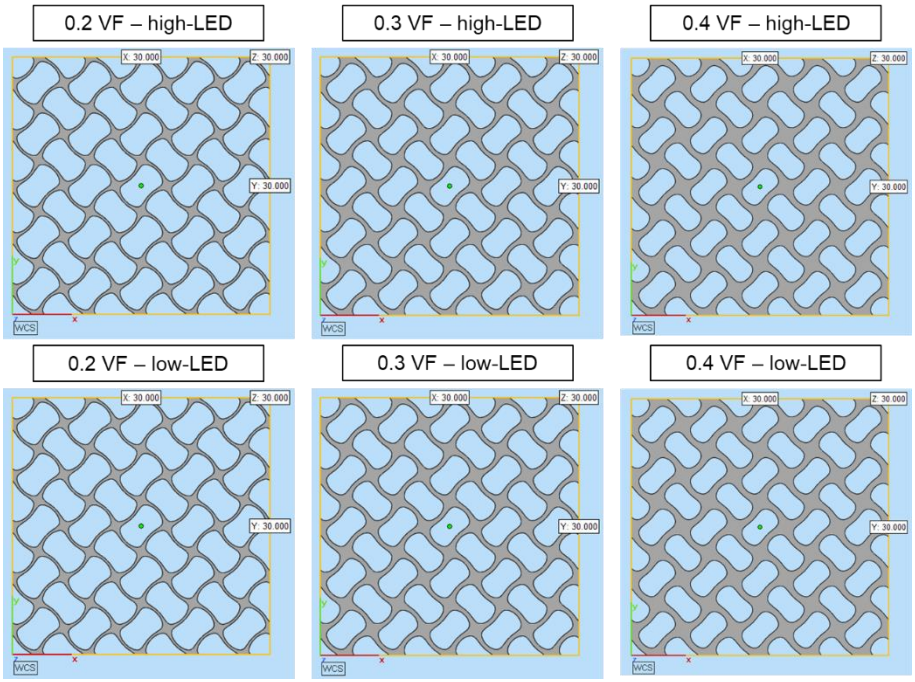

Figure 6.5. Display of the 5 x 5 UC repetition honeycomb gyroid, with size 30 x 30 x 30 mm^3 and then printed with PBF-LB, with uniform VFs and single process parameter per configuration. Figure 6.6 shows the stress-strain curves with focus on the linear elastic region and plateau. The simulation performed with the supposed VF, *Theoretical FEA*, is reported as well as the simulation computed with the VF determined from the printed lattice structures, *Sintered FEA*. In addition, *Experimental* represents the tests performed on the printed specimens. All experimental curves followed with a good agreement the curves from *Sintered FEA*, up to the end of the plateau, where local collapse made the experimental curves retard the densification onset.

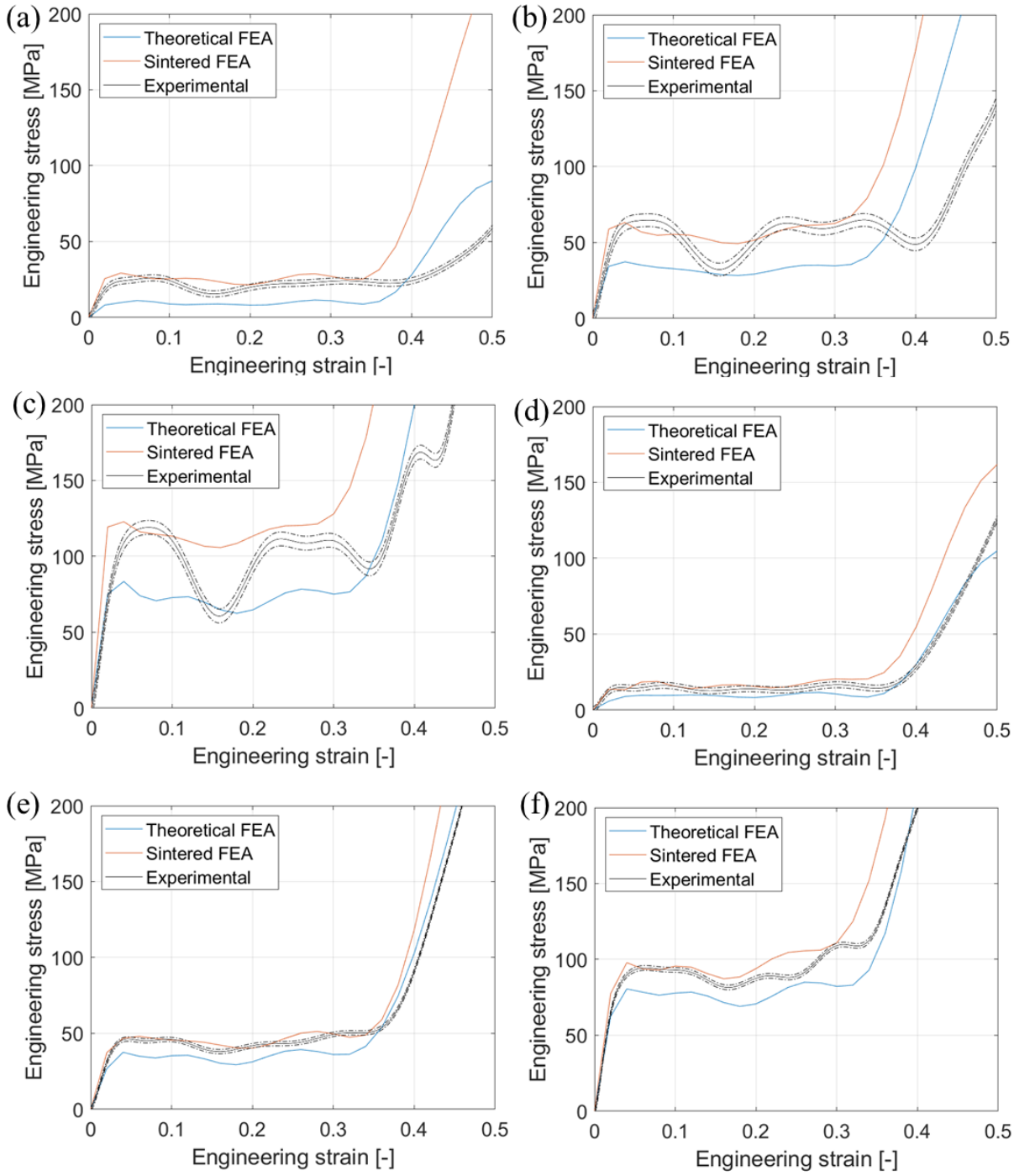

Figure 6.6. Stress-strain curves obtained from 5 x 5 UC repetition, with size 30 x 30 x 30 mm^3 for the experimental and 30 x 30 x 5 mm^3 for the computational samples, printed with 17-4 PH. The configurations are: (a) *high-LED* and 0.2 VF, (b) *high-LED* and 0.3 VF, (c) *high-LED* and 0.4 VF, (d) *low-LED* and 0.2 VF, (e) *low-LED* and 0.3 VF, (f) *low-LED* and 0.4 VF. Simulations with the theoretical and actual VF are reported with the experimental curve.

The SEA was extracted from the stress-strain curves until densification strain, computed with the intercept method for each configuration [272]. The values of densification strain, for each configuration and *high-LED*, are presented in Table 6.5 (accuracy of ± 0.001 for the *Experimental* values). The corresponding information

for *low-LED* is in Table B.1. The SEAs for the 18 different tests were determined by means of Equation 2.27 and presented in Figure 6.7. In Figure 6.7(a) are the SEAs for the *Theoretical FEA*, where the energy absorbed was higher with increased volume fraction, and *low-LED* provided higher values than *high-LED*. Figure 6.7(b) displays the SEAs for the *Sintered FEA*, and in Figure 6.7(c) are the outcomes from the experiments. Both configurations had larger volume fractions for *high-LED* than *low-LED*, and so were the corresponding SEAs.

Table 6.5. Densification strain values as obtained for the lattice structures with 5 x 5 cell repetition and *high-LED*.

Test type	**Process parameter set**	**Theoretical VF [-]**	ε_D **[-]**
Theoretical FEA	*high-LED*	0.2	0.374
		0.3	0.35
		0.4	0.34
Sintered FEA	*high-LED*	0.2	0.36
		0.3	0.34
		0.4	0.32
Experimental	*high-LED*	0.2	0.402
		0.3	0.433
		0.4	0.363

The average plateau strength, typical value used in the investigation of lattice structures [27], is reported in Figure 6.8. The *Theoretical FEA* was characterised by higher values of the strength for *low-LED* than *high-LED*, and as the VF changed from 0.2 to 0.4. The opposite trend occurred for the *Sintered FEA* set of data. The outcome for the product of experimental curves was in agreement with *Sintered FEA*, but at 0.4 VF.

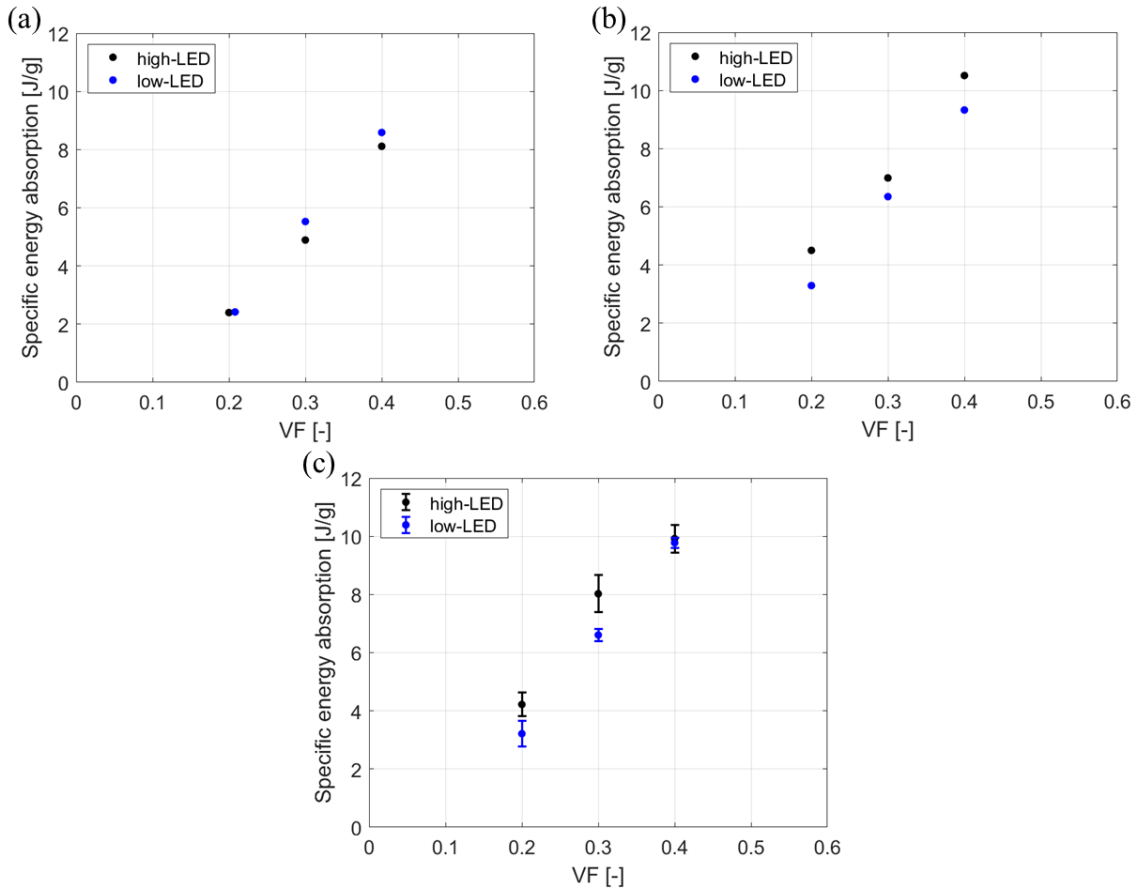

Figure 6.7. SEA for the six configurations tested and simulated with 5 x 5 cell repetition, with size 30 x 30 x 30 mm^3 for the experimental and 30 x 30 x 5 mm^3 for the computational samples. The plots report the results from (a) the FEA with theoretical volume fraction (*low-LED* with 0.2 VF is translated to avoid overlay with *high-LED* at the same VF), (b) the FEA with the actual volume fractions, (c) the experimental tests.

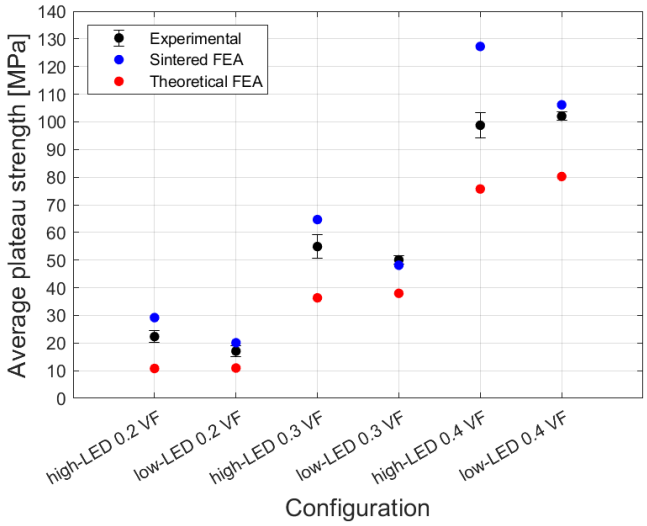

Figure 6.8. Average plateau strength for the honeycomb gyroids with 5 x 5 cell repetition, with size 30 x 30 x 30 mm^3 for the experimental and 30 x 30 x 5 mm^3 for the computational samples, from the FEA and experimental curves.

6.1.3 Wall thickness check investigation for dimensional accuracy resolution

The significant VF deviation for the printed lattices prevented a comparison between *high-LED* and *low-LED*, since the mechanical properties do not change linearly with the mass, but exponentially [273]. An inspection was carried out, by means of optical microscopy, on thin straight walls from 250 µm to 3 mm, to determine the effects of the beam compensation on the thickness of the printed parts, with *high-LED* and *low-LED*. This was done to achieve the most accurate representation of the geometry, minimising the deviation to the intended design. Figure 6.9(a) reports the absolute values for *high-LED*, the data for *low-LED* are in Figure 6.9(b). Up to 500 µm, the average deviation to the intended design was large, with values up to 87.3% for *high-LED* at 250 µm and 50 µm of BCM. Contrarily, at 1 mm thickness an increase of BCM caused shrinkage of the actual value compared to the .stl files, with the highest average deviation of -1.4% for 1.8 mm thin wall, down to -3.5% for 3 mm walls. Therefore, a 100 µm BCM was adopted in the remainder of the investigation.

Since dimensions below 600 µm were not in agreement with the dimensional accuracy of the .stl files, larger VF values than 0.2 and 0.3 were used in the remainder of the analysis. Additionally, since the 6 mm UC was found to deviate excessively, a larger dimension with a sufficient cell repetition that could be tested to avoid boundary effects [150], was adopted. A UC of 8 mm length and a cell repetition of 4 x 4 was selected.

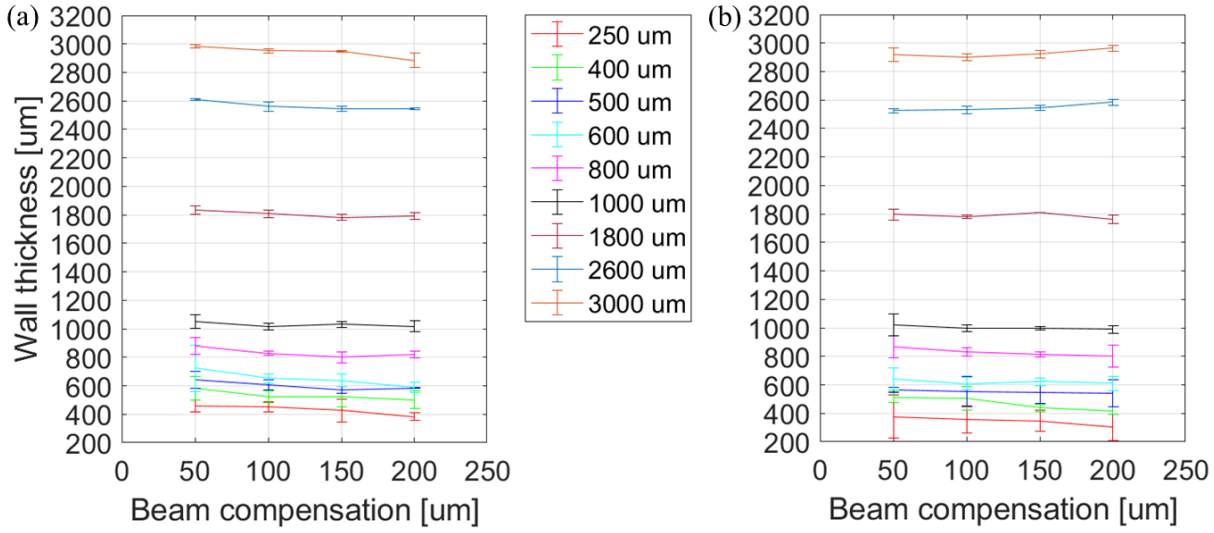

Figure 6.9. Evolution of the wall thickness, versus beam compensation, of thin walls printed with PBF-LB of 17-4 PH stainless steel, with (a) *high-LED* and (b) *low-LED*.

6.1.4 Quasi-static tests in different configurations with 4 x 4 unit cell repetition

A design of experiment was performed on the honeycomb gyroid lattice structures with UC of 8 mm length and 4 x 4 cell repetition, for the quasi-static testing condition. A combination of 18 different lattice structures was considered, as shown in Figure 6.10. The structures were either uniform or functionally graded in VF, and with single or two material models split between top and bottom of the in-plane section. In the latter case, the two top layers of UCs are referred to as top, bottom the remaining ones.

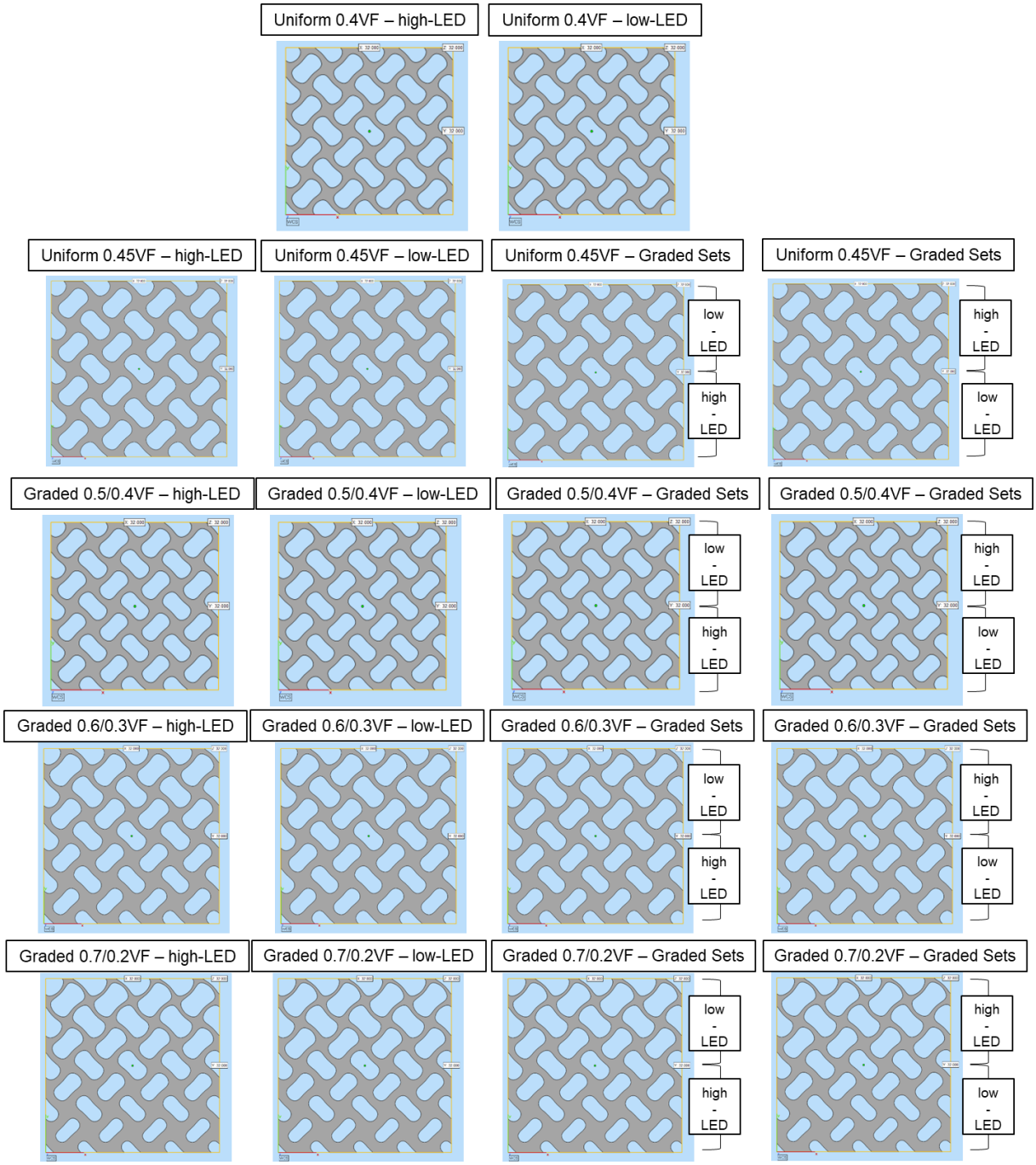

Figure 6.10. Design of experiment for the FEA of honeycomb gyroids with 17-4 PH, for the UC repetition of 4 x 4 and size 32 x 32 x 5 mm^3.

The 18 configurations were simulated by means of the computational model validated in Section 6.1.1. The resolution for the configurations in this Section, as well as 6.1.5 and 6.1.6, had to be changed to 80 (63 µm element mesh size), following the sensitivity study depicted in Appendix A. The graded configurations with two process parameters are referred to as *high-LED*/*low-LED* when *high-LED* is at the bottom, *low-LED*/*high-LED* vice versa. Figure 6.11 contains the stress-strain curves split between uniform and graded VF. Figure 6.11(a) shows a flat plateau before densification. The strength peak with 0.4 VF was 41.4% and 46.5% than 0.45 VF for *high-LED* and *low-LED*, respectively. Grading of the process parameters contributed to a change in the material response to compression. Larger grading, Figure 6.11(b) to (d), caused the gradual increment of the plateau slope.

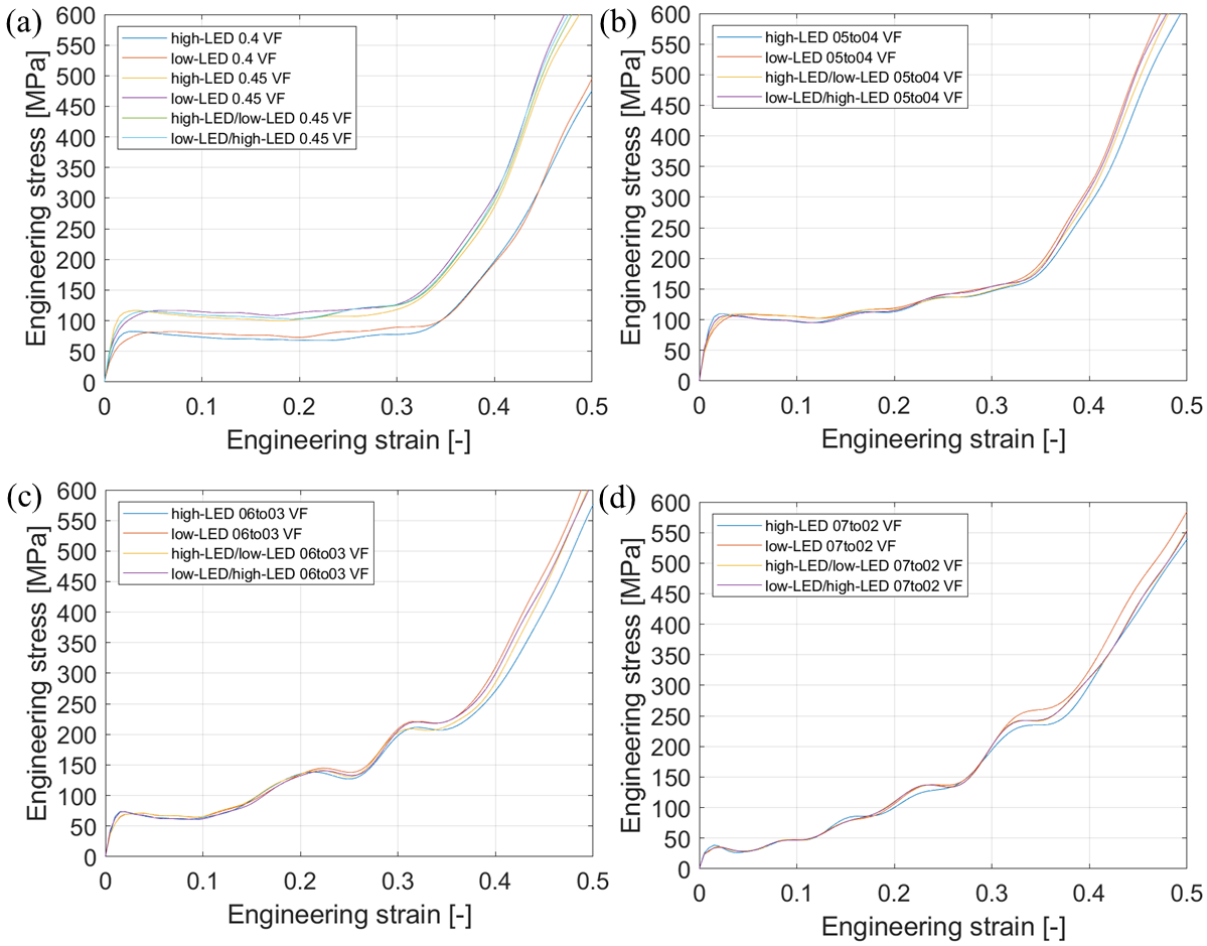

Figure 6.11. Stress-strain curves from the 18 computational configurations, with size 32 x 32 x 5 mm^3, in Figure 6.10 : (a) uniform 0.4 and 0.45 VF, with single and graded materials; (b) 0.5 to 0.4 VF grading, with single and graded materials; (c) 0.6 to 0.3 VF grading, with single and graded materials; (d) 0.7 to 0.2 VF grading, with single and graded materials.

The dissimilar compression behaviour is explained in Figure 6.12, for *high-LED* and same strain of 40%. Uniform VF, Figure 6.12(a), homogeneously compressed the lattice across the four layers. In Figure 6.12(b) to (d) the top UC layers have a decreasing VF, and the bottom UC layers have an increasing VF; therefore, a transition to a local layer by layer failure is favoured.

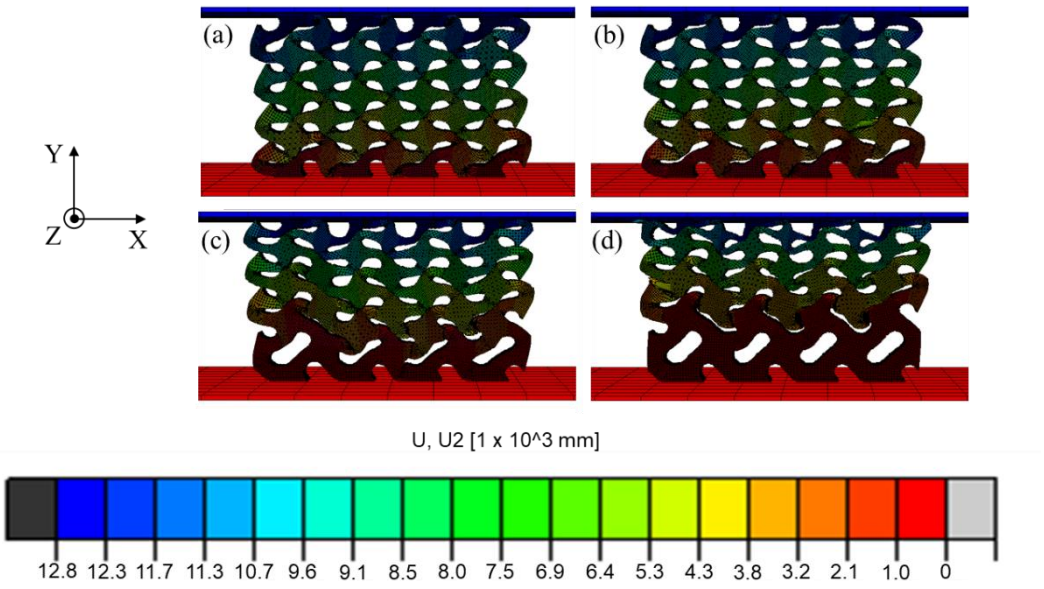

Figure 6.12. Overview of the compression behaviour at 40% strain for lattice structures with *high-LED*, 4 x 4 UC repetition and size 32 x 32 x 5 mm^3.

(a) uniform 0.45 VF, (b) graded 0.5 VF to 0.4 VF, (c) graded 0.6 VF to 0.3 VF and (d) graded 0.7 VF to 0.2 VF.

The SEAs were calculated from the stress-strain curves at ε_D, summarised in Appendix B and reported in Figure 6.13. A uniform VF supplied the highest SEA of 13.9 J/g for *low-LED* and *low-LED*/*high-LED*. Among the functional grading, Figure 6.13(d) depicts the 20.2 J/g capabilities of *high-LED*.

Six configurations were printed by means of PBF-LB with 17-4 PH, presented in Figure 6.14. The resulting VFs are reported in the figure, where for the graded structures the average is indicated.

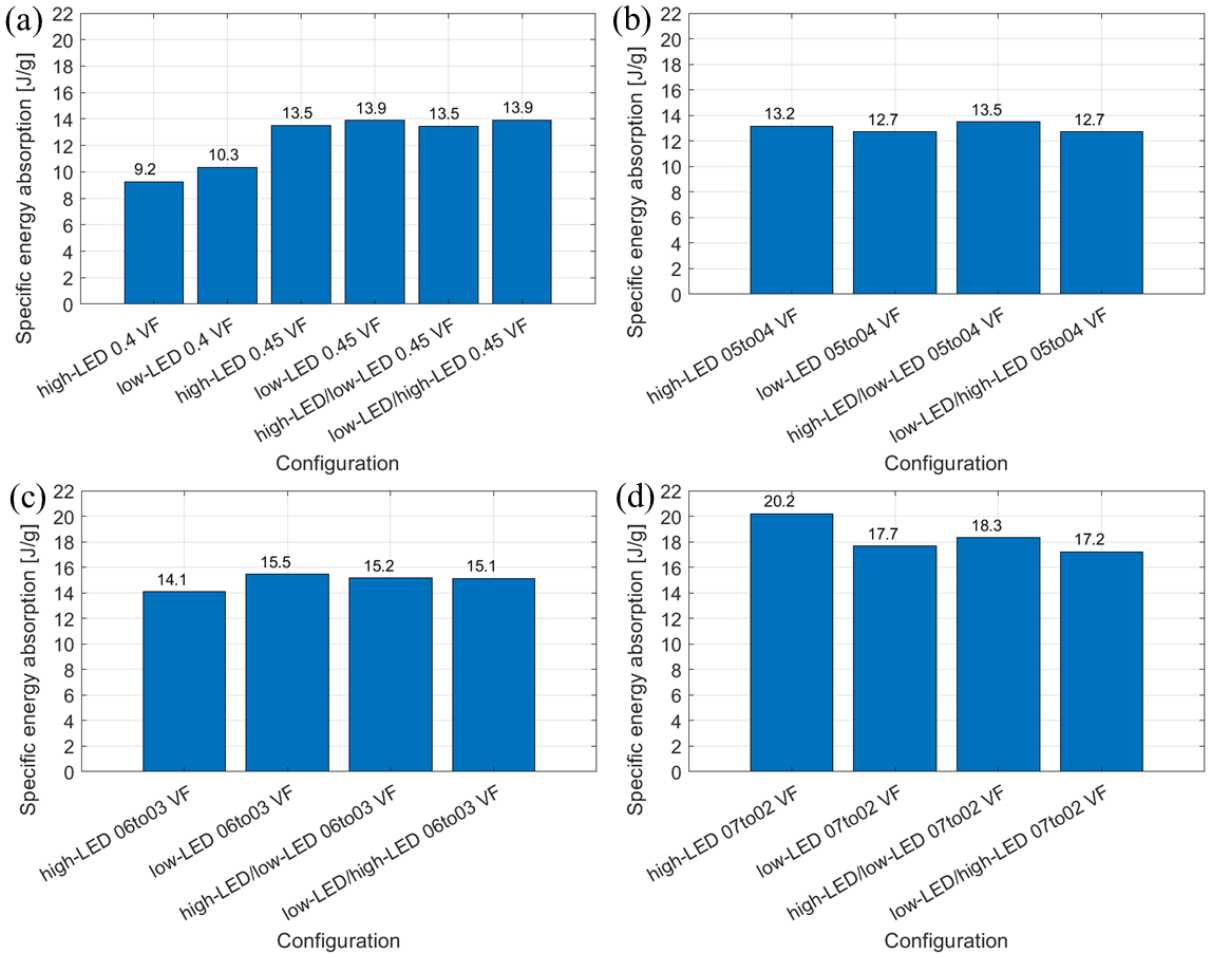

Figure 6.13. Specific energy absorption from the 18 computational configurations, with size 32 x 32 x 5 mm^3, in Figure 6.10. The plots are split, from (a) to (d), with the same order as in Figure 6.11.

An analysis of the deviation for the printed lattice structures from the .stl was executed in different locations of the UCs. In Figure 6.15, the contemplated dimensions are pointed out. Figure 6.15(a) and Figure 6.15(b) represent the uniform and functionally graded lattice structures, respectively. Measurements were taken on each sample that was physically tested, on all locations marked with the same corresponding letter across the in-plane section for what concerns uniform lattices, and on all locations marked with identical dimension name at the same height along the BD in relation to the functionally graded structures. Images were taken under the optical microscope and the dimensions measured and automatically analysed through a MATLAB script. In Figure 6.17 the *d* measurements for the uniform (a) high-LED and (b) low-LED parameter sets are shown. It can be noticed that the former LED caused larger thicknesses across the curvature region, as opposed to the lower LED. In addition, the transition for high-LED to the area with the *b* measurement is more irregular, which can cause additional crack initiation spots. The surface roughness looks however worse for low-LED, in turn adding potential crack initiation regions. In Table 6.6 the measurements can be appreciated for the .stl and the printed lattices, along with the standard deviation for the latter.

The stress-strain curves for the 6 experimental configurations are reported in Figure 6.17(a-c). In the plateau region, the engineering stress of lattices with *high-LED* resulted as high as 42.9% for the case of uniform VF, Figure 6.17(a), and 25% for the graded configurations, Figure 6.17(b), than *low-LED*. The highest stress peaks were reached in the configurations with graded material model in Figure 6.17(c).

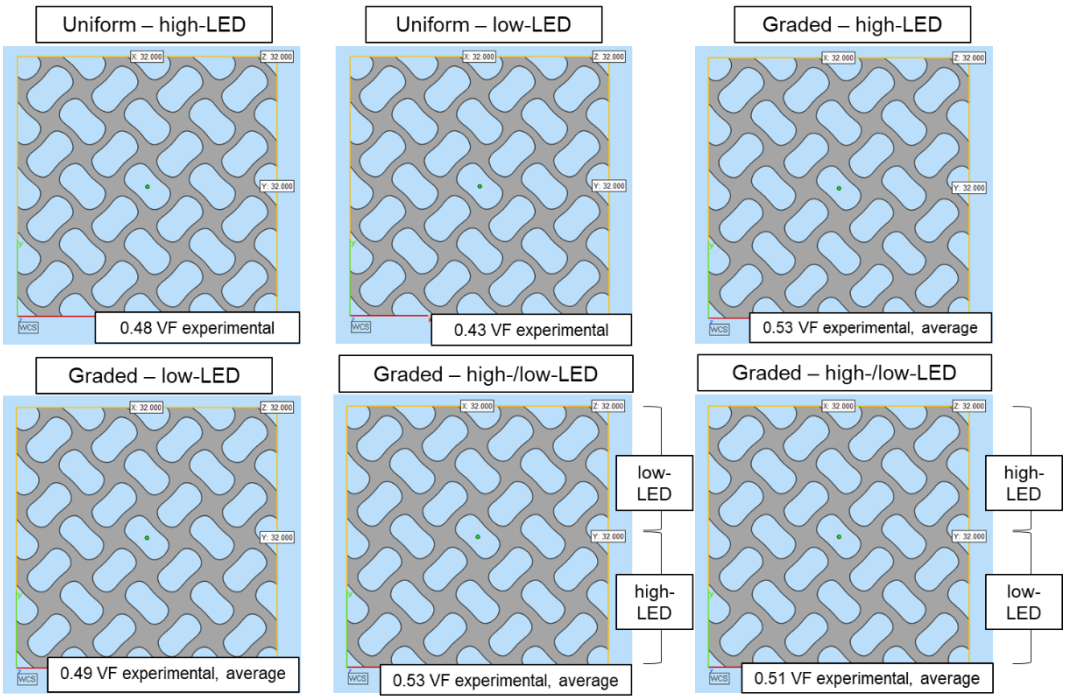

Figure 6.14. Overview of the 4 x 4 UC repetition experimental honeycomb gyroids, with size 32 x 32 x 32 mm^3 and printed with PBF-LB, with uniform or functionally graded VF. The actual VFs are specified.

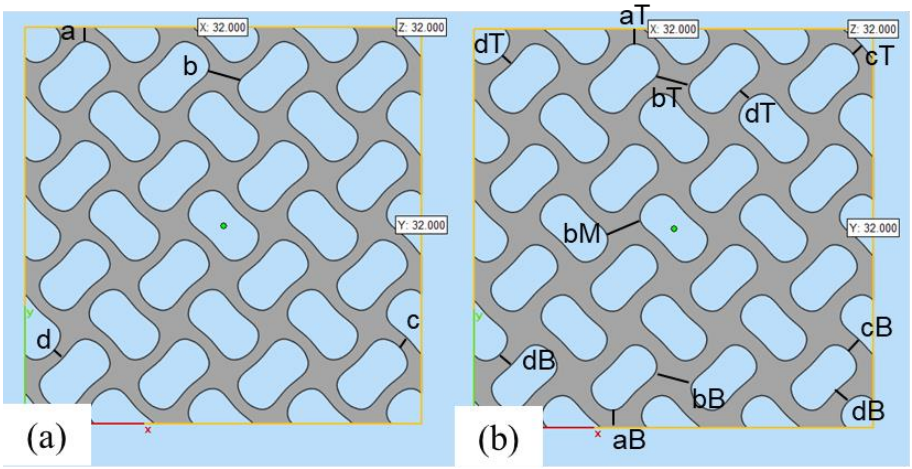

Figure 6.15. Dimensions checked for the printed lattice structures with 4 x 4 UC repetition and size 32 x 32 x 32 mm^3. (a) Uniform VF structures, (b) functionally graded lattices.

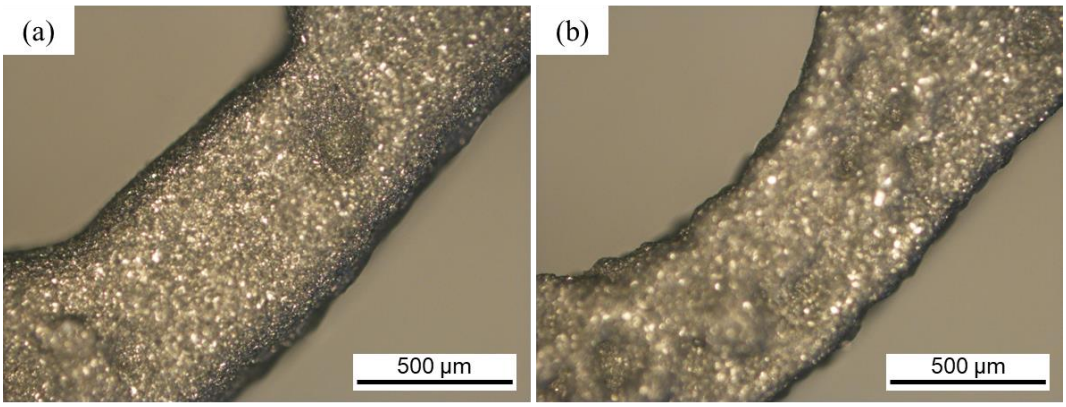

Figure 6.16. Overview of the *d* measurements for the uniform (a) high-LED and (b) low-LED parameter sets, from the printed lattice structures with 4 x 4 UC repetition and size 32 x 32 x 32 mm^3.

Table 6.6. Wall thickness check for the experimental 4 x 4 UC repetition lattice structures, with size 32 x 32 x 32 mm^3, for a comparison with the intended .stl thicknesses. The reported values for the printed lattices are the average of the taken measurements, while the error is the standard deviation.

Lattice Set	**a(aT) [µm]**	**aB [µm]**	**b(bT) [µm]**	**bM [µm]**	**bB [µm]**	**c(cT) [µm]**	**cB [µm]**	**d(dT) [µm]**	**dB [µm]**
Uniform .stl	1150	/	2640	/	/	950	/	950	/
high-LED 0.4 VF	1416 ± 79	/	2751 ± 110	/	/	1237 ± 151	/	1128 ± 30	/
low-LED 0.4 VF	1304 ± 40	/	2601 ± 47	/	/	1081 ± 27	/	1063 ± 58	/
Functionally graded .stl	1180	1410	2730	2930	3090	980	1300	1000	1280
high-LED graded VF	1427 ± 34	1536 ± 77	2708 ± 14	2919 ± 42	3003 ± 15	1183 ± 151	1460 ± 94	1126 ± 5	1473 ± 1
low-LED graded VF	1313 ± 28	1497 ± 40	2656 ± 13	2851 ± 24	3118 ± 12	1103 ± 34	1421 ± 13	1128 ± 2	1388 ± 71
high-LED/*low-LED* graded VF	1331 ± 22	1698 ± 34	2655 ± 5	2999 ± 34	3216 ± 19	1097 ± 82	1575 ± 23	1128 ± 48	1584 ± 77
low-LED/*high-LED* graded VF	1543 ± 19	1462 ± 21	2967 ± 9	3013 ± 15	3127 ± 13	1352 ± 169	1377 ± 11	1263 ± 56	1369 ± 130

The SEAs were extrapolated at the correspondent ε_D values, summarised in Appendix B and compared with the corresponding FEA counterpart, and shown in Figure 6.18. In addition, the average plateau strengths are depicted in Figure 6.19. The uniform VF *high-LED* and the graded VF *low-LED* structures had comparable average VF, with the former showing a 11.4% increase in SEA and 33.5% in average plateau strength than the latter. Considering the graded VF *high-LED*, the graded VF *high-LED/low-LED* and the graded VF *low-LED/high-LED*, with similar VF, the former exhibited 6.0% higher SEA and 30.2% larger average plateau strength than the second lattice, and 12.4% higher SEA and 54.0% larger plateau strength than the third lattice structure.

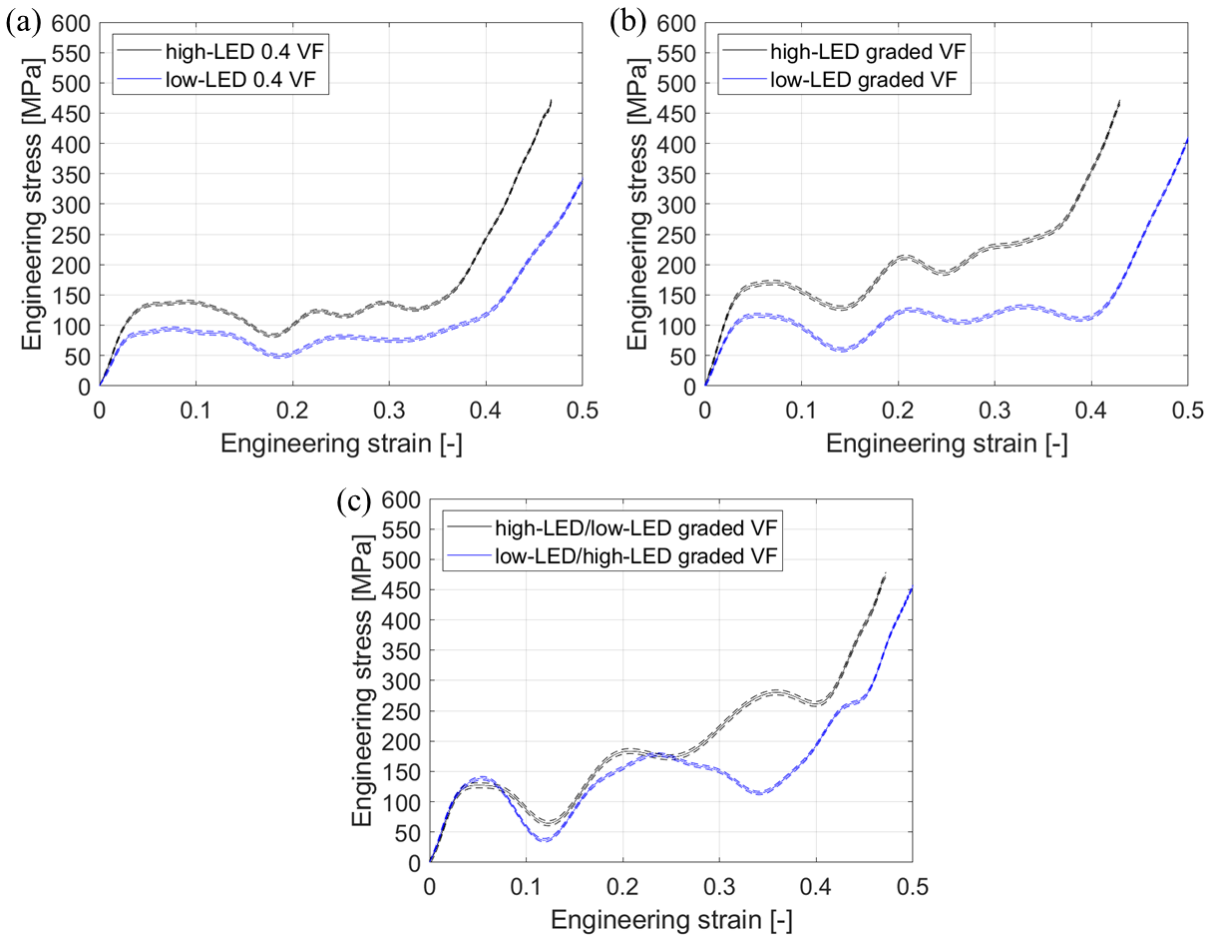

Figure 6.17. Experimental stress-strain curves, obtained from 4 x 4 UC repetition configurations with size 32 x 32 x 32 mm^3 : (a) *high-LED* and *low-LED*, 0.4 VF, (b) *high-LED* and *low-LED*, graded VF, (c) *high-LED*/*low-LED* and *low-LED/high-LED*, graded VF.

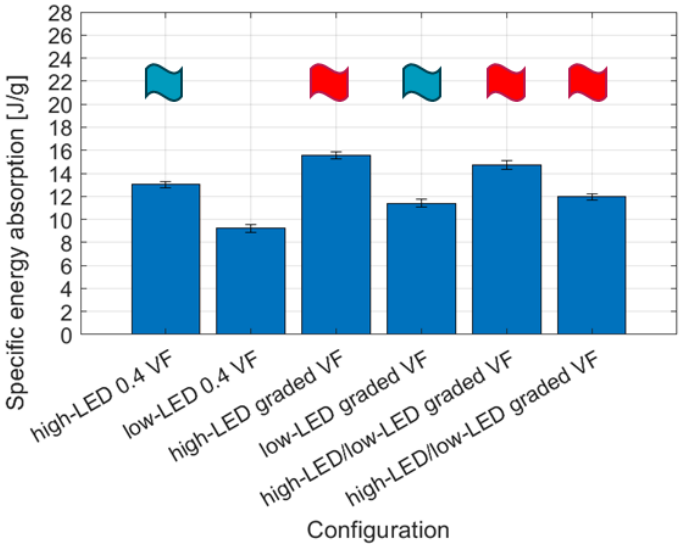

Figure 6.18. Experimental SEA at ε_D from the stress-strain curves in Figure 6.17. The flags point out configurations with similar VF from the PBF-LB process.

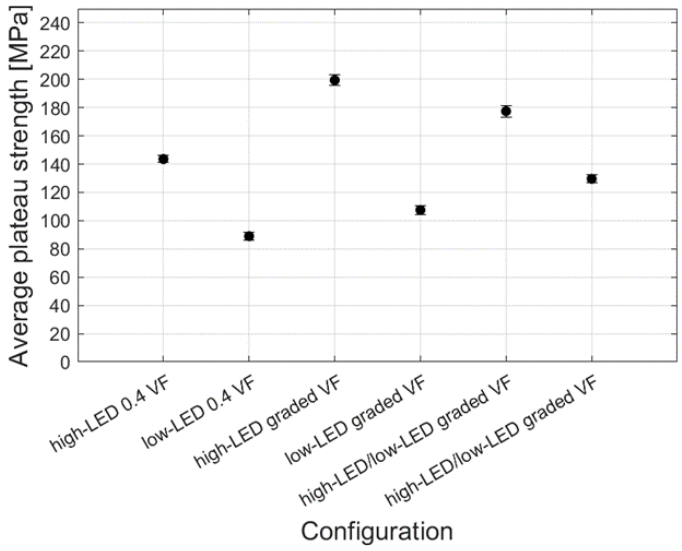

Figure 6.19. Experimental average plateau strength for the honeycomb gyroids with 4 x 4 UC repetition and size 32 x 32 x 32 mm^3.

6.1.5 Quasi-static and dynamic tests on 16 x 16 x 16 mm^3 cubes and 2 x 2 unit cell repetition

A smaller configuration was chosen for the purpose of physical testing in dynamic conditions, considering the testing limitations from Section 3.11. An identical set of configurations as Section 6.1.4 was selected, and the lattices are depicted in Figure 6.20.

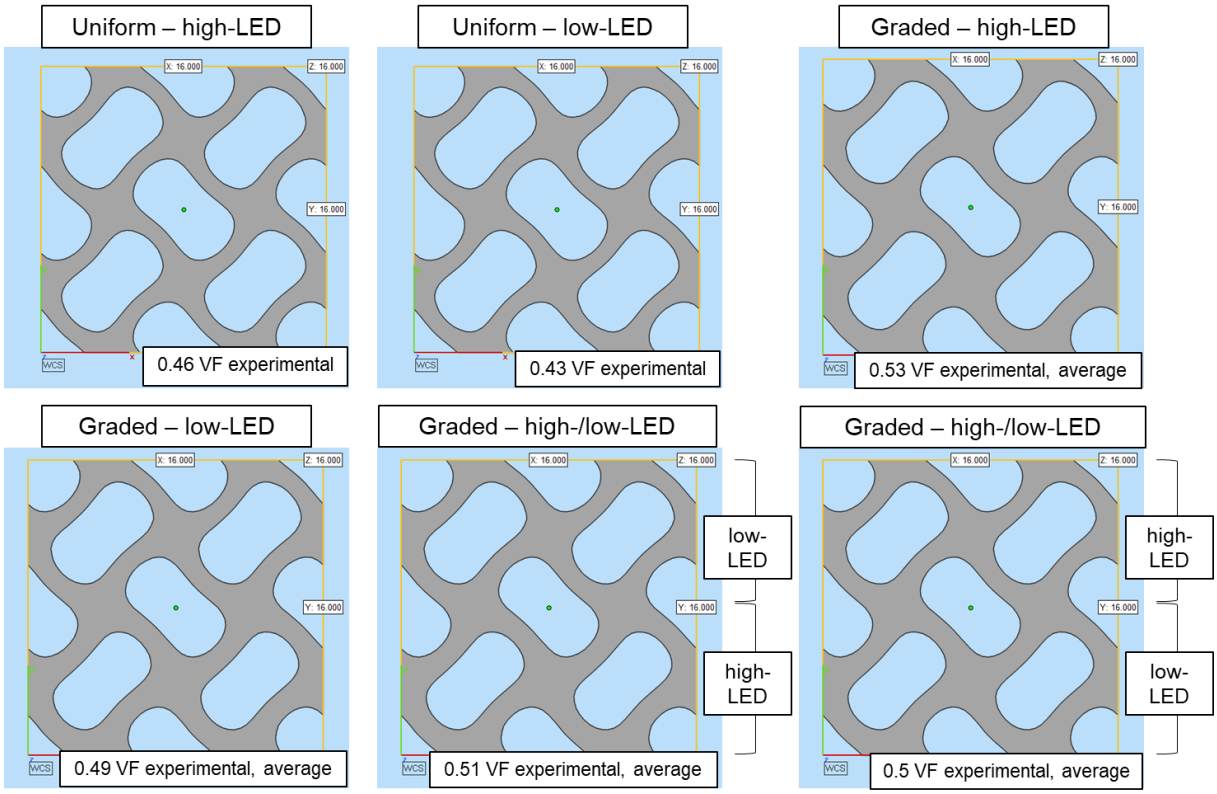

Figure 6.20. Overview of the experimental 2 x 2 UC repetition lattices, with size 16 x 16 x 16 mm^3, representing a smaller configuration of the structures presented in Figure 6.14. The volume fractions are uniform or functionally graded, and the material models are *high-LED* and *low-LED*, considered singularly and graded. The printed VFs are specified.

The geometrical accuracy of the printed lattices was performed as indicated in Figure 6.21. Table 6.7 contains the deviation of the measurements for the printed lattices to the .stl, along with the standard deviation for the former.

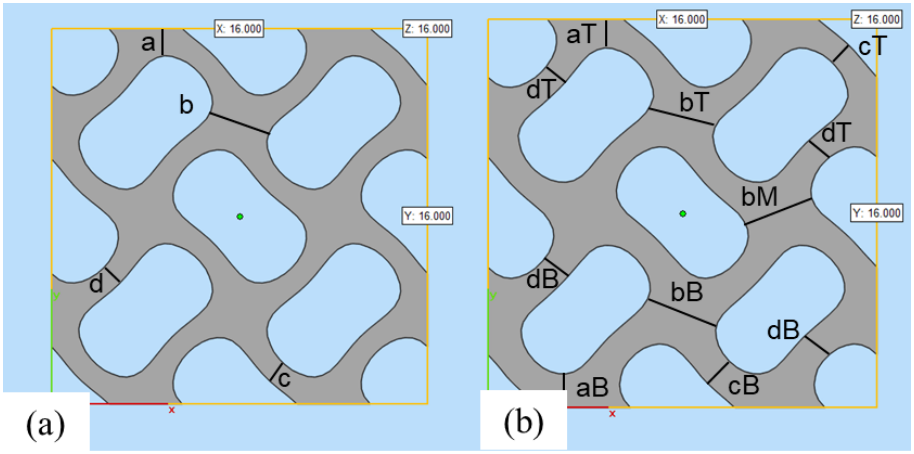

Figure 6.21. Dimensions checked for the experimental lattice structures with 2 x 2 UC repetition and size 16 x 16 x 16 mm^3. (a) Uniform VF structures, (b) functionally graded lattices.

Table 6.7. Wall thickness check for the experimental 2 x 2 UC repetition lattice structures, with size 16 x 16 x 16 mm^3, for a comparison with the intended .stl thicknesses. The reported values for the printed lattices are the average of the taken measurements, while the error is the standard deviation.

Lattice Set	**a(aT) [%]**	**aB [%]**	**b(bT) [%]**	**bM [%]**	**bB [%]**	**c(cT) [%]**	**cB [%]**	**d(dT) [%]**	**dB [%]**
Uniform .stl	1150	/	2640	/	/	960	/	960	/
high-LED 0.4 VF	1398 ± 78	/	2768 ± 100	/	/	1240 ± 166	/	1079 ± 55	/
low-LED 0.4 VF	1274 ± 14	/	2598 ± 56	/	/	1066 ± 49	/	1042 ± 81	/
Functionally graded .stl	1180	1400	2800	2940	3030	1000	1280	1050	1230
high-LED graded VF	1408 ± 6	1534 ± 56	2712 ± 8	2956 ± 77	3057 ± 6	1153 ± 156	1448 ± 99	1131 ± 13	1459 ± 50
low-LED graded VF	1295 ± 13	1477 ± 3	2677 ± 5	2899 ± 27	3114 ± 3	1125 ± 44	1416 ± 23	1103 ± 4	1385 ± 86
high-LED/*low-LED* graded VF	1342 ± 12	1696 ± 13	2692 ± 8	3048 ± 7	3250 ± 7	1092 ± 69	1562 ± 23	1112 ± 59	1551 ± 73
low-LED/*high-LED* graded VF	1537 ± 27	1471 ± 46	2973 ± 3	3024 ± 53	3155 ± 9	1367 ± 175	1361 ± 2	1287 ± 67	1373 ± 153

The related stress-strain curves for the 6 experimental and computational configurations are reported in Figure 6.22. The graphs can be considered as the repetition of what was obtained in Figure 6.17, though with a smaller sample size. Considering the experimental curves, among the structures with one process parameter comparable engineering stress values were detected with *high-LED* and *low-LED*. A similar trend was found for the graded VF structures with one process parameter, except for a stress drop for what concerned *high-LED*, to a value 54.8% of the corresponding lowest peak for *low-LED*. The lattices with process parameters and VF grading, had a comparable deformation up to ~ 0.2 strain, beyond which *high-LED/low-LED* underwent a sudden increase to 246.5 MPa before the last stress drop and densification; *low-LED/high-LED* experienced a stable stress increment until the structure eventually densified earlier than the other structure.

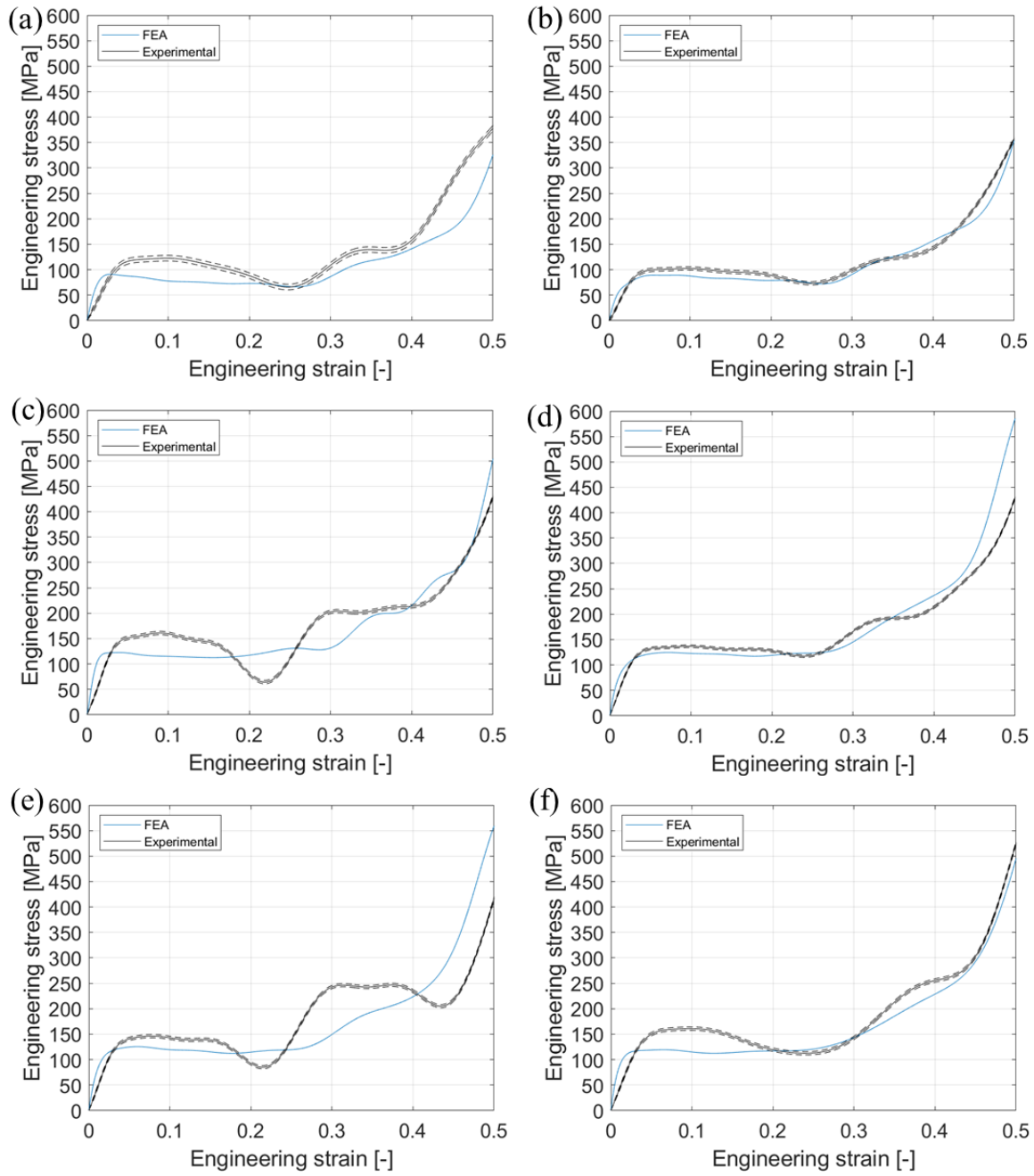

Figure 6.22. Stress-strain curves, obtained from 2 x 2 UC repetition configurations, with size 16 x 16 x 16 mm^3 for the experimental and 16 x 16 x 5 mm^3 for the computational samples, printed with 17-4 PH: (a) *high-LED* and (b) *low-LED* with 0.4 VF; graded VF with (c) *high-LED*, (d) *low-LED*, (e) *high-LED*/*low-LED*, (f) *low-LED*/*high-LED*.

The ε_D values, visible in Appendix B and compared with the FEA values, were used to determine the SEAs, shown in Figure 6.23(a) and (b). The corresponding average plateau strengths are displayed in Figure 6.24. Lower SEAs were detected for experiments than the corresponding simulations from the FEA model. The values are, compared to the computational model, from left to right, 86.3%, 85.0%, 90.2%, 83.6%, 105.1% (overestimating) and 92.7%. The computational results of the average plateau strength with *high-LED* had lower values than the corresponding structures with *low-LED*, as well as *high-LED/low-LED* compared to *low-LED/high-LED*. Experimentally, the opposed trend occurred. The deviation of the average value for the experiment to FEA corresponded to, from left to right, 15.9%, 2.2%, 10.3%, 1.5%, 9.0% and 6.1%.

Considering the experimental results, the uniform VF *high-LED* and the uniform VF *low-LED* structures had comparable average VF, with the latter showing only a 3.7% increase in SEA and 7.7% reduction in average plateau strength than the former. Concerning the graded VF *low-LED*, the graded VF *high-LED/low-LED* and the graded VF *low-LED/high-LED*, with similar VF, the second exhibited 25.5% higher SEA and 8.5% larger average plateau strength than the first lattice, and 11.4% higher SEA and 1.8% larger plateau strength than the third lattice structure.

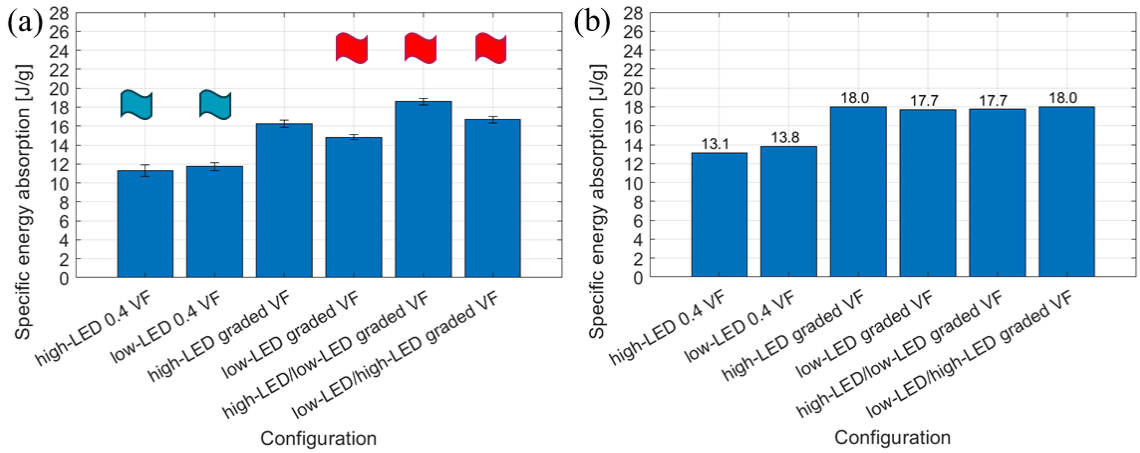

Figure 6.23. SEA at ε_D from the experimental stress-strain curves from Figure 6.20, with size 16 x 16 x 16 mm^3 for the experimental and 16 x 16 x 5 mm^3 for the computational samples: (a) Experimental and (b) FEA tests. The flags point out configurations with similar VF from the PBF-LB process.

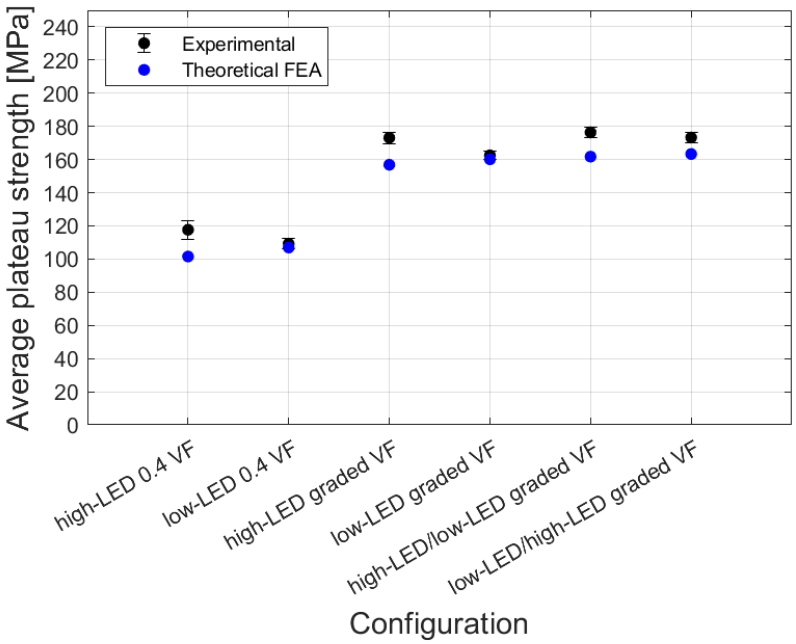

Figure 6.24. Average plateau strength for the honeycomb gyroids with 2 x 2 UC repetition, with size 16 x 16 x 16 mm^3 for the experimental and 16 x 16 x 5 mm^3 for the computational samples. Experimental and FEA results are compared.

The six configurations were then investigated under dynamic load, 1000/s and 2000/s. Because of time restrictions, only the FEA simulations were analysed and discussed. The stress-strain curves are in Figure C. 1(a-c). The mechanical curves with uniform 0.4 VF had the lowest response at any test condition, while the graded configurations provided stress-strain curves that intertwined each other at higher values. The detailed stress-strain curves, under the quasi-static and dynamic conditions, for *low-LED/high-LED* are shown in Figure 6.25. From the figure, it can be inferred that the plateaux of the quasi-static condition resulted as flat, and both dynamic tests displayed a peak at the end of the elastic region. Specifically, the increase of strain rate from 1000/s to 2000/s induced a larger peak before the decrease in stress across the plateau. In addition, an earlier densification phase was induced, occurring at lower strain for the 2000/s condition.

The ε_D values for each configuration and test type are presented in Appendix B, and the SEAs in Figure 6.26(a-c). The lowest energy absorption capability was for the configurations with uniform 0.4 VF, and *low-LED* had better performance than *high-LED*. As for the quasi-static condition, the peak was reached by the *high-LED* with graded VF as well as *low-LED*/*high-LED* at 18 J/g; the highest values for the dynamic tests were 17.4 J/g for the graded VF *high-LED* at 1000/s, and 16.3 J/g for *low-LED*/*high-LED* at 2000/s.

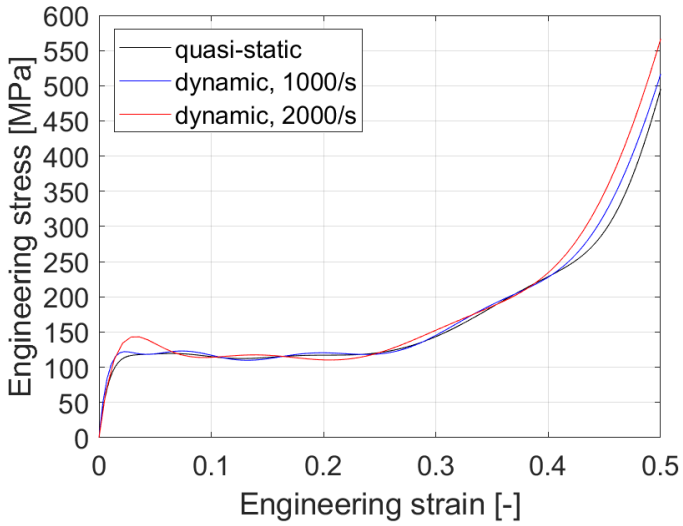

Figure 6.25. Stress-strain curves at different strain rates from the FEA simulations, obtained from the 2 x 2 UC repetition and 16 x 16 x 16 mm^3 lattices in Figure 6.20, with the grading configuration *low-LED/high-LED*. The quasi-static curve is in black, the dynamic at 1000/s in blue and the dynamic at 2000/s in red.

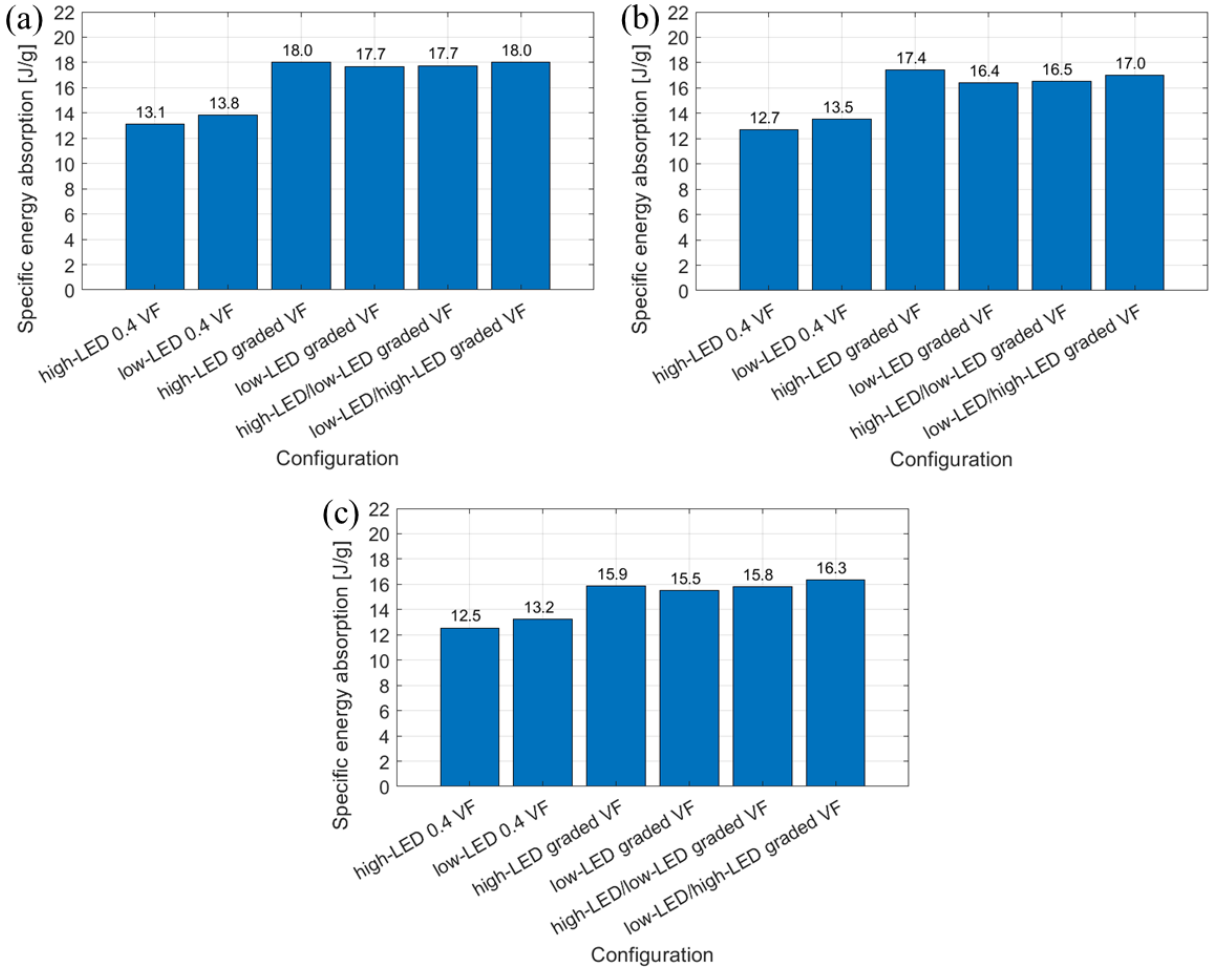

Figure 6.26. SEA extrapolated from the computational 2 x 2 UC repetition and 16 x 16 x 16 mm^3 lattices in Figure 6.20. The testing conditions are: (a) quasi-static, (b) 1000/s dynamic, (c) 2000/s dynamic.

6.1.6 Accuracy problems and damage model for the computational analysis

To determine the reasons for deviation and the accuracy of the computational curves to the experiments, two ways were followed. The first consisted in changing the material model in terms of E, σ_Y, stress values. The second considered the Johnson-Cook (J-C) damage model along with modifications to the material model. It was not possible to extract the J-C coefficients (C, D_1, D_2, D_3, D_5), therefore they were taken from the literature for the 15-5 PH martensitic stainless steel (respectively: 0.01368, 0.1136, 4.6159, 7.1074, -0.4944) [157]. The study was performed on uniform lattices with *high-LED* and *low-LED* for the 2 x 2 cell repetition configurations, respectively the *Uniform – high-LED* and *Uniform – high-LED* from Figure 6.20. Details of the modifications are in Table 6.8, while the plots are in Figure 6.27 and Figure 6.28, for *high-LED* and *low-LED* respectively. Figure 6.27(a) and Figure 6.28(a) reveal that a modification of properties approached the FEA model to the corresponding experimental curves, although a stiffer response was still detected. Considering the J-C model, Figure 6.27(b) and Figure 6.28(b), a more flat plateau was observed for *high-LED*, reaching similar values to the experiment with reduced material model; conversely, *low-LED* was characterised by a divergence for all attempts.

Table 6.8. Properties modified for the accuracy problem between computational and experimental results.

Investigation	Label	Values
Material model	M1	0.9*E, 0.9*σ_Y
	M2	0.9*E, 0.9*stresses
	M3	0.85*E, 0.85*σ_Y
	M4	0.85*E, 0.85*stresses
	M5	0.8*E, 0.8*σ_Y
	M6	0.8*E, 0.8*stresses
J-C + material model	J-C	/
	J-C1	0.9*E, 0.9*σ_Y
	J-C2	0.85*E, 0.85*σ_Y
	J-C2FC	0.85*E, 0.85*σ_Y, 0.4 FC
	J-C3	0.8*E, 0.8*σ_Y
	J-C3FC	0.8*E, 0.8*σ_Y, 0.4 FC
	J-C4	0.7*E, 0.7*σ_Y

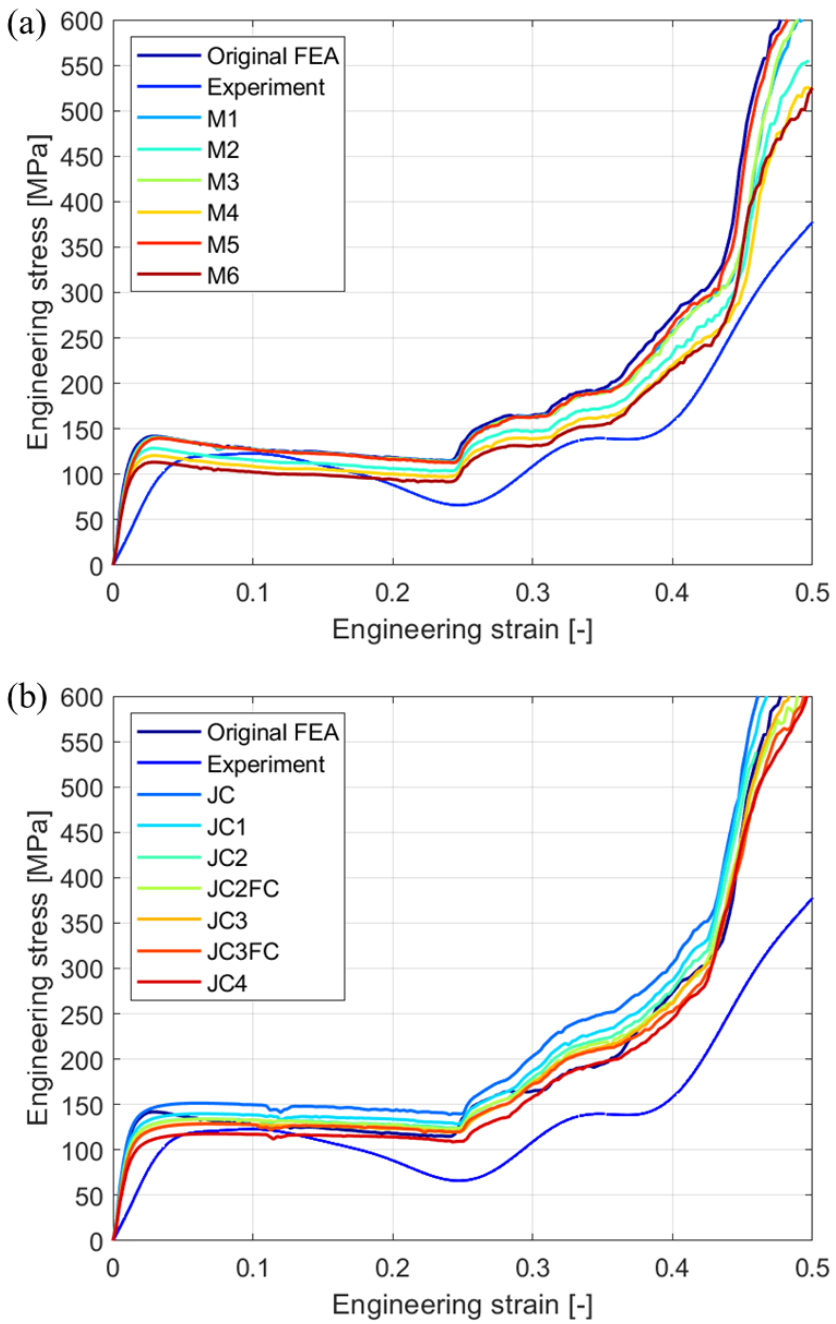

Figure 6.27. Matching investigation for the 2 x 2 cell repetition uniform lattice structure, with size 16 x 16 x 16 mm^3 for the experimental and 16 x 16 x 5 mm^3 for the computational samples, considered with *high-LED*. (a) Modifications on the material model, (b) J-C model and modifications on the material model.

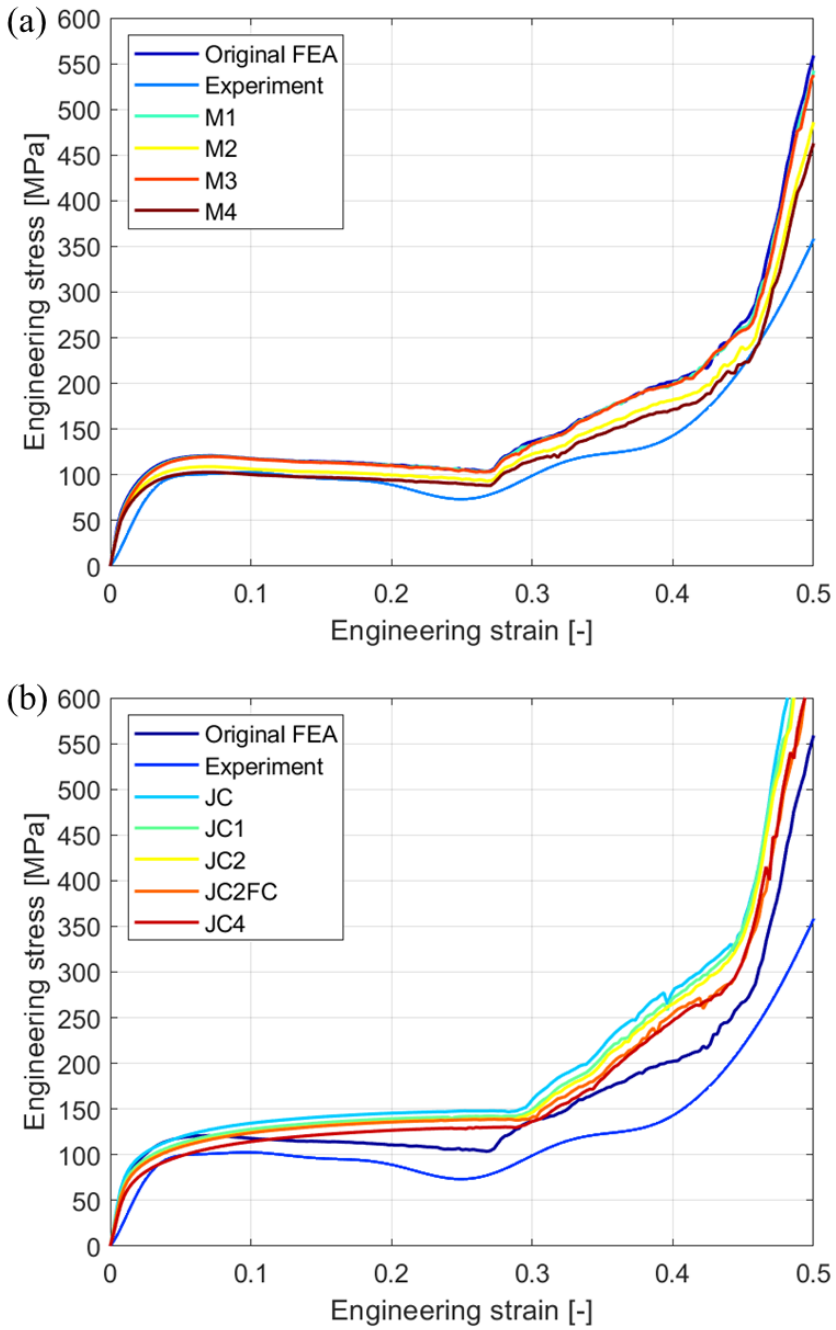

Figure 6.28. Matching investigation for the 2 x 2 cell repetition uniform lattice structure, with size 16 x 16 x 16 mm^3 for the experimental and 16 x 16 x 5 mm^3 for the computational samples, considered with *low-LED*. (a) Modifications on the material model, (b) J-C model and modifications on the material model.

6.2 Discussion

This Section discusses the most important features that emerged during the experimental and computational investigation of the honeycomb gyroid lattice structures printed with PBF-LB 17-4 PH. They are the outcomes

on the quasi-static results, the results on the behaviour at different strain rates, and the considerations on the accuracy of the FE model.

6.2.1 On the quasi-static computational and experimental results for honeycomb gyroid lattice structures

In Sections 6.1.2, 6.1.4 and 6.1.5, quasi-static experimental and computational investigations were conducted on honeycomb gyroid lattice structures with 17-4 PH and different cell repetitions. Considerations on the investigations are as follow.

With the first structures in Section 6.1.2, 5 x 5 cell repetition and 6 mm UC were examined to have the same configuration used for the validation [151] and avoid boundary effects [150]. From Figure 6.6, Figure 6.7 and Figure 6.8, it can be noted that rise of VF from 0.2 to 0.4 caused, for each process parameter, an obvious increase in the mechanical response of the lattice structures, as more material increases the general strength of the lattice structure [27]. Although ε_D decreases with the increasing of the VF, because the thicker UCs will come to contact earlier, higher average plateau strength occurred as previously found by Qiu et al for other TPMS based lattice structures [274]. Crashworthy capabilities of lattice structures are provided by determining the related SEA values. Even if better energy absorption is reached, increasing the VF implies a rise in the overall weight. Designing a crashworthy structure requires focus on the latter variable as well, because an increment will provide detrimental effects to the final performance of the structure and fuel consumption [275].

The VF selected to print lattice structures by means of PBF-LB affects in turn the accuracy of the printed parts, due to the dissimilar geometrical features that are obtained. Considering Section 6.1.2, the minimum and maximum unit cell thicknesses for the 0.2, 0.3 and 0.4 VF are presented, as well as the deviation of the volume fractions of the printed lattices to the .stl files (shown in Table 6.4). In particular, higher VF improved the accuracy by reducing the volume fraction deviation, and *high-LED* caused the largest variation. The technical limitations of the processing conditions, as surface roughness along the unit cell is increased due to thermal concentration in regions with high curvature for an excessive powder melting [271], are a key factor in the resulting accuracy issues. Previous studies determined how the meander strategy is not the ideal scan strategy for the PBF-LB process of lattice structures, because it does not precisely follow the borders of the thin walls. Vrána et al [276] demonstrated that a concentric scan strategy solved the surface roughness on lattices for a wide range of strut diameters from 0.6 to 3 mm. In this work, honeycomb gyroid was printed with the extrusion direction along the BD. The advantage of a concentric scan strategy is that the unit cell, curved, is scanned at each layer following the actual curved shape. The laser does not interrupt at each scan line, terminating on the internal and external thin walls, thus avoiding high surface roughness. In Chapter 5, the meander scan strategy

was used, hence its adoption for the lattice structures in this study. In addition, the largest discrepancy caused by the highest *LED* can be explained by considering Figure 5.4. The melt pools generated by *high-LED*, Figure 5.4(a), resulted larger than *low-LED*, Figure 5.4(b), determining an additional complication to the scanning of the lattices. Contrasts between VF from different *LED*s can be found in the work by Freeman et al [25]. In Section 6.1.3, straight thin walls were investigated at different thicknesses to determine the minimum threshold providing the lowest surface roughness and deviation to the intended design. Walls with too thin theoretical thickness experienced large deviations. The most affected configuration was with the *high-LED* process parameter set, a thin wall of 250 µm, and the default 50 µm the beam compensation. It was inferred that a larger beam compensation value could avoid the scan line to melt beyond the contour limit of the theoretical .stl as well as avoid increased energy in regions with higher curvature for an excessive melt of surrounding powder. Increasing the beam compensation to 100 µm and considering the 600 µm thin wall, helped reduce the accuracy problem. Similar outcome was previously determined in the work by Vrána et al [276]. To accommodate for the minimum thin wall thickness threshold of 600 µm, and the reduction of regions within the unit cell where excessive energy would concentrate, a larger unit cell size than 6 mm was chosen for the remainder of the project. The selected unit cell dimension was 8 mm while the choice of 4 x 4 UC repetition, investigated in Section 6.1.4, was a compromise in view of the reduced version, 2 x 2 UC repetition, studied in Section 6.1.5 to be considered in dynamic conditions due to the aforementioned limitations of the physical testing equipment (see Section 3.11). Nevertheless, increasing the unit cell dimensions and in turn the thickness of the unit cells, the 4 x 4 and 2 x 2 unit cell repetitions still showed accuracy problems, as depicted in Table 6.6 and Table 6.7. The dimensions labelled as *a*, *c* and *d* resulted in an average deviation of as high as 38% and 36.7% than the .stl files, for the 4 x 4 and 2 x 2 case, respectively. Contrarily, the dimensions referred to as *b* were defined by a much lower deviation, including shrinkage. This deviation variation across the unit cell was already discussed by AlMahri et al [162]. The main cause is ascribed to non uniform thickness of the unit cells, as opposed to different unit cells with more homogeneous and higher thicknesses. In fact, it was determined that thinner walls were the ones suffering from the largest deviation with respect to the .stl files.

The computational model, created in Abaqus, was meant to provide a tool for the prediction of the deformation behaviour of honeycomb gyroid lattice structures with functional grading and process parameter variation. The FEA was characterised by deviations from the intended designs of the generated meshes and was caused by their staircase effect (see Figure 6.2). Furthermore, there was accuracy discrepancy of the printed lattices to the FEA model. The printed lattices and their actual volume fraction deviated from the intended design in determined areas. The complexity of the honeycomb gyroid UCs, characterised by a change in wall thickness, determines a printed shape that is not following the intended design during PBF-LB. The cause is due to the physical phenomena occurring while the laser scans each specific location, in particular the reduced thermal conductivity of the powder surrounding the thin walls of the lattices, and the meander scan strategy that does not follow precisely the UC shape. The result is overmelting in thin regions (see Section 6.1.3), and the

irregular thickness transition along the UC determines initiation for local collapse and subsequent gliding of the structure while being compressed. In this study, the factor that was not considered is the presence of residual particles on the printed structures. In fact, the 2D feature of the honeycomb gyroid is extruded, which allowed to remove residual particles attached to the surfaces during the blasting process.

The discrepancy between printed and simulated lattice structures to the theoretical VFs implied limited comparisons between uniform VF lattices with different LEDs or graded VF lattices with dissimilar combinations of LEDs. This, including the stress-strain curves which act as result of the deformation behaviour to external load. Considering the 5 x 5 UC repetition, Figure 6.6, the experimental curves followed, with a good agreement, the *Sintered FEA* curves in the linear elastic and plateau region, confirming that only a small amount of weight was due to attached residual particles. The main difference for experimental curves was the presence of local collapse, due to instability from crack initiation sites of the printed lattices. This is a deviation from the homogeneous structures from FEA, that will need refinement as future work (as discussed in Chapter 7 and 8). The collapse of the experimental curves caused the structures to deform for longer strain values before densification, with gliding of the UCs that contributed to strength loss. This led some curves to follow the densification of *Theoretical FEA*. The presence of local collapse for the printed lattices was also noted with regards to the 4 x 4 UC repetition lattices response in Figure 6.17. In Figure 6.17(a-b) the structures with *low-LED* showed decreased stress because of the lower resulting average VF. A similar trend is followed in Figure 6.17(c), with the additional consideration that *high-LED/low-LED* has more material printed with *high-LED* which is present at the bottom layers; therefore, the highest strength of the lattice. The lattices in Figure 6.17(c) also include a layer of interface between the two *LED*s that introduces a third different microstructure for a few layers during the printing process, for a change in mechanical properties.

Taking into account the mentioned accuracy issues and their causes, with the FEA a trend for the deformation behaviour of the honeycomb gyroid lattice structures printed with 17-4 PH was extracted. In particular, the design of experiment presented in Section 6.1.4 demonstrated that the response of the honeycomb gyroid UC can be tuned depending on various functional grading as well as a change in material model. Various functional grading configurations were considered, following previous works such as the study by Niknam et al on strut-based or different TPMS based lattices [267]. The rationale is to vary the VF to enhance the performance of lattice structures. This, because a grading in the compressive load direction leads to a different response than a uniform VF distribution with the possibility of moving the deformation away from a sensitive object. In particular, the result is extended elongation and increased energy absorption. The range of uniform and graded lattice structures provided the expected distinction in response to compression, and the outcome is following described. As depicted in Figure 6.11, the configurations with the uniform VF showed a reasonable flat plateau before densification. A homogeneous compression of the UCs was at 40% strain, confirming that a lattice

structure with these characteristics will not show a slope in the plateau, up to densification. Substantial differences arose for the graded configurations. The smallest grading range, from 0.5 to 0.4, depicted a situation where the initial mechanical response was lower than the uniform structures. However, the engineering stress increased to a higher level at later engineering strain values. The difference became more evident when the other two grading configurations were analysed. By grading from 0.7 to 0.2, the top layer resulted weaker than any other configuration, which caused a sequential compression of the layers from top to bottom and left the uncompressed bottom layer at 40% strain. Investigations on different lattices with functional grading, to extract benefits as opposed to the correspondent uniform structure, are present in the literature such as Yang et al [170]. As for the lattices within the same configuration, the *high-LED* is characterised by an extended plateau, which means higher ε_D, than *low-LED*. This is explained with the behaviour of the standard specimens from Chapter 5. *High-LED*/*low-LED* followed the trend of *high-LED* more than *low-LED*/*high-LED*, because of the higher quantity of material at the bottom produced with *high-LED*. For each configuration the functional grading and mechanical properties both contribute to the resulting energy absorbed during compression. As a result, the 0.5 to 0.4 VF lattices presented a higher SEA for the configuration with *high-LED* and *high-LED*/*low-LED*. The same outcome occurred for the 0.7 to 0.2 VF configurations, with larger absolute values. Therefore, it can be inferred that grading with a large range between the bottom and top layers of unit cells allows for an extended ε_D. The latter affects the SEA capability in terms of an increase, which approaches the values determined as suitable to withstand the required energy involved in absorption applications [166,277]. This, considering that the in-plane direction is the weakest for the honeycomb gyroid unit cell investigated in this work.

The comparison regarding the SEA of uniform VF structures, between experimental and computational investigations, can be seen in Figure 6.7 and Figure 6.23. At comparable VF, higher SEA is obtained, experimentally and computationally, for *low-LED*. The reason is attributed to the better capacity of the LED to work harden, in agreement with Freeman et al, where higher content of retained austenite was found to be more performant for energy absorption applications due to their capacity of work hardening [25]. At increasing VF, for example 0.3 and 0.4 VF in Figure 6.7(a), the difference is more evident, the SEA resulting higher for *low-LED*, 12.9% and 5.9% respectively. 0.2 VF is defined by extremely low thickness that, during the bending and rotation of the thin walls, not enough compaction of the compressed UC layers occurred. The presence of more material (higher VF) is linked to the emergence of specific characteristic for each *LED*. Such an outcome was found by Li et al [26], where the strut diameter of the lattice structure was as low as 350 μm, no microscopic morphology differences were detected, and divergent *LED*s induced close SEAs. At this UC size, the better performance with *low-LED* derives from the mechanical properties of the material models. As described in Figure 5.9, although *high-LED* showed a higher σ_Y, *low-LED* entered an earlier strain hardening phase to reach a similar UTS to *high-LED*. The higher retained austenite content for *low-LED* is responsible for this behaviour during compression for the lattice structure. From Figure 6.7(b) and (c), the average values

of the experimental tests are in good agreement with the *Sintered FEA*. However, the reason lies in the bigger mass for lattices with *high-LED* than *low-LED*, that increases exponentially the mechanical properties with mass (and VF). To consider SEAs for functionally and process parameters graded lattices, Figure 6.18 and Figure 6.23 must be considered. In these experiments an earlier failure occurred, for the structures with average 0.45 VF and *low-LED*, which shows that lattices with uniform or graded VF, and only *high-LED* or *high-LED* at the bottom, resulted having higher SEA. The explanation is that *low-LED* is a process parameter that provides higher porosity, as demonstrated in Section 5.1.1.

6.2.2 A comparison between deformation behaviour at different strain rates

The investigation at different strain rates was performed with the 2 x 2 cell repetition lattice structures, only by means of FEA as explained in Section 6.1.5. As explained in Section 6.2.1, a unit cell repetition equal to or higher than 4 x 4 is needed to avoid boundary effects when investigating the behaviour of lattices structures under deformation. However, in Section 3.5 it was explained that, for the purpose of investigating dynamic conditions at high strain rates, limitations on the samples' dimensions to fit the testing equipment did not allow to consider the 4 x 4 cell repetition with size 32 x 32 x 32 mm^3, but a reduced configuration of 2 x 2 unit cell repetition and size 16 x 16 x 16 mm^3. This restraint led to the results obtained in Section 6.1.5, where the mechanical response characterisation of the dynamic conditions is presented. Nevertheless, the trend of the reduced configuration is compatible with the trend from the 4 x 4 cell repetition, extracted in Sections 6.1.4 and 6.1.5, and can considered as a reference to characterise the lattice behaviour at different strain rates.

From Figure 6.25 and Figure C. 1, it is possible to distinguish the characteristics of the mechanical response for each strain rate. The quasi-static simulations are characterised by a steadier response in the elastic region and plateau and the structures with 0.45 VF show higher stress than 0.4 VF. The lattices with *low-LED* start the plateau earlier than the others, with *high-LED*/*low-LED* and *low-LED*/*high-LED* that instead show a behaviour in the middle. Of the last two, having *high-LED* at the top provided higher stiffness because it is the first response to the compression load. The two dynamic tests, at 1000/s and at 2000/s, provided analogous elastic response. The main difference for the dynamic conditions is that the elastic response ended at higher stress values, before a decrease across the plateau. It was discovered that a strain dependent material, as 17-4 PH, undergoes an increment in yield strength with the strain rate, both in standard specimens [161] and in lattice structures [162]. In lattice structures, as described in Section 2.7.4, high strain rate impacts involve different properties affecting the deformation behaviour, which are the rate dependence of the base materials, the micro-inertia, the trapped and flowing gases in the lattice structure, the macro-inertia and the wave transmission properties. The deformation mode transition is therefore responsible for the yield strength enhancement [278]. In this study, this behaviour, resembling a stretching-dominated lattice structure, is more pronounced for the 2000/s case and leads to lower SEA. Such a mechanical response was found in standard

specimens [138], where an increase in work hardening rate occurred for the second highest strain rate across the plateau, that led to an increase in engineering stress at high strain values.

The dynamic test conditions, examined on the FEA simulations, resulted less performant in terms of SEA, as can be seen in Figure 6.26, down to 11.8% lower for 2000/s. The deformation response changes with strain rate, with a peak that forms at the end of the elastic region and decreasing stress in the plateau. In the literature, better response for dynamic conditions was determined by AlMahri et al [162], similar outcome by Li et al [168]. The model proposed in this study, however, is not supported by experimental tests to validate, and the limitations on the model that does not consider a proper damage fracture can affect the dynamic response of the FEA. Comparing 1000/s and 2000/s, a better performance was reached with the former strain rate. The reason can be found in the stress peak for the 2000/s configuration, that weakened the structures for the following compression strain values. As found by Brando et al [279], the σ_Y and UTS increase with the strain rate, while the ductility decreases. The highest SEA among the dynamic conditions is with the graded VF and *high-LED* lattice. The reason is in the extended plateau that allows for absorbing more energy.

6.2.3 Accuracy of the computational analysis, the role of Johnson-Cook model and comparison with the literature

The choice of the element type *C3D8R* was taken because of its capability of reporting with good accuracy the stress and strains in its integration point, when contact is involved. However, the meshing with hexahedral elements results problematic for the lattice structures generated in this study, as pointed out by Maskery et al [171]. The continuous change of shape of the UC is a factor in the accuracy problems of the UC. Conversely, a tetrahedral mesh (C3*D10*) would approximate better the surface contour, as explained by Mehmert [172] although the issues related to the self-contact problem prevented its use. Therefore, the mesh element type is one of the factors that must be addressed to approximate better the surface contour while solving the self-contact problem.

From Section 6.1.5, and particularly in and Figure 6.23, the deviation between the experimental and the computational lattices can be appreciated. The early failures of the experimental tests brought a deviation for the SEA that went from as low as 5.1% up to 16.4%. It is therefore important to take into account this when considering the present model in predicting the behaviour of lattice structures under compression, including dynamic conditions. As specified in Section 6.1.6, an attempt was made to understand the flaws of the computational model that made the FEA results diverge from the experimental results. On the experimental side, the outcomes were affected by local collapses on the UCs and sliding in the lattices, that caused the stress drop over strain. Moreover, a dissimilarity in the stiffnesses between FEA and experiments was found, as highlighted by Qiu et al [274]. On the FEA side, the lack of a damage fracture in the model caused the divergence between experiments and FEA. Therefore, modifying the material model, Figure 6.27(a) and Figure

6.28(a), helped approaching the FEA results to the experimental tests. Reducing all properties by 10% led to a close matching to the experimental curve. Therefore, stress wise an accuracy for the stress values of 10% is reached in the computational model.

For better precision, the J-C model must be considered, Figure 6.27(b) and Figure 6.28(b). A better representation of the elastic region was extracted, although the dissimilarity in the stiffness is still present. Introducing the coefficients for J-C model, the peaks at the end of the elastic region disappeared. Nonetheless, the coefficients taken from the literature are for a martensitic stainless steel [157] with high content of martensite. The plots cannot be considered representative of the *LED*s considered in this thesis and are used only to show a change of trend. This explains why, only modifying the material model in addition to the J-C model, the experimental curves were approached. In addition, the plots for *high-LED* resulted flat in the plateau region, meaning that the J-C coefficients are suitable for *high-LED*. Conversely, the plot for *low-LED* diverged from the unmodified FEA curve with a high slope plateau. Considering the not suitable J-C coefficients, only a 30% reduction of the material model, for *high-LED*, gives a stress-strain curve with reasonable trend than the experiment. This means that further experiments for appropriate J-C coefficients can lead to a proper match between FEA and experimental results.

A comparison with investigations on lattice structures from the literature is here presented, to infer the energy absorption capabilities of the honeycomb gyroid lattices with 17-4 PH of this thesis.

Some aluminium alloys show exceptional properties, for example the AA7075 [280]. Zhang et al demonstrated that it is possible to obtain comparable or even higher values of SEA for lattice structures printed with AlSi10Mg in quasi-static conditions [22]. The stiffness of the UCs investigated there, is higher than the honeycomb gyroid in the in-plane direction, as seen in Section 3.6. Therefore, the SEAs obtained by Zhang et al [22], up to 38 J/g for a uniform dodecahedral uniform structure, are obtained thanks to the intrinsic mechanical properties of the UCs.

Titanium alloys, such as Ti6Al4V, show high strength and low ductility [281], and Zhang et al investigated network and sheet solid TPMS lattice structures printed with this alloy under quasi-static conditions [23]. This provided SEAs ranging from 17.5 J/g for a uniform structure up to 28.5 J/g for a functionally graded structure with nanoparticles addition. As a result, the functional grading and material development allowed to achieve more performant material.

As for 316L stainless steel applied to TPMS lattices under quasi-static conditions, Li et al [24] analysed the response of graded and uniform skeleton and sheet diamond structures. The mechanical response of the structures, whose UCs have higher stiffness than the honeycomb gyroid, provided extended ductility and lower values of stress than 17-4 PH. The functional grading of those lattice structures increased the SEA from uniform lattices, but did not produce SEAs higher than 20.5 J/g.

Quasi-static compression tests were also performed on lattice structures printed with maraging steels, whose microstructure is similar to 17-4 PH, martensitic phase with low content of retained austenite, and the mechanical properties approach 17-4 PH [282]. In the study by Ku et al [55], a strut-based lattice structure, based on the stiff cubic UC in the main lattice directions, was tested in compression and provided SEAs up to 35.1 J/g. This implies that high strength steels can be used in combination with lattice structures for the purpose of increasing the specific energy absorption in crashworthy applications.

Considering the examples provided in the literature about functional grading or material modifications, it is important to stress that similar order of magnitude for SEA is obtained in this study, even if the stiffness of the honeycomb gyroid UC, in the in-plane direction, results the lowest as described in Section 3.6. In fact, the stiffness ranges from a minimum of 3.8% up to a 36% of the value determined on the UCs investigated so far. This confirms that the exceptional strain hardening behaviour of 17-4 PH helps lattice structures reaching high energy absorbed during compression. Functional grading as well as different *LED*s can tweak the microstructure and the mechanical response of lattice structures under deformation.

6.3 Summary

This Chapter focuses on the application of the strain hardening 17-4 PH stainless steel to produce with PBF-LB honeycomb gyroid lattice structures for crashworthy applications. A computational model was developed, validated and applied to different configurations of lattice structures. A comparison with experimental results was carried out. The main findings are summarised below:

(1) A computational model was created and validated against a material model of PA2200. Challenges in the meshing of the honeycomb gyroids were pointed out.

(2) Printing lattice structure with three uniform VFs and the *LED*s from Chapter 5 was performed. A good agreement between the FEA and experimental testing was obtained. *High-LED* provided the highest energy absorption, and challenges in printing the lattices were faced.

(3) An investigation on straight thin walls provided 600 µm as the lowest threshold to avoid tolerance issues. The meander scan strategy was one of the causes, as well as the wide melt pools from the printing process. The unit cell size of 8 mm was therefore chosen.

(4) A design of experiment with 18 configurations and 4 x 4 cell repetition provided a comparison between uniform and functionally graded structures, with the additional variable of *LED*. The outcome is that the largest grading from 0.7 to 0.2 caused the highest SEAs, up to 20.2 J/g for the uniform lattice with *high-LED*.

(5) Physical lattice structures were printed out of the previous design of experiment. Dimensional deviation was found, due to the dissimilarity between the mesh and .stl files along with limitations of the meander strategy. Higher SEA was extracted for the structures with *high-LED* as opposed to *high-LED*/*low-LED* because of the higher tendency of structural failure for *low-LED* over strain. Better performance was found also in the uniform *high-LED* than graded *low-LED* thanks to the extended plateau.

(6) The difference in UC number for the 2 x 2 cell repetition structures, and resulting VF, led to dissimilarities in compressive response. The same printing challenges were found, along with local collapses during the physical experiments, even if the trends between experiments and FEA were in good agreement. The FEA showed that the graded VF with *high-LED* and *low-LED/high-LED* provide more SEA, but the experimental flaws caused *high-LED*/*low-LED* to prevail.

(7) Dynamic tests were performed with FEA. The designed lattice structures changed the response to the external load, from a quasi-static to a dynamic case. The elastic response reached a more pronounced peak moving in the dynamic case at 2000/s; the plateau for the dynamic conditions was characterised by a decrease until densification. The dynamic conditions provided lower SEA than the quasi-static condition with a peak of 17.4 J/g for the graded VF *high-LED* at 1000/s.

(8) The SEA values from this study were compared with results from the literature. Considering a range of materials, including 17-4 PH, functional and material grading, and different unit cells (all stiffer than the honeycomb gyroid), a maximum SEA of 38 J/g was found. Considering the largest SEA from this study, 20.2 J/g for the graded structure from 0.7 to 0.2 VF and uniform *high-LED*, the potential of the PBF-LB honeycomb gyroid UC with 17-4 PH for effective crashworthy applications was inferred.

7 Conclusions

The aim of this work was to provide a comprehensive understanding of the deformation behaviour of two strain hardening stainless steels in the plastic regime produced with PBF-LB, 316L and 17-4 PH, to develop a new approach for energy absorption improvement through a combination of microstructure tailoring and cellular structure design. Honeycomb gyroid lattice structures were printed with 17-4 PH, at different strain rates for the purpose of crashworthy applications. Conclusions from each Results Chapter are here provided.

7.1 The role of deformation slip and twinning-induced plasticity in PBF-LB 316L in the plastic regime

Chapter 4 studied the twinning-induced plasticity mechanism in PBF-LB 316L stainless steel. The as-printed properties of the material were extracted to infer the absence of twinning and residual stress. Mechanical properties of a standard tensile geometry were obtained, and the deformation was replicated with good accuracy with an FEA model to be used for twinning investigation. The TWIP behaviour was analysed by means of a tapered geometry to obtain, on the same specimen, information on the evolution of stress, plastic strain, hardness and twin concentration. The FEA model was accompanied by experiments to infer information on the onset and development of twinning over plastic strain. The main conclusions are summed up as follows.

A process parameter from the processability region provided typical PBF-LB microstructures, with preferential orientation of the grains along the BD (which corresponds to the thermal gradient direction). A random orientation of the dendrites was obtained together with a weak texture of the crystallites. Moreover, no twinning was detected forming from the PBF-LB process. This explains the reason why a homogeneous material model can be used to describe a PBF-LB microstructure. The absence of twinning in the as-printed material means that no residual stress occurred during the solidification process and the strain hardening mechanism occurs during the plastic deformation.

Higher values of yield strength, ultimate tensile strength and ductility for 316L printed with PBF-LB were extracted as opposed to conventional manufacturing technique. The strength is given by the hierarchical microstructure spanning a wide range of size for the material microstructure, Hall-Petch effect, and the dislocations that are present in the as-printed condition and that form during the deformation. Dislocation pinning is another phenomenon previously characterised that allowed for the generation of twin bands, that increased in concentration with plastic strain thus causing the extended ductility up to 55%.

An FEA model was used in support of the experimental investigations to extract physical properties. A validation process was performed based on the results from the standard specimen. The homogeneous material

model proved to be consistent with the experimental outcome. The approach enabled the preliminary analysis on the tapered geometries that were used for the determination of the onset and development of twinning in the study.

A tapered specimen was used with a specific geometry that allows for a load-bearing area reduction across the gauge length. The tapered angle of 1.4° for the selected geometry was effective in the generation of information on twinning with a single test due to a reasonable section of the gauge length affected by deformation during the quasi-static test. The FEA played an important role in defining the proper geometry to use.

Experiments on the tapered geometry showed that the deformation mechanisms linked to TWIP take place since the beginning of the plastic regime and continued up to the fracture of the specimen at 60% plastic strain, increasing in magnitude with the plastic strain. Twinning presents two phases. Preferred oriented grains start twinning first, and then the others follow while a reorientation of the grains continuously changes due to the acting load. Grain size is another fundamental in activation of twinning. Small grains show a negligible contribution to the overall twinning mechanism. They are instead characterised by dislocation movement, whose high concentration does not allow for reaching the SFE to form twin bands. The concentration of twin bands was negligible up to 15% plastic strain and then suddenly increased. This proves that twinning is a strain hardening phenomenon that occurs in synergy with deformation gliding. The latter is the preponderant mechanism until the SFE for twinning is reached in all large grains. It is responsible for the increase in stress and hardness while only locally twinning is activated. Hardness is another quantity that continuously increases at any plastic strain because of both deformation mechanisms.

The work proves the effectiveness of a tapered geometry for the investigation of strain hardening occurring in PBF-LB 316L. This methodology is suitable to study the onset and evolution of twinning in PBF-LB 316L, as well as the complex interaction with deformation glide, under different laser process parameters for a prediction over the material for the activation rate of twinning. By exploring the process window of 316L, it is possible to control the material's microstructures, and this enables designers to 3D print components with tailored microstructures for specific deformation behaviours. Given the possibility of printing complex shapes by PBF-LB, this allows PBF-LB to be used in crashworthy applications. Therefore, this methodology is advisable for the investigation of strain hardening materials.

7.2 Importance of linear energy density for the microstructural and TRIP control of PBF-LB 17-4 PH

In Chapter 5 the transformation-induced plasticity behaviour shown by 17-4 PH stainless steel produced with PBF-LB was investigated by varying the linear energy density. The as-fabricated conditions were analysed, and it was inferred that different energy densities produce dissimilarities in starting phase content and

microstructural features, as well as mechanical properties under deformation. Finally, based on the obtained results, the final microstructural features were determined, and the differences explained due to the contrasting TRIP activity that involved them. The main conclusions are presented as follows.

Process parameter sets from the processability region were considered at different extremes. This helped comprehending that different linear energy densities, while providing high density, have a consequence on the phases present in the material, the microstructure, the grains size, the grain orientation and crystal texture. This is due to the different cooling rate provided by the printing process parameters that favours or prevents the transformation of the austenite into martensite or ferrite. Higher energy causes more BCC, therefore higher hardness and irregularity in the grain size due to remelting of the layers beneath.

The mechanical testing captured the differences detected by the material investigation. A higher content of FCC, given by the lower energy density, caused a reduction in σ_Y of 55.4% compared to the other process parameter set. However, the reduced stiffness was counterbalanced by a sudden increase in strength in the plastic regime, to reach a 4% increment in ultimate tensile strength. This is caused by the TRIP activity that characterises this steel. The preponderance of the TRIP activity as opposed to a specimen with lower FCC, as in the case of higher energy density, is a reason for the earlier failure of the specimen due to locally reduced ductility at the necking.

The fractured surfaces provided an explanation of the mechanical curves. Higher energy density leads to larger content of BCC in the material. The resulting necking regions show a mixture between brittle, due to harder phase, and ductile, typical of softer phase, fracture. The presence of higher content of FCC given by lower energy density accomplished a ductile behaviour at the necking region, revealing the divergent outcome.

The study showed how in-situ XRD analysis during mechanical testing is a powerful tool to investigate the phase evolution of a TRIP steel over strain. Higher energy density caused 17-4 PH to contain 34.2% of the FCC than a lower energy density. The XRD analysis explained the dissimilar TRIP activity for the two process parameters and the role of plastic strain. In addition, a similar final phase content was determined. The specific evolution requires microstructural investigation to understand how the same result was obtained.

The microstructures investigated after the failure of the tensile tested specimens were largely influenced by the as-fabricated conditions and the TRIP activity. Higher energy density left larger grain size distribution that underwent a more predominant recrystallisation of the microstructure, that might have been beneficial for the extended ductility of the specimen. Furthermore, the lower FCC content did not allow for a redistribution of the orientation of the crystallites in the material, as occurred for the lower energy density configuration.

The study stresses the importance of the control on the microstructure and phase content of the as-fabricated 17-4 PH steel with PBF-LB. Each phase and microstructure provide bespoke properties to the printed material. Specifically, in terms of hardness, yield and ultimate strength, and elongation at failure. The differences that arise allow a control of the starting conditions to engineer specific feedback from the material. This is important

to obtain the required strength, ductility or hardness depending on the final application that needs at the same time a stainless steel with resistance to wear. Experimental activities on the processability region can be accompanied by the generation of a computational model that receives the experimental results as input, to create a database for the prediction of the starting microstructure and phase content, as well as the mechanical properties that derive from the tuning of the energy density (represented by a set of laser process parameters). The combination of the experimental and the computational approach represents a critical starting point for the solution of the optimisation problem linked to the design of new applications to be used in the field of energy absorption.

7.3 Towards a computational model for the prediction of lattice structures compressive behaviour

In Chapter 6 the deformation behaviour of honeycomb gyroid lattice structures printed with PBF-LB 17-4 PH stainless steel was studied. A computational model was validated under quasi-static conditions and used for investigation on the energy absorption of uniform lattice structures. The comparison with experiments showed good accuracy. The dimensional deviation in the printing process required further investigation to determine the smallest thickness threshold. This led to a study on uniform and graded lattices under quasi-static and dynamic conditions, for energy absorption considerations. The main conclusions can be summarised as follows.

A FEA model was validated against experimental curves under quasi-static condition. This is important to couple experimental activities with computational modelling for an optimisation of the investigation process.

The model, applied to uniform lattices with two 17-4 PH process parameters, showed good agreement with the experiments although physical limitations were exhibited by PBF-LB. This points out the importance of a valid printing process other than the FEA model, for a match as close as possible between the two approaches. The printing process, with the used process parameters, generates accurate wall thicknesses past 600 μm with a beam compensation of 100 μm. This analysis supports the choice of the unit cell of the lattice, 8 mm in this study.

The computational model shows an important limitation in the prediction of the deformation behaviour of lattice structures under compression with high accuracy. The reason resides in the lack of a ductility damage model (such as the J-C model) that enables an accurate description of the deformation of the material considering, among the others, the thickness of the material, the strain hardening rate over strain and the temperature at which the test occurs. While the plateau behaviour is described with a reasonable agreement, apart from the stress drops, the stiffness of the elastic response and the densification are not matched with the material model used in this study.

The FEA design of experiment under quasi-static condition, on lattice structures with uniform and graded VF and process parameters, proved that a large VF grading range provides an extended ε_D for higher specific energy absorption. Specifically, for the unit cell geometry used, the graded lattice with *high-LED* showed the best performance thanks to the largest ε_D. This result is strongly dependent on the unit cell and size, therefore each configuration needs specific investigation.

Although the divergent VFs for printed lattices did not allow to compare all configurations under quasi-static condition, the structures with similar VFs are shown to provide a good agreement with the computational model, considering the limitations of the latter. This is important because it explains that FEA is a powerful tool to describe the deformation of lattice structures, when all deformation models are considered.

A comparison between computational analysis at quasi-static and dynamic conditions revealed that increasing the strain rate follows experimental studies from the literature, where different physical principles occur: increment of the stiffness and eventual stress reduction in the plateau. The strain hardening behaves differently, and experimental tests are needed to validate the obtained results in this thesis.

The specific energy absorption values from this thesis are comparable to strut-based and other TPMS based lattices from the literature. This concludes that a lattice structure, based on the honeycomb gyroid unit cell, can be used for energy absorption purposes at quasi-static and dynamic conditions thanks to the demonstrated good absorption capabilities of the unit cell in the investigated in-plane direction. The latter is known to have the lowest stiffness among all the unit cells of lattice structures. These results make the honeycomb gyroid a good absorber in this direction and a high-performance structure in the out-of-plane. Therefore, the honeycomb gyroid printed with strain hardening 17-4 PH is a suitable structure for crashworthy applications.

The work provides the importance of adopting a computational model for predicting the deformation behaviour of lattice structures printed with PBF-LB. The homogeneous material model that PBF-LB materials supplies enables reliable results of lattice structures under deformation, also with complex materials as TRIP steels. The methodology is a first step towards the prediction of energy absorption. It is crucial to integrate the model with the proper damage fracture information to reliably describe the failure of the lattice structures at any strain rate. The main benefit for designers is that such a process reduces the physical experiments to perform in order to validate a crashworthy component.

8 Future work

This thesis aimed at examining PBF-LB processed TWIP and TRIP steels, and the use of these materials in lattice structures crashworthy applications. However, as these deformation behaviours depend on complicated mechanisms, laser scanning processes and related microstructural features or phase content, this PhD cannot be exhaustive of the investigated phenomena and how they affect the energy absorption. In this Chapter, some critical topics are presented that need consideration to obtain a comprehensive knowledge of the strain hardening mechanisms and their application to energy absorption components.

This project proved that strain hardening mechanisms occur in the plastic regime, even locally in favourable oriented grains during the elastic deformation. It is of interest to explore different process parameters of the process window for 316L, aiming at determining how different microstructures and grain size distribution affect the plastic strain threshold and the resulting twin bands concentration, for a deformation response with higher strength or ductility. Another fundamental aspect to consider is a range of energy density to apply to 17-4 PH, because different as-built microstructures and phase contents are reached, in particular retained austenite. As a consequence, dissimilar transformation-induced plasticity phenomena are obtained which can accommodate for a mechanical response to deformation that is with higher strength or ductility. Such investigations will lead to a customisation of the microstructure, phase composition and mechanical properties response when it comes to designing crashworthy applications.

The tapered design used for 316L in this study, is advisable to be applied to the study of 17-4 PH. In this project, an in-situ XRD analysis was performed during the mechanical testing, but it is not always possible to have access to such facilities. The tapered design can provide deformation information on the same specimen at different strain values, and XRD analysis can be performed on specific cross-sections. A similar approach can be transferred to the context of lattice structures. In this thesis, it has been shown that the deformation of lattice structures depends on the uniformity or grading of the VF or the process parameters. Performing interrupted tests or tests to failure on graded lattices and following the same approach in Chapter 4, a designer could retrieve precious information in terms of the activation of strain hardening mechanisms in specific locations of the lattice structures.

One of the main important features throughout the entire research was the PBF-LB scan strategy, meander with 67 degrees rotation of the scan lines at each layer increase. The latter provides a random formation of the melt pools throughout the build and the homogenous heat dissipation through the printed material causes generally a random orientation of the grains. The results obtained in this thesis are based on the homogenous material models obtained due to that choice. In the literature, it has been demonstrated that dissimilar scan strategies have different effects on the resulting microstructures and phase content. A stripe strategy, for example, forces a direction to the melt pools and the microstructure can result highly textured. Among the others, the concentric strategy has been extensively described as the most suitable for lattice structures, thanks

to its capability of following the thin wall contours of the lattices. In this research, surface tolerance issues have been shown with the meander strategy. Performing the entire investigation of this thesis with a concentric scan strategy would provide a better approximation of the borders and less defects for crack initiation. Moreover, specific activation of the strain hardening phenomena might be expected.

One of the main focusses of this research has been to generate a computational model to predict the deformation behaviour of TPMS based lattice structures under deformation, at different strain rates. The material model of 17-4 PH provides a good first step into the description of the deformation trend for lattice structures printed with 17-4 PH. However, inaccuracy of the stiffness and failure modes of the unit cells have been observed, that the model has not been able to replicate. It is crucial to perform additional tests on 17-4 PH for the extraction of coefficients for the Johnson-Cook failure mode and describe with high accuracy the deformation of the lattice structures.

The analysis on lattice structures from Chapter 6 has been concluded with a comparison of honeycomb gyroids, considered in different configurations at different strain rates. The results are presented in terms of computational model only. The lack of proper available equipment did not allow for an experimental investigation at the same 1000/s and 2000/s rates, investigated with FEA. The next step is to perform physical dynamic experiments on the lattices considered for this project, and extract the energy absorption. It is known that dynamic analyses are based on different physical principles than quasi-static investigations. Hence, physical experiments would give feedback on the computational model and eventual modifications to apply to the model.

Finally, this project focused on the energy absorption capabilities of the honeycomb gyroid lattice structure along its in-plane direction, providing information on the capabilities of the structure with strain hardening 17-4 PH. For this unit cell, to complete the analysis it is important to consider a similar approach on the out-of-plane direction, that is characterised by the highest stiffness among the unit cells to consider for lattice structures. A computational and experimental analysis would result in SEA values that could overcome any other results obtained so far in the literature. The gathered information will be a fundamental step into the development of lattice structures for driving the deformation and designing damage-tolerant lattice structures. The literature has extensively studied the mechanisms underlying shear band activities emerging during strut-based structures deformation, to provide prediction of the local deformation behaviour in hybrid configurations, for controlled mechanical strength and damage path [154,283]. Different unit cells and orientations were investigated to increase the compression capabilities and decrease the transmitted stress to the protected object. Replicating a similar approach with the honeycomb gyroid or other TPMS based lattices will open up new scenarios to crashworthy applications.

This project addressed with good results the research questions that were presented in Chapter 1, in terms of the capabilities of understanding complex deformation mechanisms and their applications into the energy absorption. However, this Chapter has highlighted the importance of a few considerations necessary for a

deeper understanding of the phenomena involved in these materials and structures, for more accurate results. This is crucial for the final aim of applying the found results to industrial applications.

Appendix

A. Sensitivity study for the honeycomb gyroid lattice structures

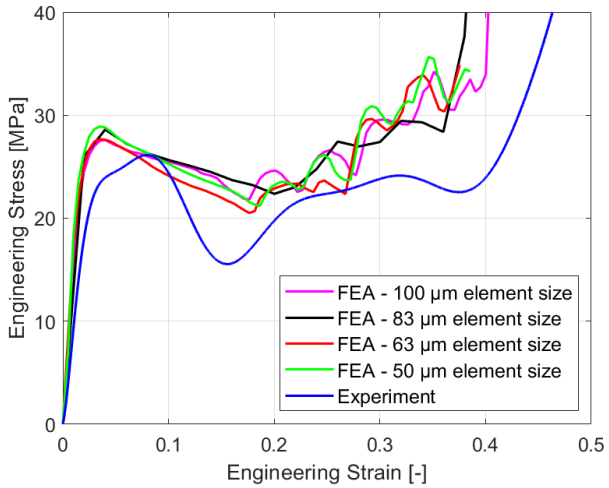

Figure. A.1. Stress-strain curves for the mesh sensitivity analysis of the FEA model for the UC with 6 mm length size. 50, 60, 80 and 100 resolutions correspond to 100 µm, 83 µm, 63 µm and 50 µm mesh element size, respectively.

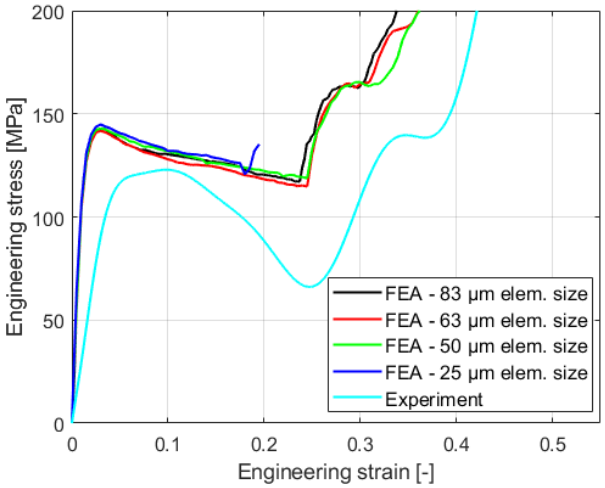

Figure. A.2. Stress-strain curves for the mesh sensitivity analysis of the FEA model for the UC with 8 mm length size. 60, 80, 100 and 200 resolutions correspond to 83 µm, 63 µm, 50 µm and 25 µm mesh element size, respectively.

B. Densification strains for SEA determination on honeycomb gyroid lattice structures

Here are presented the tables with the ε_D obtained from the experimental and computational curves for the honeycomb gyroid lattices.

Table B.1. Densification strain values as obtained for the lattice structures with 5 x 5 cell repetition and *low-LED* (accuracy of ± 0.001 for the *Experimental* values).

Test type	**Process parameter set**	**Theoretical VF [-]**	**ε_D [-]**
Theoretical FEA	*high-LED*	0.2	0.374
		0.3	0.35
		0.4	0.34
	low-LED	0.2	0.36
		0.3	0.36
		0.4	0.34
Sintered FEA	*high-LED*	0.2	0.36
		0.3	0.34
		0.4	0.32
	low-LED	0.2	0.36
		0.3	0.35
		0.4	0.31
Experimental	*high-LED*	0.2	0.402
		0.3	0.433
		0.4	0.362
	low-LED	0.2	0.394
		0.3	0.383
		0.4	0.353

Table B.2. Densification strain values for the lattice structures with UC repetition of 4 x 4 and UC length of 8 mm, for the configurations from Figure 6.10.

VF	Process parameter set	ε_D [-]
Uniform 0.4	*high-LED*	0.367
	low-LED	0.375
Uniform 0.45	*high-LED*	0.359
	low-LED	0.353
	high-LED/*low-LED*	0.354
	low-LED/*high-LED*	0.358
Graded 0.5 to 0.4	*high-LED*	0.365
	low-LED	0.351
	high-LED/*low-LED*	0.363
	low-LED/*high-LED*	0.356
Graded 0.6 to 0.3	*high-LED*	0.383
	low-LED	0.391
	high-LED/*low-LED*	0.391
	low-LED/*high-LED*	0.393
Graded 0.7 to 0.2	*high-LED*	0.453
	low-LED	0.421
	high-LED/*low-LED*	0.433
	low-LED/*high-LED*	0.426

Table B.3. Densification strain values for the 4 x 4 UC repetition, for the configurations investigated from Figure 6.14 (accuracy of ± 0.001 for the *Experimental* values).

Test type	**VF**	**Process parameter set**	ε_D **[-]**
FEA	Uniform 0.4	*high-LED*	0.347
		low-LED	0.349
	Graded 0.5 to 0.4	*high-LED*	0.334
		low-LED	0.328
		high-LED/*low-LED*	0.325
		low-LED/*high-LED*	0.332
Experimental	Uniform 0.4	*high-LED*	0.436
		low-LED	0.445
	Graded 0.5 to 0.4.5 to 0.4	*high-LED*	0.403
		low-LED	0.420
		low-LED/*high-LED*	0.416
		low-LED/*high-LED*	0.404

Table B.4. Densification strain values for the 2 x 2 UC repetition lattices, for the configurations investigated in Figure 6.20 (accuracy of ± 0.001 for the *Experimental* values).

Test type	**VF**	**Process parameter set**	ε_D **[-]**
FEA	Uniform 0.4	*high-LED*	0.407
		low-LED	0.418
	Graded 0.5 to 0.4	*high-LED*	0.4
		low-LED	0.407
		high-LED/*low-LED*	0.388
		low-LED/*high-LED*	0.417
Experimental	Uniform 0.4	*high-LED*	0.439
		low-LED	0.453

	Graded 0.5 to 0.4	*high-LED*	0.480
		low-LED	0.461
		high-LED/*low-LED*	0.471
		low-LED/*high-LED*	0.462

Table B.5. Densification strain values obtained for the 2 x 2 UC repetition lattices, for the quasi-static and dynamic conditions.

Test type	**VF**	**Process parameter set**	ε_D **[-]**
Quasi-static	Uniform 0.4	*high-LED*	0.432
		low-LED	0.419
	Graded 0.5 to 0.4	*high-LED*	0.432
		low-LED	0.418
		high-LED/*low-LED*	0.423
		low-LED/*high-LED*	0.430
Dynamic, 1000/s	Uniform 0.4	*high-LED*	0.419
		low-LED	0.408
	Graded 0.5 to 0.4	*high-LED*	0.422
		low-LED	0.390
		high-LED/*low-LED*	0.403
		low-LED/*high-LED*	0.41
Dynamic, 2000/s	Uniform 0.4	*high-LED*	0.410
		low-LED	0.390
	Graded 0.5 to 0.4	*high-LED*	0.394
		low-LED	0.380
		high-LED/*low-LED*	0.384
		low-LED/*high-LED*	0.407

C. FEA data from computational model

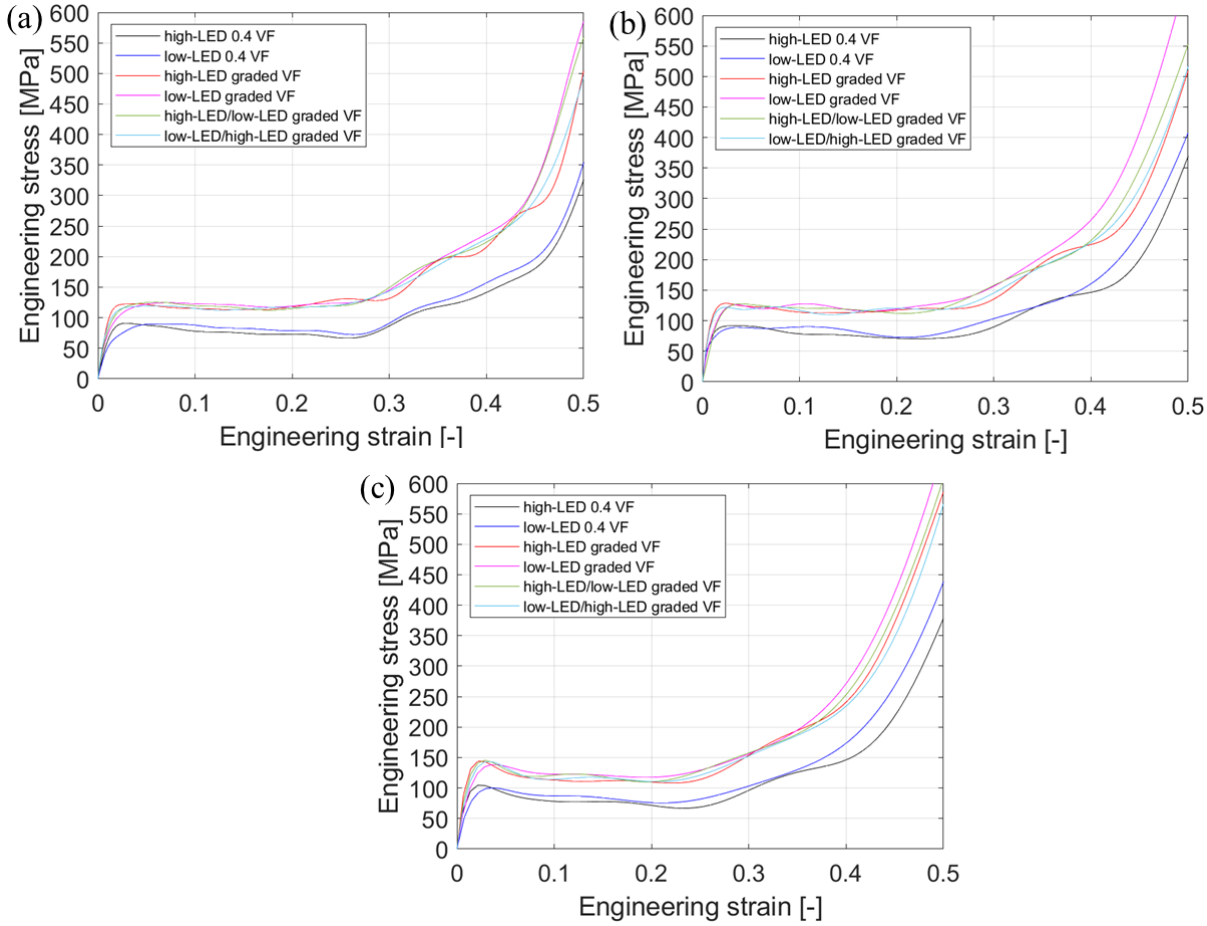

Figure C. 1. Stress-strain curves obtained from the 2 x 2 UC repetition lattices in Figure 6.20. The testing conditions are: (a) quasi-static, (b) dynamic at 1000/s, (c) dynamic at 2000/s.

Bibliography

[1] ASTM Standard. Standard terminology for additive manufacturing technologies, 10.04 (n.d.).

[2] T. DebRoy, H.L. Wei, J.S. Zuback, T. Mukherjee, J.W. Elmer, J.O. Milewski, A.M. Beese, A. Wilson-Heid, A. De, W. Zhang, Additive manufacturing of metallic components – Process, structure and properties, Prog Mater Sci 92 (2018) 112–224. https://doi.org/10.1016/j.pmatsci.2017.10.001.

[3] I. Gibson, D.W. Rosen, B. Stucker, Additive manufacturing technologies: Rapid prototyping to direct digital manufacturing, Springer US, 2010. https://doi.org/10.1007/978-1-4419-1120-9.

[4] Arcam announces CoCr process for metals 3D printing, Develop3D (2016). https://develop3d.com/develop3d-blog/arcam-announces-cocr-process-for-metals-3d-printing/.

[5] The Role of AM in the Automotive Industry, 3Dnatives 2 (2021). https://www.3dnatives.com/en/the-role-of-am-in-the-automotive-industry/#!

[6] B. Jagadeesh, P. Kuppan, Experimental investigations on the material behaviour of SLM fabricated SS316L, Mater Today Proc (2023). https://doi.org/10.1016/j.matpr.2023.08.064.

[7] M. Benedetti, A. du Plessis, R.O. Ritchie, M. Dallago, N. Razavi, F. Berto, Architected cellular materials: A review on their mechanical properties towards fatigue-tolerant design and fabrication, Materials Science and Engineering R: Reports 144 (2021). https://doi.org/10.1016/j.mser.2021.100606.

[8] F. Nalli, L. Cortese, F. Concli, Ductile damage assessment of Ti6Al4V, 17-4PH and AlSi10Mg for additive manufacturing, Eng Fract Mech 241 (2021). https://doi.org/10.1016/j.engfracmech.2020.107395.

[9] J. Noronha, J. Dash, J. Rogers, M. Leary, M. Brandt, M. Qian, Titanium Multi-Topology Metamaterials with Exceptional Strength, Advanced Materials (2024). https://doi.org/10.1002/adma.202308715.

[10] W.T. Carter, M.G. Jones, Direct Laser Sintering of Metals, n.d.

[11] F. Rest, M. Brackenwagen, V. Droßbach, Data Sheet 17-4PH | 1.4548, n.d. www.sd-metals.com.

[12] M.S. Pham, B. Dovgyy, P.A. Hooper, Twinning induced plasticity in austenitic stainless steel 316L made by additive manufacturing, Materials Science and Engineering: A 704 (2017) 102–111. https://doi.org/10.1016/j.msea.2017.07.082.

[13] S. Sabooni, A. Chabok, S.C. Feng, H. Blaauw, T.C. Pijper, H.J. Yang, Y.T. Pei, Laser powder bed fusion of 17–4 PH stainless steel: A comparative study on the effect of heat treatment on the microstructure evolution and mechanical properties, Addit Manuf 46 (2021). https://doi.org/10.1016/j.addma.2021.102176.

[14] L. Facchini, N. Vicente, I. Lonardelli, E. Magalini, P. Robotti, M. Alberto, Metastable austenite in 17-4 precipitation-hardening stainless steel produced by selective laser melting, Adv Eng Mater 12 (2010) 184–188. https://doi.org/10.1002/adem.200900259.

[15] M. Seabra, J. Azevedo, A. Araújo, L. Reis, E. Pinto, N. Alves, R. Santos, J. Pedro Mortágua, Selective laser melting (SLM) and topology optimization for lighter aerospace componentes, in: Procedia Structural Integrity, Elsevier B.V., 2016: pp. 289–296. https://doi.org/10.1016/j.prostr.2016.02.039.

[16] A. Ajdari, H. Nayeb-Hashemi, A. Vaziri, Dynamic crushing and energy absorption of regular, irregular and functionally graded cellular structures, Int J Solids Struct 48 (2011) 506–516. https://doi.org/10.1016/j.ijsolstr.2010.10.018.

[17] P. Heinl, L. Müller, C. Körner, R.F. Singer, F.A. Müller, Cellular Ti-6Al-4V structures with interconnected macro porosity for bone implants fabricated by selective electron beam melting, Acta Biomater 4 (2008) 1536–1544. https://doi.org/10.1016/j.actbio.2008.03.013.

[18] H.N.G. Wadley, N.A. Fleck, A.G. Evans, Fabrication and structural performance of periodic cellular metal sandwich structures, Compos Sci Technol 63 (2003) 2331–2343. https://doi.org/10.1016/S0266-3538(03)00266-5.

[19] T. Maconachie, M. Leary, B. Lozanovski, X. Zhang, M. Qian, O. Faruque, M. Brandt, SLM lattice structures: Properties, performance, applications and challenges, Mater Des 183 (2019). https://doi.org/10.1016/j.matdes.2019.108137.

[20] G. Dong, Y. Tang, Y.F. Zhao, A 149 Line Homogenization Code for Three-Dimensional Cellular Materials Written in MATLAB, Journal of Engineering Materials and Technology, Transactions of the ASME 141 (2019). https://doi.org/10.1115/1.4040555.

[21] M. Afshar, A.P. Anaraki, H. Montazerian, J. Kadkhodapour, Additive manufacturing and mechanical characterization of graded porosity scaffolds designed based on triply periodic minimal surface architectures, J Mech Behav Biomed Mater 62 (2016) 481–494. https://doi.org/10.1016/j.jmbbm.2016.05.027.

[22] X. Zhang, S. Yan, X. Xie, Y. Li, C. Wang, P. Wen, Multi-dimensional hybridized TPMS with high energy absorption capacity, Int J Mech Sci 273 (2024). https://doi.org/10.1016/j.ijmecsci.2024.109244.

[23] J. Zhang, Y. Liu, B.B. Babamiri, Y. Zhou, M. Dargusch, K. Hazeli, M.X. Zhang, Enhancing specific energy absorption of additively manufactured titanium lattice structures through simultaneous manipulation of architecture and constituent material, Addit Manuf 55 (2022). https://doi.org/10.1016/j.addma.2022.102887.

[24] Z. Li, Z. Kuai, J. Li, B. Liu, M. Zhao, Z. Yang, F. Liu, P.K. Bai, W. Huo, Effect of heat treatment on compression properties of the 316L diamond structure fabricated through selective laser melting, Journal of Materials Research and Technology 25 (2023) 5076–5095. https://doi.org/10.1016/j.jmrt.2023.06.268.

[25] F.S.H.B. Freeman, L.M. Jones, A.D. Goodall, H. Ghadbeigi, I. Todd, Structural metamaterial lattices by laser powder-bed fusion of 17-4PH steel, Additive Manufacturing Letters 8 (2024) 100190. https://doi.org/10.1016/j.addlet.2023.100190.

[26] D. Li, X. Zhang, R. Qin, J. Xu, D. Yue, B. Chen, Influence of processing parameters on AlSi10Mg lattice structure during selective laser melting: Manufacturing defects, thermal behavior and

compression properties, Opt Laser Technol 161 (2023). https://doi.org/10.1016/j.optlastec.2023.109182.

[27] A. du Plessis, N. Razavi, M. Benedetti, S. Murchio, M. Leary, M. Watson, D. Bhate, F. Berto, Properties and applications of additively manufactured metallic cellular materials: A review, Prog Mater Sci 125 (2022). https://doi.org/10.1016/j.pmatsci.2021.100918.

[28] M. Armstrong, H. Mehrabi, N. Naveed, An overview of modern metal additive manufacturing technology, J Manuf Process 84 (2022) 1001–1029. https://doi.org/10.1016/j.jmapro.2022.10.060.

[29] E. Ramirez-Cedillo, J.A. Sandoval-Robles, L. Ruiz-Huerta, A. Caballero-Ruiz, C.A. Rodriguez, H.R. Siller, Process planning guidelines in selective laser melting for the manufacturing of stainless steel parts, in: Elsevier B.V., 2018: pp. 973–982. https://doi.org/10.1016/j.promfg.2018.07.125.

[30] B. Ferrar, L. Mullen, E. Jones, R. Stamp, C.J. Sutcliffe, Gas flow effects on selective laser melting (SLM) manufacturing performance, J Mater Process Technol 212 (2012) 355–364. https://doi.org/10.1016/j.jmatprotec.2011.09.020.

[31] E. Ramirez-Cedillo, M.J. Uddin, J.A. Sandoval-Robles, R.A. Mirshams, L. Ruiz-Huerta, C.A. Rodriguez, H.R. Siller, Process planning of L-PBF of AISI 316L for improving surface quality and relating part integrity with microstructural characteristics, Surf Coat Technol 396 (2020). https://doi.org/10.1016/j.surfcoat.2020.125956.

[32] C.A. Biffi, J. Fiocchi, P. Bassani, A. Tuissi, Continuous wave vs pulsed wave laser emission in selective laser melting of AlSi10Mg parts with industrial optimized process parameters: Microstructure and mechanical behaviour, Addit Manuf 24 (2018) 639–646. https://doi.org/10.1016/j.addma.2018.10.021.

[33] A.G. Demir, P. Colombo, B. Previtali, From pulsed to continuous wave emission in SLM with contemporary fiber laser sources: effect of temporal and spatial pulse overlap in part quality, International Journal of Advanced Manufacturing Technology 91 (2017) 2701–2714. https://doi.org/10.1007/s00170-016-9948-7.

[34] S. Giganto, S. Martínez-Pellitero, J. Barreiro, P. Leo, M.A. Castro-Sastre, Impact of the laser scanning strategy on the quality of 17-4PH stainless steel parts manufactured by selective laser melting, Journal of Materials Research and Technology 20 (2022) 2734–2747. https://doi.org/10.1016/j.jmrt.2022.08.040.

[35] X. Tang, S. Zhang, C. Zhang, J. Chen, J. Zhang, Y. Liu, Optimization of laser energy density and scanning strategy on the forming quality of 24CrNiMo low alloy steel manufactured by SLM, Mater Charact 170 (2020). https://doi.org/10.1016/j.matchar.2020.110718.

[36] D. Koutny, D. Palousek, L. Pantelejev, C. Hoeller, R. Pichler, L. Tesicky, J. Kaiser, Influence of scanning strategies on processing of aluminum alloy EN AW 2618 using selective laser melting, Materials 11 (2018). https://doi.org/10.3390/ma11020298.

[37] M. ÖZAKINCI, R. ÜNAL, The Effect of Scanning Strategy On Mechanical Properties and Delamination During Brake Caliper Manufacturing With Selective Laser Melting (SLM), Journal of Polytechnic (2023). https://doi.org/10.2339/politeknik.1214999.

[38] J. Metelkova, Y. Kinds, K. Kempen, C. de Formanoir, A. Witvrouw, B. Van Hooreweder, On the influence of laser defocusing in Selective Laser Melting of 316L, Addit Manuf 23 (2018) 161–169. https://doi.org/10.1016/j.addma.2018.08.006.

[39] Z. Gan, O.L. Kafka, N. Parab, C. Zhao, L. Fang, O. Heinonen, T. Sun, W.K. Liu, Universal scaling laws of keyhole stability and porosity in 3D printing of metals, Nat Commun 12 (2021). https://doi.org/10.1038/s41467-021-22704-0.

[40] P. Bajaj, A. Hariharan, A. Kini, P. Kürnsteiner, D. Raabe, E.A. Jägle, Steels in additive manufacturing: A review of their microstructure and properties, Materials Science and Engineering: A 772 (2020). https://doi.org/10.1016/j.msea.2019.138633.

[41] C.N. Hsiao, C.S. Chiou, J.R. Yang, Aging reactions in a 17-4 PH stainless steel, 2002.

[42] H. Bhadeshia, R. Honeycombe, Steels - Microstructure and Properties, 3rd ed., 2006.

[43] Science of Alloying, 74 (n.d.). https://www.tf.uni-kiel.de/matwis/amat/iss/kap_9/illustr/s9_2_1.html#:~:text=Elements%20which%20tend%20to%20stabilize,austenite%20is%20stable%2C%20see%20above.

[44] K.H. Buschow, R.W. Jürgen Cahn, M.C. Flemings, B.K. Ilschner, Edward J, S. Mahajan, Encyclopedia of Materials - Science and Technology, Volumes 1-11 - Permalloys and Invar, Elsevier (2001). Retrieved from https://app.knovel.com/hotlink/pdf/id:kt00B7AHQ1/encyclopedia-materials/permalloys-and-invar.

[45] A. Zahid, ME 431-Introduction to Engineering Materials Lecture 1 Introduction to the Course, n.d.

[46] Alokesh. Pramanik, A.Kumar. Basak, Stainless steel : microstructure, mechanical properties and methods of application, n.d.

[47] Steels for aircraft structures, Introduction to Aerospace Materials (2012) 232–250. https://doi.org/10.1533/9780857095152.232.

[48] https://learnmech.com/what-is-ttt-diagram-isotherma/, Elsevier Ltd, n.d.

[49] R.E. Hackenberg, The historical development of phase transformations understanding in ferrous alloys, in: Phase Transformations in Steels, Elsevier Ltd, 2012: pp. 3–55. https://doi.org/10.1533/9780857096104.1.3.

[50] https://www.doitpoms.ac.uk/, Elsevier Ltd, 2015.

[51] K. Datta, R. Delhez, P.M. Bronsveld, J. Beyer, H.J.M. Geijselaers, J. Post, A low-temperature study to examine the role of ε-martensite during strain-induced transformations in metastable austenitic stainless steels, Acta Mater 57 (2009) 3321–3326. https://doi.org/10.1016/j.actamat.2009.03.039.

[52] R. Singh, Welding, corrosion-resistant alloys—Stainless steel, in: Applied Welding Engineering, Elsevier, 2020: pp. 251–271. https://doi.org/10.1016/b978-0-12-821348-3.00019-7.

[53] M. Maalekian, M. Maalekian, The Effects of Alloying Elements on Steels (I), 2007.

[54] N. Novak, D. Kytyr, V. Rada, T. Doktor, O. Al-Ketan, R. Rowshan, M. Vesenjak, Z. Ren, Compression behaviour of TPMS-filled stainless steel tubes, Materials Science and Engineering: A 852 (2022). https://doi.org/10.1016/j.msea.2022.143680.

[55] M.H. Ku, K. Ni, Q.E. Lin, S.H. Chang, T.W. Hsu, C.L. Li, C.K. Wang, M.W. Wu, Novel laser powder bed fusion Corrax maraging stainless steel lattice with superior specific strength and energy absorption, Journal of Materials Research and Technology 25 (2023) 5240–5248. https://doi.org/10.1016/j.jmrt.2023.07.027.

[56] S. Hossein Nedjad, M. Yildiz, A. Saboori, Solidification behaviour of austenitic stainless steels during welding and directed energy deposition, Science and Technology of Welding and Joining 28 (2023) 1–17. https://doi.org/10.1080/13621718.2022.2115664.

[57] Austenitic Steels, 57 (n.d.). https://www.totalmateria.com/en-us/articles/austenitic-steels/.

[58] S. Zhang, Q. Wang, R. Yang, C. Dong, Composition equivalents of stainless steels understood via gamma stabilizing efficiency, Sci Rep 11 (2021) 5423. https://doi.org/10.1038/s41598-021-84917-z.

[59] R. Saluja, K.M. Moeed, THE EMPHASIS OF PHASE TRANSFORMATIONS AND ALLOYING CONSTITUENTS ON HOT CRACKING SUSCEPTIBILITY OF TYPE 304L AND 316L STAINLESS STEEL WELDS, n.d.

[60] K.R. Upadhyaya, M.N. Shetty, Energy absorption in low cycle fatigue in 9Cr-lMo and 304 stainless steels, 1991.

[61] E. Ratte, S. Leonhardt, W. Bleck, M. Franzen, P. Urban, Energy absorption behaviour of austenitic and duplex stainless steels in a crash box geometry, Steel Res Int 77 (2006) 692–697. https://doi.org/10.1002/srin.200606449.

[62] A. Oñate, M. Castro, C. Medina, J.P. Sanhueza, V. Tuninetti, M. Meléndrez, D. Rojas, Influence of martensite and grain size on the mechanical behavior of austenitic Fe–C–Mn–Ni–Al medium Mn steels with TWIP mechanism under uniaxial tension/compression and micromechanical creep, Mater Chem Phys 328 (2024) 129966. https://doi.org/10.1016/j.matchemphys.2024.129966.

[63] S. Astafurov, E. Astafurova, Phase composition of austenitic stainless steels in additive manufacturing: A review, Metals (Basel) 11 (2021). https://doi.org/10.3390/met11071052.

[64] Stainless Steel 1.4404: Chemical Composition, n.d.

[65] J. Zhang, S. Xie, T. Li, Z. Liu, S. Zheng, H. Zhou, A study of multi-stage energy absorption characteristics of hybrid sheet TPMS lattices, Thin-Walled Structures 190 (2023). https://doi.org/10.1016/j.tws.2023.110989.

[66] C.J. Ejeh, I. Barsoum, A.M. Abou-Ali, R.K. Abu Al-Rub, Combining multiple lattice-topology functional grading strategies for enhancing the dynamic compressive behavior of TPMS-based metamaterials, Journal of Materials Research and Technology 27 (2023) 6076–6093. https://doi.org/10.1016/j.jmrt.2023.10.247.

[67] B. Barkia, P. Aubry, P. Haghi-Ashtiani, T. Auger, L. Gosmain, F. Schuster, H. Maskrot, On the origin of the high tensile strength and ductility of additively manufactured 316L stainless steel: Multiscale investigation, J Mater Sci Technol 41 (2020) 209–218. https://doi.org/10.1016/j.jmst.2019.09.017.

[68] M. Iannuzzi, Stress corrosion cracking, Elsevier, 2011. https://doi.org/10.1533/9780857093769.4.570.

[69] C.D. Horvath, Advanced steels for lightweight automotive structures, in: Materials, Design and Manufacturing for Lightweight Vehicles, Elsevier, 2020: pp. 39–95. https://doi.org/10.1016/B978-0-12-818712-8.00002-1.

[70] M.C.S. Marques, A.N. de Moura, C.M. de Alcântara, F.M.S.B. de Carvalho, R. Bussoloti, W. da S. Labiapari, J. Vatavuk, Microstructure and mechanical properties of a martensitic stainless steel (0.2%C–12%Cr) after quenching and partitioning (Q&P) process, Journal of Materials Research and Technology 24 (2023) 3937–3955. https://doi.org/10.1016/j.jmrt.2023.04.018.

[71] C. Garcia-Cabezon, C.G. Hernández, M.A. Castro-Sastre, A.I. Fernandez-Abia, M.L. Rodriguez-Mendez, F. Martin-Pedrosa, Heat treatments of 17-4 PH SS processed by SLM to improve its strength and biocompatibility in biomedical applications, Journal of Materials Research and Technology 26 (2023) 3524–3543. https://doi.org/10.1016/j.jmrt.2023.08.104.

[72] S.R. Narasimharaju, W. Zeng, T.L. See, Z. Zhu, P. Scott, X. Jiang, S. Lou, A comprehensive review on laser powder bed fusion of steels: Processing, microstructure, defects and control methods, mechanical properties, current challenges and future trends, J Manuf Process 75 (2022) 375–414. https://doi.org/10.1016/j.jmapro.2021.12.033.

[73] C. Li, Y. Wang, H. Zhan, T. Han, B. Han, W. Zhao, Three-dimensional finite element analysis of temperatures and stresses in wide-band laser surface melting processing, Mater Des 31 (2010) 3366–3373. https://doi.org/10.1016/j.matdes.2010.01.054.

[74] M.J. Bin Suleiman Ahmad, M.A. Bin Ahmad, R. Bin Ibrahim, M. Bin Mohamad, N.B. Abu Kasim, M.R. Bin Dato' Abdul Kadir, S. Bin Muhamad, Y. Itoh, K. Hanada, T. Shimizu, Effect of sintering conditions on mechanical properties and microstructure of Titanium alloy produced by Metal Injection Moulding (MIM), in: Adv Mat Res, 2013: pp. 164–169. https://doi.org/10.4028/www.scientific.net/AMR.686.164.

[75] Y. Liu, Y. Yang, D. Wang, A study on the residual stress during selective laser melting (SLM) of metallic powder, International Journal of Advanced Manufacturing Technology 87 (2016) 647–656. https://doi.org/10.1007/s00170-016-8466-y.

[76] K. Guo, L. Qiao, Z. Huang, N. Anwer, Y. Cao, A computational model of melt pool morphology for selective laser melting process, International Journal of Advanced Manufacturing Technology 121 (2022) 1651–1673. https://doi.org/10.1007/s00170-022-09366-y.

[77] S.A. David, S.S. Babu, J.M. Vitek, Welding: Solidification and Microstructure, 2003. www.tms.org/pubs/journals/JOM/0306/David-.

[78] G. Gong, J. Ye, Y. Chi, Z. Zhao, Z. Wang, G. Xia, X. Du, H. Tian, H. Yu, C. Chen, Research status of laser additive manufacturing for metal: a review, Journal of Materials Research and Technology 15 (2021) 855–884. https://doi.org/10.1016/j.jmrt.2021.08.050.

[79] P.A. Hooper, Melt pool temperature and cooling rates in laser powder bed fusion, Addit Manuf 22 (2018) 548–559. https://doi.org/10.1016/j.addma.2018.05.032.

[80] H. Jacobi, K. Schwerdtfeger, Dendrite Morphology of Steady State Unidirectionally Solidified Steel, n.d.

[81] D. Hu, R. Kovacevic, Sensing, modeling and control for laser-based additive manufacturing, 2003.

[82] A.J. Pinkerton, L. Li, Modelling the geometry of a moving laser melt pool and deposition track via energy and mass balances, J Phys D Appl Phys 37 (2004) 1885–1895. https://doi.org/10.1088/0022-3727/37/14/003.

[83] G.M. Karthik, E.S. Kim, P. Sathiyamoorthi, A. Zargaran, S.G. Jeong, R. Xiong, S.H. Kang, J.W. Cho, H.S. Kim, Delayed deformation-induced martensite transformation and enhanced cryogenic tensile properties in laser additive manufactured 316L austenitic stainless steel, Addit Manuf 47 (2021). https://doi.org/10.1016/j.addma.2021.102314.

[84] Y.M. Wang, T. Voisin, J.T. McKeown, J. Ye, N.P. Calta, Z. Li, Z. Zeng, Y. Zhang, W. Chen, T.T. Roehling, R.T. Ott, M.K. Santala, P.J. Depond, M.J. Matthews, A. V. Hamza, T. Zhu, Additively manufactured hierarchical stainless steels with high strength and ductility, Nat Mater 17 (2018) 63–70. https://doi.org/10.1038/NMAT5021.

[85] K. Saeidi, X. Gao, Y. Zhong, Z.J. Shen, Hardened austenite steel with columnar sub-grain structure formed by laser melting, Materials Science and Engineering: A 625 (2015) 221–229. https://doi.org/10.1016/j.msea.2014.12.018.

[86] M. Ma, Z. Wang, X. Zeng, A comparison on metallurgical behaviors of 316L stainless steel by selective laser melting and laser cladding deposition, Materials Science and Engineering: A 685 (2017) 265–273. https://doi.org/10.1016/j.msea.2016.12.112.

[87] T. Voisin, J.B. Forien, A. Perron, S. Aubry, N. Bertin, A. Samanta, A. Baker, Y.M. Wang, New insights on cellular structures strengthening mechanisms and thermal stability of an austenitic stainless steel fabricated by laser powder-bed-fusion, Acta Mater 203 (2021). https://doi.org/10.1016/j.actamat.2020.11.018.

[88] J.W. Christian, S. Mahajant, Deformation Twinning, 1995.

[89] F. He, C. Wang, B. Han, G. Yeli, X. Lin, Z. Wang, L. Wang, J.J. Kai, Deformation faulting and dislocation-cell refinement in a selective laser melted 316L stainless steel, Int J Plast 156 (2022). https://doi.org/10.1016/j.ijplas.2022.103346.

[90] X. Wu, M. Yang, F. Yuan, G. Wu, Y. Wei, X. Huang, Y. Zhu, Heterogeneous lamella structure unites ultrafine-grain strength with coarse-grain ductility, Proc Natl Acad Sci U S A 112 (2015) 14501–14505. https://doi.org/10.1073/pnas.1517193112.

[91] S. Gao, Z. Hu, M. Duchamp, P.S.S.R. Krishnan, S. Tekumalla, X. Song, M. Seita, Recrystallization-based grain boundary engineering of 316L stainless steel produced via selective laser melting, Acta Mater 200 (2020) 366–377. https://doi.org/10.1016/j.actamat.2020.09.015.

[92] M.S. Pham, S.R. Holdsworth, Dynamic strain ageing of AISI 316L during cyclic loading at 300°C: Mechanism, evolution, and its effects, Materials Science and Engineering: A 556 (2012) 122–133. https://doi.org/10.1016/j.msea.2012.06.067.

[93] Y. Sun, R.J. Hebert, M. Aindow, Effect of heat treatments on microstructural evolution of additively manufactured and wrought 17-4PH stainless steel, Mater Des 156 (2018) 429–440. https://doi.org/10.1016/j.matdes.2018.07.015.

[94] S. Vunnam, A. Saboo, C. Sudbrack, T.L. Starr, Effect of powder chemical composition on the as-built microstructure of 17-4 PH stainless steel processed by selective laser melting, Addit Manuf 30 (2019). https://doi.org/10.1016/j.addma.2019.100876.

[95] S.A. David, J.M. Vitek, Correlation between solidification parameters and weld microstructures, 1989.

[96] C.L. Leone, H.W. Kerr, The Ferrite to Austenite Transformation in Stainless Steels Given austenite from primary phase ferrite, further decomposition of ferrite to austenite occurs in the solid state by a diffusion controlled mechanism, n.d.

[97] P. Ponnusamy, B. Sharma, S.H. Masood, R.A.R. Rashid, R. Rashid, S. Palanisamy, D. Ruan, A study of tensile behavior of SLM processed 17-4 PH stainless steel, in: Mater Today Proc, Elsevier Ltd, 2021: pp. 4531–4534. https://doi.org/10.1016/j.matpr.2020.12.1104.

[98] P. Ponnusamy, S.H. Masood, D. Ruan, S. Palanisamy, R.A.R. Rashid, O.A. Mohamed, Mechanical performance of selective laser melted 17-4 PH stainless steel under compressive loading, n.d.

[99] H.E. Sabzi, S.H. Lim, D. Della Crociata, R. Castellote-Alvarez, M. Simonelli, D. San-Martín, X. Hao, P.P. Choi, P.E.J. Rivera-Díaz-del-Castillo, Genetic design of precipitation-hardening stainless steels for additive manufacturing, Acta Mater 274 (2024). https://doi.org/10.1016/j.actamat.2024.120018.

[100] F.S.H.B. Freeman, A. Lincoln, J. Sharp, A. Lambourne, I. Todd, Exploiting thermal strain to achieve an in-situ magnetically graded material, Mater Des 161 (2019) 14–21. https://doi.org/10.1016/j.matdes.2018.11.011.

[101] M. Soleimani, A. Kalhor, H. Mirzadeh, Transformation-induced plasticity (TRIP) in advanced steels: A review, Materials Science and Engineering: A 795 (2020). https://doi.org/10.1016/j.msea.2020.140023.

[102] J.R. Patel, M. Cohent, Criterion for the action of applied stress in the martensitic transformation, n.d.

[103] I. Tamura, Deformation-induced martensitic transformation and transformation-induced plasticity in steels, 1982.

[104] K. Nohara, Y. Ono, N. Ohashi, Composition and grain size dependencies of strain-induced martensitic transformation in metastable austenitic stainless steels, Tetsu-To-Hagane 63 (1977) 772–782. https://doi.org/https://doi.org/10.2355/tetsutohagane1955.63.5_772.

[105] H.S. Noh, J.H. Kang, K.M. Kim, S.J. Kim, Different Effects of Ni and Mn on Thermodynamic and Mechanical Stabilities in Cr-Ni-Mn Austenitic Steels, Metall Mater Trans A Phys Metall Mater Sci 50 (2019) 616–624. https://doi.org/10.1007/s11661-018-5042-0.

[106] L. Liu, B. He, M. Huang, The Role of Transformation-Induced Plasticity in the Development of Advanced High Strength Steels, Adv Eng Mater 20 (2018). https://doi.org/10.1002/adem.201701083.

[107] G.B. Olson, M. Cohen, Kinetics of Nucleation Strain-Induced Martensitic, Metallurgical Transactions A 6 (1975) 791–795. https://doi.org/https://doi.org/10.1007/BF02672301.

[108] J. V. Gordon, S.P. Narra, R.W. Cunningham, H. Liu, H. Chen, R.M. Suter, J.L. Beuth, A.D. Rollett, Defect structure process maps for laser powder bed fusion additive manufacturing, Addit Manuf 36 (2020). https://doi.org/10.1016/j.addma.2020.101552.

[109] K. V. Yang, P. Rometsch, T. Jarvis, J. Rao, S. Cao, C. Davies, X. Wu, Porosity formation mechanisms and fatigue response in Al-Si-Mg alloys made by selective laser melting, Materials Science and Engineering: A 712 (2018) 166–174. https://doi.org/10.1016/j.msea.2017.11.078.

[110] S.M. Yusuf, Y. Chen, R. Boardman, S. Yang, N. Gao, Investigation on porosity and microhardness of 316L stainless steel fabricated by selective laser melting, Metals (Basel) 7 (2017). https://doi.org/10.3390/met7020064.

[111] Y. Parikh, J. Carter, M. Kuttolamadom, Investigation of porosity & microstructure-induced property variations in additive manufactured stainless steel 316L, 2020. https://www.researchgate.net/publication/342165648.

[112] N.T. Aboulkhair, M. Simonelli, L. Parry, I. Ashcroft, C. Tuck, R. Hague, 3D printing of Aluminium alloys: Additive Manufacturing of Aluminium alloys using selective laser melting, Prog Mater Sci 106 (2019). https://doi.org/10.1016/j.pmatsci.2019.100578.

[113] M. Tang, P.C. Pistorius, J.L. Beuth, Prediction of lack-of-fusion porosity for powder bed fusion, Addit Manuf 14 (2017) 39–48. https://doi.org/10.1016/j.addma.2016.12.001.

[114] J. Hajnys, M. Pagac, O. Kotera, J. Petru, S. Scholz, Influence of basic process parameters on mechanical and internal properties of 316l steel in slm process for renishaw AM400, MM Science Journal 2019 (2019) 2790–2794. https://doi.org/10.17973/MMSJ.2019_03_2018127.

[115] M. Yakout, M.A. Elbestawi, S.C. Veldhuis, Density and mechanical properties in selective laser melting of Invar 36 and stainless steel 316L, J Mater Process Technol 266 (2019) 397–420. https://doi.org/10.1016/j.jmatprotec.2018.11.006.

[116] A. Thanki, L. Goossens, R. Mertens, G.M. Probst, W. Dewulf, A. Witvrouw, S. Yang, Study of keyhole-porosities in selective laser melting using X-ray computed tomography, E-Journal of Nondestructive Testing 24 (2019). https://doi.org/10.58286/23754.

[117] A. Ozsoy, E. Aydogan, A.F. Dericioglu, Selective laser melting of Nano-TiN reinforced 17-4 PH stainless steel: Densification, microstructure and mechanical properties, Materials Science and Engineering: A 836 (2022). https://doi.org/10.1016/j.msea.2021.142574.

[118] R. Li, J. Liu, Y. Shi, L. Wang, W. Jiang, Balling behavior of stainless steel and nickel powder during selective laser melting process, International Journal of Advanced Manufacturing Technology 59 (2012) 1025–1035. https://doi.org/10.1007/s00170-011-3566-1.

[119] A. Simchi, Direct laser sintering of metal powders: Mechanism, kinetics and microstructural features, Materials Science and Engineering: A 428 (2006) 148–158. https://doi.org/10.1016/j.msea.2006.04.117.

[120] R. McCann, M.A. Obeidi, C. Hughes, É. McCarthy, D.S. Egan, R.K. Vijayaraghavan, A.M. Joshi, V. Acinas Garzon, D.P. Dowling, P.J. McNally, D. Brabazon, In-situ sensing, process monitoring and

machine control in Laser Powder Bed Fusion: A review, Addit Manuf 45 (2021). https://doi.org/10.1016/j.addma.2021.102058.

[121] M.J. Matthews, G. Guss, S.A. Khairallah, A.M. Rubenchik, P.J. Depond, W.E. King, Denudation of metal powder layers in laser powder bed fusion processes, Acta Mater 114 (2016) 33–42. https://doi.org/10.1016/j.actamat.2016.05.017.

[122] D. Wang, S. Wu, F. Fu, S. Mai, Y. Yang, Y. Liu, C. Song, Mechanisms and characteristics of spatter generation in SLM processing and its effect on the properties, Mater Des 117 (2017) 121–130. https://doi.org/10.1016/j.matdes.2016.12.060.

[123] S.A. Khairallah, A.T. Anderson, A. Rubenchik, W.E. King, Laser powder-bed fusion additive manufacturing: Physics of complex melt flow and formation mechanisms of pores, spatter, and denudation zones, Acta Mater 108 (2016) 36–45. https://doi.org/10.1016/j.actamat.2016.02.014.

[124] M. Simonelli, C. Tuck, N.T. Aboulkhair, I. Maskery, I. Ashcroft, R.D. Wildman, R. Hague, A Study on the Laser Spatter and the Oxidation Reactions During Selective Laser Melting of 316L Stainless Steel, Al-Si10-Mg, and Ti-6Al-4V, Metall Mater Trans A Phys Metall Mater Sci 46 (2015) 3842–3851. https://doi.org/10.1007/s11661-015-2882-8.

[125] A.S. Wu, D.W. Brown, M. Kumar, G.F. Gallegos, W.E. King, An Experimental Investigation into Additive Manufacturing-Induced Residual Stresses in 316L Stainless Steel, Metall Mater Trans A Phys Metall Mater Sci 45 (2014) 6260–6270. https://doi.org/10.1007/s11661-014-2549-x.

[126] C.R. Knowles, T.H. Becker, R.B. Tait, Residual stress measurements and structural integrity implications for selective laser melted Ti-6Al-4V, n.d.

[127] M.F. Zaeh, G. Branner, Investigations on residual stresses and deformations in selective laser melting, Production Engineering 4 (2010) 35–45. https://doi.org/10.1007/s11740-009-0192-y.

[128] J.P. Kruth, J. Deckers, E. Yasa, R. Wauthlé, Assessing and comparing influencing factors of residual stresses in selective laser melting using a novel analysis method, Proc Inst Mech Eng B J Eng Manuf 226 (2012) 980–991. https://doi.org/10.1177/0954405412437085.

[129] C. Qiu, M. Al Kindi, A.S. Aladawi, I. Al Hatmi, A comprehensive study on microstructure and tensile behaviour of a selectively laser melted stainless steel, Sci Rep 8 (2018). https://doi.org/10.1038/s41598-018-26136-7.

[130] A. AlFaify, J. Hughes, K. Ridgway, Controlling the porosity of 316L stainless steel parts manufactured via the powder bed fusion process, Rapid Prototyp J 25 (2019) 162–175. https://doi.org/10.1108/RPJ-11-2017-0226.

[131] M. Güden, S. Enser, M. Bayhan, A. Taşdemirci, H. Yavaş, The strain rate sensitive flow stresses and constitutive equations of a selective-laser-melt and an annealed-rolled 316L stainless steel: A comparative study, Materials Science and Engineering: A 838 (2022). https://doi.org/10.1016/j.msea.2022.142743.

[132] A. Bintu, G. Vincze, C.R. Picu, A.B. Lopes, J.J. Grácio, F. Barlat, Strain hardening rate sensitivity and strain rate sensitivity in TWIP steels, Materials Science and Engineering: A 629 (2015) 54–59. https://doi.org/10.1016/j.msea.2015.01.080.

[133] M.A. Meyers, K.K. Chawla, Mechanical Behavior of Materials, Cambridge University Press, 2009.

[134] H. Conrad, Thermally activated deformation of metals, n.d.

[135] S. Enser, M. Güden, A. Taşdemirci, K. Davut, The strain rate history effect in a selective-laser-melt 316L stainless steel, Materials Science and Engineering: A 862 (2023). https://doi.org/10.1016/j.msea.2022.144439.

[136] J. Talonen, H. Hänninen, Formation of shear bands and strain-induced martensite during plastic deformation of metastable austenitic stainless steels, Acta Mater 55 (2007) 6108–6118. https://doi.org/10.1016/j.actamat.2007.07.015.

[137] T. LEBRUN, K. TANIGAKI, K. HORIKAWA, H. KOBAYASHI, Strain rate sensitivity and mechanical anisotropy of selective laser melted 17-4 PH stainless steel, Mechanical Engineering Journal 1 (2014) SMM0049–SMM0049. https://doi.org/10.1299/mej.2014smm0049.

[138] X. Wang, Y. Liu, T. Shi, Y. Wang, Strain rate dependence of mechanical property in a selective laser melted 17–4 PH stainless steel with different states, Materials Science and Engineering: A 792 (2020). https://doi.org/10.1016/j.msea.2020.139776.

[139] F. Khodabakhshi, M.H. Farshidianfar, A.P. Gerlich, M. Nosko, V. Trembošová, A. Khajepour, Microstructure, strain-rate sensitivity, work hardening, and fracture behavior of laser additive manufactured austenitic and martensitic stainless steel structures, Materials Science and Engineering: A 756 (2019) 545–561. https://doi.org/10.1016/j.msea.2019.04.065.

[140] X. feng WANG, T. ya SHI, H. bin WANG, S. ze ZHOU, W. fei PENG, Y. gang WANG, Effects of strain rate on mechanical properties, microstructure and texture of Al—Mg—Si—Cu alloy under tensile loading, Transactions of Nonferrous Metals Society of China (English Edition) 30 (2020) 27–40. https://doi.org/10.1016/S1003-6326(19)65177-0.

[141] I. Maskery, N.T. Aboulkhair, A.O. Aremu, C.J. Tuck, I.A. Ashcroft, Compressive failure modes and energy absorption in additively manufactured double gyroid lattices, Addit Manuf 16 (2017) 24–29. https://doi.org/10.1016/j.addma.2017.04.003.

[142] M.F. Ashby, The properties of foams and lattices, Philosophical Transactions of the Royal Society A: Mathematical, Physical and Engineering Sciences 364 (2006) 15–30. https://doi.org/10.1098/rsta.2005.1678.

[143] L.J. Gibson, Cellular solids, MRS Bull 28 (2003) 270–274. https://doi.org/10.1557/mrs2003.79.

[144] H.A. Schwarz, Gesammelte Mathematische Abhandlungen, Springer, Berlin Heidelberg, 1890.

[145] O. Al-Ketan, R.K.A. Al-Rub, R. Rowshan, Mechanical Properties of a New Type of Architected Interpenetrating Phase Composite Materials, Adv Mater Technol 2 (2017). https://doi.org/10.1002/admt.201600235.

[146] I. Maskery, L. Sturm, A.O. Aremu, A. Panesar, C.B. Williams, C.J. Tuck, R.D. Wildman, I.A. Ashcroft, R.J.M. Hague, Insights into the mechanical properties of several triply periodic minimal surface lattice structures made by polymer additive manufacturing, Polymer (Guildf) 152 (2018) 62–71. https://doi.org/10.1016/j.polymer.2017.11.049.

[147] A. Alghamdi, T. Maconachie, D. Downing, M. Brandt, M. Qian, M. Leary, Effect of additive manufactured lattice defects on mechanical properties: an automated method for the enhancement of lattice geometry, International Journal of Advanced Manufacturing Technology 108 (2020) 957–971. https://doi.org/10.1007/s00170-020-05394-8.

[148] Y. Sun, Q.M. Li, Dynamic compressive behaviour of cellular materials: A review of phenomenon, mechanism and modelling, Int J Impact Eng 112 (2018) 74–115. https://doi.org/10.1016/j.ijimpeng.2017.10.006.

[149] L. Zhang, S. Feih, S. Daynes, S. Chang, M.Y. Wang, J. Wei, W.F. Lu, Energy absorption characteristics of metallic triply periodic minimal surface sheet structures under compressive loading, Addit Manuf 23 (2018) 505–515. https://doi.org/10.1016/j.addma.2018.08.007.

[150] I. Maskery, A.O. Aremu, L. Parry, R.D. Wildman, C.J. Tuck, I.A. Ashcroft, Effective design and simulation of surface-based lattice structures featuring volume fraction and cell type grading, Mater Des 155 (2018) 220–232. https://doi.org/10.1016/j.matdes.2018.05.058.

[151] I. Maskery, I.A. Ashcroft, The deformation and elastic anisotropy of a new gyroid-based honeycomb made by laser sintering, Addit Manuf 36 (2020). https://doi.org/10.1016/j.addma.2020.101548.

[152] N. Yang, Z. Quan, D. Zhang, Y. Tian, Multi-morphology transition hybridization CAD design of minimal surface porous structures for use in tissue engineering, CAD Computer Aided Design 56 (2014) 11–21. https://doi.org/10.1016/j.cad.2014.06.006.

[153] S. Banait, C. Liu, M. Campos, M.S. Pham, M.T. Pérez-Prado, Coupled effect of microstructure and topology on the mechanical behavior of Inconel718 additively manufactured lattices, Mater Des 224 (2022). https://doi.org/10.1016/j.matdes.2022.111294.

[154] C. Liu, J. Lertthanasarn, M.S. Pham, The origin of the boundary strengthening in polycrystal-inspired architected materials, Nat Commun 12 (2021). https://doi.org/10.1038/s41467-021-24886-z.

[155] A. Bertocco, G. Iannitti, A. Caraviello, L. Esposito, Lattice structures in stainless steel 17-4PH manufactured via selective laser melting (SLM) process: dimensional accuracy, satellites formation, compressive response and printing parameters optimization, International Journal of Advanced Manufacturing Technology 120 (2022) 4935–4949. https://doi.org/10.1007/s00170-022-08946-2.

[156] L. Li, Y. Zhang, X. Cui, Z. Said, S. Sharma, M. Liu, T. Gao, Z. Zhou, X. Wang, C. Li, Mechanical behavior and modeling of grinding force: A comparative analysis, J Manuf Process 102 (2023) 921–954. https://doi.org/10.1016/j.jmapro.2023.07.074.

[157] X. Zhang, W. Yao, X. Zhu, Z. Hu, W. Zhu, H. Huang, W. Li, Determination of Johnson–Cook Constitutive of 15-5 PH Steel Processed by Selective Laser Melting, Materials 16 (2023). https://doi.org/10.3390/ma16020800.

[158] G.R. Johnson, W.H. Cook, A CONSTITUTIVE MODEL AND DATA FOR METALS SUBJECTED TO LARGE STRAINS, HIGH STRAIN RATES AND HIGH TEMPERATURES, n.d.

[159] G.R. Johnson, FRACTURE CHARACTERISTICS OF THREE METALS SUBJECTED TO VARIOUS STRAINS, STRAIN RATES, TEMPERATURES AND PRESSURES, 1985.

[160] H. Yin, W. Zhang, L. Zhu, F. Meng, J. Liu, G. Wen, Review on lattice structures for energy absorption properties, Compos Struct 304 (2023). https://doi.org/10.1016/j.compstruct.2022.116397.

[161] N.B. Ghisi, H. Ramos, L. Kindleyside, N.T. Aboulkhair, R. Santiago, The influence of the characteristic microstructure of additively manufactured AlSi10Mg on the plastic behaviour at various strain rates, Mater Des 223 (2022). https://doi.org/10.1016/j.matdes.2022.111112.

[162] S. AlMahri, R. Santiago, D.W. Lee, H. Ramos, H. Alabdouli, M. Alteneiji, Z. Guan, W. Cantwell, M. Alves, Evaluation of the dynamic response of triply periodic minimal surfaces subjected to high strain-rate compression, Addit Manuf 46 (2021). https://doi.org/10.1016/j.addma.2021.102220.

[163] W. Ma, Z. Li, S. Xie, Crashworthiness analysis of thin-walled bio-inspired multi-cell corrugated tubes under quasi-static axial loading, Eng Struct 204 (2020). https://doi.org/10.1016/j.engstruct.2019.110069.

[164] H. Zhu, P. Wang, D. Wei, J. Si, Y. Wu, Energy absorption of diamond lattice cylindrical shells under axial compression loading, Thin-Walled Structures 181 (2022). https://doi.org/10.1016/j.tws.2022.110131.

[165] S. Soni, S.K. Pradhan, Improving crash worthiness and dynamic performance of frontal plastic automotive body components, in: Mater Today Proc, Elsevier Ltd, 2019: pp. 2308–2313. https://doi.org/10.1016/j.matpr.2019.09.118.

[166] J. Jackowski, P. Posuniak, K. Zielonka, R. Jurecki, Experimental Testing of Energy-Absorbing Structures Used to Enhance the Crashworthiness of the Vehicles, Energies (Basel) 16 (2023). https://doi.org/10.3390/en16052183.

[167] M. Gidlewski, L. Prochowski, L. Jemioł, D. Żardecki, The process of front-to-side collision of motor vehicles in terms of energy balance, Nonlinear Dyn 97 (2019) 1877–1893. https://doi.org/10.1007/s11071-018-4688-x.

[168] X. Li, L. Xiao, W. Song, Compressive behavior of selective laser melting printed Gyroid structures under dynamic loading, Addit Manuf 46 (2021). https://doi.org/10.1016/j.addma.2021.102054.

[169] O. Al-Ketan, R. Rowshan, R.K. Abu Al-Rub, Topology-mechanical property relationship of 3D printed strut, skeletal, and sheet based periodic metallic cellular materials, Addit Manuf 19 (2018) 167–183. https://doi.org/10.1016/j.addma.2017.12.006.

[170] C. Yang, Q.M. Li, Y. Wang, Compressive properties of cuttlebone-like lattice (CLL) materials with functionally graded density, European Journal of Mechanics, A/Solids 87 (2021). https://doi.org/10.1016/j.euromechsol.2021.104215.

[171] I. Maskery, L.A. Parry, D. Padrao, R.J.M. Hague, I.A. Ashcroft, FLatt Pack: a research-focussed lattice design program, n.d. www.github.com/ian27ax/FLatt.

[172] P. Mehmert, Quality Analysis of Additively Manufactured Metals. Simulation Approaches, Processes, and Microstructure Properties, Elsevier Ltd, 2023. https://doi.org/https://doi.org/10.1016/B978-0-323-88664-2.00014-2.

[173] Renishaw (n.d.), The power of Additive Manufacturing Additive Manufacturing systems, (n.d.).

[174] https://www.linkedin.com/pulse/modulation-matters-how-build-all-features-great-small-marc-saunders/, (2018).

[175] Renishaw, QuantAM Manual, n.d.

[176] Technical Data Sheet LPW 316L, MDPI AG, 2017. www.lpwtechnology.com.

[177] G. Verma, Autodesk Fusion 360 Black Book, BPB Publications (2018). https://www.google.co.uk/books/edition/AUTODESK_FUSION_360_BLACK_BOOK/BYxjDwAAQBAJ?hl=en&gbpv=0&kptab=overview (accessed December 18, 2023).

[178] H. K. D. H. Bhadeshia, An aspect of the nucleation of burst martensite, J Mater Sci 17 (1982) 383–386. https://doi.org/https://doi.org/10.1007/BF00591473.

[179] ASTM International, Designation: E8/E8M − 13a Standard Test Methods for Tension Testing of Metallic Materials 1, 2022. https://doi.org/10.1520/E0008_E0008M-13A.

[180] Standard Test Method for Microindentation Hardness of Materials 1, n.d.

[181] ASTM International, Standard Test Methods of Compression Testing of Metallic Materials at Room Temperature, n.d.

[182] M. Gumustas, C.T. Sengel-Turk, A. Gumustas, S.A. Ozkan, B. Uslu, Effect of Polymer-Based Nanoparticles on the Assay of Antimicrobial Drug Delivery Systems, in: Multifunctional Systems for Combined Delivery, Biosensing and Diagnostics, Elsevier, 2017: pp. 67–108. https://doi.org/10.1016/B978-0-323-52725-5.00005-8.

[183] B. Jóźwik, A. Radoń, S. Topolska, J. Kalabis, M. Karpiński, W. Burian, D. Kołacz, M. Polak, A. Brudny, W. Łoński, A. Kolano-Burian, Influence of SLM printing parameters and hot isostatic pressure treatment on the structure and properties of CuNi3Si1 alloy, J Alloys Compd 947 (2023). https://doi.org/10.1016/j.jallcom.2023.169531.

[184] https://www.technoorg.hu/news-and-events/articles/high-resolution-scanning-electron-microscopy-1/, 5 (2023).

[185] Scanning Electron Microscopy, 2013.

[186] V. Randle, O.E. Randle, Texture Analysis. Introduction to Macrotexture, Microtexture & Orientation Mapping, n.d. www.crcpress.com.

[187] F. Bachmann, R. Hielscher, H. Schaeben, Grain detection from 2d and 3d EBSD data-Specification of the MTEX algorithm, Ultramicroscopy 111 (2011) 1720–1733. https://doi.org/10.1016/j.ultramic.2011.08.002.

[188] A.F. Ismail, K.C. Khulbe, T. Matsuura, RO Membrane Characterization, in: Reverse Osmosis, Elsevier, 2019: pp. 57–90. https://doi.org/10.1016/b978-0-12-811468-1.00003-7.

[189] D.G. Brandon, The structure of high-angle grain boundaries, Acta Metallurgica 14 (11) (1966) 1479–1484. https://doi.org/https://doi.org/10.1016/0001-6160(66)90168-4.

[190] M.N. Gussev, K.J. Leonard, In situ SEM-EBSD analysis of plastic deformation mechanisms in neutron-irradiated austenitic steel, Journal of Nuclear Materials 517 (2019) 45–56. https://doi.org/10.1016/j.jnucmat.2019.01.034.

[191] M. Drakopoulos, T. Connolley, C. Reinhard, R. Atwood, O. Magdysyuk, N. Vo, M. Hart, L. Connor, B. Humphreys, G. Howell, S. Davies, T. Hill, G. Wilkin, U. Pedersen, A. Foster, N. De Maio, M. Basham, F. Yuan, K. Wanelik, I12: The Joint Engineering, Environment and Processing (JEEP) beamline at Diamond Light Source, J Synchrotron Radiat 22 (2015) 828–838. https://doi.org/10.1107/S1600577515003513.

[192] D. Šišak Jung, T. Donath, O. Magdysyuk, J. Bednarcik, High-energy X-ray applications: current status and new opportunities, Powder Diffr 32 (2017) S22–S27. https://doi.org/10.1017/s0885715617001191.

[193] M.L. Hart, M. Drakopoulos, C. Reinhard, T. Connolley, Complete elliptical ring geometry provides energy and instrument calibration for synchrotron-based two-dimensional X-ray diffraction, J Appl Crystallogr 46 (2013) 1249–1260. https://doi.org/10.1107/S0021889813022437.

[194] J. Filik, A.W. Ashton, P.C.Y. Chang, P.A. Chater, S.J. Day, M. Drakopoulos, M.W. Gerring, M.L. Hart, O. V. Magdysyuk, S. Michalik, A. Smith, C.C. Tang, N.J. Terrill, M.T. Wharmby, H. Wilhelm, Processing two-dimensional X-ray diffraction and small-angle scattering data in DAWN 2, J Appl Crystallogr 50 (2017) 959–966. https://doi.org/10.1107/S1600576717004708.

[195] N.L. Church, C.E.P. Talbot, L.D. Connor, S. Michalik, N.G. Jones, Functional fatigue during superelastic load cycling of Ti2448 (Ti-24Nb-4Zr-8Sn, wt%), Materialia (Oxf) 28 (2023). https://doi.org/10.1016/j.mtla.2023.101719.

[196] P.J. Potts, X-Ray Fluorescence Theory, n.d.

[197] S. Nasrazadani, S. Hassani, Modern analytical techniques in failure analysis of aerospace, chemical, and oil and gas industries, in: Handbook of Materials Failure Analysis with Case Studies from the Oil and Gas Industry, Elsevier, 2015: pp. 39–54. https://doi.org/10.1016/B978-0-08-100117-2.00010-8.

[198] Dassault Systèmes, SIMULIA User Assistance 2021 - Abaqus, 13 (n.d.).

[199] W. Huang, Y. Zhan, C. Zhang, W. Lyu, Y. Li, J. Shao, Tensile resistance and shear-tension interaction relationship of T-type perfobond rid shear connectors, Journal of Building Engineering 89 (2024). https://doi.org/10.1016/j.jobe.2024.109183.

[200] P. Wang, Y. Bian, F. Yang, H. Fan, B. Zheng, Mechanical properties and energy absorption of FCC lattice structures with different orientation angles, Acta Mech 231 (2020) 3129–3144. https://doi.org/10.1007/s00707-020-02710-x.

[201] K. Hibbitt, B. Karlsson, J. Hajnyš, E. Sorensen, ABAQUS User's Manual and Theory Manual, MDPI AG, Providence, RI, USA, 2017.

[202] Leon. Lapidus, G.F. Pinder, Numerical solution of partial differential equations in science and engineering, Wiley, 1982.

[203] F. Zeng, Y. Yang, G. Qian, Fatigue properties and S-N curve estimating of 316L stainless steel prepared by SLM, Int J Fatigue 162 (2022). https://doi.org/10.1016/j.ijfatigue.2022.106946.

[204] M. Bakhtiarian, H. Omidvar, A. Mashhuriazar, Z. Sajuri, C.H. Gur, The effects of SLM process parameters on the relative density and hardness of austenitic stainless steel 316L, Journal of Materials Research and Technology 29 (2024) 1616–1629. https://doi.org/10.1016/j.jmrt.2024.01.237.

[205] A.B. Kale, J. Singh, B.K. Kim, D.I. Kim, S.H. Choi, Effect of initial microstructure on the deformation heterogeneities of 316L stainless steels fabricated by selective laser melting processing, Journal of Materials Research and Technology 9 (2020) 8867–8883. https://doi.org/10.1016/j.jmrt.2020.06.015.

[206] X. Wang, J.A. Muñiz-Lerma, M. Attarian Shandiz, O. Sanchez-Mata, M. Brochu, Crystallographic-orientation-dependent tensile behaviours of stainless steel 316L fabricated by laser powder bed fusion, Materials Science and Engineering: A 766 (2019). https://doi.org/10.1016/j.msea.2019.138395.

[207] W.J. Sames, F.A. List, S. Pannala, R.R. Dehoff, S.S. Babu, The metallurgy and processing science of metal additive manufacturing, International Materials Reviews 61 (2016) 315–360. https://doi.org/10.1080/09506608.2015.1116649.

[208] H. Ding, Q. Tang, Y. Zhu, C. Zhang, H. Yang, Cavitation erosion resistance of 316L stainless steel fabricated using selective laser melting, Friction 9 (2021) 1580–1598. https://doi.org/10.1007/s40544-020-0443-7.

[209] D. Ma, A.D. Stoica, Z. Wang, A.M. Beese, Crystallographic texture in an additively manufactured nickel-base superalloy, Materials Science and Engineering: A 684 (2017) 47–53. https://doi.org/10.1016/j.msea.2016.12.028.

[210] H.L. Wei, J. Mazumder, T. DebRoy, Evolution of solidification texture during additive manufacturing, Sci Rep 5 (2015). https://doi.org/10.1038/srep16446.

[211] S. Dépinoy, Influence of solidification conditions on chemical heterogeneities and dislocations patterning in additively manufactured 316L stainless steel, Materialia (Oxf) 24 (2022). https://doi.org/10.1016/j.mtla.2022.101472.

[212] W.F. Savage, E.F. Nippes, T.W. Miller, Microsegregation in 70Cu-30Ni Weld Metal Principles of solidification mechanics are outlined and applied to a study of cupro-nickel welds, n.d.

[213] H. Gong, K. Rafi, H. Gu, T. Starr, B. Stucker, Analysis of defect generation in Ti-6Al-4V parts made using powder bed fusion additive manufacturing processes, Addit Manuf 1 (2014) 87–98. https://doi.org/10.1016/j.addma.2014.08.002.

[214] R.K. Desu, H. Nitin Krishnamurthy, A. Balu, A.K. Gupta, S.K. Singh, Mechanical properties of Austenitic Stainless Steel 304L and 316L at elevated temperatures, Journal of Materials Research and Technology 5 (2016) 13–20. https://doi.org/10.1016/j.jmrt.2015.04.001.

[215] A.K. Agrawal, A. Singh, A. Vivek, S. Hansen, G. Daehn, Extreme twinning and hardening of 316L from a scalable impact process, Mater Lett 225 (2018) 50–53. https://doi.org/10.1016/j.matlet.2018.04.044.

[216] M. Güden, H. Yavaş, A.A. Tanrıkulu, A. Taşdemirci, B. Akın, S. Enser, A. Karakuş, B.A. Hamat, Orientation dependent tensile properties of a selective-laser-melt 316L stainless steel, Materials Science and Engineering: A 824 (2021). https://doi.org/10.1016/j.msea.2021.141808.

[217] Z. Sun, X. Tan, S.B. Tor, W.Y. Yeong, Selective laser melting of stainless steel 316L with low porosity and high build rates, Mater Des 104 (2016) 197–204. https://doi.org/10.1016/j.matdes.2016.05.035.

[218] M. Marya, V. Singh, S. Marya, J.Y. Hascoet, Microstructural Development and Technical Challenges in Laser Additive Manufacturing: Case Study with a 316L Industrial Part, Metallurgical and Materials Transactions B: Process Metallurgy and Materials Processing Science 46 (2015) 1654–1665. https://doi.org/10.1007/s11663-015-0310-5.

[219] C. Bean, F. Wang, M.A. Charpagne, P. Villechaise, V. Valle, S.R. Agnew, D.S. Gianola, T.M. Pollock, J.C. Stinville, Heterogeneous slip localization in an additively manufactured 316L stainless steel, Int J Plast 159 (2022). https://doi.org/10.1016/j.ijplas.2022.103436.

[220] M.R. Barnett, A rationale for the strong dependence of mechanical twinning on grain size, Scr Mater 59 (2008) 696–698. https://doi.org/10.1016/j.scriptamat.2008.05.027.

[221] D. Zhao, J. Dong, K.Y. Xie, Effect of local twin Schmid factor on the tension twinning activities in a highly textured Mg–3Al–1Zn alloy under different strain paths, MRS Commun 12 (2022) 217–222. https://doi.org/10.1557/s43579-022-00165-w.

[222] R. Snell, S. Tammas-Williams, L. Chechik, A. Lyle, E. Hernández-Nava, C. Boig, G. Panoutsos, I. Todd, Methods for Rapid Pore Classification in Metal Additive Manufacturing, JOM 72 (2020) 101–109. https://doi.org/10.1007/s11837-019-03761-9.

[223] D. Dong, J. Wang, C. Chen, X. Tang, Y. Ye, Z. Ren, S. Yin, Z. Yuan, M. Liu, K. Zhou, Influence of Aging Treatment Regimes on Microstructure and Mechanical Properties of Selective Laser Melted 17-4 PH Steel, Micromachines (Basel) 14 (2023). https://doi.org/10.3390/mi14040871.

[224] H.R. Lashgari, Y. Xue, C. Onggowarsito, C. Kong, S. Li, Microstructure, Tribological Properties and Corrosion Behaviour of Additively Manufactured 17-4PH Stainless Steel: Effects of Scanning Pattern, Build Orientation, and Single vs. Double scan, Mater Today Commun 25 (2020). https://doi.org/10.1016/j.mtcomm.2020.101535.

[225] T. Mukherjee, J.S. Zuback, A. De, T. DebRoy, Printability of alloys for additive manufacturing, Sci Rep 6 (2016). https://doi.org/10.1038/srep19717.

[226] M.S. Moyle, N. Haghdadi, X.Z. Liao, S.P. Ringer, S. Primig, On the microstructure and texture evolution in 17-4 PH stainless steel during laser powder bed fusion: Towards textural design, J Mater Sci Technol 117 (2022) 183–195. https://doi.org/10.1016/j.jmst.2021.12.015.

[227] S. Dobson, S. Vunnam, D. Frankel, C. Sudbrack, T. Starr, POWDER VARIATION AND MECHANICAL PROPERTIES FOR SLM 17-4 PH STAINLESS STEEL, n.d.

[228] P.D. Nezhadfar, R. Shrestha, N. Phan, N. Shamsaei, Fatigue behavior of additively manufactured 17-4 PH stainless steel: Synergistic effects of surface roughness and heat treatment, Int J Fatigue 124 (2019) 188–204. https://doi.org/10.1016/j.ijfatigue.2019.02.039.

[229] V.P. Matilainen, H. Piili, A. Salminen, O. Nyrhilä, Preliminary Investigation of Keyhole Phenomena during Single Layer Fabrication in Laser Additive Manufacturing of Stainless Steel, in: Phys Procedia, Elsevier B.V., 2015: pp. 377–387. https://doi.org/10.1016/j.phpro.2015.11.052.

[230] A. Steponaviciute, A. Selskiene, K. Stravinskas, S. Borodinas, G. Mordas, 17-4 PH stainless-steel as a material for high resolution laser metal deposition, in: Mater Today Proc, Elsevier Ltd, 2021: pp. 2268–2272. https://doi.org/10.1016/j.matpr.2021.08.143.

[231] Y. Wu, J. Shao, FCC-BCC phase transformation induced simultaneous enhancement of tensile strength and ductility at high strain rate in high-entropy alloy, Int J Plast 169 (2023). https://doi.org/https://doi.org/10.1016/j.ijplas.2023.103730.

[232] R. Hossain, F. Pahlevani, M.Z. Quadir, V. Sahajwalla, Stability of retained austenite in high carbon steel under compressive stress: An investigation from macro to nano scale, Sci Rep 6 (2016). https://doi.org/10.1038/srep34958.

[233] M. Mahmoudi, A. Elwany, A. Yadollahi, S.M. Thompson, L. Bian, N. Shamsaei, Mechanical properties and microstructural characterization of selective laser melted 17-4 PH stainless steel, Rapid Prototyp J 23 (2017) 280–294. https://doi.org/10.1108/RPJ-12-2015-0192.

[234] M.J. Uddin, H.R. Siller, R.A. Mirshams, T.A. Byers, B. Rout, Effects of proton irradiation on nanoindentation strain-rate sensitivity and microstructural properties in L-PBF 17–4 PH stainless steels, Materials Science and Engineering: A 837 (2022). https://doi.org/10.1016/j.msea.2022.142719.

[235] Z. Hu, H. Zhu, H. Zhang, X. Zeng, Experimental investigation on selective laser melting of 17-4PH stainless steel, Opt Laser Technol 87 (2017) 17–25. https://doi.org/10.1016/j.optlastec.2016.07.012.

[236] N. Guennouni, A. Barroux, C. Grosjean, D. Maisonnette, E. Nivet, E. Andrieu, D. Poquillon, L. Laffont, C. Blanc, Comparative study of the microstructure between a laser beam melted 17-4PH stainless steel and its conventional counterpart, Materials Science and Engineering: A 823 (2021). https://doi.org/10.1016/j.msea.2021.141718.

[237] S. An, D.R. Eo, H. Lim, I. Sohn, K. Choi, Prediction of martensitic transformation and residual stress field on 17–4 PH stainless steel fabricated by laser powder bed fusion, Addit Manuf 91 (2024). https://doi.org/10.1016/j.addma.2024.104339.

[238] S.Y. Liu, H.Q. Li, C.X. Qin, R. Zong, X.Y. Fang, The effect of energy density on texture and mechanical anisotropy in selective laser melted Inconel 718, Mater Des 191 (2020). https://doi.org/10.1016/j.matdes.2020.108642.

[239] T.H. Hsu, P.C. Huang, M.Y. Lee, K.C. Chang, C.C. Lee, M.Y. Li, C.P. Chen, K.K. Jen, A.C. Yeh, Effect of processing parameters on the fractions of martensite in 17-4 PH stainless steel fabricated by selective laser melting, J Alloys Compd 859 (2021). https://doi.org/10.1016/j.jallcom.2020.157758.

[240] S. An, D.R. Eo, I. Sohn, K. Choi, Homogenization on solution treatment and its effects on the precipitation-hardening of selective laser melted 17-4PH stainless steel, J Mater Sci Technol 166 (2023) 47–57. https://doi.org/10.1016/j.jmst.2023.04.055.

[241] K. Li, J. Zhan, T. Yang, A.C. To, S. Tan, Q. Tang, H. Cao, L.E. Murr, Homogenization timing effect on microstructure and precipitation strengthening of 17–4PH stainless steel fabricated by laser powder bed fusion, Addit Manuf 52 (2022). https://doi.org/10.1016/j.addma.2022.102672.

[242] Y. Sun, R.J. Hebert, M. Aindow, Effect of heat treatments on microstructural evolution of additively manufactured and wrought 17-4PH stainless steel, Mater Des 156 (2018) 429–440. https://doi.org/10.1016/j.matdes.2018.07.015.

[243] M.S. Moyle, N. Haghdadi, X.Z. Liao, S.P. Ringer, S. Primig, On the microstructure and texture evolution in 17-4 PH stainless steel during laser powder bed fusion: Towards textural design, J Mater Sci Technol 117 (2022) 183–195. https://doi.org/10.1016/j.jmst.2021.12.015.

[244] H.K. Rafi, D. Pal, N. Patil, T.L. Starr, B.E. Stucker, Microstructure and Mechanical Behavior of 17-4 Precipitation Hardenable Steel Processed by Selective Laser Melting, J Mater Eng Perform 23 (2014) 4421–4428. https://doi.org/10.1007/s11665-014-1226-y.

[245] A. Yadollahi, M. Mahmoudi, A. Elwany, H. Doude, L. Bian, J.C. Newman, Effects of crack orientation and heat treatment on fatigue-crack-growth behavior of AM 17-4 PH stainless steel, Eng Fract Mech 226 (2020). https://doi.org/10.1016/j.engfracmech.2020.106874.

[246] P.D. Nezhadfar, E. Burford, K. Anderson-Wedge, B. Zhang, S. Shao, S.R. Daniewicz, N. Shamsaei, Fatigue crack growth behavior of additively manufactured 17-4 PH stainless steel: Effects of build orientation and microstructure, Int J Fatigue 123 (2019) 168–179. https://doi.org/10.1016/j.ijfatigue.2019.02.015.

[247] M. Alnajjar, F. Christien, K. Wolski, C. Bosch, Evidence of austenite by-passing in a stainless steel obtained from laser melting additive manufacturing, Addit Manuf 25 (2019) 187–195. https://doi.org/10.1016/j.addma.2018.11.004.

[248] H. Eskandari, H.R. Lashgari, L. Ye, M. Eizadjou, H. Wang, Microstructural characterization and mechanical properties of additively manufactured 17–4PH stainless steel, Mater Today Commun 30 (2022). https://doi.org/10.1016/j.mtcomm.2021.103075.

[249] C. Li, Y. Chen, X. Zhang, T. Liu, Y. Peng, K. Wang, Effect of heat treatment on microstructure and mechanical properties of 17-4PH stainless steel manufactured by laser-powder bed fusion, Journal of Materials Research and Technology 26 (2023) 5707–5715. https://doi.org/10.1016/j.jmrt.2023.08.283.

[250] T. LeBrun, T. Nakamoto, K. Horikawa, H. Kobayashi, Effect of retained austenite on subsequent thermal processing and resultant mechanical properties of selective laser melted 17-4 PH stainless steel, Mater Des 81 (2015) 44–53. https://doi.org/10.1016/j.matdes.2015.05.026.

[251] A. Ahadi, Q. Sun, Stress-induced nanoscale phase transition in superelastic NiTi by in situ X-ray diffraction, Acta Mater 90 (2015) 272–281. https://doi.org/10.1016/j.actamat.2015.02.024.

[252] Y. Li, S. Liu, H. Zhi, X. Yang, J. Zhang, Y. Wang, In-situ generation of high-strength AISI 1045 steel with SiO2 nano-precipitation by selective laser melting (SLM), J Manuf Process 94 (2023) 374–386. https://doi.org/10.1016/j.jmapro.2023.03.064.

[253] P. Šimonová, W. Pabst, J. Cibulková, Crystallite size of pure tin oxide ceramics and its growth during sintering determined from XRD line broadening – A methodological case study and a practitioners' guide, Ceram Int 47 (2021) 35333–35347. https://doi.org/10.1016/j.ceramint.2021.09.076.

[254] A.R. Bushroa, R.G. Rahbari, H.H. Masjuki, M.R. Muhamad, Approximation of crystallite size and microstrain via XRD line broadening analysis in TiSiN thin films, Vacuum 86 (2012) 1107–1112. https://doi.org/10.1016/j.vacuum.2011.10.011.

[255] E. Pakizeh, M. Moradi, A. Ahmadi, Effect of sol-gel pH on XRD peak broadening, lattice strain, ferroelectric domain orientation, and optical bandgap of nanocrystalline Pb 1.1(Zr0.52Ti0.48)O3, Journal of Physics and Chemistry of Solids 75 (2014) 174–181. https://doi.org/10.1016/j.jpcs.2013.09.005.

[256] T.H. Hsu, Y.J. Chang, C.Y. Huang, H.W. Yen, C.P. Chen, K.K. Jen, A.C. Yeh, Microstructure and property of a selective laser melting process induced oxide dispersion strengthened 17-4 PH stainless steel, J Alloys Compd 803 (2019) 30–41. https://doi.org/10.1016/j.jallcom.2019.06.289.

[257] D. Krizan, B.C. De, Analysis of the Strain-Induced Martensitic Transformation of Retained Austenite in Cold Rolled Micro-Alloyed TRIP Steel, (n.d.). https://doi.org/10.2374/SRI07SP1.

[258] B. AlMangour, M. Luqman, D. Grzesiak, H. Al-Harbi, F. Ijaz, Effect of processing parameters on the microstructure and mechanical properties of Co–Cr–Mo alloy fabricated by selective laser melting, Materials Science and Engineering: A 792 (2020). https://doi.org/10.1016/j.msea.2020.139456.

[259] M. Soleimani, A. Kalhor, H. Mirzadeh, Transformation-induced plasticity (TRIP) in advanced steels: A review, Materials Science and Engineering: A 795 (2020). https://doi.org/10.1016/j.msea.2020.140023.

[260] L.E. Murr, E. Martinez, J. Hernandez, S. Collins, K.N. Amato, S.M. Gaytan, P.W. Shindo, Microstructures and Properties of 17-4 PH Stainless Steel Fabricated by Selective Laser Melting, Journal of Materials Research and Technology 1 (2012) 167–177. https://doi.org/https://doi.org/10.1016/S2238-7854(12)70029-7.

[261] X. Lijun, L. Zhiwen, X. Haifeng, Z. Chao, S. Mingxuan, W. Chang, Z. Shulan, Investigation on the precipitate morphology and fraction characterization by atomic force microscopy, Ultramicroscopy 253 (2023). https://doi.org/10.1016/j.ultramic.2023.113796.

[262] W. Wei, J.C. Xiao, C.F. Wang, Q. Cheng, F.J. Guo, Q. He, M.S. Wang, S.Z. Jiang, C.X. Huang, Hierarchical microstructure and enhanced mechanical properties of SLM-fabricated GH5188 Co-superalloy, Materials Science and Engineering: A 831 (2022). https://doi.org/10.1016/j.msea.2021.142276.

[263] H. Pirgazi, M. Sanjari, S. Tamimi, B. Shalchi Amirkhiz, L.A.I. Kestens, M. Mohammadi, Texture evolution in selective laser melted maraging stainless steel CX with martensitic transformation, J Mater Sci 56 (2021) 844–853. https://doi.org/10.1007/s10853-020-05290-2.

[264] Z. Sun, X. Tan, S.B. Tor, C.K. Chua, Simultaneously enhanced strength and ductility for 3D-printed stainless steel 316L by selective laser melting, NPG Asia Mater 10 (2018) 127–136. https://doi.org/10.1038/s41427-018-0018-5.

[265] Y. Chen, X. Wang, J. shen, Y. Peng, Y. Jiang, X. Yang, S.B. Leen, J. Gong, Deformation mechanisms of selective laser melted 316L austenitic stainless steel in high temperature low cycle fatigue, Materials Science and Engineering: A 843 (2022). https://doi.org/10.1016/j.msea.2022.143123.

[266] W. Li, L. Meng, S. Wang, H. Zhang, X. Niu, H. Lu, Plastic deformation behavior and strengthening mechanism of SLM 316L reinforced by micro-TiC particles, Materials Science and Engineering: A 884 (2023). https://doi.org/10.1016/j.msea.2023.145557.

[267] H. Niknam, A.H. Akbarzadeh, Graded lattice structures: Simultaneous enhancement in stiffness and energy absorption, Mater Des 196 (2020). https://doi.org/10.1016/j.matdes.2020.109129.

[268] Lube-Tech, Polymer Tribology, Lube: The European Lubricants Industry Magazine 135 (2016) 32–37.

[269] M. Zheng, Y. Li, C. Wang, J. Bai, L. Wang, Z. Liu, M. Abdel Wahab, Prediction of contact stress in bolted joints using the Polynomial Chaos-Kriging model, Eng Fail Anal 154 (2023). https://doi.org/10.1016/j.engfailanal.2023.107646.

[270] L. Yue, H. Liu, Z. Cheng, Q. Kan, G. Kang, Dynamic crushing behavior of a novel bi-directional gradient lattice structure under axial and oblique impact loadings, Thin-Walled Structures 198 (2024). https://doi.org/10.1016/j.tws.2024.111697.

[271] W. Song, G. Feng, G. Yu, G. Shi, L. Xiao, Dynamic mechanical behavior of additively manufactured bio-inspired metallic lattice structure subjected to high strain rate impact loading, Int J Impact Eng 181 (2023). https://doi.org/10.1016/j.ijimpeng.2023.104752.

[272] İ.K. Odacı, M. Güden, C. Kılıçaslan, A. Taşdemirci, The varying densification strain in a multi-layer aluminum corrugate structure: Direct impact testing and layer-wise numerical modelling, Int J Impact Eng 103 (2017) 64–75. https://doi.org/10.1016/j.ijimpeng.2016.10.014.

[273] H. Zhou, D.Z. Zhang, N. He, M. Zhao, Topology optimization of multi-morphology composite lattice structure with anisotropy properties, Compos Struct 321 (2023). https://doi.org/10.1016/j.compstruct.2023.117294.

[274] N. Qiu, Y. Wan, Y. Shen, J. Fang, Experimental and numerical studies on mechanical properties of TPMS structures, Int J Mech Sci 261 (2024). https://doi.org/10.1016/j.ijmecsci.2023.108657.

[275] G. He, H. Yang, T. Chen, Y. Ning, H. Zou, F. Zhu, Lattice Structure Design Method Aimed at Energy Absorption Performance Based on Bionic Design, Machines 10 (2022). https://doi.org/10.3390/machines10100965.

[276] R. Vrána, J. Jaroš, D. Koutný, J. Nosek, T. Zikmund, J. Kaiser, D. Paloušek, Contour laser strategy and its benefits for lattice structure manufacturing by selective laser melting technology, J Manuf Process 74 (2022) 640–657. https://doi.org/10.1016/j.jmapro.2021.12.006.

[277] H. Chi, B. Gong, Analysis of energy conversion law in vehicle collision accident, in: J Phys Conf Ser, Institute of Physics Publishing, 2020. https://doi.org/10.1088/1742-6596/1486/7/072014.

[278] Z. Zheng, C. Wang, J. Yu, S.R. Reid, J.J. Harrigan, Dynamic stress-strain states for metal foams using a 3D cellular model, J Mech Phys Solids 72 (2014) 93–114. https://doi.org/10.1016/j.jmps.2014.07.013.

[279] G. Brando, F. Romana Andreacola, I. Capasso, D. Forni, E. Cadoni, Strain-rate response of 3D printed 17-4PH stainless steel manufactured via selective laser melting, Constr Build Mater 409 (2023). https://doi.org/10.1016/j.conbuildmat.2023.133971.

[280] ASM Handbook Committee, Properties and Selection Nonferrous Alloys and Special-Purpose Materials, 1990. https://doi.org/https://doi.org/10.31399/asm.hb.v02.9781627081627.

[281] M. Simonelli, Y.Y. Tse, C. Tuck, On the texture formation of selective laser melted Ti-6Al-4V, Metall Mater Trans A Phys Metall Mater Sci 45 (2014) 2863–2872. https://doi.org/10.1007/s11661-014-2218-0.

[282] J. Samei, H. Asgari, C. Pelligra, M. Sanjari, S. Salavati, A. Shahriari, M. Amirmaleki, M. Jahanbakht, A. Hadadzadeh, B.S. Amirkhiz, M. Mohammadi, A hybrid additively manufactured martensitic-maraging stainless steel with superior strength and corrosion resistance for plastic injection molding dies, Addit Manuf 45 (2021). https://doi.org/10.1016/j.addma.2021.102068.

[283] M.S. Pham, C. Liu, I. Todd, J. Lertthanasarn, Damage-tolerant architected materials inspired by crystal microstructure, Nature 565 (2019) 305–311. https://doi.org/10.1038/s41586-018-0850-3.